VNIVERSITAT DE VALÈNCIA

Doctoral Programme in Nanoscience and Nanotechnology

Institute of Molecular Science (ICMol)

Doctoral Dissertation

LIGHT-EMITTING DIODES BASED ON PEROVSKITES AND THERMALLY ACTIVATED DELAYED FLUORESCENCE

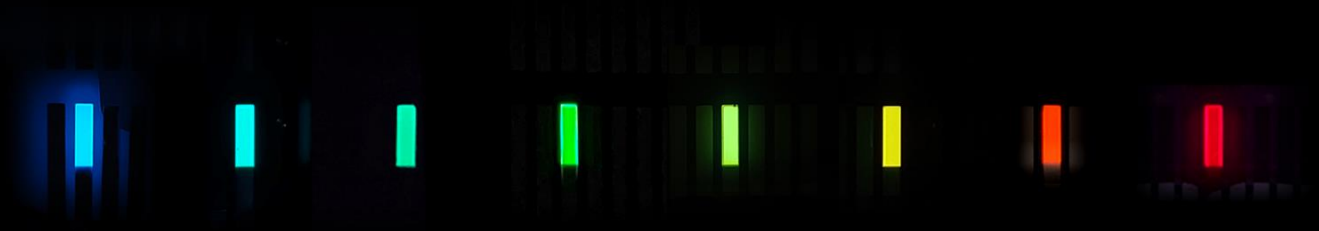

Michele Forzatti

November 2025

Directors:

Prof. Dr. Hendrik Jan Bolink

Prof. Dr. Daniel Tordera Salvador

VNIVERSITAT DE VALÈNCIA

Doctoral Programme in
Nanoscience and Nanotechnology

Institute of Molecular Science (ICMol)

Doctoral Dissertation:

LIGHT-EMITTING DIODES BASED ON PEROVSKITES AND THERMALLY ACTIVATED DELAYED FLUORESCENCE

Michele Forzatti

November 2025

Directors:

Prof. Dr. Hendrik Jan Bolink

Prof. Dr. Daniel Tordera Salvador

Prof. Dr. Hendrik Jan Bolink, catedràtic d'Universitat i investigador en el Institut de Ciència Molecular (ICMol) de la Universitat de València, i **Prof. Dr. Daniel Tordera Salvador**, professor titular i investigador en el Institut de Ciència Molecular (ICMol) de la Universitat de València, certifiquen que la memòria presentada per l'estudiant de doctorat Michele Forzatti, amb el títol "*Light-emitting diodes based on perovskites and thermally activated delayed fluorescence*", correspon a la seua Tesi Doctoral i ha sigut realitzada sota la seua direcció i tutoria, autoritzant mitjançant aquest escrit la presentació d'aquesta.

A Paterna (València), a 18 de novembre de 2025

Prof. Dr. Hendrik Jan Bolink
(Director i tutor)

HENDRIK JAN| BOLINK
Firmado digitalmente por HENDRIK JAN|BOLINK
Fecha: 2025.11.18 15:56:59 +01'00'

Prof. Dr. Daniel Tordera Salvador
(Director)

Firmado por DANIEL ANTONIO TORDERA SALVADOR - NIF:***7252** el día 18/11/2025 con un certificado emitido por ACCV RSA1 CLIENTE

Dedicada al mè pà

Index

Chapter 1.

Introduction and aim of the thesis

1.1. Overview

Light plays a fundamental role in human life. In addition to enabling vision, it influences our circadian rhythms, mood, productivity, and even long-term health.[1] Historically, humans were exposed to consistent daily cycles of light and darkness dictated by the solar day. Due to its importance, it is natural that we have sought to control light, giving rise to artificial lighting. Artificial lighting has allowed humans to fade the boundaries of day and night and extend activity beyond daylight hours.[2]

Early humans turned to fire-based sources such as torches, oil lamps, and candles. Though simple and portable, these sources were inefficient, produced smoke, and carried fire hazards. The advent of gas lighting in the 18th and 19th centuries marked a significant leap, particularly in urban areas, where streets and buildings could be illuminated more uniformly. This was followed by a major technological breakthrough with the invention of the incandescent light bulb by Thomas Edison in 1879. By heating a tungsten filament until it glowed, incandescent bulbs provided a warm and steady light.

However, incandescent bulbs were notoriously energy-inefficient, converting only about 1-5% of the electricity they consumed into light, with the rest being emitted as heat.[3] In today's world, where energy conservation and sustainability are global priorities, more efficient lighting technologies can play a crucial role in reducing energy consumption, lowering carbon emissions, combating climate change, and advancing environmental sustainability.[3] According to the International Energy Agency (IEA), in 2020 lighting accounted for about 15% of global electricity consumption in buildings (residential + commercial) and for approximately 4.5% to 5% of total CO_2 emissions.[4]

In the mid-20th century, fluorescent lights offered a more efficient substitute for incandescent bulbs. These lamps used electric discharge through mercury vapor to generate ultraviolet light, which then activated a phosphor coating to emit visible light. They were more efficient than incandescent bulbs, converting 10-15% of the electricity into light, but presented issues like delayed start-up, flickering, and mercury content, leading to environmental and disposal concerns.[5] In the 21st century, solid-state lighting technology advanced significantly, with light-emitting diodes (LEDs) establishing themselves as the primary lighting solution. LEDs offer high energy efficiency up to 25%, long lifespans, reduced use of toxic materials and the ability to tune brightness and color, revolutionizing lighting in homes, industries, and public spaces.

Meanwhile, modern electronic devices such as smartphones, tablets, laptops and televisions rely heavily on their display as the primary interface for the users to see and interact with. The parameters that define a display's quality, like resolution, brightness, contrast, color accuracy, refresh rate, and power efficiency, are deeply connected to the underlying display technology used. LCD (Liquid Crystal Display) is still one of the most common and widely used display technologies worldwide, using a constant backlight shining through liquid crystals to create images.

However, in high-end smartphones and some premium TVs, organic LEDs (OLEDs) are becoming increasingly popular due to their unique properties and advantages over traditional display technologies, such as superior contrast, wider viewing angles, faster response times, thin and lightweight design, high color purity and power efficiency. Color purity is a critical parameter that reflects the ability of a display to produce saturated and spectrally narrow colors and provide a wider and more accurate color gamut, enhancing the realism and fidelity of images. Power efficiency is particularly relevant in portable devices like smartphones and laptops, where battery life becomes crucial. Display power consumption often constitutes a significant fraction of overall device energy use (35%-50%), especially at high screen brightness, directly influencing operational time between charges.

For the above-mentioned reasons, research into emerging solid-state lighting technologies continues, as it holds significant promise for advancing display performance and energy efficiency in modern devices and significantly reducing the ecological footprint of lighting.

1.2. Fundamentals of organic light-emitting diodes

Organic light-emitting diodes (OLEDs) are solid-state thin film devices that convert electrical energy into visible light through the radiative recombination of charge carriers in organic semiconductor layers.

1.2.1. Working principles

Organic semiconductors

Organic molecules can be deposited as an amorphous molecular thin film (with a range of deposition techniques described in Paragraph 1.2.4). For a relatively small subset of organic molecules with specific structural features, charges can be injected into their thin films when sandwiched between two electrodes, conducting electricity. Since they show conductivity and other properties associated with semiconductor materials, like absorption and emission of light in the visible spectral range, these materials are known as organic semiconductors.

The behavior of electrons in molecules is described by mathematical functions called molecular orbitals. Each molecular orbital has a calculated energy level and is said to be able to "hold" two electrons. Most organic molecules have an even number of electrons and no unpaired ones; in the ground, most stable state, electrons fill these discrete energy levels completely beginning from the lowest in energy. In this state, the molecule has a total spin angular momentum of 0, for which reason the ground state is said to be a *singlet* state. Of all the orbitals filled with electrons, the one having the highest energy is termed the *highest occupied molecular orbital* (HOMO). Conversely, the orbital among the unfilled ones that has the lowest electron energy is called the *lowest unoccupied molecular orbital* (LUMO). The HOMO and the LUMO may be considered as analogous to valence and conduction bands, respectively, in conventional semiconductor physics.

If an electron is moved to an upper empty orbital, the molecule is said to be in an excited state. This state is unstable, so the molecule tends to release its energy to return to the ground state. When the excess energy is released as light, the process is called luminescence. Luminescence can be classified depending on how the energy is transferred to the system. If the excited state is created via the absorption of light, it will be termed *photoluminescence* (PL). In 1953, it was discovered that by applying a high voltage to thin films of fluorescent organic dyes, light was emitted.[6] The phenomenon (emission of light subsequent to the transfer of energy to a molecule by an electric field or current) is known as *electroluminescence* (EL).

Single-layer OLEDs

The simplest OLED device (hereafter also simply referred to as 'device' throughout this thesis) architecture that can be made is an anode, an organic semiconductor film and a cathode. When a sufficient voltage is applied, since the HOMOs of the molecules are occupied and cannot accept additional charge, an electron can be transferred from the cathode to the LUMOs, forming an electron current. At the same time, an electron can be removed from the HOMOs and transferred to the anode, which can be conceptualized as supplying a "lack of an electron", named *hole*, forming a hole current. This "sandwich-type" arrangement in which an organic semiconductor is interposed between two electrodes is called *vertical*; current flows perpendicular to the semiconductor surface, through the bulk of the semiconductor film. After their injection, charges then migrate through the film following the electric field. The sought-after event is that the electrons and holes encounter and form a chargeless electron–hole pair that can transport energy, called *exciton*. In organic semiconductors, excitons are highly

localized as they are confined to local sites or molecules (even though their energy can still be transferred to neighboring molecules). The energy of these excited states can be released (*decay*) with the emission of light (*radiatively*), producing the wanted electroluminescence. The wavelength of the light emission corresponds to the exciton energy. Different molecules have different energy levels, hence emission colors.

In the most common layer arrangement, the positive electrode ('p') is placed at the bottom and is transparent, while the negative electrode ('n') is placed on top of the intrinsic ('i') emissive layer (EML) and is opaque to reflect the photons emitted by the EML under bias that travel towards it downwards. The resulting devices with this 'p-i-n' architecture, which will be implicitly referred to throughout the thesis, are therefore said to be *bottom-emitting*.

Multi-layer OLED architectures

Ideally, electrons and holes should be injected applying as little bias as possible, and each electron should recombine with a hole rather than leaving the organic semiconductor at the counter-electrode. In 1987, Tang and Van Slyke understood that both can be obtained with a more complicated device architecture, reporting, for the first time, OLED emission at operating voltage and efficiency levels suitable for actual applications.[7] In particular, they found that inserting injection layers between the electrodes and the light-emitting compound (in other words, using a layered heterostructure with multiple different materials, **Figure 1.1a**) significantly enhances the recombination efficiency. Such electron and hole injection and transport materials (EIL, ETL, HIL, HTL) should be chosen according to their energy levels and to the work functions (that is, the energy required to remove an electron from the surface of a conductor) of the cathode and anode: they should possess either a HOMO level positioned between the work function of the anode and the HOMO of the light-emitting material, or a LUMO level located between the LUMO of the light-emitting material and the work function of the cathode. The resulting energy level diagram provides a clear visual representation of these alignments, serving as a practical tool to evaluate charge injection barriers (**Figure 1.1b**). This formation of a graded energy junction lowers the charge injection barriers, thereby decreasing the turn-on voltage required for light emission. To prevent charges from escaping the organic film without undergoing recombination, blocking layers can be introduced (EBL, HBL). Blocking materials have a high LUMO (or low HOMO) and are placed between the injection layer and the emissive layer, on the anode or cathode side, respectively.

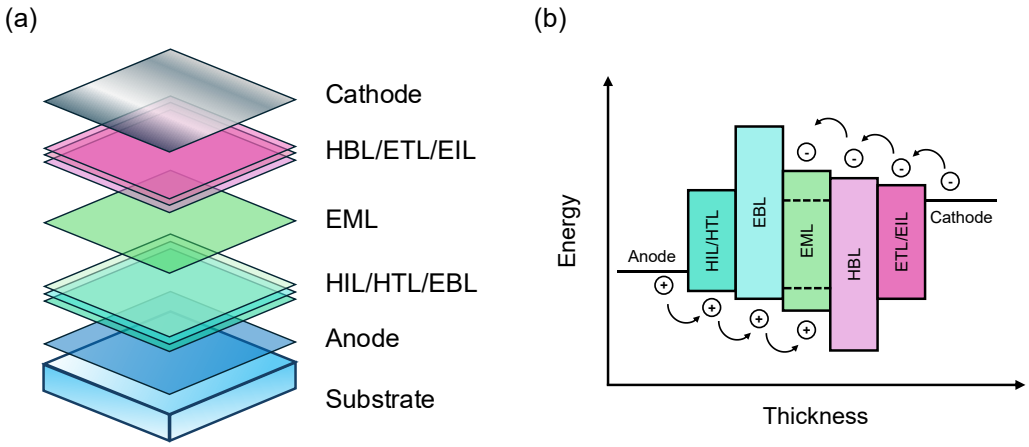

Figure 1.1. (a) Multi-layer OLED architecture. (b) Energy level diagram of the various layers. The dashed lines represent the HOMO and LUMO levels of the emissive material.

The asymmetrical and directional layer structure causes charge injection and recombination to occur efficiently only under forward bias. When the device is reverse-biased, the charge flow is minimal due to the large injection barriers. In other words, OLED devices exhibit diode characteristics (hence the name).

Commonly employed materials

Cathode materials should have a low work function to reduce the barrier at the metal-organic interface and facilitate electron injection. Examples include Yb, Ca, Al and Ba. However, their low work function also entails high chemical reactivity and ease of oxidation. The cathode sensitivity to oxygen is one of the primary reasons for hermetic sealing or encapsulation of OLED devices.

Anodes, too, should have a reasonable work function (to match with the HTLs) and be transparent (to let light through) while having a high conductivity. Transparent conductive oxides (TCO) possess all these characteristics and are therefore the most commonly employed anode materials. Among them, indium-tin oxide (ITO) has been used as an electrode for liquid crystal displays for many years already, meaning that the technology and infrastructures for its fabrication are already readily available.

PEDOT:PSS ((poly(3,4-ethylenedioxythiophene)–polystyrene sulfonic acid), a mixture of two polymers **Figure 1.2**), is a very commonly used HIL as its work function of about 5.1 – 5.3 eV[8] improves hole injection. It can be fabricated via spin-coating (see Paragraph 1.2.4) and has the added benefit of smoothening the rough ITO surface, preventing filamentary current injection due to high local fields and short circuits in the devices.

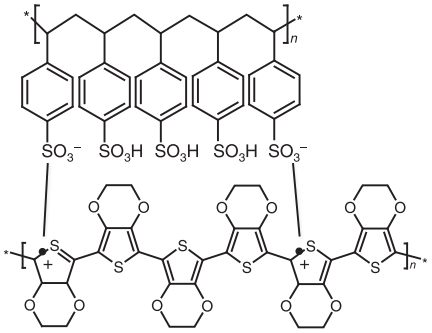

Figure 1.2. Chemical structure of the mixture of PEDOT (bottom) with PSS (top), PEDOT:PSS.

Various PEDOT:PSS formulations, such as AI 4083 and CH 8000, differ in their PEDOT-to-PSS ratio, leading to differences in conductivity and work function. To overcome particularly large hole injection potential barriers between the anode and the overlying organic layer, a polymer blend of PEDOT:PSS and a copolymer of perfluorosulfonic acid and polytetrafluoroethylene (PFI) can be spin-coated instead. The vertical self-organization of the two components results in a surface-enriched PFI layer with a gradually increasing work function (from 5.2 to 5.95 eV) through the layer (*GraHIL*, gradient HIL).[9,10]

The function of the HTL is to deliver the holes to the EML efficiently. Two commonly used HTL materials are 1,1-bis[(di-4-tolylamino)phenyl]cyclohexane (TAPC) and 1,3-bis(N-carbazolyl)benzene (mCP). Their chemical structure is illustrated in **Figure 1.3a-b**.

The function of the ETL is to deliver the electrons to the EML efficiently. An ideal ETL material should therefore possess a LUMO level closely matched with cathode to facilitate electron injection, as well as a

high electron mobility for electron transport. Two commonly used ETL materials are 1,3,5-tris(N-phenylbenzimidizol–2-yl)benzene (TPBi) and 2,4,6-tris[3-(diphenylphosphinyl)phenyl]-1,3,5-triazine (PO-T2T). Their chemical structure is illustrated in **Figure 1.3c-d**.

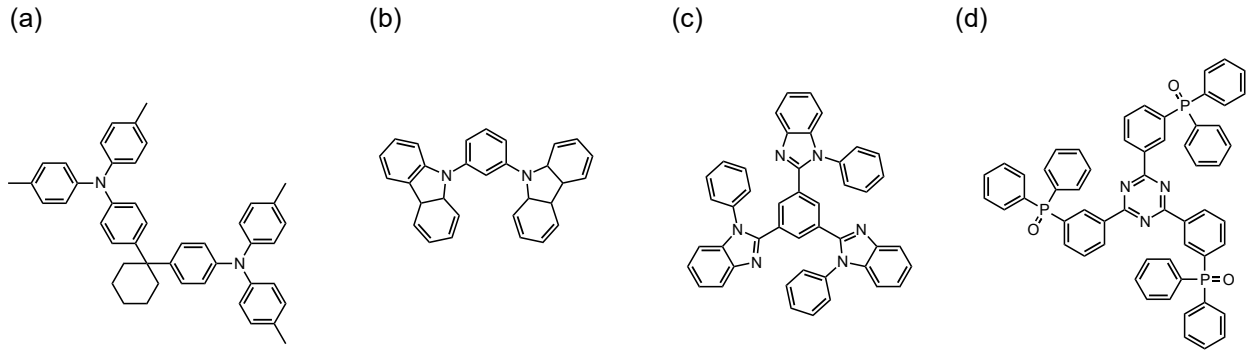

Figure 1.3. Chemical structure of common HTL and ETL materials. (a) TAPC. (b) mCP. (c) TPBi. (d) PO-T2T.

The chemical structures of the selected compounds are representative of those of most transport materials: they feature rigid aromatic and conjugated backbones to allow π–π electron delocalization and support charge mobility, with HTLs units being electron-rich (e.g. triphenylamine, carbazole, phenylcarbazole) and ETLs units being electron-deficient (aromatic heterocycles like triazine and/or strong electron-withdrawing substituents like –P=O).

Singlet and triplet excitons

The molecules that find themselves in an excited state by recombination of opposite charges have one of four possible spin states. One of them has a zero spin angular momentum and is therefore a singlet state, just like the ground state, while three of them have a total spin of 1 and are called *triplet* states. The triplet excited states are degenerate (they have the same energy) and have a lower energy than the singlet excited state. When excitons are generated by recombination of opposite charges, since the process is independent of the spin of the recombining charges,[11] the singlets state are created with a probability of only 25%, in contrast to a 75% probability for triplets.

Singlet excited states can readily decay to singlet ground states through a process known as *fluorescence*. In OLEDs revolving around molecules that can only emit via fluorescence, only about one-quarter of the injected electrons and holes recombine to produce light inside the device at best (assuming 100% carrier balance and 100% fluorescence quantum efficiency, see Eq. 1.4 below). Other organic compounds contain heavy metals such as iridium or platinum that introduce relativistic angular momentum to the electrons. This enables the normally prohibited radiative relaxation of triplets called *phosphorescence* and thus the successful conversion of all injected charge carriers into photons inside the device. However, even if allowed, the process remains slower than fluorescence. As a consequence, the triplet exciton lifetime is longer compared to that of singlet excitons, making them more susceptible to quenching (that is, loss of energy without emission) and requiring the adoption of mitigation strategies, as explained in the next paragraph.

Common EML structure

Most quenching mechanisms become more likely when the distance between emitter molecules decreases (aggregation-caused quenching, ACQ). For example, triplet-triplet annihilation (TTA) can take

place when two molecules each in a triplet excited state interact: an electron from one triplet-excited molecule exchanges with an electron from the other, resulting in one molecule being promoted to a higher-energy singlet excited state while the other returns to the ground state. The process follows the Dexter mechanism, where electron exchange occurs only when the molecular wavefunctions overlap, requiring intermolecular distances shorter than about 1 nm. Moreover, close packing can lead to the formation of molecular aggregates or excimers, which often have different electronic states that favor non-radiative decay pathways instead of light emission. These factors jointly result in emitters' luminescence getting quenched when emitter molecules are too close together.

For this reason, emitters in OLEDs are typically dispersed in a host matrix ("*host-dopant system*") at low concentrations (1-10% by weight or molar) rather than forming a neat, pure emitter film (**Figure 1.4**, left). The host material, which is said to be *doped*, is designed to absorb charge carriers and transfer the energy to the dispersed emitter (*dopant* or *guest*) molecules: during operation, the excited states are first formed in the host material, then the energy is transferred to the dopant guest molecules through dipole-dipole interaction (Förster) or exchange induced (Dexter) energy transfer processes.[12] In some cases, electrons and holes can also be sequentially trapped in the LUMO and HOMO of the dopant molecules, when these levels lie below and above those of the host, respectively, leading to direct recombination on the dopant. The already mentioned mCP and 4,4-N,N′-dicarbazole-1,1′-biphenyl (CBP) are examples of host materials. Unfortunately, the choice of a suitable host for a certain emitter is not always easy, as a good host material should have a larger band gap and triplet energy levels than those of the guest,[13] high charge mobility, compatibility with the guest molecule in forming homogeneous thin films, and good thermal and electrochemical stability, all simultaneously.

Alternatively, emitter molecules can be inserted into OLEDs in the form of sub-monolayers with a thickness smaller than 1 nm, called *ultrathin EMLs* (UEMLs). Molecules forming UEMLs are not arranged as a continuous film (the term "layer" is still used, but only implying the deposition of material) but are instead dispersed as isolated islands on top of the underlying layer.[14–17] UEMLs represent a special, two-dimensional form of emitter doping, where the materials on both sides of the dopant molecules can be considered as the host, while the inserted ultrathin layer itself acts as the dopant guest,[18] with the electroluminescent mechanism still predominantly involving a host-guest energy transfer. Compared to traditional doped emissive layers, UEML-based OLEDs have a simpler preparation process, as it avoids the complicated and expensive co-evaporation technology (when the emissive layer is thermally evaporated) and reduces material consumption.

UEMLs can be inserted into a single material, typically a common host one like mCP or CBP, or into heterojunction HTL/ETL interfaces (**Figure 1.4**, right), which takes advantage of the naturally forming recombination zone at the interface (due to the holes and electrons confinement). Moreover, if the two materials that sandwich the emitters can form exciplexes (that is, intermolecular excited states of donor−acceptor complexes, whose formation cannot be impeded by the island-like UEMLs as they are discontinuous), an additional process besides direct exciton formation on the UEML can occur, namely an energy transfer from exciplexes to the emitters.[19] In this way, the exciplexes can act as "sensitizers", funneling energy into the UEML. The energy can also come from triplets, because exciplexes typically have small ΔE_{ST} values, enabling efficient up-conversion of triplet exciplexes via reverse intersystem crossing (described in the next paragraph) followed by Förster energy transfer, which also alleviates TTA.[19] The formation of exciplexes also has the advantage of lowering the carrier densities in the EML, reducing efficiency roll-off caused by triplet-polaron quenching, another quenching mechanism.[20] Finally, heterojunction interfaces with exciplex formation are more flexible, as even emitters that may not directly align with transport layers can still be efficiently excited via the exciplex (subject to spectral overlap between the emission band of the exciplex and the absorption of the emitter), widening the material choice. In contrast, exploiting the advantages of mixed hosts in traditional host-dopant system

is very challenging, requiring an precise control of co-deposition rates of three components simultaneously.[19]

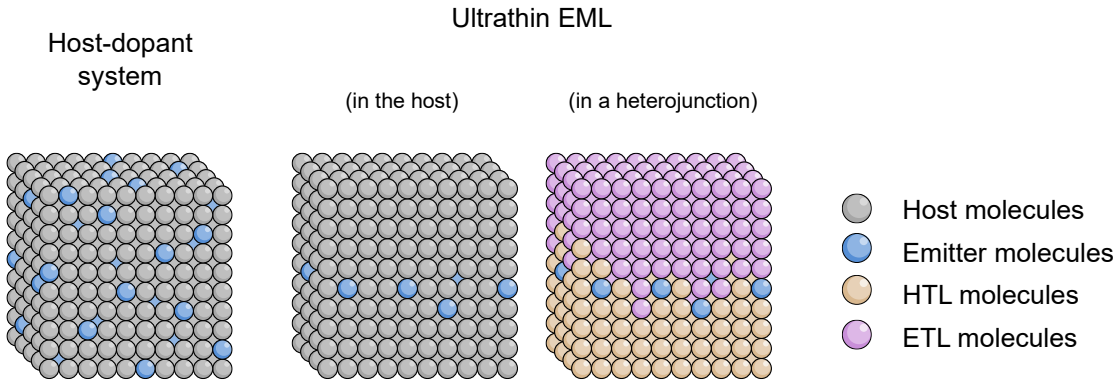

Figure 1.4. Schematic representation of different OLED emissive layer structures.

1.2.2. Thermally activated delayed fluorescence

Exciton recombination, through which organic semiconductors emit light, is governed by quantum-mechanical rules that limit light emission. In recent decades, both the academic and the industry world have put together big efforts to achieve higher and higher luminance efficiency by finding workarounds to exploit or bypass those quantum rules. Each marks a technological milestone in the nature of the emitting material and, in turn, the devices' efficiency and architecture,[21] that allowed to divide the evolution of the OLED technology into just as many "generations".

Phosphorescent OLED (PhOLED) technology was the first major generational shift and made it possible for nearly all injected charge carriers to be successfully converted into photons inside the device. Unfortunately, it has issues due to the high cost, toxicity, and scarcity of heavy metal containing compounds. To solve the problem, a different mechanism that allows light emission from triplet states is needed. A promising alternative avenue consists in exploiting the thermal upconversion of triplet excitons to emissive singlet excited states, a process known as *reverse intersystem crossing* (rISC), thereby increasing the fraction of radiatively decaying excitons. The delayed emission from these singlet excitons is known as *thermally activated delayed fluorescence* (TADF, **Figure 1.5**).

Not all molecules exhibit TADF. Under the framework of first-order time-dependent perturbations, Born-Oppenheimer adiabatic approximation, and Fermi's golden rule, the rISC rate can be expressed as:[22]

$$k_{\mathrm{rISC}} = k_{\mathrm{ISC}} e^{-\frac{\Delta E_{\mathrm{ST}}}{k_{\mathrm{B}} T}} \tag{1.1}$$

Where k_{ISC} is the intersystem crossing rate, ΔE_{ST} is the singlet triplet energy gap, k_{B} is the Boltzmann constant and T is the temperature. Therefore, for a molecule to achieve TADF, it needs to have a small energy gap (<100 meV) between the singlet and the triplet excited states. Molecular design for TADF molecules remains an active research topic because the same molecular feature that minimize ΔE_{ST}, namely a small wavefunction overlap between ground state and excited state, also lowers the transition dipole moment and the radiative recombination rate. Slightly twisted donor-acceptor geometries are very common as they manage to have a slightly higher transition dipole moment than fully orthogonal units while retaining a small ΔE_{ST}. Molecules with alternating electron-rich and electron-deficient atoms

in a rigid framework ("*multi-resonant TADF molecules*") also have high oscillator strength, thanks to localized excitons, while still allowing small ΔE_{ST}.

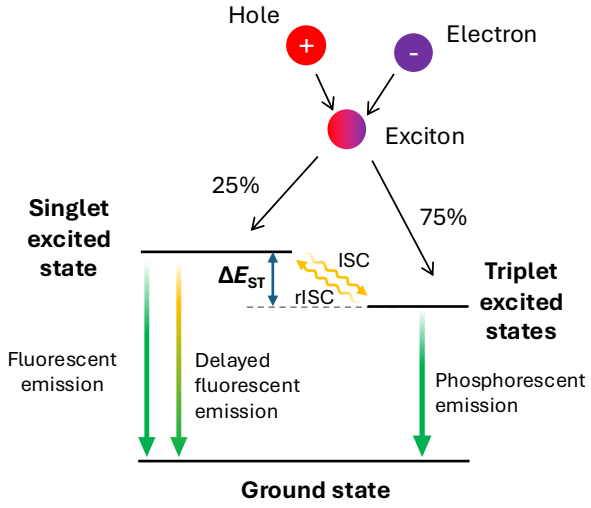

Figure 1.5. Energy diagram for different emission mechanisms in OLED devices.

1.2.3. Figures of merit

To assess the performance of an OLED device, it is common to measure the current density and light output as functions of the applied bias, and to present these measurements in a plot with dual y-axes and in semi-logarithmic display. As the light output is quantified with a photometric quantity called *luminance*, the resulting curves are known as current density–voltage–luminance (*J*–*V*–*L*) characteristics.

Current density

The current density *J* is the amount of charge per unit time that flows through a unit area of a device. In SI base units, the electric current density is measured in amperes per square meter. (A m^{-2}).

Luminance

The energy of electromagnetic radiation, like the visible light emitted by OLEDs, is called radiant energy. The amount of radiant energy emitted in all directions per unit time is the *radiant power* Φ_e (or '*flux*'; 'e' for "energetic", to avoid confusion with photometric quantities), while the *spectral* radiant power $\Phi_{e,\lambda}$ is the radiant power per unit wavelength. In the display and lighting industry, it might be more useful to know how bright a light source appears, rather than how much radiant power they produce. The conversion is not straightforward because the sensitivity of receptors in the human eye is wavelength dependent. For example, a green-emitting source is perceived as brighter than a red- or a blue-emitting one with the same radiant power. To account for this, *photometric* quantities have been introduced.

The measure of the *perceived power* of emitted light (in all directions) is called *luminous power* Φ_v ('v' for "visual"); its SI (International System of Units) unit is the lumen (lm). It is calculated by performing a weighted sum of the radiant power of a light source at each wavelength with the eye's response to that wavelength, a function called *luminous efficiency function* $\bar{y}(\lambda)$ (**Figure 1.6**).

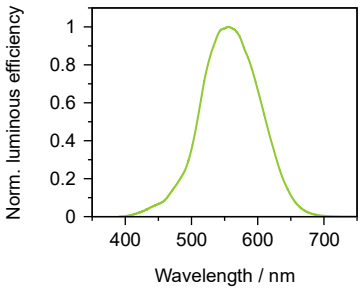

Figure 1.6. 2-deg photopic luminous efficiency for different wavelengths (that is, the luminous efficiency function; Sharpe, Stockman, Jagla & Jägle, 2005).[23]

The luminous efficiency function is unitless and normalized to a peak value of unity at 555 nm. A constant is then needed to convert radiometric units (the watts per nanometer of the spectral radiant power $\Phi_{e,\lambda}$) to photometric units (the lumens of the *luminous power* Φ_v). Its value is equivalent to the luminous power in lumens of a monochromatic light source at 555 nm producing 1 watt of radiant power and was fixed at 683.002 to make it consistent with earlier definitions.

In symbols:

$$\Phi_v = 683.002\ \text{lm/W} \cdot \int_0^\infty \bar{y}(\lambda)\, \Phi_{e,\lambda}(\lambda) \mathrm{d}\lambda \tag{1.2}$$

The ratio of the luminous power to the radiant power is called the *luminous efficacy K*.

For general lighting, the total amount of visible light emitted in all directions is informative enough. However, in OLEDs for displays, the direction of emitted light is also important, as it should be directed toward the viewer. Imagining a display and a light bulb with the same luminous power, the display will appear brighter (if watched from the front) as it concentrates the light in a smaller solid angle. Hence, how bright a display would look to the user is better described by the luminous power per unit solid angle, called *luminous intensity*. The SI unit of luminous intensity is the candela (cd). A common candle emits light with roughly 1 cd luminous intensity, just as a light source that emits monochromatic green light with a wavelength of 555 nm and that has a radiant power of 1/683.002 watts per steradian in a given direction.

Luminous intensity does not account for how large or small the light source is. To compare devices of different sizes, *luminance L* (that is, luminous intensity per unit area, cd m^{-2} or nt) is used.

Luminous current efficiency

The luminous current efficiency is a measure for the "light output per current input", and it is calculated as:

$$\text{Luminous current efficiency} = \frac{L}{J} \tag{1.3}$$

It is expressed in cd A^{-1}.

Internal/external quantum efficiency

The internal quantum efficiency (IQE) and external quantum efficiency (EQE) quantify how effectively an OLED device emits light.

Internal quantum efficiency η_{int} indicates how much light is generated from a given amount of injected charge and is related to the electron/hole balance γ (which accounts for charge carriers that pass through the device without recombining), to the exciton generation efficiency ζ_s (which accounts for recombination events that do not result in the formation of an exciton) and to the fluorescence/phosphorescence quantum efficiency q through the equation:

$$\eta_{\text{int}} = \gamma\, \zeta_s\, q \tag{1.4}$$

Then, a portion of the generated light gets reflected, transferred or absorbed in the active layers or in the substrate. The ratio of photons emitted in forward direction by the device to electrons injected into it is called the external quantum efficiency:

$$\text{EQE} = \frac{\text{number of photons emitted in forward direction}}{\text{number of electrons injected into the OLED}} \tag{1.5}$$

It is usually expressed as a percentage. It is related to the IQE through the light outcoupling efficiency (LOE) η_o, which is, the ratio of extracted to generated light.

The EQE typically decreases at high current injections. This phenomenon is known as efficiency roll-off and it is due to the luminescence quenching associated with the higher density of excitons (as explained in Paragraph 1.2.1).[24]

Color coordinates

Light composed of different wavelengths produces different sensations on the eye that we call colors. Mathematically, each color that can be generated and perceived can be represented as a point (tuple of numbers) in a color space. Most color spaces have three dimensions because we have a trichromatic vision. Almost all defined color spaces are based on the experiments on human color perception carried out by Wright and Guild around 1930.[25,26] From them, the *International Commission on Illumination* (CIE, from the French name "*Commission Internationale de l'éclairage*") defined the XYZ color space, where the *X*, *Y* and *Z* values are the result of the overlap integral between the emission spectrum of the light source and a set of color-matching functions (**Figure 1.7a**).

In this model, presented in 1931, because of the definition of one of the three functions, the *Y* component of any point in the space describes the perceived brightness. This allows the separation of the color information in two parts. The remaining two dimensions besides the luminance one are jointly interpreted as the *chromaticity*. Together, the luminance coordinate *Y* and the chromaticity coordinates *x* and *y* (obtained by dividing the *X* and *Y* values by *X*+*Y*+*Z*) allow the identification of all physically realizable color values and the representation of all possible chromaticities visible to the average person as a 2D diagram. Mathematically, this diagram is a plane of the three-dimensional color space corresponding to a specific brightness value (the maximum one) and is referred to as *CIE 1931 color space chromaticity diagram* or *CIE chromaticity diagram* (**Figure 1.7b**). Its curved edge, usually called the *spectral locus*, encloses all visible chromaticities and corresponds to pure spectral (monochromatic) colors. At the very bottom of the diagram, the straight-line segment connecting the ends of the spectrum is called the *line of purples* and it contains fully saturated colors that nevertheless do not correspond to a single wavelength but to mixtures of red and violet light.

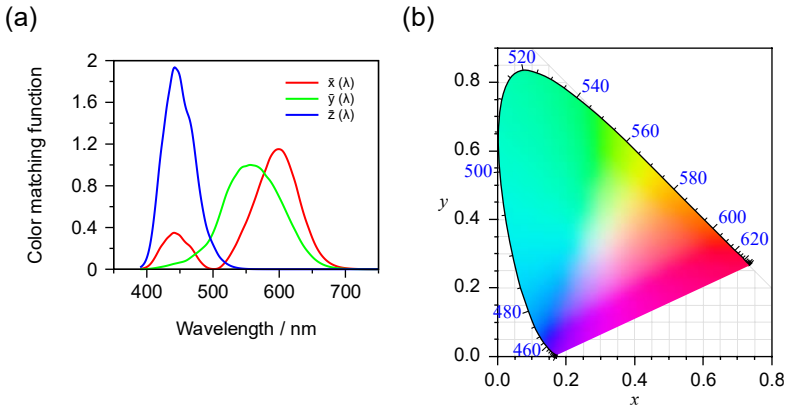

Figure 1.7. (a) The CIE XYZ standard observer color-matching functions. (b) CIE 1931 color space chromaticity diagram.

Operational lifetime

The organic materials in OLEDs degrade over time due to chemical reactions, morphological changes, and quenching processes triggered by charge injection and exciton formation, which gradually reduce light emission efficiency. Hence, for applications such as displays and lighting, stability and durability are as important as efficiency for the commercial viability and long-term usability of OLED-based products. Operational lifetime is typically measured by driving the OLED at a fixed current and continuously recording the emitted light intensity over time. It is then quantified with LT_{50}, a standard metric defined as the time it takes for an OLED's luminance to drop to 50% of its initial value under specified operating conditions.

1.2.4. Device fabrication and deposition techniques

The organic semiconductor layers and the electrodes in bottom-emitting OLED devices need to be supported by a substrate. For daily laboratory work, a glass substrate is typically used. As previously mentioned, the bottom electrode is the anode and typically consists of ITO.

Organic layers are deposited sequentially on top of the anode by either thermal evaporation or solution-processing methods.

Thermal evaporation

Thermal evaporation is a physical vapor deposition (PVD) technique where a material is heated in a vacuum until it evaporates, and the resulting vapor then condenses onto a substrate, forming a thin film.

A thermal evaporation machine consists of three basic components: a metal or glass vacuum chamber that can be evacuated, a holder for the substrate and a heatable container for the organic material (**Figure 1.8a**). The latter is usually a ceramic crucible, which is heated up by a resistive-heating filament placed outside it to convert the organic materials to the vapor state. When this happens bypassing the liquid phase, as is often the case, the material is said to sublime. The substrate holder is located above the crucible, with the substrate facing down. Evaporation chambers often include other components, like quartz oscillators to continuously monitor the evaporation rate (usually in the range of 0.05 – 0.1 nm s^{-1}) and a shutter to control the final film thickness. In the case of guest–host doped layers, the host and dopant are deposited simultaneously from two distinct sources. The relative deposition rate of the dopant with respect to that of the host material determines the doping concentration.

Thin film growth can take place via different mechanisms, including island growth (Volmer–Weber mode), layer growth (Frank-Van der Merwe mode), and layer-island growth (Stranski–Krastanov mode),[27] depending on the relative strength of interactions between adsorbate and substrate. Island growth occurs when adsorbate–adsorbate interactions are stronger than adsorbate–substrate interactions, leading to the formation of isolated islands that later coalesce. Layer growth by following layers happens when adsorbates bond more strongly to the substrate. A balanced interaction between adsorbates and the substrate results in layer–island growth, where both mechanisms coexist.

Solution-processing methods

Solution-processing methods are so named because the organic materials are first dissolved in a solvent with a concentration of around 5–10 mg ml^{-1} and then deposited onto the substrate. Some examples include spin coating, blade coating, spray coating and inkjet printing. In spin coating, the substrate is placed on a holder and covered with the solution. A machine called *spin coater* rotates the substrate with a set angular velocity (typical values are in the range 400–5000 rounds per minute) for 30–120 s. The rotation throws off excess solution and a thin film is formed as the solvent evaporates (**Figure 1.8b**). The thickness depends on the solution viscosity and on the spin speed. In the case of host–guest doped layers, a mixed solution containing both the host and the dopant molecules dissolved in a common solvent is used, with the doping concentration being determined by their relative weights in the solution.

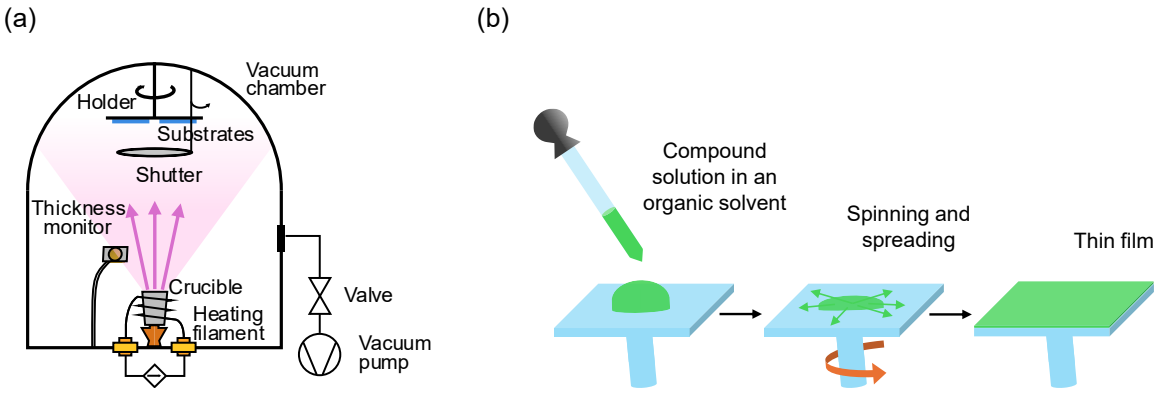

Figure 1.8. Schematic representation of (a) the basic structure of a thermal evaporation machine and (b) of the spin coating deposition method.

Other deposition methods

Inorganic materials, like SnO_x and Al_2O_3, can be used in OLEDs as transport layers or to protect the devices from moisture and oxygen. Thin films of these materials can be deposited through atomic layer deposition (ALD). In this chemical vapor deposition (CVD) technique, a film is grown on a substrate by exposing its surface to alternate gaseous species. In the case of SnO_x, the precursors are tetrakis(dimethylamino)tin (TDAT) and water. Every time a reactant gas is introduced into the reaction chamber, its molecules are adsorbed by the surface. The excess molecules are purged by a vacuum pump before the following gas is introduced and can react with the adsorbed precursor to form a monolayer film. The cycle is repeated to form a high-quality film.

Pulsed laser deposition (PLD) is a PVD technique that involves focusing a pulsed laser on target material in a vacuum chamber. Due to the high laser energy density, the material is vaporized by each laser pulse into a plasma plume directed towards the substrate, which then condenses as a thin film. For example, ITO can be deposited using this technique by using a SnO_2:In_2O_3 ceramic target. Direct current (DC)

magnetron sputtering is a similar PVD technique in which the energy for the target material atoms to be vaporized comes from bombarding ionized gas molecules instead of a laser.

After all the layers have been deposited, the cathode is thermally evaporated onto the organic layers through a shadow mask that determines the active area. For that, boat-shaped vessels made of metal such as tungsten are generally used as evaporation resistive heating sources.

1.3. Metal halide perovskites

Metal halide perovskites are a class of compounds with semiconducting properties. The term "perovskite" was first coined by Gustav Rose in 1839, who discovered, in the Ural mountains of Russia, a black, brown or yellow mineral having $CaTiO_3$ as chemical formula and decided to name it after the Russian nobleman and mineralogist Count Lev Alekseyevich von Perovski. The above-mentioned mineral lends its name to the class of compounds which have the same type of crystal structure, known as the perovskite structure, described for the first time in 1926 by Victor Goldschmidt.

Metal halide perovskites have outperformed rival materials from other classes of compounds in a variety of optoelectronic applications, like solar cells, LEDs and detectors for X-rays and visible light, thanks to their extraordinary physical properties that will be discussed below.

1.3.1. Crystal structure

Perovskites have a general chemical formula ABX_3. Of particular interest in optoelectronics are metal halide perovskites (MHPs), where A is a large monovalent cation, B is a smaller divalent cation and X is a halide. B and X atoms assemble to form BX_6 octahedra located at the center of the unit cell, with A cations located at the corners sitting between the octahedra (**Figure 1.9**, left). The corner-sharing octahedra extend towards three dimensions, forming a three-dimensional (3D) structure (**Figure 1.9**, right).

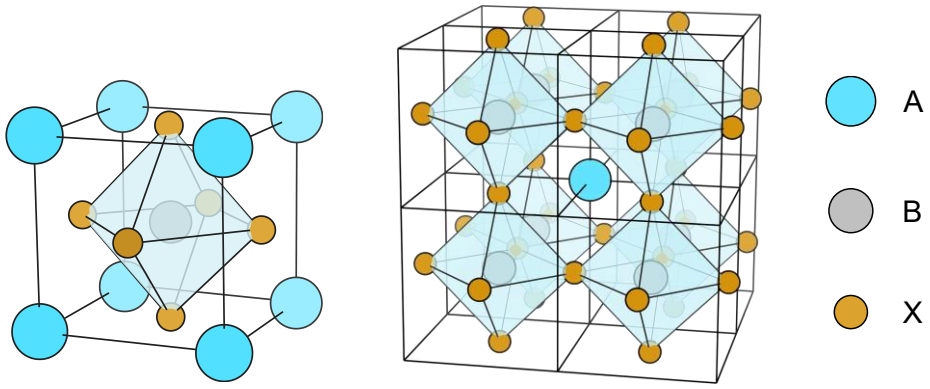

Figure 1.9. Unit cell of an ideal cubic perovskite ABX_3 (left) and their extended crystalline structure (right).

The relative size of the ions determines the stability of the structure. Empirically, it was found that the BX_6 octahedra are stable for r_B/r_X values in the range 0.442–0.895, while the overall structure is stable for $t = (r_A + r_x)/\left(\sqrt{2}(r_B + r_X)\right)$ values in the range 0.9–1.0 (even though values between 0.71–0.9 can also give rise to a perovskite structure, just a distorted one that belongs to the tetragonal or

orthorhombic crystal systems rather than cubic).[28–30] t is called the *Goldschmidt tolerance factor*. Based on these rules, Cs^+, methylammonium ($CH_3NH_3^+$, MA^+) and formamidinium ($HC(NH_2)_2^+$, FA^+) are widely used as the A-site cation in synthetic MHPs; Pb^{2+} and Sn^{2+} are for the B site, and Cl^-, Br^- and I^- for the X site.[29]

1.3.2. Electronic structure

In organic semiconductors, the electronic structure is said to be localized and is usually described in terms of molecular orbitals. Perovskites, on the other hand, are crystalline semiconductors rather than molecular solids; as a consequence of the periodic arrangement of the atoms, electrons and holes are delocalized and can be described with band theory. According to this theory, the overlap of atomic orbitals in crystalline solids forms continuous ranges of energy levels which the electrons can have called *bands*. The closest bands to the Fermi level (that is, the energy needed to add one electron to a solid) are called *valence band* (VB) and *conduction band* (CB). The energy difference between the VB maximum (VBM) and the CB minimum (CBM) of a material is called the *band gap* (E_g).

According to theoretical calculations, in lead halide perovskites (MHPs where B = Pb^{2+}), the CB is composed mostly of Pb^{2+} 6*p* orbitals and has nonbonding to weakly antibonding character, while the VB originates mainly from a Pb 6*s* – X *p* overlap (**Figure 1.10**).[31] Even though both bonding and antibonding orbitals exist in the valence band, the VBM corresponds to the antibonding states.[32,33]

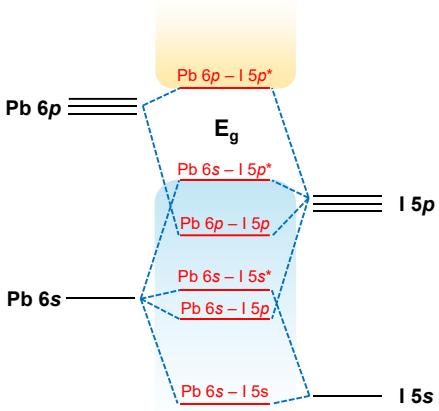

Figure 1.10. Molecular orbital diagram for the interaction between Pb and I atoms in $APbI_3$. Adapted from Ref. 33.

The antibonding character of the VBM is opposite to that of most conventional semiconducting materials, which typically have bonding states near the VBM and antibonding states near the CBM. The particular electronic structure of perovskites is responsible for their remarkable properties, including their defect tolerance.[34,35] All crystals inevitably have defects (like vacancies, interstitials, anti-sites). Defects are undesirable because the states they create can "trap" charge carriers, holding them, preventing them from participating in conduction or recombination in the usual way and even facilitating their non-radiative recombination (**Figure 1.13**), but in perovskites they surprisingly do not prevent the material from achieving good electronic properties. Due to the previously mentioned antibonding character of the CBM and VBM, the electronic energy levels of the constituent elements are resonant (meaning that they have the same energy) with the valence and conduction bands. As a result,

any defect states (nonbonding in nature[36]) formed by adding or removing these elements tend to lie within the bands themselves (or near the band edges, "shallow states") rather than within the band gap ("deep states", **Figure 1.11**).[37] Carriers trapped there can be easily re-excited back into the conduction/valence band, reducing (but not eliminating) the probability of non-radiative recombination via defects. Since bond breaking underpins the formation also of other defects such as anti-sites, surface defects and dislocations, this defect-tolerant electronic structure argument can be extended to those as well.

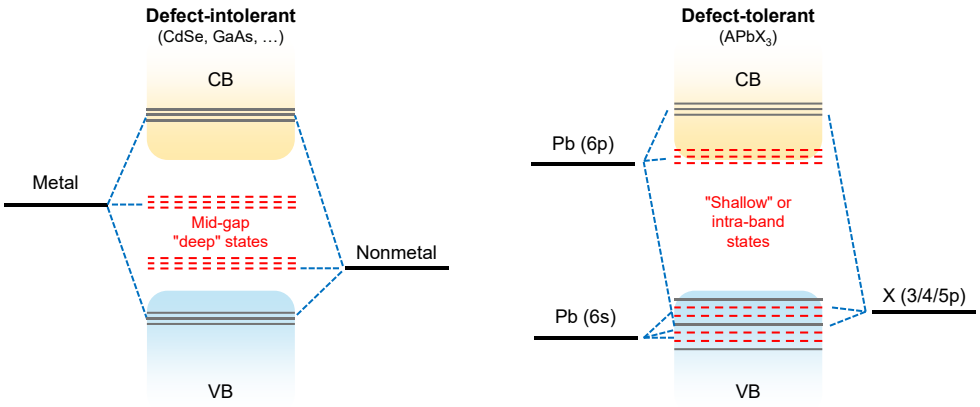

Figure 1.11. Comparison between defect-intolerant (left) and defect-tolerant (right, exemplified by lead halide perovskites) electronic structures. In defect-intolerant materials, creating a defect gives rise to localized electronic states in the middle of the bandgap. In perovskites, many common defects are predicted by DFT calculations to introduce shallow levels. Adapted from Ref. 38.

1.3.3. Optoelectronic properties

Besides their defect tolerance, halide perovskites have a series of properties arising directly from their intrinsic electronic structure that make them attractive materials for optoelectronic applications.

High absorption coefficients, high carrier mobility, and long charge carrier diffusion lengths

Perovskites have large absorption coefficients (due to the direct bandgaps with strong oscillator strengths) and high charge-carrier mobility values in the tens of $cm^2\ V^{-1}\ s^{-1}$, thanks to relatively dispersive conduction and valence bands (meaning the bands have a low effective mass).[39]

Moreover, the defect tolerance of the electronic structure suppresses non-radiative recombination and enables long carrier lifetimes, which combined with the high mobility results in long charge-carrier diffusion lengths in the micrometer range.[40,41]

Bandgap tuning

The bandgap of ABX_3 perovskites is direct and can be tuned by compositional engineering. X can be Cl, Br or I. Advancing down the halide group, the decreased electronegativity and the bigger atomic radius result in a smaller metal–halide orbital overlap and the X p (3p, 4p or 5p for Cl, Br or I, respectively) level shifts upward in energy, increasing the energy of the valence band (while the conduction band is less influenced as it is mostly constituted of the Pb p atomic orbitals). Therefore, the substitution of chlorine with bromine or iodine leads to a bandgap narrowing, identifiable by a bathochromic shift in the absorption spectrum (**Figure 1.12**). B substitution also has control over the band gap; Sn^{2+} substitution

of Pb^{2+} causes a reduction in the band gap.[42] Although A cations have no direct contributions to the formation of the CBM and VBM, they can influence the B–X bond length and, in turn, the bandgap. Large A-site cations tend to increase the B–X atomic distance, reducing orbital overlap and consequently widening the band gap.[32]

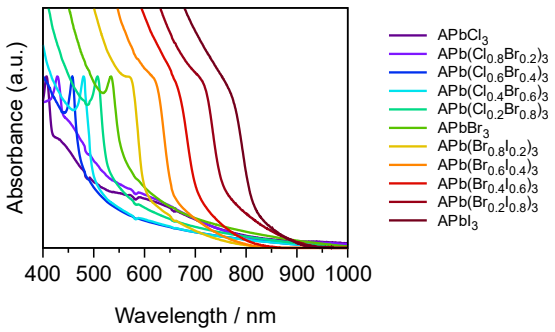

Figure 1.12. Absorption spectrum of perovskite films with different halide composition. A = $(FA_{0.8}MA_{0.1}GA_{0.1})_{0.87}Cs_{0.13}$. The redshift in the spectrum that accompanies the substitution of chlorine with bromine or iodine is associated with a bandgap narrowing.

When the morphological size of the crystals of metals or of semiconductors is reduced to the nanoscale (the same size regimen as visible wavelengths of light), size-dependent optical and electronic properties start to be revealed due to quantum-confinement effects. To be more precise, the confinement causes a splitting of the continuous band diagrams into discrete states and increases the energy of the lowest excited energetic state, causing a blue-shifted emission. Therefore, changes in morphological size can be exploited to tune the optical properties of nanosized perovskite crystals (*nanocrystals*, NCs). The binding energy (E_b) of excitons (the energy required to separate the bound electron-hole pair into free charge carriers) also increases due to the quantum confinement, which stabilizes them and increases the probability of radiative recombination. The structural, *molecular* dimensionality can also be changed, for example by inserting long-chain alkylammonium cations that result in the synthesis of layered perovskites, with a certain number of octahedral layers between long-chain organic layers.[43–45]

Narrow PL spectrum

In photoluminescence, perovskites have full-width at half-maximum (FWHM) values lower than 20 nm, compared to 30 nm for other quantum-dot emitters and 40 nm for organic compounds.[46] A narrow emission corresponds to a high color purity, which leads to displays with more vivid colors.

The low-cost fabrication (due to facile processability from solution and the low raw material cost of only ~2 $ per g[47]) has also contributed, together with their exceptional properties, to their wide and expanding use in optoelectronics. However, despite the advantages outlined above, it is important to note that the vast majority of perovskite compositions currently employed in optoelectronic applications contain toxic lead. This poses a significant barrier to their use in consumer products, as they do not comply with governmental regulations such as the Restriction of Hazardous Substances (RoHS) directive. Encouragingly, ongoing research is focused on developing lead-free perovskites with comparable optoelectronic properties, and substantial progress has been made. In parallel, efforts are

also underway to devise safe encapsulation techniques and efficient recycling strategies for lead-based perovskites.

1.3.4. Perovskites for LEDs

Perovskites were first explored and widely celebrated for their performance in solar cells, where their ability to harvest light is crucial. However, it was soon realized that the same intrinsic electronic properties that make them excellent absorbers (such as direct bandgaps, high radiative recombination rates, and tunable emission) also make them highly suitable for use in light-emitting diodes. Moreover, even in the case of the other properties of perovskites that are advantageous for solar cells but limit the efficiency of LEDs (such as their low exciton binding energies), the remarkable versatility of perovskite materials has enabled the development of tailored strategies to overcome these limitations, discussed more in detail in Paragraph 1.3.5, allowing their full potential to be harnessed in this field of optoelectronics as well.

As a testament to their versatility, perovskites can serve in LEDs as either the emissive layer or as part of the charge transport layers.

Perovskites as emissive layers

When perovskites are used as emissive layers, the resulting devices are called perovskite light-emitting diodes (PeLEDs). In this case, the devices have a structure and a working principle similar to OLEDs, as both have a layered device architecture and are based on the principle of injecting electrons and holes into a central emissive layer where radiative recombination occurs. The main difference, already mentioned at the beginning of Paragraph 1.3.2, is that inorganic semiconductors like perovskites possess a distinct conduction mechanism, with the behavior of charge carriers being described using band theory, and the excitons being delocalized over many lattice sites (unlike in organic materials where they are confined to local sites or molecules). So, while the drift and diffusion of electrons and holes through dedicated transport layers is similar in OLEDs and PeLEDs, in the latter case charges are eventually injected into extended electronic bands instead of molecular orbitals: the CB for electrons and the VB for holes.

Ideally, when the electrons and the holes meet in the perovskite layer, they recombine (that is, excited electrons from the CB lose their energy and decay into the VB) to produce photons (**Figure 1.13**, left). This bimolecular radiative recombination process is the most important one in PeLEDs. However, electrons and holes can recombine in other ways. For example, the dominant fate of charges that are trapped in the localized states within the band gap associated with defects is their fast, non-radiative annihilation, a process known as Shockley-Read-Hall (SRH) recombination (**Figure 1.13**, center). The higher the defect density, the lower the lifetime of the carriers. Another undesired process is Auger recombination, where electrons and holes recombine from the CB and VB, just as in radiative recombination, but the extra energy is given to another carrier instead of being released through a photon (**Figure 1.13**, right). Thus, to increase the device efficiency, efforts must be made to maximize the bimolecular radiative recombination rate.

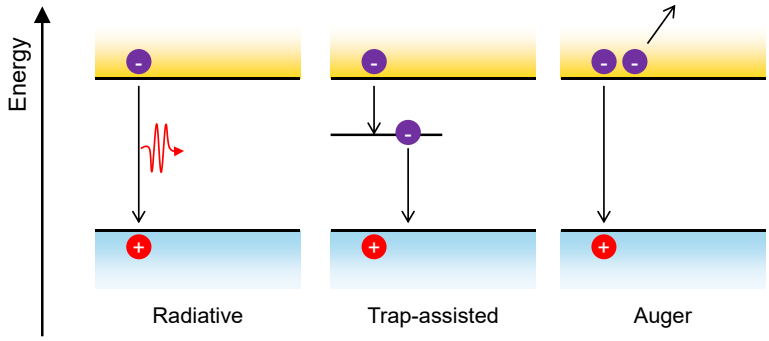

Figure 1.13. Schematic representation of various recombination mechanisms expected to occur in a PeLED. From left to right: radiative recombination, trap-assisted or Shockley–Read–Hall recombination, and Auger recombination.

These recombination processes, which also involve electrons and holes generated via the absorption of light, directly influence the so-called photoluminescence quantum yield (PLQY). It is defined as the ratio of the number of photons emitted to the number of photons absorbed by a material, indicating how efficiently absorbed energy is converted into emitted light. Since radiative recombination increases PLQY while non-radiative recombination decreases it, PLQY is closely linked to the performance of PeLEDs, with higher PLQY values reflecting more efficient light emission and enhanced device brightness and efficiency. Perovskite films consisting of NCs are particularly compelling as light emitters because of their higher binding energy of excitons, high radiative recombination rates and high PLQYs originating from the quantum confinement effect.

Compared with OLEDs, PeLED devices offer clear advantages in luminescence color purity and production cost. However, their luminescence efficiency still lags behind: the most efficient PeLED has achieved an EQE of 32.1%,[48] which remains below the ≈40% record of OLEDs.[49] A more critical challenge lies in stability, as the best PeLEDs currently reach an estimated T_{50} of only 30 000 hours at an initial luminance of 100 cd m^{-2},[50] shorter than the 600 000 hours reported for OLEDs.[51] This gap in operational durability represents one of the main obstacles to the industrial adoption of PeLED technology.

Perovskites as transport layers

The high conductivity and transparency in the visible region of some perovskite compositions make them also appealing to use as transport layers in OLEDs. Moreover, the low solubility of their thin films in low-polarity organic solvents, such as chloroform, chlorobenzene, or toluene, allows subsequent solution processing of additional layers to form multilayered structures. Despite this, before this thesis work, there were only 5 reports in literature of perovskites being employed in this way.

In 2016, Tian and coworkers demonstrated, for the first time, the use of a metal halide perovskite-based HTL for OLEDs.[52] Methylammonium lead chloride ($MAPbCl_3$) was chosen for its transparency in the visible region (band gap of ≈3.1 eV) and facile solution-processing. The thickness of the layer was 25 nm and the EML was then spin-coated directly onto it. Devices with the perovskite HTL showed higher current density than the control devices with a PEDOT:PSS HTL, indicating superior charge injection and transport, as well as a higher brightness and EQE.

In 2017, red PhOLEDs with an all-inorganic $CsPbBr_3$ perovskite-based HTL were reported by Zhang et al., who commented on the high hole mobility (> 1000 $cm^2\ V^{-1}\ s^{-1}$) and a relatively shallow VBM of 5.85 eV.[53] The layer was deposited via spin coating to a final thickness of 30 nm; any extra solvent was pumped

away in vacuum before annealing for improved film morphology.[54] The insertion of a $CsPbBr_3$ film and a mCP electron and exciton blocking layer between the PEDOT:PSS HIL and the EML improved the performance up to a current efficiency of 10.6 cd A^{-1}, which was ascribed to the better hole injection and transport.

In the same year, solution-processed $MAPbI_3$ was used in a similar way in tris-(8-hydroxyquinoline) aluminum (Alq_3)-based OLEDs.[55] To obtain smooth and homogeneous films with a thickness in the range 12 – 32 nm, the precursor solution solvent had to be washed away with nonpolar diethyl ether while spinning[56] (for details, see Paragraph 1.3.5 and **Figure 1.14**). Despite a higher HOMO level and rougher film morphology compared to PEDOT:PSS, the excellent hole mobility and the alleged stronger adhesion with the ITO resulted in an enhanced hole injection. The perovskite HIL also increased the OLEDs' durability, which was attributed to a combination of improved charge balance, the spin-coating of the layer being from dry organic solution (the water-based fabrication of PEDOT:PSS films potentially introduces water damage of OLEDs) and its low reactivity compared to PEDOT:PSS, whose strongly acidic and hygroscopic nature etches and deteriorates ITO.

In 2018, the introduction of perovskite HTLs into TADF-based OLEDs was explored for the first time.[57] The low-dimensional $CzEA_2PbBr_4$ perovskite (40 nm-thick layer) prepared via a reaction of $PbBr_2$ and 2-(9H-carbazol-9-yl)ethanaminium bromide (CzEABr, both dissolved in dimethyl sulfoxide) was inserted between PEDOT:PSS and the solution-processed EML consisting of 2,4,5,6-tetrakis(carbazol-9-yl)-1,3-dicyanobenzene (4CzIPN) doped in mCP. A twofold increase in efficiency was obtained, thanks to a suppression of the exciton quenching by PEDOT:PSS (testified by a higher PLQY of the mCP:4CzIPN film) and a promotion of the RISC rate (and thus triplet utilization) via the external heavy-atom effect, indicated by a higher delayed fluorescence ratio compared to that of the EML atop glass.

In 2019, extraordinarily thick OLEDs using $MAPbCl_3$ as the transport layers were fabricated.[40] Because of their poor solubility in solvents, perovskites are difficult to process into thick layers through solution-based methods, which is why the thick $MAPbCl_3$ films had to be deposited by thermal co-evaporation of methylammonium chloride (MACl) and lead chloride ($PbCl_2$). OLEDs with the fluorescent emitter Alq_3 and thick (1 000 nm) $MAPbCl_3$ HTL and ETL had comparable driving voltages with respect to devices with thin (50 nm) organic transport layers. On the contrary, no electroluminescence (below 200 V) was detected from devices with micrometer-thick organic transport layers. OLEDs with 1 000 nm-thick cesium tin chloride ($CsSnCl_3$) perovskite transport layers were also fabricated and were found to have comparable device performance to the $MAPbCl_3$ counterparts with the same thickness, but without the issues of lead toxicity and volatility of MACl. Finally, OLEDs combining thick $MAPbCl_3$ transport layers with phosphorescence-based and TADF-based emitters were also demonstrated. Tuning the thickness of the perovskite HTL and ETL maximized the LOE, enabling EQEs of about 30% while still ensuring a total transport layer thickness of 2 000 nm.

1.3.5. Deposition of perovskite thin films

Generally, the formation of the perovskite takes place in concomitance with the deposition of its precursors onto a substrate. Similarly to the thin films of organic semiconducting materials, the main deposition techniques to synthesize perovskites in the form of thin films are solution-processing methods like spin coating and thermal evaporation.

Perovskite film preparation via spin coating

The perovskite precursors, namely the organic or inorganic A^+ halides and the B^{2+} metal halides, are soluble in polar organic solvents like dimethylformamide (DMF), dimethyl sulfoxide (DMSO) and γ-butyrolactone (GBL). After dissolving the precursors, the solution is spin-coated onto the substrate. As the solvent evaporates, the local concentration of the precursors increases, triggering the nucleation and growth of the perovskite phase.

These solvents have a relatively high boiling point, which leads to prolonged perovskite crystal growth and large grains.[58] While beneficial for solar cells, for PeLEDs smaller grains are preferred for better charge confinement and increased radiative recombination probability.[9] Different strategies have been reported to confine the size of the crystals within the film deposition. A popular one consist in dripping an anti-solvent in which the precursors are not soluble, like toluene, chloroform or chlorobenzene, on the substrate while the precursors solution is still spinning, flushing out the good solvent and inducing rapid crystallization (**Figure 1.14**).[58] The films are then typically annealed to remove any residual solvent and form a dense and uniform perovskite film. The grains obtained with this method, developed by Lee and coworkers and named *nanocrystal pinning* (NCP), have a size ranging from 100 to 250 nm. A further reduction (<100 nm) can be achieved by adding an additive like TPBi into the antisolvent, which can infiltrate into the grain boundaries (*additive-based nanocrystal pinning*, A-NCP).[9,59]

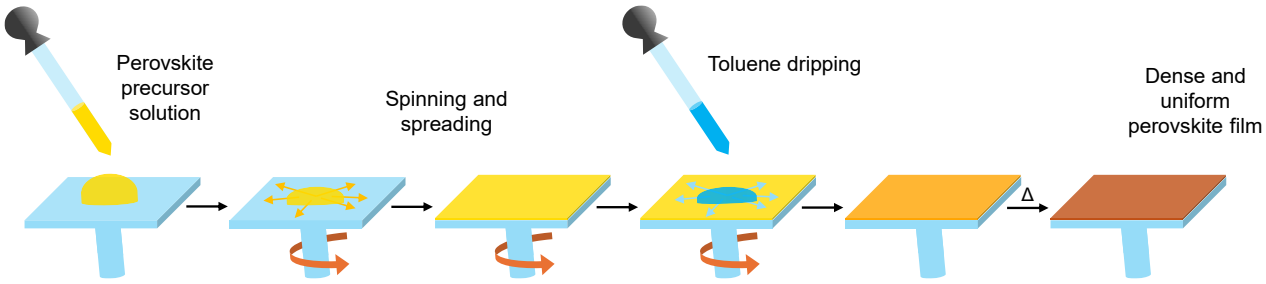

Figure 1.14. Schematic representation of the nanocrystal pinning (NCP) method for fast nucleation in polycrystalline perovskite films.

The additives can also be added to the precursors solution with the same objective. Some examples include large ammonium cations or ligands like butylammonium (BA), which act as surfactants impeding the growth of 3D perovskite grains,[60,61] and phosphonic acids like benzylphosphonic acid (BPA), which can attach as a ligand to the undercoordinated Pb atoms on the surface of 3D perovskites and was reported to reduce the average grain size of $(FA_{0.7}MA_{0.1}GA_{0.2})_{0.87}Cs_{0.13}PbBr_3$ grains from 205 to 123 nm.[18] Moreover, if the perovskite thin films are further exposed to phosphonic acids solutions after deposition, the molecules can penetrate into the large perovskite crystals, bind to the surface sites and split the large crystal domains into nanosized in situ core/shell structures.[62]

Alternatively and as an exception to the rule at the beginning of the paragraph, films with perovskite nanocrystals (PeNCs) can be deposited by first synthesizing them ex situ and then depositing their colloidal suspension onto the substrate.[63] The two main methods for PeNCs synthesis are hot-injection (HI) and ligand-assisted re-precipitation (LARP). In the first method, the oleate salt of the A cation, prepared by reacting oleic acid (OA) with an A cation salt, is rapidly injected into a hot solution of PbX_2 in 1-octadecene (ODE) at high temperatures (140 – 200 °C). The solvent also contains organic molecules with a long aliphatic chain, like the already mentioned OA or oleylamine (OAm), which prevent aggregation of the particles acting as capping ligands. The temperature and the reaction time before quenching in ice-cold water determine the particles' size and, in turn, the bandgap. In the LARP method, the perovskite precursors, namely the Pb and A cation halide salts, are dissolved in a good solvent like DMF. The obtained solution is then injected into a solvent mixture with a low polarity (typically toluene and 1-butanol) in which the ligands have previously been dissolved. The polarity difference induces the precipitation of PeNCs. After the particles have been synthesized, they are isolated and purified with sequential centrifugation steps. The obtained suspension in a nonpolar solvent (like toluene) can then

be spin-coated to obtain a thin film. However, the resulting films suffer from low NCs concentration, low conductivity due to long insulating ligands and potential aggregation during film formation. These drawbacks, which add up to the need for additional synthesis, purification and redispersion steps, make nanocrystalline films based on traditional colloidal nanocrystals less attractive.[64]

Thermal evaporation

Perovskite films can also be deposited via thermal evaporation. Being a PVD technique, thermal evaporation has the advantages of higher purity, finer control over film thickness, no limitations due to precursors solubility, no intermixing of layers caused by partial dissolution of a previously deposited one during the deposition and compatibility with a wider range of substrates.

In *single-source thermal evaporation*, the perovskite is previously synthesized in powder form (for example, by dry mechanochemical method, or by solution-grown single crystals) and then transferred to the thermal evaporation for deposition.[65] Despite resembling the vacuum deposition of organic semiconductor films, the behavior during heating is fundamentally different, because organic molecules remain chemically unchanged during evaporation and sublime intact. On the contrary, in the case of perovskites, during the thermal evaporation process raw materials may first decompose into volatile species and/or fragments that are the species that actually evaporate (*vaporization*), move across the chamber (*transport*) and then self-assemble again into a perovskite film when depositing onto the substrate (d*eposition and film growth*).[27] Island growth is the predominant deposition mechanism for MHPs thin films, largely due to the lattice mismatch between the substrate surface and the perovskite crystals in most adsorbate-substrate combinations.[27]

In *dual-source co-evaporation*, the perovskite precursor materials are put into different crucibles and evaporated simultaneously onto the substate (**Figure 1.15**). The relative evaporation rates determine the stoichiometric composition of the films. By co-evaporating a larger number of precursors (*multi-source co-evaporation*), mixed-halide and/or mixed-A-cation perovskites can be obtained. Precise control over the deposition rate of each precursor is necessary to achieve the desired perovskite stoichiometry.

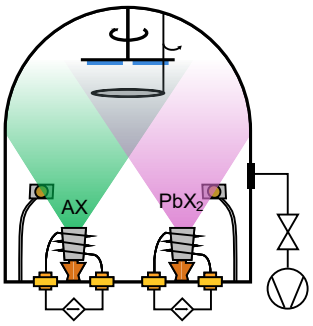

Figure 1.15. Schematic representation of the dual-source co-evaporation process for the deposition of $APbX_3$ lead halide perovskite.

Finally, in the *sequential deposition* technique, the precursors are individually sequentially evaporated onto the substrate, and mix and subsequently react to form the perovskite during the annealing step.

1.4. Aim of the thesis

Research into solid-state lighting is crucial for addressing global challenges such as climate change by enabling more energy-efficient devices that reduce overall electricity consumption. Furthermore, emerging display technologies like OLEDs and PeLEDs offer the potential to significantly extend battery life in portable electronics while delivering superior visual performance, making them key to advancing sustainable and high-quality display solutions for the future. However, their potential impact remains limited if the technology does not reach the broader market.

This dissertation primarily aims to develop novel device architectures for light-emitting applications towards higher performance and lower fabrication cost, crucial factors for the adoption of the technology on a large scale. Phosphorescent and TADF emitters are deposited as ultrathin layers, whose structures and working principles are investigated. Known and novel perovskite materials are synthesized and introduced as transport or emissive layers. Finally, transparent electrodes are used to broaden the scope of applications. Throughout the thesis, a wide range of processing methods, device architectures, and their relationships to optoelectronic properties will be thoroughly documented.

Chapter 2 will describe the basic device fabrication and characterization techniques, while the following ones aim to address several key challenges in the development of efficient and stable OLEDs and PeLEDs. **Chapter 3** focuses on improving charge transport and device performance through the introduction of a thermally evaporated perovskite hole-transport layer. **Chapter 4** explores the design of novel mixed-halide perovskite compositions to achieve color-tunable and structurally simplified PeLEDs. **Chapter 5** pursues strategies for realizing fully transparent devices by developing a low-damage and universally applicable deposition method for transparent electrodes. **Chapter 6** aims to combine the concepts of hyperfluorescence and ultrathin emissive layers to simultaneously achieve high efficiency, color purity, and ease of fabrication. **Chapter 7** recaps all the work and provides a general outlook on the future of light-emitting diodes. Each chapter includes an introduction, the experimental details and an extensive discussion of the results. Finally, a summary of the dissertation in Valencian and a list of abbreviations and physical quantities are provided.

Chapter 2.

Experimental methods

In this chapter, the experimental methods used to fabricate and characterize the organic and perovskite light-emitting diodes presented in this work are detailed.

2.1. Device fabrication

2.1.1. Device layout

For the fabrication of devices in a vertical "sandwich-type" arrangement, commercial square ITO-covered glass substrates with a length of 30 mm and a thickness of 1 mm were used. The ITO layer had a thickness of 150–160 nm and was patterned by the commercial supplier to leave only a 14 mm-wide strip at the center of the substrate. The organic or perovskite layers were evaporated through square shadow masks to avoid covering the edge of the ITO strip and to be able to contact it during device characterization. In the case of solution-processed layers, a towel wet with the deposition solvent was used to remove the deposited material from the strip edges, serving the same purpose. Top electrodes with a width of 1.5 mm were deposited through a shadow mask in an orthogonal direction to the center ITO stripe. The final active area of each device of 8.25 mm^2 was defined by the overlap of the ITO and the top electrodes (5.5 mm, **Figure 2.1**).

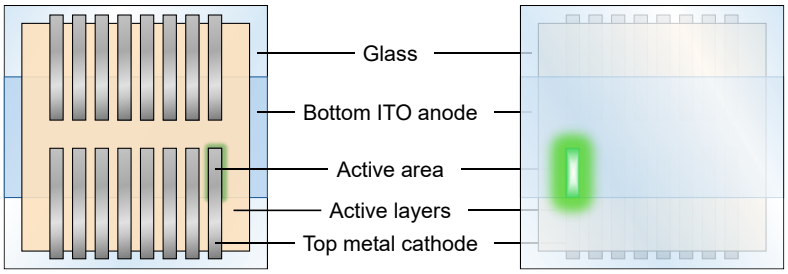

Figure 2.1. Substrate electrode layout as viewed from the top (left) and from the bottom (right), glass side. The emission comes from the bottom side.

The employed layout has the advantage of fitting sixteen devices on the same substrate, lowering the material consumption. On the other hand, not all the devices have the same potential due to the sheet resistance of ITO. Another disadvantage is that the electric field could be higher at the edge of the ITO stripe (due to a reduced organic and inorganic film thickness there) compared to the main device area, leading to faster degradation and inhomogeneous emission.

2.1.2. Cleaning

A common practice before beginning device fabrication is to first clean the ITO surface by placing the substrates for 3-5 min in different ultrasonic baths. For the devices fabricated in this work, the established cleaning procedure involved sequential washing with tap water and household detergent (dishwasher or liquid soap), deionized water, and isopropanol. Then, the substrates were treated for 15 minutes with ozone (UV–ozone cleaner Jelight 42–220, **Figure 2.3a**). The ozone removes any organic contaminants by reacting with them to form volatile products.

In semiconductor manufacturing, even small amounts of particulates pose a contamination risk. For this reason, the cleaning step, as well as the following deposition of the thin films, were carried out in a cleanroom (ISO 7 10000, 50 m^2 of surface, **Figure 2.2**) that maintains a very low concentration of

airborne particulates and is shielded from UV radiation coming from illumination to protect sensitive materials.

Figure 2.2. Class 10000 cleanroom in which the deposition of the thin films took place.

2.1.3. Layer deposition

After cleaning, the various layers were deposited using one of the techniques described in Paragraph 1.2.4 and 1.3.5. Except for PEDOT:PSS, the depositions took place in nitrogen-filled gloveboxes with water and oxygen concentrations below 10 ppm to prevent oxidation and moisture-induced degradation. All materials were used as received from commercial vendors without further purification.

Solution-processed films were deposited with a CHEMAT KW-4A 2-stage spin coater (**Figure 2.3b**).

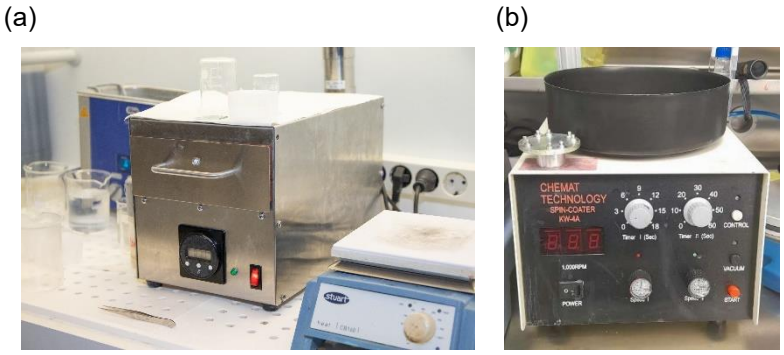

Figure 2.3. (a) UV–ozone cleaner Jelight 42–220. (b) CHEMAT KW-4A 2-stage spin coater.

Thermally evaporated organic and perovskite layers were deposited in a custom-made thermal evaporation system by The Vacuum Projects (**Figure 2.4a**). The water-cooled Pfeiffer Turbomolecular Pump was controlled by a Cressington 308R system and a Pfeiffer TPG 362 dual gauge controller. The temperature of the crucibles was controlled through a Creaphys dual evaporation control unit and the

deposition rates were monitored through a Kurt J. Lesker Company FTC-2800 multi-channel quartz crystal controller and Inficon quartz crystal microbalance (QCM) sensors (1 Å resolution). The sensors were calibrated for each material by measuring the thickness of deposited thin films with a profilometer. Metals were evaporated in a separate thermal evaporation system (**Figure 2.4b**) equipped with an Edwards FTM7 film thickness monitor. During the depositions, the background pressure was maintained around 10^{-6} mbar. Shadow masks were used during the evaporation as described above.

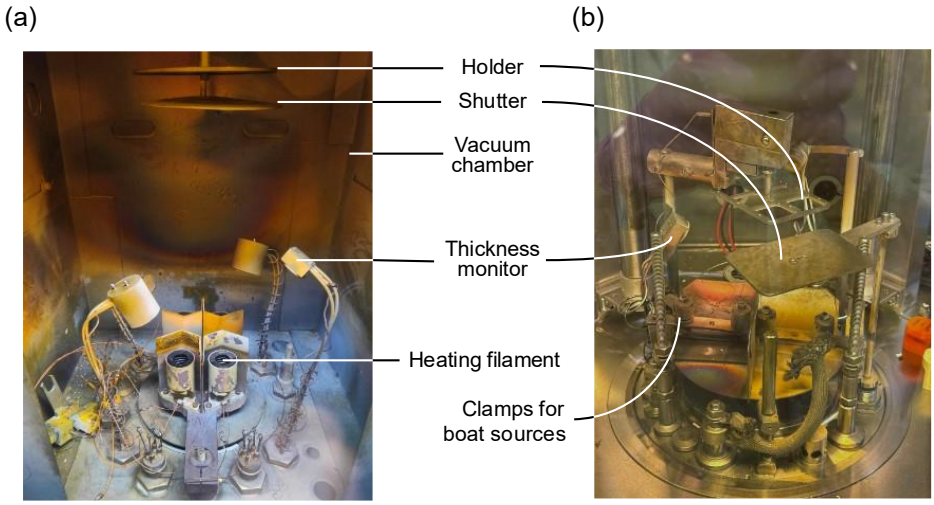

Figure 2.4. Thermal evaporation systems used for the deposition of (a) organic and perovskite layers and (b) metal cathodes.

Tin oxide (SnO_x) and aluminum oxide (Al_2O_3) films were deposited with an Arradiance GEMStar XT Thermal atomic layer deposition (ALD) system following a previously reported procedure.[66]

ITO films were deposited at room temperature either using a using a Solmates pulsed laser deposition (PLD) 200 mm system (**Figure 2.5a**) or an Amstrong DC magnetron sputtering deposition equipment (**Figure 2.5c**), both coupled to a nitrogen-filled glovebox. In the former case, a Lightmachinery IPEX-700 KrF excimer laser (**Figure 2.5b**) with a wavelength of 248 nm was employed, setting the repetition rate at 50 Hz and the fluence at 1.5–1.6 J cm^{-2}. The composition of the ceramic target was In_2O_3:SnO_2 (98:2 wt.%) and was purchased from Pi-kem. The chamber pressure of 0.033 mbar and the O_2 partial pressure of 0.007 mbar were kept constant by the injection of an oxygen/argon gas mix, as optimized in a previous work.[67] In the latter case, the circular sputtering target had a composition of In_2O_3:SnO_2 (97:3 wt.%), a diameter of 4 inches and a purity of 99.99%, while the pulsed DC power supply (TRUMPF Huettinger) was maintained at a power of 500 W and the pressure at 0.005 mbar (with a flow of the carrier gas Ar of 20 sccm).

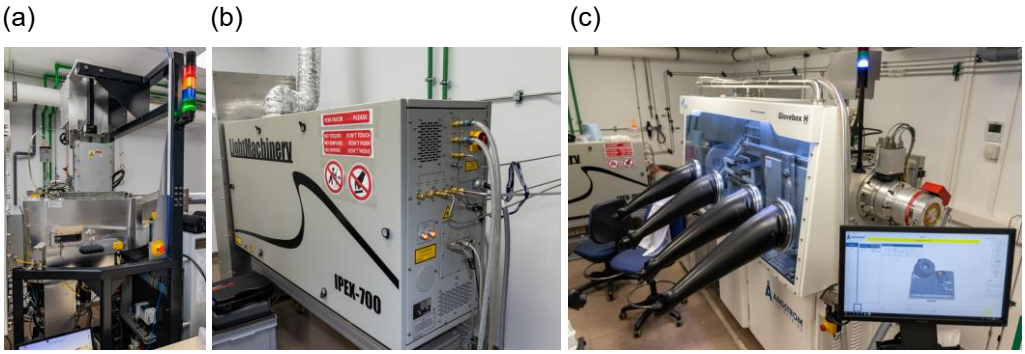

Figure 2.5. Other tools for thin film PVD. (a) Solmates PLD 200 mm system. (b) Lightmachinery IPEX-700 laser. (c) Amstrong DC magnetron sputtering deposition equipment.

2.2. Device characterization

2.2.1. Testing platform

The LED testing platform, schematically represented in **Figure 2.6**, included a Keithley 2400 source measure unit (SMU), an Avantes AvaSpec-2048L spectrometer, a large-area Hamamatsu Photonics S1337-21 Si photodiode (18 × 18 mm), a Keithley 6485 picoammeter and a custom-made sample holder with spring-loaded contacts on a printed circuit board (PCB) compatible with the substrate layout. The setup was located inside of a nitrogen-filled glovebox to prevent the samples from being exposed to air before and during the characterization.

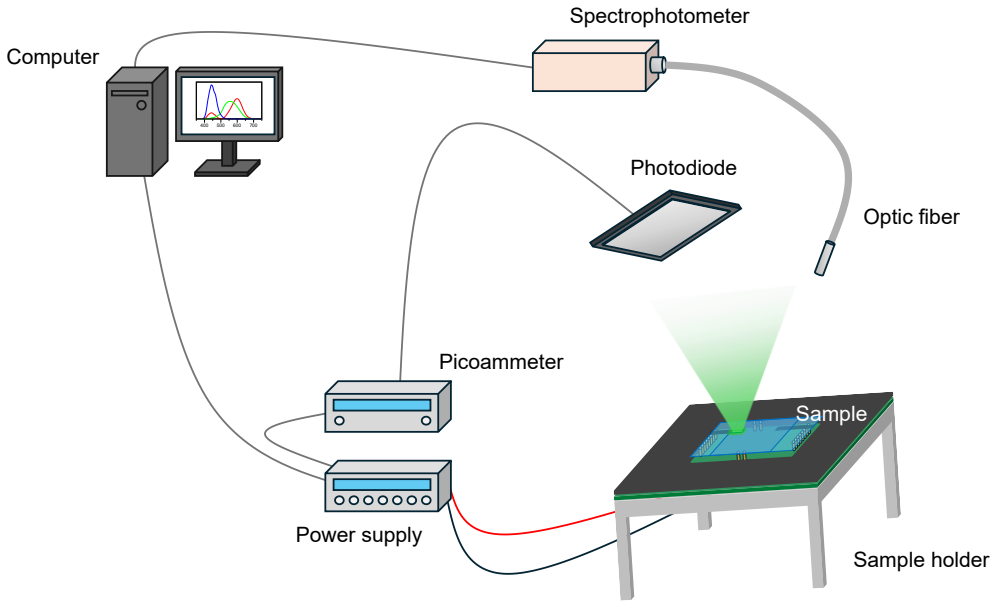

Figure 2.6. Schematic illustration of the LED testing platform.

The source measure unit was used as a power supply to drive the LED and measure the current flowing through the device. The generated light was collected either by an optic fiber connected to the spectrometer, to measure the EL spectra, or by the large-area photodiode, to measure the different figures of merit of the device. The latter produces an electrical current when it absorbs photons, which is then measured by the picoammeter. The photodiode's responsivity, that is, the ratio of generated photocurrent to incident light power Φ_e, depends on the incident light specific spectrum. For any given spectrum $I_{e,\lambda}(\lambda)$, the responsivity R (expressed in A W^{-1}) of a photodiode can be calculated with the following equation:

$$R = \frac{\int_0^\infty R_\lambda(\lambda) I_{e,\lambda}(\lambda) d\lambda}{\int_0^\infty I_{e,\lambda}(\lambda) d\lambda} \tag{2.1}$$

where $R_\lambda(\lambda)$ is the photodiode's spectral responsivity. The luminous efficacy can be calculated as:

$$K = 683.002\ {}^{lm}/_{W} \cdot \frac{\int_0^\infty \bar{y}(\lambda) I_{e,\lambda}(\lambda) d\lambda}{\int_0^\infty I_{e,\lambda}(\lambda) d\lambda} \tag{2.2}$$

The luminous power can finally be estimated starting from the diode photocurrent I_{pd} as:

$$\Phi_v = K \cdot \Phi_e = K \cdot \frac{I_{pd}}{R} \tag{2.3}$$

If an LED has an angular intensity distribution in the form $I_e(\theta) = I_e(0)\cos\theta$, its emission is called Lambertian. Under the assumption that the LED emission is Lambertian, the luminous intensity I_v in the normal direction can be estimated from the total luminous power Φ_v as:

$$I_v = \frac{\Phi_v}{\pi\ sr} \tag{2.4}$$

from which one of the most important figures of merit for LEDs, the luminance, can be calculated and reported:

$$L = \frac{I_v}{A} \tag{2.5}$$

where A is the device's area. To calculate the EQE, it is first necessary to calculate the number of photons emitted per unit time (from the radiant power through the average photon energy) and then divide it by the number of electrons injected per unit time (i.e. the current flowing through the device I):

$$EQE = \frac{\Phi_e / \overline{E_{ph}}}{I} \tag{2.6}$$

The average photon energy can be calculated from the emission spectrum $I_{e,\lambda}(\lambda)$ as follows:

$$\overline{E_{ph}} = \frac{\int_0^\infty \frac{hc}{\lambda} I_{e,\lambda}(\lambda) d\lambda}{\int_0^\infty I_{e,\lambda}(\lambda) d\lambda} \tag{2.7}$$

A Konica Minolta LS-150 luminance meter (not shown in **Figure 2.6**) was employed to account for any deviations of the photodiode's spectral responsivity with respect to the datasheet values. The instrument was equipped with a 110 close-up lens for small area measurements and controlled through the CS-S20 Data Management Software.

2.2.2. Characterization routine

After completing the device fabrication, the samples were placed in the custom setup for characterization.

1. The voltage applied to the device was manually increased while observing it until the point it started to emit light (turn-on voltage, V_{on}).
2. The device was kept on to acquire the EL spectrum by placing the optic fiber above it, which is essential to calculate the responsivity, the luminous efficacy and the average photon energy. The acquisition can be repeated at higher driving voltages to check for the spectral emission stability. The color coordinates can also be calculated from the EL spectrum.
3. The optic fiber placed above the device was swept for the photodiode and the applied voltage (V) was swept between two points (typically 0 V and the voltage corresponding to the peak luminance). The current I passing through the device and the current produced by the photodiode I_{pd} were measured for each voltage value.
4. The current density, luminance and efficiency for each swap point were calculated as described above and the data were displayed in two plots, one reporting the current density and the luminance as a function of applied bias with two ordinates in semilogarithmic display and one reporting the efficiency as a function of either the current density or, more commonly, the luminance (**Figure 2.7**). For devices emitting in the near infrared spectral range (NIR), the radiant intensity per unit area (radiance) was used instead of the luminance (as the luminous efficacy is zero or negligible).
5. To evaluate the operational lifetime of the devices, they were driven with a constant current and their luminance was monitored over time. Accelerated lifetime testing was also performed, consisting of driving the devices at elevated current densities to speed up degradation and estimate their operational stability.

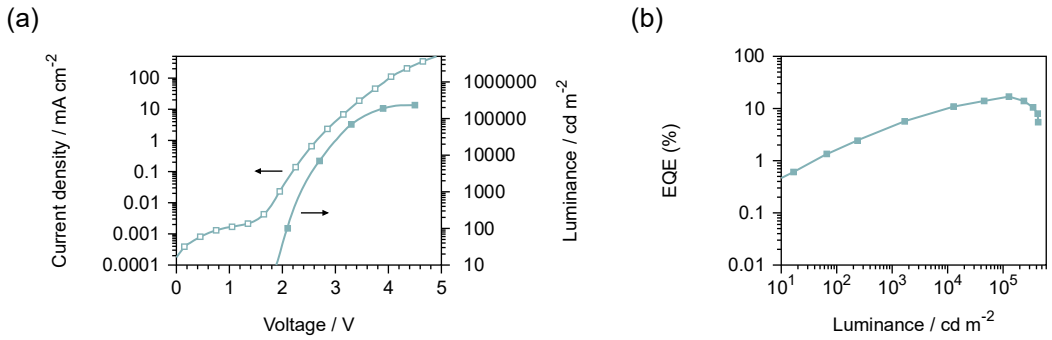

Figure 2.7. Common LED characterization data. (a) Current density – voltage – luminance (*J-V-L*) characteristics. (b) External quantum efficiency displayed as a function of luminance.

A LabVIEW program was used to control the Keithleys and the spectrometer, select the desired device within the substrate and acquire the data.

2.2.3. Supplementary characterization

Since device performance is closely linked to the morphological, electrical, electronic, and photophysical properties of their constituent layers, additional characterization techniques were employed to gain deeper understanding of these properties.

Photophysical and electronic measurements

The photoluminescence spectra were measured with the Avantes spectrometer equipped with a diode laser of integrated optics with an emission wavelength of 375 nm or with one with an emission wavelength of 405 nm.

The transmittance spectra were measured with the spectrometer equipped with an Avantes AvaLight-DS-S-BAL deuterium halogen light source and optic fibers.

The PLQY was measured with a Hamamatsu C9920-02 Absolute PL quantum yield spectrometer (**Figure 2.8a**) equipped with an A10094 integrating sphere unit, an A10080-02 monochromator, a Xe/Hg-Xe lamp and a PMA-12 photonic multichannel analyzer. The data were analyzed with U6039-05 PLQY measurement software.

Insight into the electronic structure and energy level alignment of materials used in devices is essential for understanding the positions of the valence and conduction bands, as well as the work function. This knowledge enables the optimization of charge injection and transport. Photoemission spectroscopy is a powerful tool to obtain such information; it involves illuminating the sample with monochromated UV photons, often emitted from a deuterium lamp, and counting the photoelectrons emitted from the sample. Photoelectron spectroscopy in air (PESA) systems do not require vacuum or electron energy spectrometers and are therefore smaller in size and easier to use. The PESA data for this work were acquired with an APS02 Ambient Pressure Photoemission Spectroscopy system (KP Technology Ltd) equipped with a digital TFT oscilloscope, a 2 mm gold tip and a 450 x 450 mm optical and Faraday enclosure (**Figure 2.8b**).

Figure 2.8. Equipment for photophysical and electronic characterization. (a) KP Technology APS02 PESA system. (b) Edinburgh Instruments FLS1000 photoluminescence spectrometer.

Structural characterization

The X-ray diffraction (XRD) patterns used to analyze the crystal structure, phase composition, and crystallinity of materials were collected in Bragg–Brentano geometry with an Empyrean PANalytical powder diffractometer (**Figure 2.9a**) equipped with a copper anode (operated at 45 kV and 40 mA), a hybrid monochromator (Cu Kα1) and a PIXcel detector and then analyzed using High Score software.

Scanning electron microscopy (SEM) images used to visualize the surface morphology and microstructure of materials were acquired using a Hitachi High-Tech Corporation S8010 ultra high-resolution SEM, equipped with an energy-dispersive X-ray (EDS) spectrometer.

SEM images were complemented with atomic force microscopy (AFM), which provides high-resolution, three-dimensional images of the surface of materials at the nanoscale. The measurements were carried out using a Bruker MultiMode 8 AFM (**Figure 2.9b**) equipped with a NanoScope V AFM controller. The images were obtained in tapping mode with silicon tips having a natural resonance frequency of 300 kHz and an effective spring constant of 40 N m^{-1}. The scan rate was adjusted for each image between 0.1 and 1 Hz (512 samples per line). The images were processed using Gwyddion SPM data analysis software.

Surface profiles and films' thicknesses were measured either with an Ambios Technology XP-1 stylus profiler (or "profilometer", **Figure 2.9c**) with a vertical resolution of 0.1 nm and a stylus force in the range 0.05 – 10 mg, with a KLA Alpha-Step D-500 stylus profiler or with a Filmetrics Profilm 3D optical profiler (**Figure 2.9d**). The former type operates by physically tracing the surface with a sharp tip, while optical profilers use interferometry to generate detailed surface maps.

Contact angle measurements were performed with a Ramé-hart Model 200 Standard Goniometer (**Figure 2.9e**) equipped with an automated dispensing system. Briefly, a drop of liquid is placed on the film and the angle formed by the drop at the three-phase boundary is measured. If the external angle is considered, the larger the value, the more "wettable" by the liquid the surface is. In the case of water, high values therefore correspond to hydrophilic surfaces.

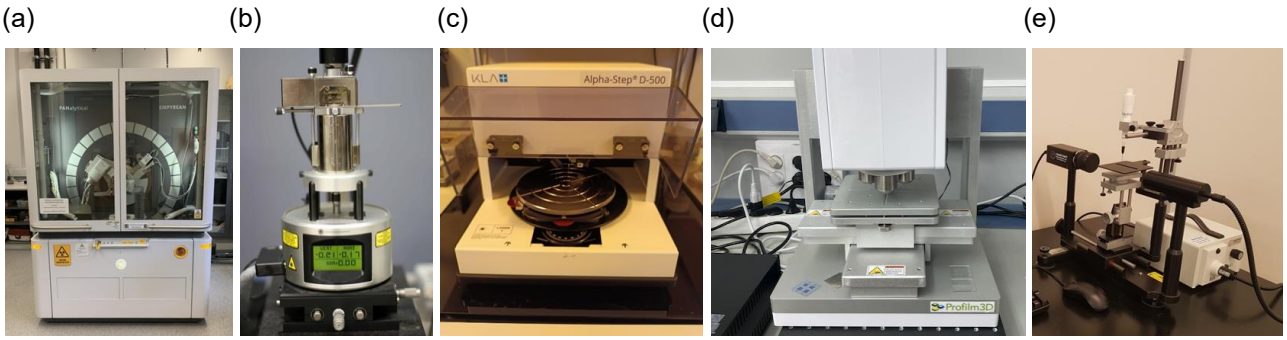

Figure 2.9. Instruments for the structural characterization of films. (a) Empyrean PANalytical powder diffractometer. (b) Bruker MultiMode 8 atomic force microscope. (c) Ambios Technology XP-1 stylus profiler. (d) Filmetrics Profilm 3D optical profiler. (e) Ramé-hart Model 200 contact angle goniometer.

Device simulations

Optical and electrical simulations of full devices are used to model and predict the behavior of light and charge carriers within LED devices and are equally important for identifying performance-limiting factors and guiding design optimization. For that, the electro-optical simulation software Setfos 5.5 (FLUXiM) was employed (**Figure 2.10**). First, the device stacks were defined by specifying the sequence of layers along with their physical and optical properties, such as thickness, refractive index, energy levels (HOMO/LUMO or bandgap), carrier mobilities, dielectric constants, and recombination parameters. Then, the calculation of outcoupling efficiency, emission spectra, and angular distribution were performed by letting the software model how light interacts with the device's multilayer structure. Internal and external quantum efficiencies could also be predicted by means of electrical simulations, which model charge injection, transport, and recombination by solving drift-diffusion equations based on the input material parameters, combined with the optical ones.

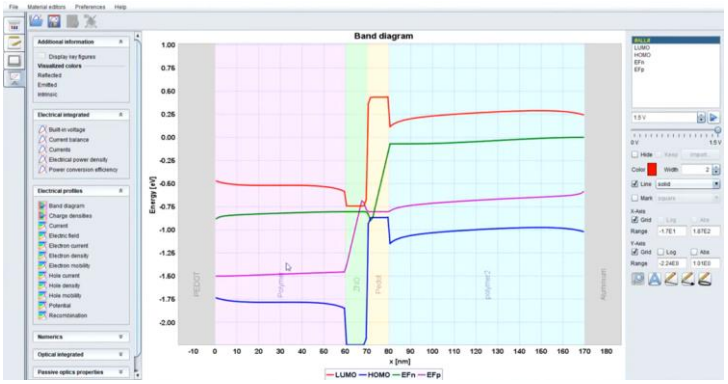

Figure 2.10. Graphical user interface of Setfos 5.5. Credit: FLUXiM.

Other device characterization tools

While routine device characterization provides essential information, in some cases advanced experimental techniques are required to reveal subtle structural, optical, or electronic features that are not accessible through standard methods.

The light emission of the devices over varied emission and polarization angles was measured with an angular luminescence spectrometer (Phelos, FLUXiM, **Figure 2.11a**) with a constant current density of 10 mA cm^{-2} and a polarization angle of 0 ° (p polarization). The capacitance *vs* frequency curves and the transient electroluminescence (TEL) signal were measured with Paios (FLUXiM, **Figure 2.11b**). The temperature-dependent *J-V-L* curves and TEL signal were measured with Paios equipped with a liquid nitrogen-based temperature module which was cooled by liquid nitrogen and heated via a heating resistor (**Figure 2.11c**).

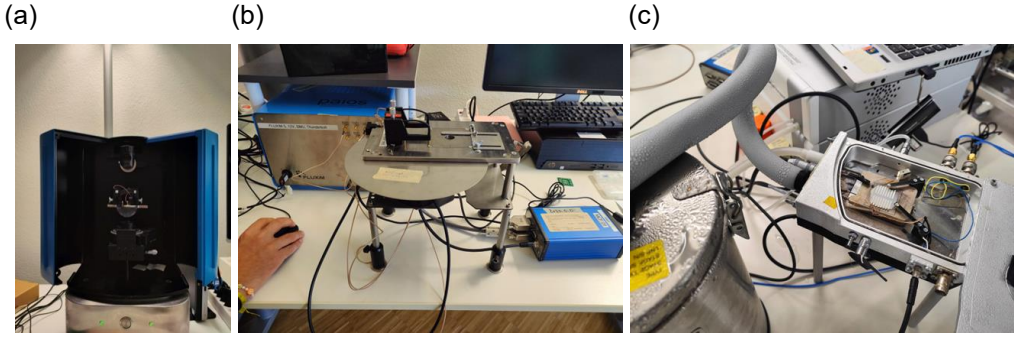

Figure 2.11. Tools for the advanced characterization of devices. (a) Phelos. (b) Paios. (c) Liquid nitrogen-based temperature module.

Chapter 3.

OLEDs comprising a perovskite transport layer and non-doped EMLs

3.1. Introduction

OLEDs offer a series of advantages over other display and lighting technologies, including higher contrast ratios, faster response times, wider viewing angles, and the possibility of fabricating thin, lightweight, and even flexible devices. However, they are expensive to make because of their materials' high cost and low utilization, the complex multi-layer fabrication, and low production yield.

First of all, thermal evaporation, the current industry manufacturing standard, requires precise vacuum conditions, highly controlled environments and expensive equipment. Secondly, OLED materials can be quite expensive, priced up to $10 000 per gram.[68] On top of that, in thermally evaporated devices, 97–98% of the prepared material does not end up getting deposited on the substrate.[68] This figure includes losses during startup, stabilization, equipment tooling, cooldown, and the unused material left in the crucible that needs periodic replacement. Finally, OLED production yield is never 100% and is in fact much lower. A report in The Elec (Korea Electronics Industry Media) from 2022 cites sources saying that Samsung's current yield rate for making QD-OLED panels was around 30%. This is because even tiny defects, contamination, or layer imperfections during the fabrication process can render panels unusable.[68] This sensitivity is, in turn, mostly due to the thin nature of OLEDs: even a microscopic particle or slight thickness variation can short-circuit the layers, create non-emissive spots, or accelerate degradation.[40]

The commonly employed host–dopant EML structure, essential to dilute the emitter and prevent ACQ, is a major contributor to the high cost of OLEDs. In fact, its stringent accuracy requirements for doping concentration i) demand more specialized co-evaporation equipment, ii) increase material utilization (because extra material is wasted during the stabilization prior to deposition)[68] and iii) makes it harder to consistently produce OLEDs with identical performance, resulting in many devices to fall outside specifications which directly lowers production yield.[69]

An alternative to the host–dopant EML configuration consists of using ultrathin non-doped emissive layers (UEMLs) composed of films of pure emitter with a thickness below 1 nm. This approach entails much lower material consumption. Indeed, it has been estimated that 70% of the material consumption can be saved if a 10 vol% emitter doped in a 10-nm-thick host is replaced with a UEML only 0.3 nm thick.[70] Unfortunately, effective implementation of this approach hinges on two key factors. On one hand, the molecules constituting the ultrathin layer, albeit statistically isolated for the most part, should still possess a low tendency of aggregating in the film. Secondly, the reduction in the emissive layer thickness aggravates the device's sensitivity to defects, shunting paths between the electrodes, instability, and performance variability caused by slight thickness variations,[71] which all lower manufacturing yield.

Another alternative strategy would be to use lower-cost and high-material utilization solution-processing techniques such as inkjet printing.[72] In contrast to thermal evaporation and other solution-based processes, inkjet printing technology achieves nearly 100% material utilization.[73] Dendrimers are perfect candidates for emitters in inkjet printing (and more in general for solution-processed OLEDs) because their highly branched, tree-like structure lends them a highly modular molecular design. Thanks to that, their peripheral dendrons (the branched arms of a dendrimer) can be made to act as steric barriers around the emissive core, suppressing ACQ and enabling simplified host-free EMLs for lower fabrication costs. However, the use of a solution process for the deposition of a layer entails complications, because depositing it could dissolve the layer beneath it,[74] impeding multilayer-stacked device structures.[72]

Halide perovskites, whose precursors are inexpensive and accessible, offer a solution to both problems when used as transport layers. Their limited solubility in the low-polarity organic solvents used for the solution processing of organic layers allows for their deposition on top to form multilayered structures. At the same time, their excellent transport properties (high charge carrier mobility and long diffusion

length) allow for very thick layers. These layers can cover particles and residues on substrates and mitigate nonuniform device thickness without compromising efficiency, a highly sought-after property, especially when using ultrathin non-doped emissive layers. In other words, perovskite layers can lower the manufacturing costs of OLEDs both by facilitating the implementation of cost-effective and low-material consumption deposition methods and by increasing device production yield.

In this work, OLEDs with a thick halide perovskite-based transport layer are reported, exploring the potential of both approaches. First, the perovskite HTL was combined with cost-effective non-doped UEMLs, based on either phosphorescent complexes or TADF compounds. The transparency of the perovskite layer also enabled the realization of micrometer-thick transparent light-emitting diodes incorporating a transparent conductive oxide as the top electrode. Then, the compatibility of the perovskite HTL with different solvents was assessed with the goal of fabricating OLEDs with a solution-processed non-doped dendrimer EML. The high performance of the obtained devices was enabled by a facile strategy to passivate trap states that will also be described in this Chapter.

3.2. Experimental section

3.2.1. Materials

Cesium chloride (CsCl, 99.999%) was purchased from Sigma Aldrich. Aqueous PEDOT:PSS dispersion was obtained from Clevios™ (P VP AI 4083). Organic materials (bis[2-(2-pyridinyl-N)phenyl-C](acetylacetonato)iridium(III), mCP, (10-(4-(4,6-diphenyl-1,3,5-triazin-2-yl)phenyl)-9,9-dimethyl-9,10-dihydroacridine and PO-T2T) and lead chloride ($PbCl_2$, 99.999%) were purchased from Lumtec. Synthesis of 9',9'''',9''''''',9'''''''''-((6-phenyl-1,3,5-triazine-2,4-diyl)bis(benzene-4,1,2-triyl))tetrakis(3,3'',6,6''-tetra-tert-butyl-9'H-9,3':6',9''-tercarbazole (tBuCz2m2pTRZ) was carried out following a previously published procedure[75] in the laboratories of the University of St Andrews.

3.2.2. Perovskite film deposition and characterization

Perovskite film deposition

The $CsPbCl_3$ films were deposited by dual-source thermal evaporation. The deposition rate for $PbCl_2$ and CsCl were kept constant at 0.75 Å/s and 0.60 Å/s, respectively. Layers referred to as m-$CsPbCl_3$ included 2 nm CsCl interlayers before and after the $CsPbCl_3$ layer (CsCl/$CsPbCl_3$/CsCl). The perovskite films were thermally annealed at 120 °C for 10 minutes after their deposition.

Solvent treatment of perovskite film

To test the resistance of the perovskite films to solvents, 100 µl of pure solvents (chloroform, toluene or chlorobenzene) were spin-coated onto 100 nm-thick m-$CsPbCl_3$ films (deposited on top of a PEDOT:PSS CH8000 layer) at 1500 rpm for 60 seconds. The films were annealed a second time at 120 °C for 10 minutes after the solvent treatment.

Perovskite film characterization

XRD patterns and AFM and SEM images of the perovskite films were acquired as described in Paragraph 2.2.3. Additionally, grazing-incidence wide-angle X-ray scattering (GIWAXS) patterns were measured in a vacuum using a customized setup equipped with a laboratory MetalJet X-ray source (Excillum) with an X-ray energy of 9.25 keV (λ = 1.34 Å) and a two-dimensional detector (Pilatus 300 K, Dectris, Switzerland, pixel size 175×175 µm). The X-ray incidence angle was set to ~ 0.5°, the sample-to-detector distance to around 114 mm and the integration time to 600 sec.

3.2.3. Device fabrication

After cleaning the ITO-coated glass substrates, a PEDOT:PSS film was deposited on top via spin-coating a PEDOT:PSS Al4083 suspension at 2000 rpm for 60 seconds, resulting in a 30 nm-thick film. The PEDOT:PSS films were then thermally treated at 150 °C for 10 min. These substrates were transferred to a thermal evaporation system, where the perovskite films were deposited according to the procedure described above. After the perovskite film deposition and annealing, the substrates were transferred back to the same thermal evaporation system where mCP, bis[2-(2-pyridinyl-N)phenyl-C](acetylacetonato)iridium(III) ($Ir(ppy)_2acac$, structure in **Figure 3.1a**) or (10-(4-(4,6-diphenyl-1,3,5-triazin-2-yl)phenyl)-9,9-dimethyl-9,10-dihydroacridine (DMAC-TRZ, **Figure 3.1b**) and PO-T2T were deposited at a rate of 0.06 nm s^{-1}, 0.001 nm s^{-1} and 0.1 nm s^{-1}, respectively, before being moved to another thermal evaporation system where Ba (5 nm) and Ag (70 nm) were deposited at a rate of 0.05 nm s^{-1}.

For the transparent devices, the thickness of the Ag layer was limited to 5 nm, before a 135 nm-thick ITO cathode was deposited by PLD according to the procedure described in Section 2.1.

For the devices with a solution-processed EML, a 10 mg ml^{-1} solution of 9',9'''',9''''''',9'''''''''-((6-phenyl-1,3,5-triazine-2,4-diyl)bis(benzene-4,1,2-triyl))tetrakis(3,3'',6,6''-tetra-tert-butyl-9'H-9,3':6',9''-tercarbazole (tBuCz2m2pTRZ, **Figure 3.1c**) in chlorobenzene was spin-coated on top of the annealed perovskite HTL at 1500 rpm for 60 s to form a 40 nm-thick EML, which was then annealed at 120 °C for 10 minutes. The rest of the layers were deposited as aforementioned.

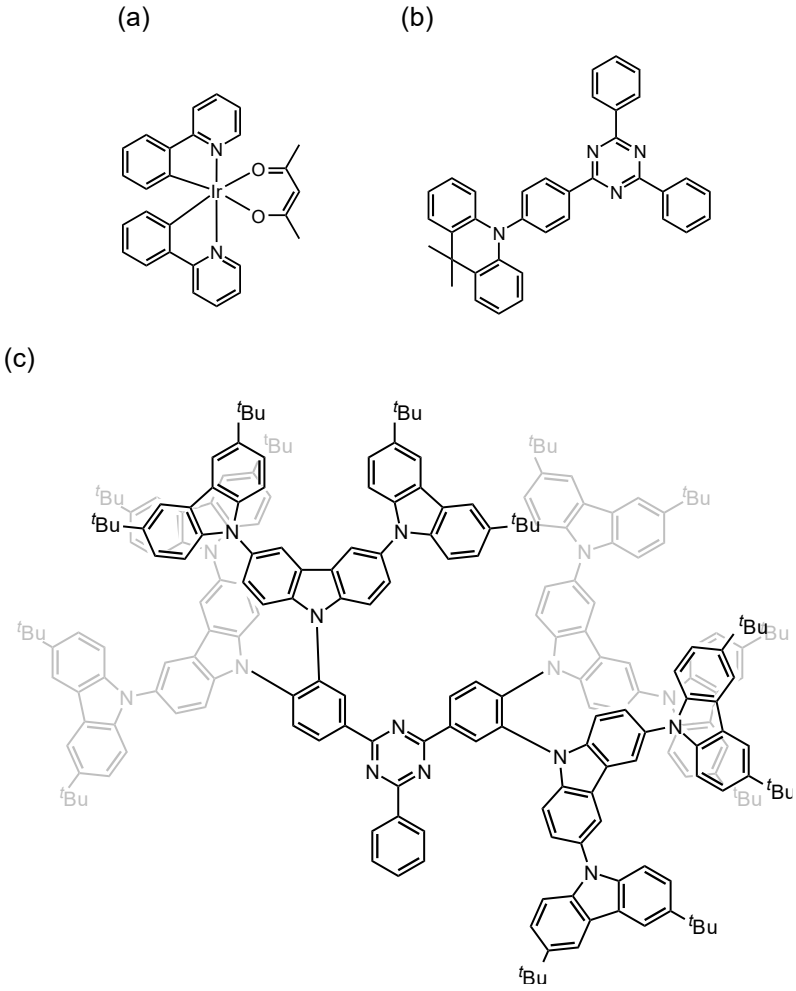

Figure 3.1. Chemical structures of the emitters used in this study. (a) $Ir(ppy)_2(acac)$. (b) DMAC-TRZ. (c) tBuCz2m2pTRZ.

3.2.4. Device characterization

Opaque devices were characterized following the standard procedure described in Paragraph 2.2.2.

In the case of transparent light-emitting diodes, which emit light from both sides, the characterization procedure was slightly adapted. First, the EL spectrum was recorded from the bottom (glass) side of the device. Subsequently, the devices were driven at three constant current density values, and the corresponding photodiode current was measured. The devices were then flipped to record the EL spectrum and photodiode current from the top side under the same driving conditions. For each current density, the ratio between the photodiode currents measured from the bottom and top sides was calculated, and the average of these three ratios was taken as the emission ratio between the two sides. Finally, the devices were flipped again, and the *J*–*V*–*L* characteristics were acquired as usual. The previously determined emission ratio was then used to estimate the combined luminance and efficiency.

3.3. Results and discussion

3.3.1. Thermally evaporated perovskite layers

As a first step, the possibility of fabricating a cesium lead chloride ($CsPbCl_3$) perovskite charge transport layer via simultaneous thermal evaporation of the perovskite precursors (CsCl and $PbCl_2$) was explored.

Both the deposition method and the perovskite compositions were rationally selected. Thermal evaporation offers precise control over the thickness and composition of the resulting films and bypasses precursor solubility constraints, making it a viable route for depositing extraordinarily thick films. As for the composition, $CsPbCl_3$ was selected instead of $CH_3NH_3PbCl_3$ or $CH_3NH_3PbBr_3$ used in previous reports, since evaporating methylammonium halides (CH_3NH_3Cl or CH_3NH_3Br) for hybrid perovskites hinders high vacuum due to their intrinsic volatility,[40] while a chloride perovskite was used due to its transparency in the visible range (**Figure 3.2**), as opposed to bromide or iodide perovskites,[76] to prevent unwanted absorption by the perovskite HTL.

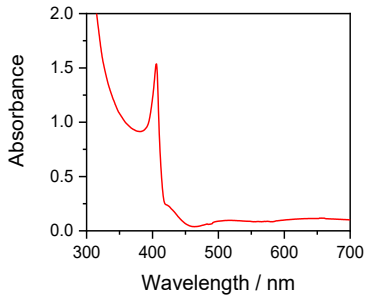

Figure 3.2. Absorption spectrum of a 200 nm-thick $CsPbCl_3$ film deposited on a PEDOT:PSS-covered ITO substrate.

However, halide vacancies in lead chloride perovskites induce deeper trap states than in iodide and bromide perovskites, making it crucial to suppress these chloride vacancies to prevent degradation caused by trap states during device operation.[77,78] Since cesium halide precursors are able to passivate the interfacial defects of inorganic perovskites,[79] thin CsCl layers (2nm) were inserted before and after the co-evaporated $CsPbCl_3$ layer. This stack, $CsCl/CsPbCl_3/CsCl$, will be referred to as modified $CsPbCl_3$ (m-$CsPbCl_3$) for simplicity.

The PL spectra of 200 nm-thick $CsPbCl_3$ and m-$CsPbCl_3$ films deposited on PEDOT:PSS were measured, showing that the PL peak of m-$CsPbCl_3$, centered around 419 nm, is improved by almost 2 times (7200 counts to 4000 counts, corresponding to a PLQY of 0.3%), proving that the surface defects are reduced by the excess CsCl on interfaces (**Figure 3.3a**). In addition, the XRD pattern (**Figure 3.3b**) of m-$CsPbCl_3$ layers shows two extra peaks at 15.8 ° and 31.8 °, which can be indexed as (100) and (200), besides the peak at 22.3 ° (101) present in the pristine $CsPbCl_3$ film. This difference indicates that the seeding CsCl layer exerts a significant influence on the subsequent crystal growth of the deposited $CsPbCl_3$ layer. Specifically, it suggests that the presence of the CsCl layer induces preferential orientation of the perovskite along the a-axis (or, in other words, most crystallites are aligned so that their a-axis is out-of-plane, while the b- and c-axes lie mostly in-plane). As a further confirmation, the XRD pattern of $CsPbCl_3$ films deposited directly on PEDOT:PSS with a CsCl layer just on top was measured and found to be identical to that of a pristine $CsPbCl_3$ film, not showing the intense (100) and (200) peaks.

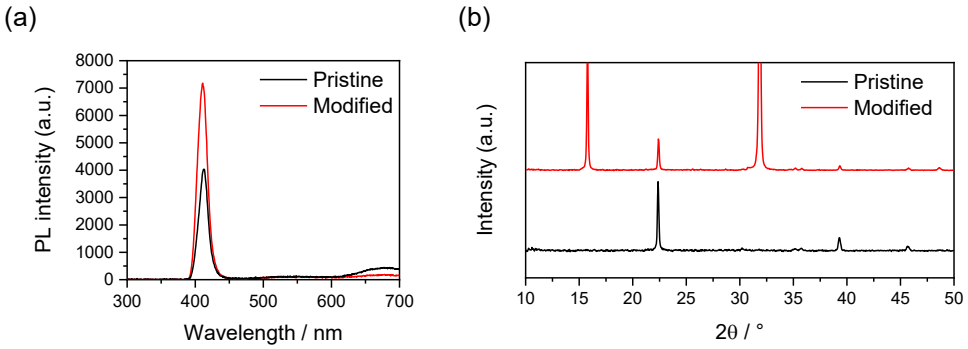

Figure 3.3. (a) PL spectra and (b) XRD patterns of 200 nm-thick $CsPbCl_3$ with ("modified") and without ("pristine") excess CsCl on top and bottom interfaces.

3.3.2. Devices with a perovskite HTL and a UEML

Next, devices comprising the m-$CsPbCl_3$ hole transport layer were fabricated with the following architecture: ITO (150 nm)/PEDOT:PSS (30 nm)/m-$CsPbCl_3$ (200 nm)/mCP (20 nm)/$Ir(ppy)_2(acac)$ (0.03 nm)/PO-T2T (60 nm)/Ba (5nm)/Ag (70 nm). The thickness of the perovskite HTL was chosen to balance quick deposition time (24 minutes) with the benefits of thicker transport layers. The emitter $Ir(ppy)_2(acac)$ was selected as it has shown very promising results both in a host-guest active layer matrix with nearly 100% internal phosphorescence efficiency,[80] as well as in the UEML of spacer-free white OLEDs.[70] mCP and PO-T2T were selected as HTL and ETL, respectively, as they have shown very efficient exciplex formation.[81,82] In addition, mCP offers good exciton confinement benefiting from high LUMO (−2.4 eV) and large E_g (3.5 eV).[53] The energy level diagram of the devices can be seen in **Figure 3.4a**.

Notably, no host material had to be simultaneously co-evaporated with the Ir complex. The simplicity of single-source evaporation of the emissive layer is indeed one of the advantages of ultrathin non-doped emissive layers. Generally, the ideal thickness of ultrathin emissive layers reflects a compromise between minimizing concentration quenching, which increases as emitter molecules come closer together due to enhanced triplet–triplet annihilation, and maximizing exciton utilization and energy transfer efficiency. The nominal thickness of the emissive layer chosen for $Ir(ppy)_2(acac)$ (0.03 nm) was the result of a thickness-dependent efficiency study, where devices with higher thicknesses (0.3 nm and 1 nm) performed equally well at low luminance values (<10 cd m^{-2}) but showed more significant efficiency roll-off at higher luminance values (**Figure 3.6a**), probably due to TTA becoming more prominent as the distance between the emitter molecules becomes progressively shorter. A further reduction in thickness, despite being advisable from a material cost perspective, would end up lowering the efficiency due to less efficient exciton utilization, as already reported.[70]

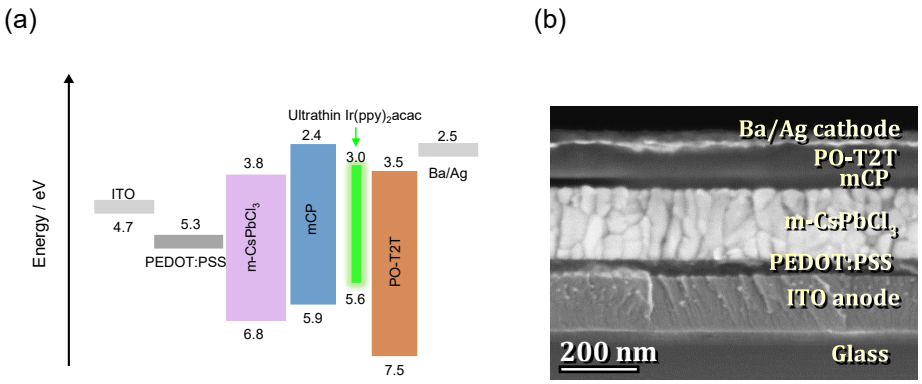

Figure 3.4. (a) Energy level diagram for the devices studied in this work. (b) Cross-sectional SEM image of a device.

The devices were first characterized by SEM, which not only confirmed the layers' thickness, but also gave supplementary information about the perovskite film morphology (**Figure 3.4b**). The film cross-section evidenced large vertical grains arranged in a compact and void-free manner, occasionally extending vertically throughout the layer, from top to bottom. This can make vertical transport more efficient, as it is not limited by grain boundaries. Furthermore, the upper and lower surfaces of the thin film appeared to be flat, which is notable considering the polycrystalline nature of $CsPbCl_3$ and is desirable towards the prevention of shunting paths. From the image it was clear that the mCP and PO-T2T layers were contiguous, which is beneficial for the formation of the exciplexes whose energy is ultimately transferred to the scattered emitter molecules for the light emission.

The devices were characterized by means of current density-voltage-luminance (*J-V-L*) scans. They showed a low turn-on voltage (3.3 V for 1 cd m^{-2}), achieved a peak luminance of 15 145 cd m^{-2} (at 15.2 V) (**Figure 3.5a**) and a peak efficiency of 52.9 cd A^{-1} (at 375 cd m^{-2}), which corresponds to an EQE of 14.3%, with negligible efficiency roll-off (49.8 cd A^{-1} at 1000 cd m^{-2}) (**Figure 3.5b**). The low turn-on voltage is characteristic of exciplex OLEDs, confirming that mCP:PO-T2T allows for efficient exciplex-based emission in this system.[83] Green-yellow emission (peak at 557 nm) from the phosphorescent $Ir(ppy)_2(acac)$ was observed (inset in **Figure 3.5c**), suggesting that charge recombination primarily occurs in the emissive layer.

The detailed shape of electroluminescence spectrum (peaked at 557 nm, with a shoulder around 528 nm) is comparable to that of other $Ir(ppy)_2(acac)$-based OLEDs,[84] with small deviations attributable to differences in the relative average orientation of the emissive dipoles that would even allow, in principle, to quantitatively determine the anisotropy factor *a* through a combination of full angle dependent spectral radiant intensity measurement and optical simulations. In any case, the EL spectra of the device driven at different voltage values indicates an immediate transfer of energy from the exciplexes generated between mCP and PO-T2T to $Ir(ppy)_2(acac)$, without saturation of the green emission with triplet excitons even under increasing driving voltage. Consequently, the CIE color coordinates of (0.40, 0.58) were quite stable for brightness increasing to over 10 000 cd m^{-2}. Moreover, the electroluminescence spectrum shows no sign of radiative recombination in the perovskite layer, in accordance the efficient energy transfer to the emissive layer[52] and the role of mCP as an exciton blocking layer.

The operational lifetime of the devices was also measured, by applying a constant current density equivalent to an initial luminance of 400 cd m^{-2}, finding an LT_{50} value of 3 h.

In order to leverage the advantageous carrier mobility of perovskite materials, devices with a 1000 nm-thick perovskite transport layer were also fabricated. The increment in thickness increased the operating voltage (5.0 V for 1 cd m^{-2}, **Figure 3.5a**) but left the current efficiency and EQE unchanged within the experimental error (54.1 cd A^{-1} peak, 51.0 cd A^{-1} at 1000 cd m^{-2}, **Figure 3.5b**), confirming that $CsPbCl_3$ is not only suitable for thick transport layers but also less sensitive than organic materials to thickness changes.

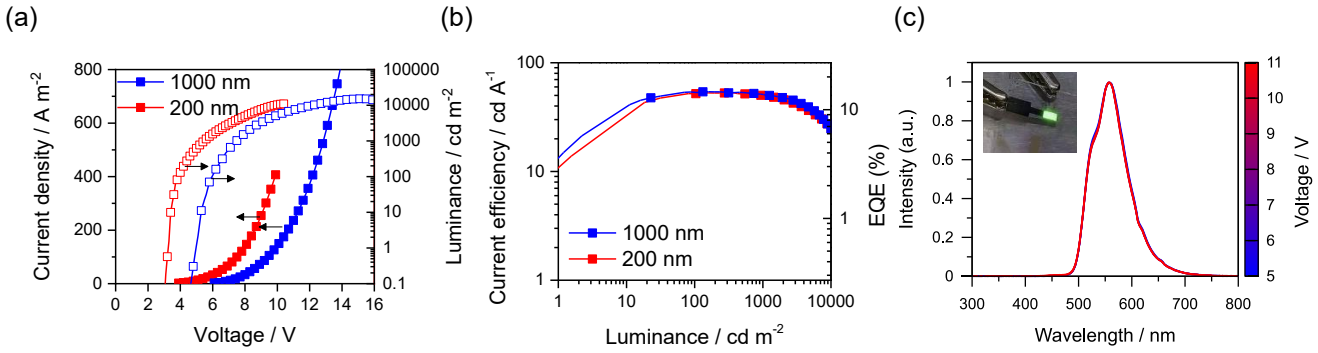

Figure 3.5. (a) *J–V–L* characteristics of devices with two different perovskite HTL thicknesses, 200 nm (red) and 1000 nm (blue). (b) EQE and current efficiency *vs* luminance plot for the same devices. (c) Normalized EL spectrum of devices with a 200 nm-thick modified perovskite HTL driven at different voltage values. Inset: photo of a working device operated at 6.0 V.

To assess the effect of the CsCl passivating layers in the m-$CsPbCl_3$ HTL, a device using pristine $CsPbCl_3$ was also prepared. The device reached a peak current efficiency of 30.7 cd A^{-1} (at a much lower luminance of 1.8 cd m^{-2}), which confirms the beneficial role of vacancy passivation (**Figure 3.6b-c**). The XRD data, together with the cross-sectional SEM picture, hint at another possible reason for the better performance of the devices containing the CsCl passivation layers. Carrier mobility is isotropic along the three unit cell dimensions only in cubic phases, but $CsPbCl_3$ exists in the orthorhombic phase below 315 K;[85] assuming the mobility is higher in the direction perpendicular to the substrate ([100] direction, *a*-axis), as hinted at by theoretical calculations on other perovskite compositions,[86,87] charges would be transported more easily across the layer where the unit cell is oriented vertically with respect to the substrate plane.

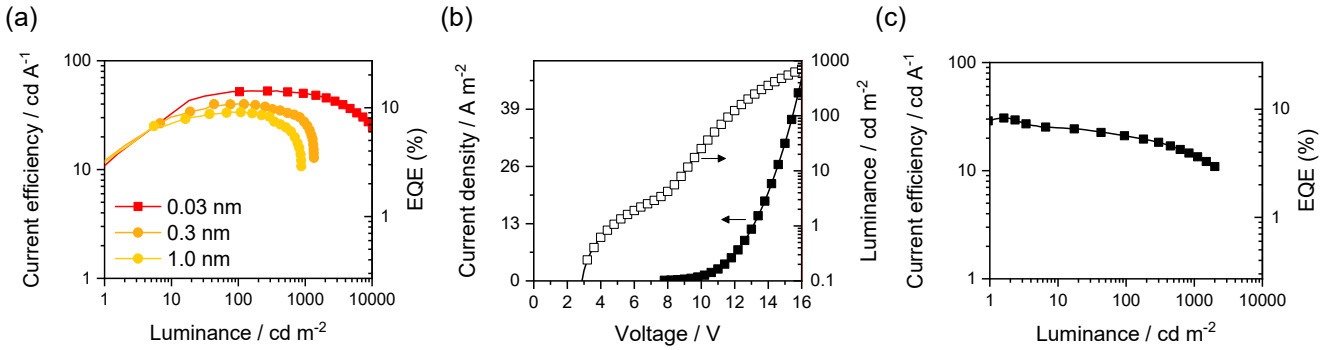

Figure 3.6. (a) EQE and current efficiency *vs* luminance plot for devices with a 200 nm-thick modified perovskite HTL and different EML thickness values. (b) *J–V–L* characteristics of a device incorporating a pristine perovskite HTL. (c) EQE and current efficiency *vs* luminance plot for the same device.

3.3.3. Role and nature of the UEML

By means of high resolution AFM images it has been previously observed that the roughness of organic surfaces increases as ultrathin layers are deposited onto them, indicating that the growth takes place via an island growth mode due to the molecular aggregation.[16] To verify if this also applies to $Ir(ppy)_2(acac)$ ultrathin emissive layers, the root mean square roughness (S_q) of a 20-nm-thick mCP film before and after the deposition of $Ir(ppy)_2(acac)$ (with a nominal thickness of 0.03 nm) was measured through AFM. Values of 0.36 nm and 0.60 nm, respectively, were found, which confirms that the growth of $Ir(ppy)_2(acac)$ layers takes place similarly to previously reported ultrathin layers.

Moreover, it is expected that the deposition of the emitter molecules not only increases the surface roughness but also produces a slightly less hydrophobic surface. To further confirm that, contact angle measurements were performed as a qualitative way of estimating how hydrophilic the different surfaces are. Four surfaces were tested: ozone-treated plain glass and three 20-nm-thick mCP films. On two of the mCP films, Ir complex layers of different thicknesses, 0.03 nm and 2 nm, were deposited. The resulting images are shown in **Figure 3.7**. Since $Ir(ppy)_2(acac)$ is more hydrophilic than mCP by virtue of its zwitterionic nature (**Figure 3.1a**), it is expected that a thick layer of Ir complex on top of an mCP layer would be more polar. This is indeed what was seen: a thicker 2-nm layer of $Ir(ppy)_2(acac)$ on top of mCP presented a higher contact angle compared to the pure mCP layer (104.1° vs 92.6°, respectively). However, when the deposited Ir complex layer was ultrathin (0.03 nm) the contact angle was similar to that of the mCP layer, concluding that the $Ir(ppy)_2(acac)$ is not in the form of a neat layer. This is beneficial for reducing molecular aggregation, eliminating concentration quenching and allowing interfacial exciplex formation, and is in agreement with what has been previously proposed.[88]

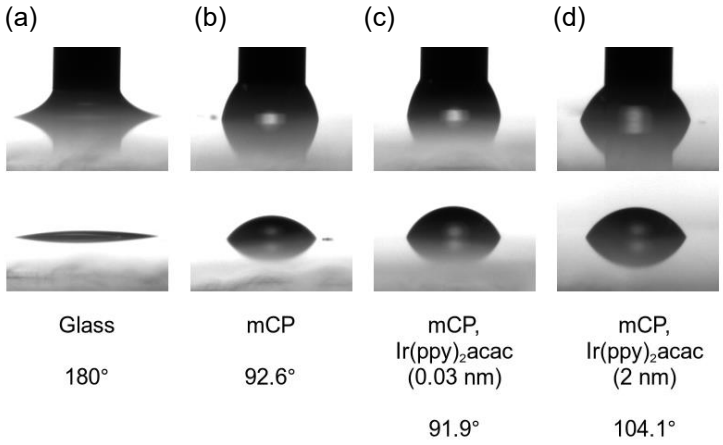

Figure 3.7. Photographs and results of contact angle measurements carried out on films: (a) Glass. (b) Glass/mCP. (c) Glass/mCP/$Ir(ppy)_2(acac)$ (0.03 nm). (d) Glass/mCP/$Ir(ppy)_2(acac)$ (2 nm).

Despite being in the form of isolated islands, ultrathin emissive layers can still affect the performance of the devices considerably. To demonstrate this, identical devices were prepared but without $Ir(ppy)_2(acac)$. The stack therefore was ITO (150 nm)/PEDOT:PSS (30 nm)/m-$CsPbCl_3$ (200 nm)/mCP (20 nm)/PO-T2T (60 nm)/Ba (5nm)/Ag (70 nm). Their *J–V–L* scans are illustrated in **Figure 3.8a**. As mentioned above, the mCP:PO-T2T pair used in this work is known to be able to form exciplexes in bi-component mixed films.[89] In the presence of the $Ir(ppy)_2(acac)$ film, the excitons are primarily formed on the exciplex host (donor:acceptor) and then the energy is efficiently transferred from the exciplex to the dopant, which is made possible by a higher T_1 level of the exciplex than that of the dopant and by a suitable overlap between the emission of exciplex and the absorption of dopant[90]. Without the Ir emitter, the exciplexes that form from accumulated charge carriers at the interface between mCP and PO-T2T cannot transfer their energy and while they are still able to decay radiatively, they do so with a lower efficiency and with a feature-less and wide emission spectrum (**Figure 3.8b**). The wavelength around which the emission is centered (531 nm) corresponds to the energy gap between the HOMO of mCP and the LUMO of PO-T2T (as can be seen in the energy level diagram in **Figure 3.4a**). Moreover, the emission spectra of such devices were characterized by a second peak at 439 nm, whose relative intensity increases with progressively higher driving voltages (**Figure 3.8b**). This peak can be attributed to radiative recombination of the carriers happening in the perovskite layer, which becomes more prominent when the emission from the mCP/PO-T2T exciplexes gets saturated.

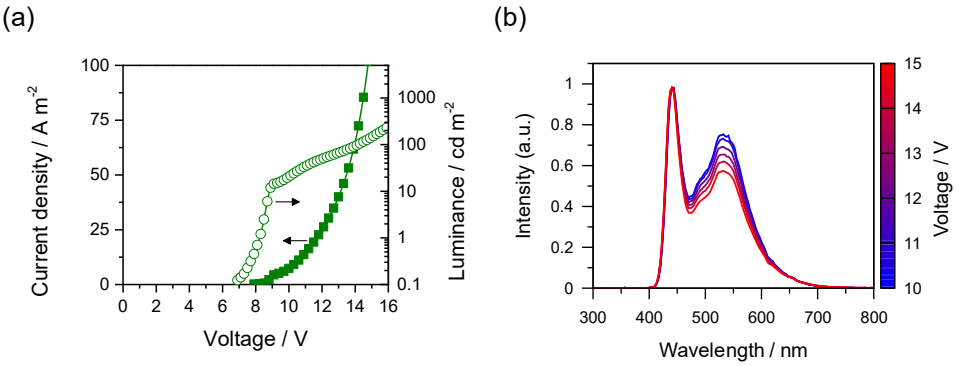

Figure 3.8. (a) *J–V–L* characteristics of a device with a modified perovskite HTL but no EML. (b) Normalized EL spectrum of the same device driven at different voltage values.

3.3.4. Transparent devices

The transparency of the organic thin films and the perovskite transport layer used in these OLEDs also allows for the development of transparent devices, where light can travel and exit in both directions, provided that the electrodes at both ends are transparent. They could then be used to provide information overlays without obstructing views in smart windows, dynamic advertising, augmented reality displays, and innovative architectural designs, just to name a few potential applications.[91–93] Conductive oxides like ITO or indium zinc oxide (IZO) can be used as top electrodes for this purpose, but the deposition of the top contact can cause sputter damage on the underlying layers (more on the subject in **Chapter 5**).[94] To solve this problem, a resistant metal buffer layer can be used to prevent plasma damage. While a metal top electrode inevitably lowers transmittance, the reduction can be limited by minimizing the metal layer thickness. Hence, to demonstrate transparent OLEDs, a device with a 1000 nm-thick perovskite transport layer and a Ba (5 nm)/Ag (5 nm)/ITO (135 nm) top cathode was fabricated, where the ITO layer was processed via PLD. The full stack was ITO (150 nm)/PEDOT:PSS (30 nm)/m-$CsPbCl_3$ (1000 nm)/mCP (20 nm)/$Ir(ppy)_2$acac (0.03 nm)/PO-T2T (60 nm)/Ba (5 nm)/Ag (5 nm)/ITO (135 nm).

The transmission varied significantly across the visible spectrum (from 410 to 700 nm) between 40 and 70% (blue curve in **Figure 3.9a**). The main reason for the transmission spectrum not to be flat is the evident interference pattern that dominates it. To investigate its origin, the transmittance of the stack was measured after the deposition of each individual layer. The resulting detailed transmittance analysis revealed that it is the perovskite transport layer, by virtue of its large thickness comparable with the wavelength of visible light, that causes the interference pattern to appear in a region of the spectrum below its bandgap. This property, which is typical of thick perovskite layers also with other compositions,[95] is beneficial though, as it allows for the perovskite layer's thickness to be used as an additional tuning parameter to adapt the proportion of light exiting each side depending on the specific application and needs.

Aesthetics also play an important role in practical applications, such as architectural window glass and mobile surfaces. The quantitative assessment of aesthetic quality can be based on two primary metrics: the average visible transmittance (AVT), which keeps both the photopic response function and the spectral power distribution of the light source into account, and the color rendering index (CRI).[96] The CRI is especially used in the window business to measure the fidelity with which colors are rendered when objects are behind the windows or, in this case, the transparent devices. Using the transmittance spectrum of the transparent OLED as input data and the CIE standard illuminant D65 to represent natural daylight,[97] it was possible to calculate an AVT of 50.6% and a CRI of 88.5. The CRI value, lower

than 100 but still higher than 80, indicates slight distortion of the color of the transmitted light and is due to a non-flat absorption spectrum over the visible range. The CIELAB color space coordinates (a*, b*) calculated for the devices in question are negative (-1.70 and -12, respectively) and thus specify greenish/bluish tones (**Figure 3.9b**), which are often preferred for modern windows over glass with reddish or yellowish tones.

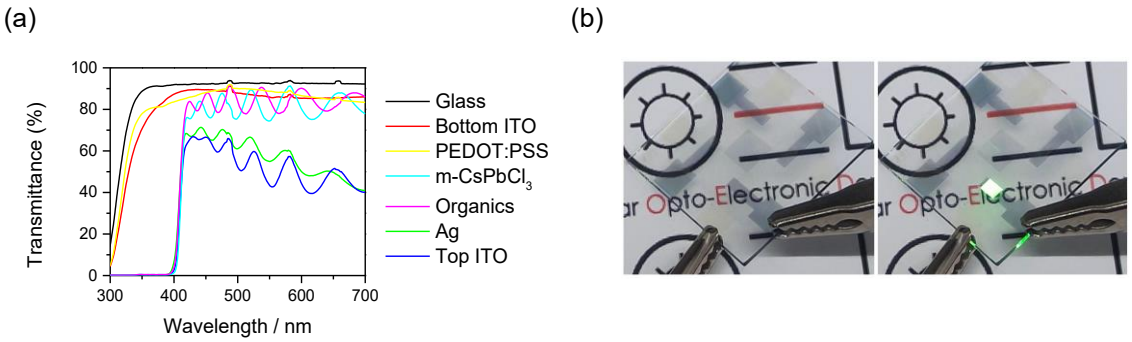

Figure 3.9. (a) Transmittance spectrum for transparent device with a thin protective metal layer and a 1000 nm-thick perovskite HTL measured after the deposition of each individual layer onto the previous ones. In the legend, only the uppermost layer is listed. (b) Photos of the same devices in their off (left) and on (right) state.

The detailed analysis of the stack transmittance also shows that the largest loss in transmittance is due to the presence of the strongly absorbing metal layers. This makes it crucial to explore alternative protective strategies that preserve both optical transmittance and structural integrity, which will be the subject of **Chapter 5**.

Then, the *J*–*V*–*L* characteristics of the devices were considered (**Figure 3.10a**). The peak luminance of the semitransparent device reached a value of 1453 cd m^{-2} when measured from the bottom (glass/ITO) side and 829 cd m^{-2} from the top (Ba/Ag/ITO) side. While the obtained values are still high enough to guarantee a very strong on/off contrast in conjunction with the high transparency (**Figure 3.9b**), they are significantly lower than what was obtained for the "opaque" device (slightly over 15 000 cd m^{-2}). This is partially due to the lower charge injection and current density, but also to a lower peak efficiency of 41.3 cd A^{-1} (EQE_{max} of 11.2%, **Figure 3.10b**) considering both top and bottom emission together, which in turn might be the result of a lower efficiency in light extraction.

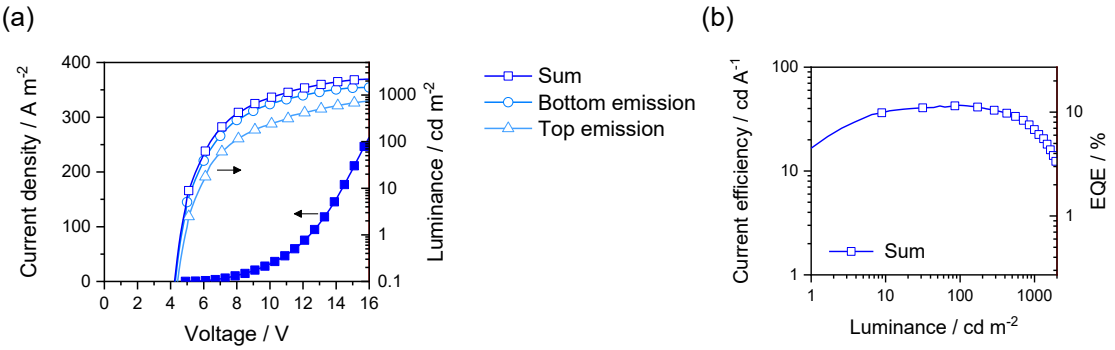

Figure 3.10. (a) *J–V–L* characteristics of transparent devices with a thin protective metal layer and a 1000 nm-thick perovskite HTL. (b) EQE and current efficiency *vs* luminance plot for the same devices.

Photon outcoupling, together with partial absorption and reflection by the metal layers, also explains the difference between peak top and bottom luminance: on the top side, light is confined within the oxide layer because of the high refractive index contrast between the top ITO layer (typically around 1.8 for commercial ITO on glass substrates) and air, but for the bottom emission, light must pass through glass as well before escaping from the device, whose index of refraction (≈1.5) is intermediate between ITO and air.[98,99]

3.3.5. Devices with a perovskite HTL and a TADF-based UEML

Despite the use of UEMLs significantly reducing the amount of material required, the high cost and limited availability of iridium and other heavy metals in phosphorescent emitters remain a notable drawback. TADF molecules offer a promising alternative by eliminating the need for heavy metals while maintaining high IQE. Since emitters are susceptible to aggregation and quenching when introduced as an ultrathin emissive layer, we selected 10-(4-(4,6-diphenyl-1,3,5-triazin-2-yl)phenyl)-9,9-dimethyl-9,10-dihydroacridine (DMAC-TRZ), a small donor–acceptor (D–A) molecule which contains methyl groups at the sp^3 carbon of the dihydroacridine donor (structure in **Figure 3.1b**) that space the emitter molecules and decrease the interaction between donors. Therefore, devices comprising the perovskite HTL and a DMAC-TRZ UEML were fabricated using the same base architecture demonstrated to be efficient with $Ir(ppy)_2(acac)$: ITO (150 nm)/PEDOT:PSS (30 nm)/m-$CsPbCl_3$ (200 nm)/mCP (10 nm)/DMAC-TRZ/$Ir(ppy)_2acac$ (0.03 nm)/PO-T2T (60 nm)/Ba (5 nm)/Ag (5 nm)/ITO (135 nm)

However, as different compounds have different tendencies to aggregate and susceptibilities to concentration quenching,[100–102] it was not guaranteed that the optimum thickness found for $Ir(ppy)_2(acac)$ would also be suitable for DMAC-TRZ. Since its incorporation as a UEML had never been reported before, it was necessary to explore the performance of various thicknesses of ultrathin DMAC-TRZ films. Three different thicknesses of DMAC-TRZ films were assessed, namely 0.1, 0.3, and 1 nm. As part of the same experimental series, the S_q of mCP films with the emitter deposited on them was also measured through AFM, finding values of 1.49, 1.50 and 1.66 nm, respectively, which showed that the growth of DMAC-TRZ layers also takes place via an island growth mode due to the molecular aggregation, like for $Ir(ppy)_2(acac)$.

The EL spectral characteristics of OLEDs containing the films with the different thickness values are illustrated in **Figure 3.11** and summarized in **Table 3.1**. All three types of devices showed bright yellowish-green electroluminescence (inset in **Figure 3.11a**). Their EL spectra showed a peak centered around 550 nm, which indicates prominent emission from the EML molecules despite a significant ~25

nm red-shift compared to the PL spectrum of DMAC-TRZ neat films (**Figure 6.7b**). In fact, this is consistent with the intramolecular charge-transfer (ICT) nature of the electronic transitions in DMAC-TRZ,[103] which makes the electronic states of the molecule sensitive to differences in polarity of the surrounding medium.[104] Light interference effects, absent in a neat film, also contribute to modify the original spectrum in the devices. In the 0.1 and 0.3 nm ultrathin films a peak shoulder at 450 nm appeared, totally absent in the devices with a 1 nm-thick DMAC-TRZ film. With the aim of understanding its origin, the EL spectra of the devices were acquired at different voltage values. While the EL spectrum of the devices with a 1 nm thick layer remained identical independently of the applied voltage (**Figure 3.11b**), in devices whose EL spectra showed a shoulder, its relative intensity (with respect to the main emission peak) grew together with the applied voltage and the luminance (**Figure 3.11c-d**). It is important to remind, once again, that the sub-nanometer thickness of the emissive layer is just nominal, meaning that the DMAC-TRZ molecules are not in the form of a neat layer. The decrease in nominal thickness from 1 nm to 0.3 or 0.1 nm hence corresponds to fewer and sparser emitter molecules that can be excited, making the saturation of their emission more pronounced, especially at higher voltage (and current) values. As a consequence, recombination in those devices also takes place within other layers. As the EL peak shoulder overlaps with the PL peak of the perovskite layer (**Figure 3.3a**), for samples with a 0.3 and a 0.1 nm thick active layer a small but non-negligeable part of the radiative recombination of the carriers occurs in the perovskite layer, similarly to devices without any EML (**Figure 3.8b**). Charge recombination happening throughout different layers negatively affects the color purity of the devices. This is seen in the CIE 1931 color points of the devices with 0.1 and 0.3 nm-thick EMLs, that are not only further away from the curved edge of the gamut (spectral locus, **Figure 3.11e**) but also move away from it as the luminance (and voltage) increases. On the contrary, the devices with a 1 nm-thick EML show a purer, voltage-independent yellowish-green color (CIE 1931 coordinates of 0.379, 0.534 at 10.0 V).

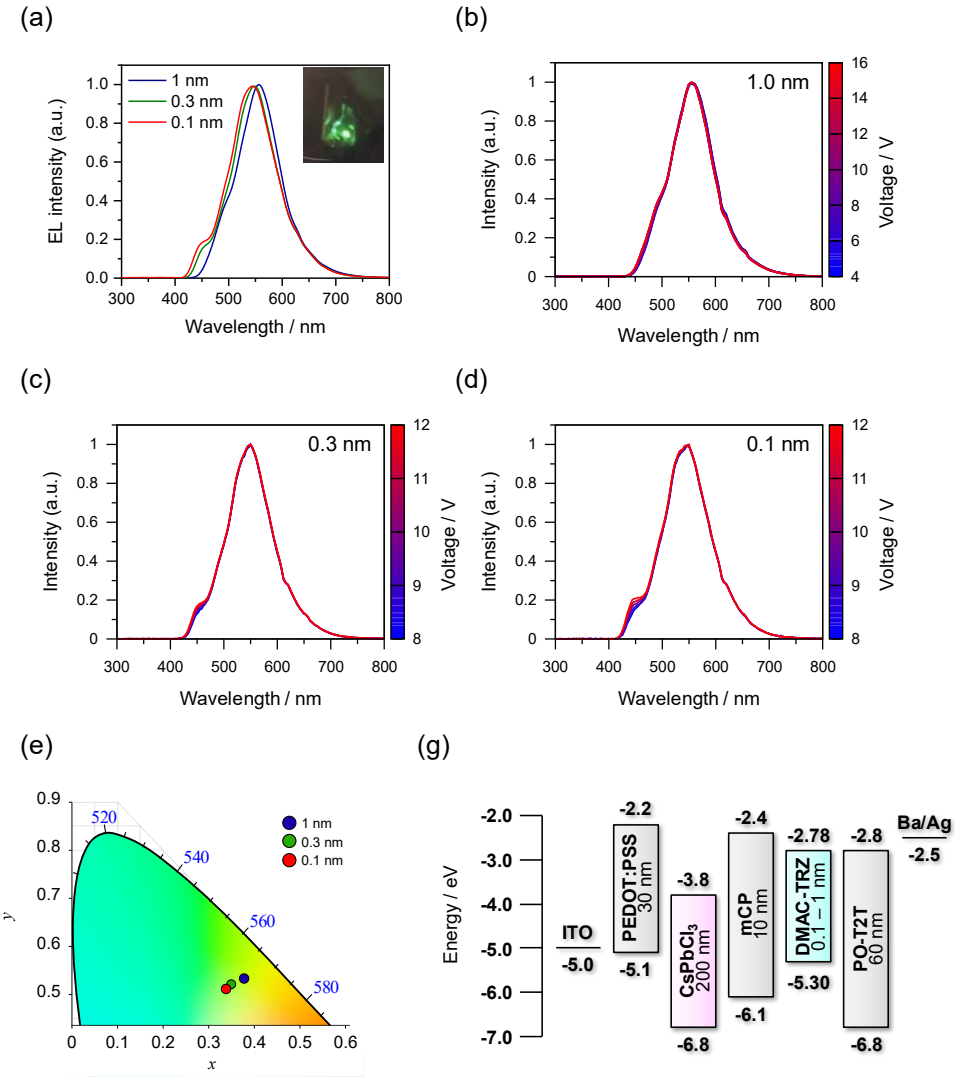

Figure 3.11. (a) EL spectra at 10.0 V for OLEDs with a m-$CsPbCl_3$ HTL and an ultrathin DMAC-TRZ EML with different thicknesses (1, 0.3 and 0.1 nm) (inset: photo of a working device with a 1-nm-thick emissive layer). (b-d) EL spectra at different voltages of devices with different DMAC-TRZ layer thicknesses: 1.0, 0.3 and 0.1 nm, respectively. (e) CIE 1931 Chromaticity Diagram showing the color points for the devices with different thicknesses (1, 0.3 and 0.1 nm) of the DMAC-TRZ-based OLEDs driven at 10 V. (g) Energy level diagram for the devices.

Apart from the color purity, as only a small fraction of charge carriers recombining within the perovskite layer do so radiatively (as deduced from the low PLQY value), devices with thinner (0.1 and 0.3 nm thick) EMLs are expected to have lower electroluminescence efficiencies. This is reflected in their *J-V-L* characteristics (**Figure 3.12a** and **Table 3.1**). Even if the three types of devices exhibited similar current density *vs* voltage characteristics, there existed some trend differences dictated by the thickness of the emissive layer. For example, devices had a turn-on voltage that decreased with increasing emissive layer thickness, with values of 3.9 and 3.3 V for 0.1 and 1 nm, respectively. In all cases, however, the *J–V* characteristics suggested that the perovskite transport layer poses little to no barrier to charge injection. From the moment they turn on, the devices' luminance increased with the voltage at the same pace. At any given voltage, the devices with a lower EML thickness had a higher current density flowing through them. This current that does not translate into a brighter light emission was the cause of their lower EL efficiency values (30.8 cd A^{-1} for the device with a thickness of 0.3 nm and 20.1 cd A^{-1} for the 0.1 nm

one). On the other hand, the efficient utilization of excitons in the devices with an EML thickness of 1.0 nm, translated into a maximum current efficiency of 67.6 cd A^{-1}, corresponding to 20.8% EQE_{max} (**Figure 3.12b**), and, in general, higher current efficiencies along the entire range of luminance. More importantly, these performances are almost identical to those reported for thick (20 nm) non-doped devices with the same emitter,[103] but were achieved by consuming 20 times less compound. The devices with an EML thickness of 1 nm performed the best also as far as the luminance is concerned, achieving a peak luminance of 11 152 cd m^{-2}, comparable to literature values.[103]

The operational lifetime of the devices was also measured, finding a LT_{50} value (at an initial luminance value of 60 cd m^{-2}) of 1.72 h.

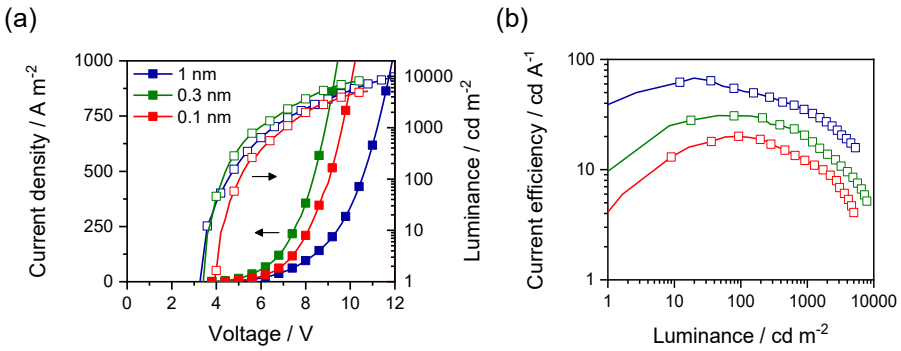

Figure 3.12. (a) *J–V–L* characteristics for OLEDs with a m-$CsPbCl_3$ HTL and an ultrathin (1, 0.3 and 0.1 nm-thick) DMAC-TRZ EML. b) Current efficiency *vs* luminance plot for the same devices.

In summary, 1 nm represents the optimal thickness that allows for a reduction in material costs without compromising the efficiency, the luminance, and the color purity, while the perovskite transport layer fulfills the important role of increasing the total device thickness without affecting the performance also in devices using a TADF-based EML.

Table 3.1. Summary of OLED characteristics for devices with a m-$CsPbCl_3$ HTL and a non-doped ultrathin DMAC-TRZ emissive layer with different thicknesses.

DMAC-TRZ layer thickness / nm ↓	EL peak position / nm (CIE xy coordinates)[a]	Turn-on voltage / V	Max. luminance / cd m^{-2} @Voltage	Max. current efficiency / cd A^{-1} @Luminance
0.1	544 (0.3380, 0.5116)	3.9	5209 @11.0 V	20.1 @92.9 cd m^{-2}
0.3	548 (0.3491, 0.5217)	3.4	8238 @10.6 V	30.8 @135 cd m^{-2}
1	556 (0.3794, 0.5341)	3.3	11 152 @13.4 V	67.6 @19.8 cd m^{-2}

a. For the devices operated at 10.0 V.

3.3.6. Devices with a perovskite HTL and a solution-processed EML

Devices with a solution-processed EML are compatible with low-cost, material-efficient fabrication techniques like inkjet printing, offering a promising route toward scalable manufacturing, and are the

object of this section. Before fabricating such devices, the expected resistance of chloride perovskite thin films to the low polarity organic solvents commonly used in OLED processing, namely toluene, chlorobenzene and chloroform, was confirmed.[52]

For that, 100 nm-thick m-$CsPbCl_3$ films (deposited on top of glass/ITO/PEDOT:PSS CH8000) were treated with the three aforementioned solvents by directly spin coating the solvent on top of them (for more details, see the Experimental section), before the thickness, XRD patterns and optical properties were measured. It was noted that the thickness of the layers did not change substantially upon solvent treatment, with a difference of less than 5 nm, compatible with the profilometer uncertainty and film-to-film variations (**Table 3.2**). In the table, and in general from here on unless otherwise specified, "pristine" refers to a perovskite film that has been modified with 2-nm-thick CsCl layers at the interfaces but has not been subjected to any solvent treatment. First, the effect of the solvents on the films' surfaces was studied by means of AFM. From a visual assessment of the topographic images, no difference could be observed in either the surface roughness or the average grain size (**Figure 3.13,** all images colored with the same scale).

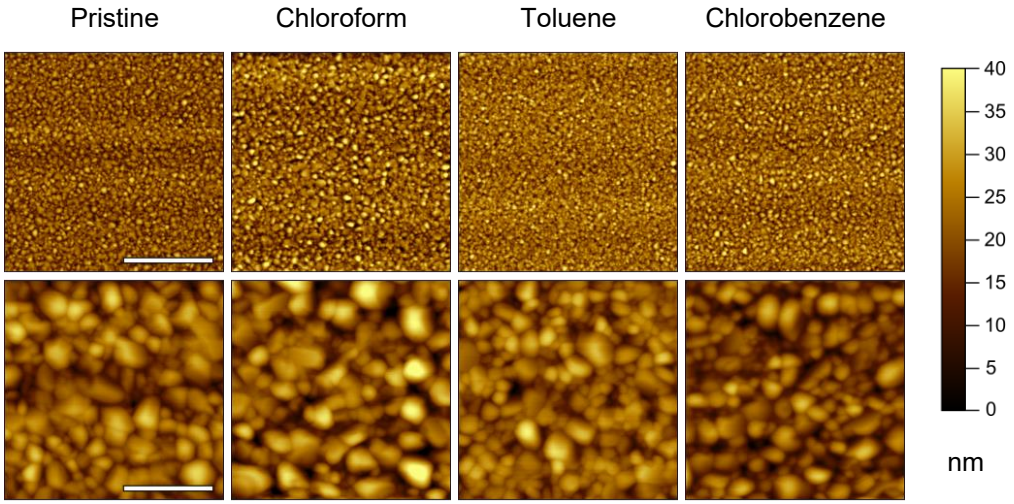

Figure 3.13. AFM topographic images of thermally deposited m-$CsPbCl_3$ thin films treated with different solvents. Top row: area = 5×5 μm^2, scale bar = 2 µm. Bottom row: area = 1×1 μm^2, scale bar = 400 nm.

The visual observations were further confirmed by the calculation of the S_q for each of the films, where a comparable value was obtained for each (**Table 3.2**).

Table 3.2. Thickness (obtained using a profilometer) and S_q (extracted from the AFM topographic images) values for thermally deposited m-$CsPbCl_3$ thin films on PEDOT:PSS, pristine and treated with different solvents. The S_q calculations were performed on a 25 μm² projected area.

	Pristine	Chloroform	Toluene	Chlorobenzene
Thickness / nm	92	96	92	88
S_q / nm	5.1	6.5	5.0	5.4

The bulk properties of the films, namely optical properties such as absorption and PL spectra, as well as the XRD patterns were also preserved across the differently treated films (**Figure 3.14**).

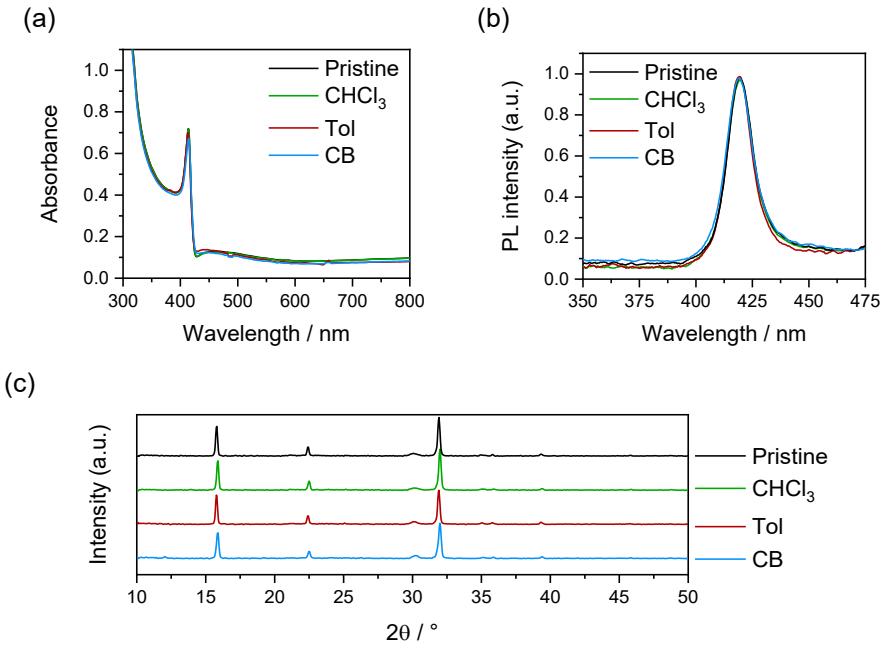

Figure 3.14. (a) Absorption and (b) PL spectra and (c) XRD patterns of m-$CsPbCl_3$ films, pristine and after being treated with different solvents. Tol = toluene, CB = chlorobenzene.

The solvent effect on the structural properties of the perovskite films was also analyzed by grazing-incidence wide-angle X-ray scattering (GIWAXS). In contrast to conventional Bragg-Brentano geometry, in grazing incidence geometry the sample is irradiated by an X-ray beam at a small incidence angle, which is not varied during the measurement. In this way, the penetration depth of the X-ray into the sample is reduced, and the signal stems primarily from the surface of the thin film.[105] This made the measurement more insightful to investigate the effect of the solvents on perovskite thin films, as it only probes the surface layers. The GIWAXS patterns for the different m-$CsPbCl_3$ films, pristine and treated with different solvents, collected with an incident angle of 0.5° and already converted to a q-space, are shown in **Figure 3.15a**. First of all, all 2D GIWAXS plots appear almost identical, with no significant differences between them. This becomes even more apparent when comparing the normalized azimuthally integrated GIWAXS profiles (**Figure 3.15b**), where the overall signal is integrated along the

azimuthal angle interval from 0 to 90°. Moreover, the azimuthal intensity distribution of 100 and 110 Bragg rings at $q \sim 1.1$ Å^{-1} and 1.56 Å^{-1} confirms the already speculated preferential orientation of the (100) planes parallel to the substrate.

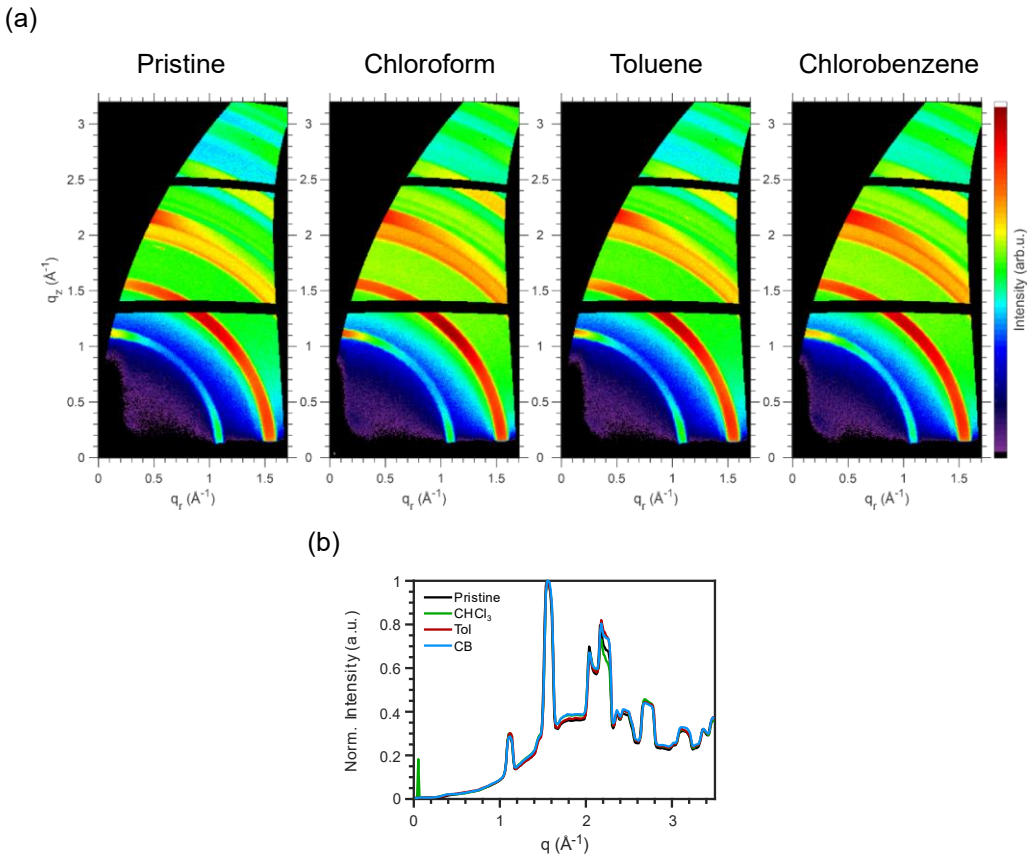

Figure 3.15. (a) 2D GIWAXS patterns for m-$CsPbCl_3$ films, pristine and treated with different solvents. (b) Normalized azimuthally integrated GIWAXS profiles for the same samples. Tol = toluene, CB = chlorobenzene.

Having confirmed that the m-$CsPbCl_3$ films are compatible with the subsequent solution-processing of other layers from a variety of solvents, devices were fabricated with the following architecture: ITO (150 nm)/PEDOT:PSS CH8000 (40 nm)/m-$CsPbCl_3$ (100 nm)/tBuCz2m2pTRZ (40 nm)/PO-T2T (40 nm)/Ba (5 nm)/Ag (70 nm). The emissive layer is composed of a spin-coated neat film of tBuCz2m2pTRZ (chemical structure in **Figure 3.1c**), a TADF dendrimer whose number and distribution of the peripheral meta-connected donor dendron moieties have been intentionally devised, among other considerations, so that the density with which they are packed together suppresses the quenching of the emission caused by intermolecular interactions.[75] Thanks to this, excellent optoelectronic properties (PLQY of 86% and ΔE_{ST} of 40 meV) are retained even in pristine films. In these devices, PEDOT:PSS CH8000 was used in place of the high-conductivity PEDOT:PSS Al4083 used in the devices with a thermally evaporated EML. This is because it showed better performances in preliminary tests (in particular, a twofold increase in efficiency, probably because of better charge balance). A thickness of 100 nm was selected for the perovskite layer to allow faster deposition and because a thicker (200 nm) layer was less necessary as the EML was not ultrathin.

Given the perovskite layer's compatibility with any non-polar solvent, chlorobenzene was selected among the tested options due to its prior use in the spin-coating of tBuCz2m2pTRZ in high-performance solution-processed OLEDs.[75] A cross-sectional SEM image of the entire stack was acquired to gain insight into the perovskite/emissive layer interface (**Figure 3.16a**). As expected, the perovskite layer showed no sign of solvent damage and appeared smooth and homogeneously covered by the upper tBuCz2m2pTRZ layer.

Figure 3.16c shows the EL spectra of the devices at different voltages. Pure green emission (peak at 565 nm, CIE coordinates of 0.457, 0.530, **Figure 3.16d**) was observed from the TADF dendrimer, suggesting that charge recombination occurs in the non-doped emissive layer and that there is efficient hole transport from the perovskite layer to the dendrimer molecules. The emission spectrum was independent of the applied voltage, so the CIE color coordinates also did not change with increasing luminance. **Figure 3.16e-f** shows the *J–V–L* characteristics and the current efficiency *vs* luminance curves of the devices. They reached a peak luminance of 4660 cd m^{-2} (at 10.6 V) with a turn-on voltage of 5.1 V. The current efficiency was above 15 cd A^{-1} at a high luminance of 1000 cd m^{-2}. However, when compared with a previous report,[75] the peak efficiency of these devices was lower, possibly due to a mismatch between the energy levels of the perovskite and the active layer. The addition of an electron-blocking layer could increase the efficiency by confining electrons within the EML (**Figure 3.16b**), but its incorporation is challenging as orthogonal solvent systems or cross-linkable materials are required to ensure resistance to subsequent solution processing steps.

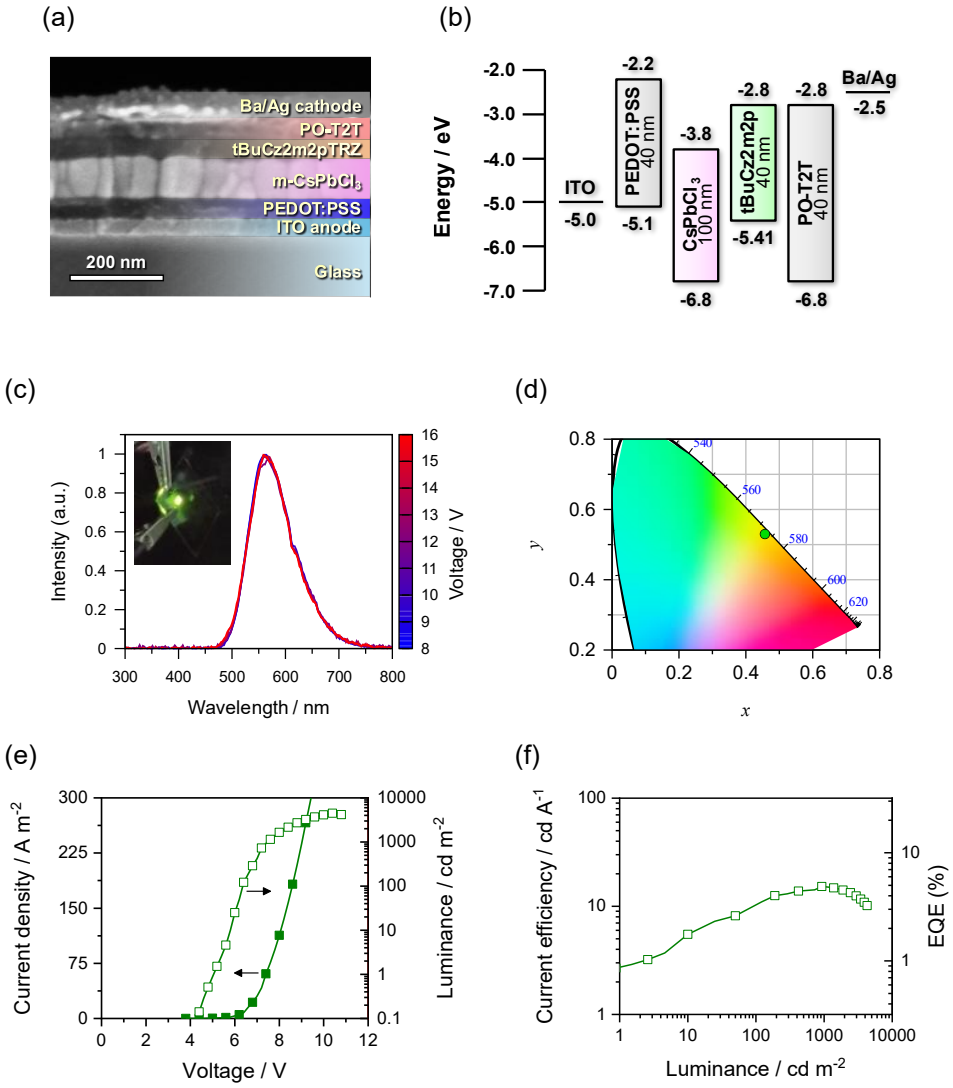

Figure 3.16. (a) Cross-sectional SEM image of a device with a m-$CsPbCl_3$ HTL and a solution-processed tBuCz2m2pTRZ EML. (b) Energy level diagram for the devices. (c) EL spectrum at different voltage values for the same device (inset: photo of a working device operated at 6 V). (d) Corresponding color point in the CIE chromaticity diagram. (e) *J*–*V*–*L* characteristics and (f) current efficiency *vs* luminance for the same devices.

3.4. Conclusions

In this chapter, the possibility of fabricating a $CsPbCl_3$ perovskite thin films by dual-source co-evaporation and employing them as HTL in OLEDs with non-doped EMLs was demonstrated.

First, the optical and structural properties of the films were assessed through a variety of characterization techniques, and a simple strategy to passivate interfacial defects was presented.

Then, the perovskite was used as a HTL in devices with an ultrathin (0.03 nm-thick) layer of the very well-known phosphorescent emitter $Ir(ppy)_2(acac)$, the nature of which was also studied in detail. The resulting devices achieved a high peak current efficiency of 52.9 cd A^{-1} (51.0 cd A^{-1} at 1000 cd m^{-2}, indicating low efficiency roll-off). More importantly, the thickness of the perovskite layer could be increased all the way to the micrometer regime (1000 nm) without a decrease in efficiency, which was

only possible by virtue of the extremely high charge carrier mobility of perovskites. The demonstrated lower sensitivity to thickness changes also reduces the requirement for strict thickness control and the higher thickness mitigates optical interference and variations in electroluminescence with viewing angle.[40] Transparent devices with a buffer metal layer and a PLD ITO cathode were also fabricated.

The Ir-containing emitter was later replaced with a TADF one, DMAC-TRZ, to avoid the use of high cost and rare heavy metals, also in the form of UEML, but for which another optimal layer thickness of 1 nm was found. The devices reached a luminance of 11 152 cd m^{-2} and a current efficiency of 67.6 cd A^{-1}.

Finally, the compatibility of the perovskite film with the processing from solution of subsequent layers was confirmed and exploited to fabricate OLEDs with a thick, neat and spin-coated EML of a TADF dendrimer, tBuCz2m2pTRZ, which reached a peak luminance of 4660 cd m^{-2} and a current efficiency of 15 cd A^{-1} at 1000 cd m^{-2}.

As a whole, perovskites emerge from this study as a promising material platform for driving down OLED manufacturing costs, by enabling ultrathin layers (and thereby reducing the material consumption), by being compatible with the cheaper TADF emitters and with low-material utilization and low-cost solution-processing methods, and by increasing the device production yield, an advancement that will be crucial for the widespread commercialization of the technology.

In that regard, a thermal evaporation process for the deposition of the perovskite films was presented. Besides yielding smooth, high-purity uniform films with precise thickness control, substrate independence, and scalability to large-area production, it is a well-established technique used in the commercial production of OLEDs, facilitating the transfer of the laboratory-scale success to a commercial scale. Moreover, recent advances in other vacuum perovskite deposition methods, such as single-source evaporation, two step vapor-processing and pulsed laser deposition, offer the potential for further simplifying the fabrication process by eliminating the need for co-evaporation of precursors.[106–108]

3.5. Author contribution and acknowledgements

In this chapter, Michele Forzatti fabricated the devices with a 1000 nm-thick perovskite HTL and those with a TADF-based EML and characterized them. He carried out the experiments regarding the nature of the UEML and the resistance of the perovskite film towards solvents. Dr. Sang-Hyun Chin developed the dual-source co-evaporation process of $CsPbCl_3$ and the defect passivation strategy, fabricated the devices with a 200 nm-thick perovskite HTL and a $Ir(ppy)_2(acac)$ UEML and characterized them. Dr. Kassio Zanoni performed the AFM measurements. Dr. Cristina Roldán-Carmona acquired the SEM images. Dr. Vladimir Held performed the GIWAXS measurements. Dr. David Hall and Dr. Dianming Sun synthesized tBuCz2m2pTRZ. Jorge Ferrando designed the sample holder of the LED testing platform and programmed the LabVIEW software to control the Keithleys and acquire the data. Dr. Chris Dressen programmed the LabVIEW software to control the Keithley and the spectrometer.

Chapter 4.

Halide mixing in doped perovskites for color-tunable, HTL-free and high efficiency light-emitting diodes

4.1. Introduction

Precise bandgap tuning is critical for achieving optimal performance and the desired properties of optoelectronic devices, such as solar cells, photodetectors, light-emitting diodes (LEDs) and lasers.[109] Halide perovskites have the attractive merit of offering greater bandgap tunability than that achievable in traditional semiconductors (e.g. III-Vs or II-VIs) by virtue of the numerous different combinations of A, B and X ions that can give rise to a perovskite structure. Alloying different halides (X) allows for straightforward bandgap tuning, as it does not entail a change in the material's fundamental properties. This has enabled blue, green, red and NIR perovskite single crystals, colloidal nanocrystals suspensions and thin films.[110–112]

However, the practical implementation of this approach in PeLEDs has been challenging due to poor color stability, short operational lifetime under electrical bias, and severe PL quenching.[112,113] Moreover, such devices almost always comprised three, four or even five layers between the electrodes[114,115] or required further treatment of the as-casted films,[112] both of which complicate the device fabrication and increase costs.

The main cause of color instability in mixed-halide PeLEDs is halide segregation. Under electrical bias or even optical excitation, halide ions in the perovskite lattice can migrate due to the relatively low activation energy for ion movement. In mixed-halide perovskites, this ion migration leads to phase segregation, where e.g. regions enriched in iodide or chloride and regions enriched in bromide form within the emissive layer.[116] Many segregation events nucleate at vacancies and grain-boundary trap sites, as they provide paths for ion migration. Hence, any strategies that reduce vacancy concentration and passivate surfaces and interfaces can help mitigate the issue.[117]

Recently, Xiong et al. reported the incorporation of a phosphonic acid molecular dopant, (4-(9H-carbazol-9-yl)butyl)phosphonic acid (4PACz), as a means of passivating shallow traps (mostly Br vacancies) and adjusting the charge conduction behavior in halide perovskites. The molecules' strong electron-withdrawing abilities induce the transition from n- to p-type conductivity, move the Fermi level across the bandgap and shift the VBM while retaining high PLQYs. This enabled the demonstration of enhanced efficiency and ultrahigh brightness in PeLEDs with an HTL-free architecture.[118]

The molecular dopant has only been reported for wide-bandgap perovskite semiconductors with a full bromide composition. However, its ability to passivate Br vacancies held promise to restore color stability in PeLEDs based on mixed-halide perovskites while simultaneously simplifying their device architecture, which is why it was decided to study the use of 4PACz in this scenario. In particular, the effects of the compound's electron-withdrawing abilities on the structural, electronic and optical properties of perovskite films with mixed chloride-bromide or bromide-iodide compositions were studied. Its effect on the intrinsic proneness to halide segregation were assessed, also through the fabrication of PeLEDs with a simple HTL-free architecture. The performances of these devices were thoroughly evaluated, and detailed morphological studies were carried out to explain the observed differences.

4.2. Experimental section

4.2.1. Materials

Lead bromide ($PbBr_2$, >99.999%), lead iodide (PbI_2, >99.999%), formamidinium bromide (FABr, >99.5%), formamidinium iodide (FAI, >99.5%), methylammonium chloride (MACl, >99.5%), (4-(3,6-dibromo-9H-carbazol-9-yl)butyl)phosphonic acid (4PACz, >99%), TPBi (>99.8%) and PO-T2T (>99%) were purchased from Lumtec. Cesium bromide (CsBr, >99.999%) was purchased from Alfa Aesar.

Methylammonium bromide (MABr, >99.99%), methylammonium iodide (MAI, >99.99%), guanidinium iodide (GAI, >99.5%) and formamidinium chloride (FACl, >99.99%) were purchased from Greatcellsolar. Guanidinium bromide (GABr, >98%), guanidinium chloride (GACl, >99%), chloroform ($CHCl_3$, ≥99%) and DMSO (≥99.5%) were purchased from Sigma Aldrich. Cesium Iodide (CsI, >99.0%), cesium chloride (CsCl, >99.0%) and lead chloride ($PbCl_2$, >99.0%) were purchased from TCI. PEDOT:PSS (Clevios P VP AL 4083) was purchased from Heraeus. 2-[1-[difluoro[(trifluoroethenyl)oxy]methyl]-1,2,2,2-tetrafluoroethoxy]-1,1,2,2-tetrafluoroethanesulfonic acid (Nafion™ Dispersion Solution, 5%, DE520 CS type) was purchased from Fujifilm.

4.2.2. Device fabrication

Perovskite precursor solution preparation

The precursor solutions for the single-halide perovskite films were prepared by dissolving FAX, MAX, GAX, CsX and PbX_2 (X = Cl, Br or I) at a molar ratio of 0.8:0.1:0.1:0.15:1 in DMSO with a concentration of 0.95 mol l^{-1}. For doped perovskite films, 4PACz was also dissolved at a molar ratio of 0.05 (relative to Pb^{2+}). After full powder solubilization, the solutions were filtered using 0.22 µm polytetrafluoroethylene filters. The precursor solutions for the mixed-halide perovskite films were then prepared by mixing appropriate amounts of the single-halide precursor solutions.

Perovskite film deposition

150 µl of the perovskite precursor solution were pre-spun at 500 rpm for 10 s, and then spin-cast at 5 000 rpm for 90 s. After 40 s during the second step, 120 µl of a 2 mg ml^{-1} TPBi solution in chloroform were dripped onto the spinning substrate. Finally, the samples were annealed at 90 °C for 10 min.

Device fabrication

After cleaning the ITO-coated glass substrates, the perovskite films were deposited directly on top according to the procedure described above. For some devices, a HIL with a gradient work function (GraHIL) was deposited before the perovskite; for that a solution with 1:1 weight ratio of PEDOT:PSS to Nafion™ dispersion was spin coated on the ITO substrates to form a 75 nm thickness layer, which was then annealed at 150 °C for 15 min. In either case, after the perovskite film deposition, the substrates were transferred to two thermal evaporation systems where PO-T2T (20 nm), Ba (3 nm) and Ag (100 nm) were sequentially evaporated at rates of 0.06 nm s^{-1} and 0.1 nm s^{-1} for the ETL and cathode, respectively.

4.3. Results and discussion

4.3.1. Halide mixing in doped perovskite films

Before anything else, the possibility of forming stable 4PACz-doped mixed-halide perovskite films was ascertained.[61] For this, doped perovskite films of $(FA_{0.8}MA_{0.1}GA_{0.1})_{0.87}Cs_{0.13}Pb(Cl_xBr_{1-x})_3$ and $(FA_{0.8}MA_{0.1}GA_{0.1})_{0.87}Cs_{0.13}Pb(Br_{1-x}I_x)_3$ were fabricated using the additive-based nanocrystal pinning (A-NCP) method (**Figure 1.14**).[9] FA is formamidinium, GA is guanidinium and MA is methylammonium. *x* was varied from 0 to 1 in 0.2 intervals for each category, yielding a total of 11 distinct film compositions (**Figure 4.1a**). The phosphonic acid 4PACz was dissolved at a molar ratio of 5% (with respect to Pb^{2+}) in all the precursor DMSO solutions. From now on, the A-site cation composition used in this work ($(FA_{0.8}MA_{0.1}GA_{0.1})_{0.87}Cs_{0.13}$) will be jointly abbreviated to "A" in the condensed chemical formulae for simplicity.

First, EDS was used to verify that the halide ratios in selected films were the same as in the precursor solutions (**Figure 4.1b** and **Table 4.1**).

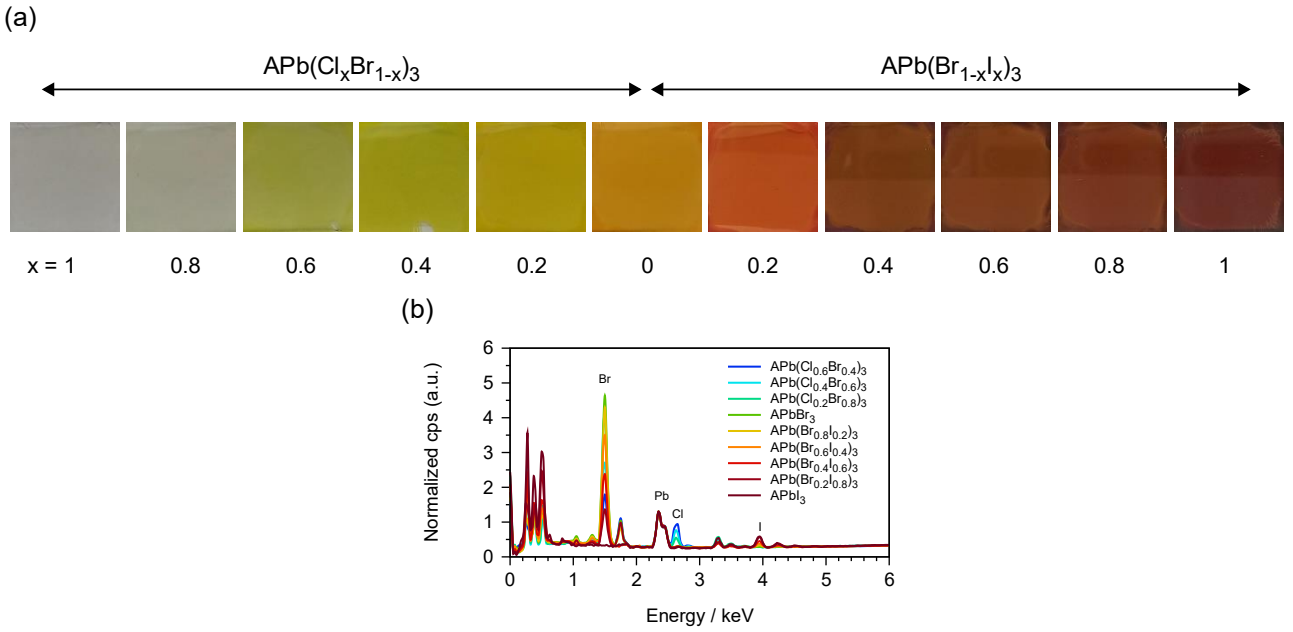

Figure 4.1. (a) Photographs of the prepared 4PACz-doped $APb(Cl_xBr_{1-x})_3$ and $APb(Br_{1-x}I_x)_3$ films. (b) Energy-dispersive X-ray spectra of some of the films. The peaks used for the estimation of the elemental ratios have been marked. The other peaks correspond to other elements present in the perovskite films (e.g. C, N and O from the organic cations or Cs) or in the substrate (e.g. Si and O from the glass substrate).

Table 4.1. Molar halide ratios in selected doped $APb(Cl_xBr_{1-x})_3$ and $APb(Br_{1-x}I_x)_3$ films estimated from the energy-dispersive X-ray spectra of the films.

Composition ↓	Cl or I fraction[a]
$APb(Cl_{0.6}Br_{0.4})_3$	0.59
$APb(Cl_{0.4}Br_{0.6})_3$	0.44
$APb(Cl_{0.2}Br_{0.8})_3$	0.20
$APb(Br_{0.8}I_{0.2})_3$	0.21
$APb(Br_{0.6}I_{0.4})_3$	0.36
$APb(Br_{0.4}I_{0.6})_3$	0.62
$APb(Br_{0.2}I_{0.8})_3$	0.80

a. With respect to the total anion molar fraction.

Elemental mapping was also performed on the films, which showed that they all have a uniform composition throughout (**Figure 4.2**).

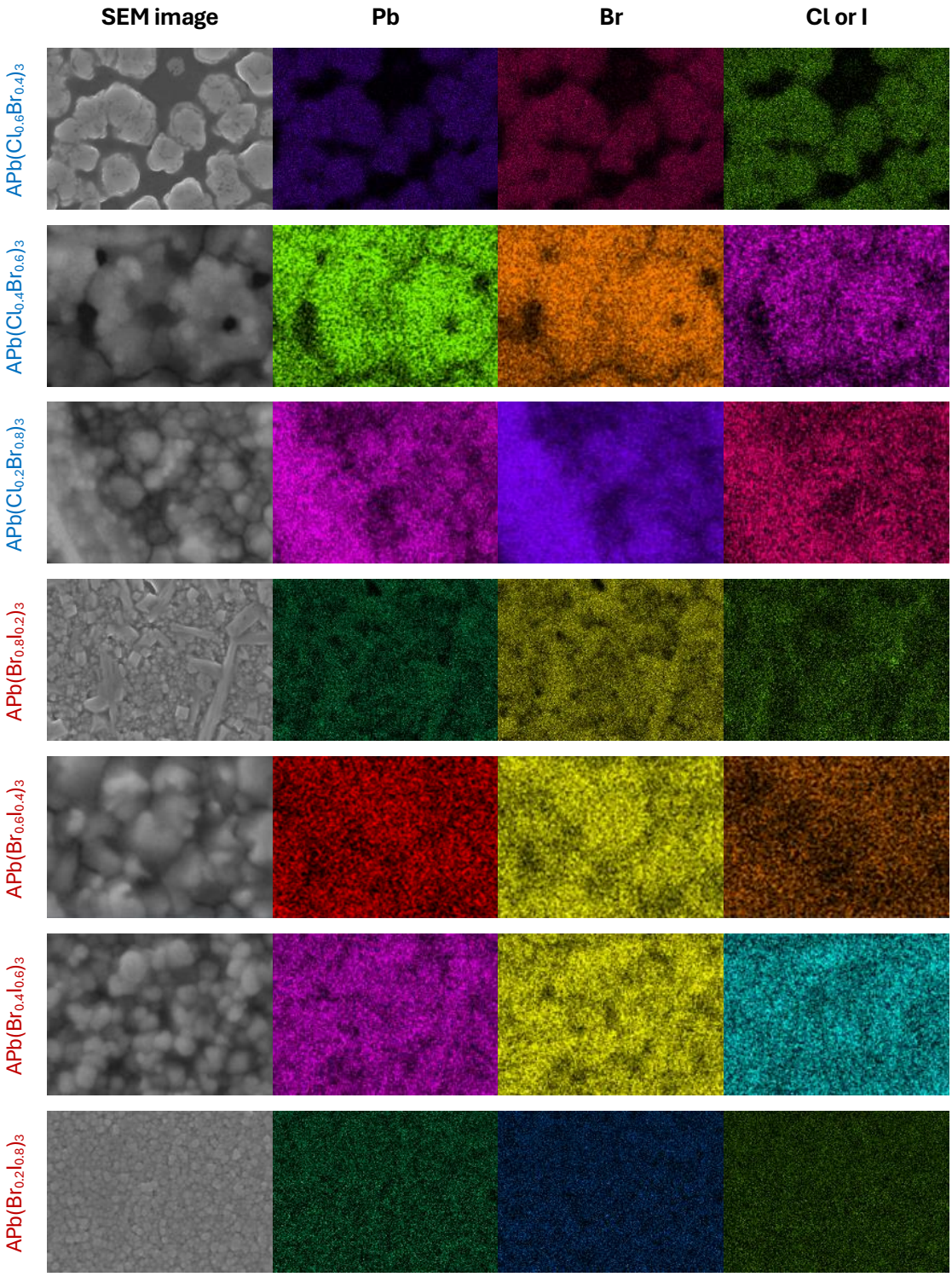

Figure 4.2. Elemental maps taken by EDS-SEM of doped perovskite films with various compositions. The color intensity represents the concentration of a particular element at each point (brighter colors indicate regions with higher concentrations of the element).

Then, the formation of a perovskite phase in the obtained films was confirmed by means of XRD. The patterns (**Figure 4.3a**) indicated that the precursors crystallized in a pure cubic perovskite structure for

all compositions.[111] As expected, the XRD peaks shift towards higher diffraction angles as the composition of halide ions is changed from I to Br and then from Br to Cl, which is due to the change of the ionic radius of the halide atoms[119] and indicates a decrease in the lattice parameters. The experimentally determined unit cell size obtained with Bragg's law ranges from 5.74 Å for $APbCl_3$ to 6.34 Å for $APbI_3$ (**Table 4.2**). An accentuated preferred crystal orientation along the (100) direction was also found, especially for mixed bromide-chloride compositions, as deduced from the relative intensity of the diffraction peaks associated with the (100) and (200) families of planes (at 2θ = 14.835 ° and 29.967 ° for $APbBr_3$).

Secondly, the films' optical properties were measured, starting from their absorption spectra (**Figure 4.3b**). The absorption onset is sharp in all materials, which is expected for direct semiconductors and which allowed for the experimental determination of the optical gap (Tauc plot in **Figure 4.3c**). Moreover, it blue-shifts as the halide composition changes in a perfectly linear fashion ($R^2 > 0.999$, **Figure 4.3d**), following the Vegard's law for lattice constants of alloys.[120] The absorbance profile is comprised of two main contributions, namely an excitonic peak at lower energies, which is indicative of tightly bound excitons,[121] and an extended absorption edge, representing the continuum of valence-to-conduction band electronic excitations.[122] The exciton component becomes less resolved as the bandgap decreases until it disappears for the $APb(Br_{1-x}I_x)_3$ compositions with $x > 0.2$, which reflects the more pronounced ionic character in Cl and Br-based perovskites.[122] The PL spectra of the obtained films display a single emission line in all cases (**Figure 4.3e** and **Table 4.3**), which progressively red-shifts with increasing I molar ratio, and blue-shifts with increasing Cl molar ratio until $x = 0.4$, after which no PL could be detected. The low photoluminescence efficiency of chloride compositions is an intrinsic characteristic of perovskites, regardless of the composition or crystal size.[111,122–124] The peaks are quasi-resonant with the absorption edge (average Stokes shift: 82 meV), symmetrical and narrow, with FWHM values in the range 80 – 100 meV (18 – 45 nm, **Table 4.3**), indicating no phase separation in the as-prepared films, as anticipated from the elemental maps. This allowed for a wide tunability of the emission, ranging from 499 nm for $APb(Cl_{0.4}Br_{0.6})_3$ to 788 nm for $APbI_3$. The PLQY was also measured. When comparing different compositions, the addition of a small amount of iodine to $APbBr_3$ causes a significant drop in the quantum yield, which is another very known property of halide perovskites;[111,123] the mixed-halide compositions $APb(Br_{0.8}I_{0.2})_3$ and $APb(Br_{0.6}I_{0.4})_3$ had the lowest PLQY values (< 1%). When the amount of iodine is increased, the PLQY increases, peaking at 32% for $APb(Br_{0.2}I_{0.8})_3$, the highest value obtained among the studied compositions (**Figure 4.3f**). These characteristics make the narrow-bandgap films suitable light converters for downconversion displays, since they can be fabricated easily and with low-cost, have a narrowband emission that yields excellent color purity, a high PLQY, and intense absorption coefficients values that allow their thickness to be kept very thin when used as downconversion layers (an essential requirement for the fine patterns of high-resolution displays).[125] As mentioned, on the other end of the bandgap array, the luminescence of doped $APb(Cl_xBr_{1-x})_3$ films decreases as the amount of chlorine increases and drops beyond the detection limit of the setup for x values above 0.4.

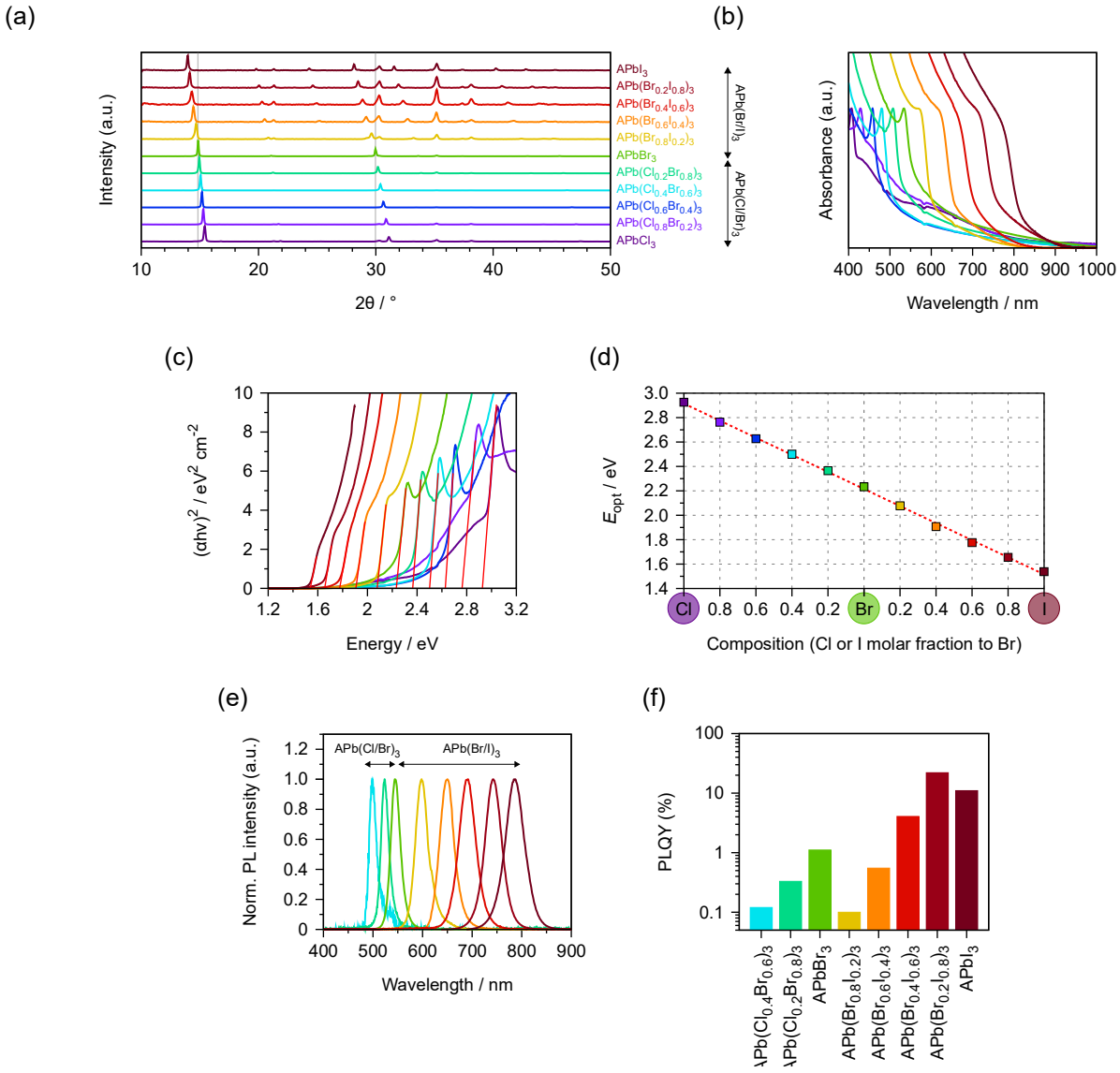

Figure 4.3. Structural and optical properties of 4PACz-doped $APb(Cl_xBr_{1-x})_3$ and $APb(Br_{1-x}I_x)_3$ films. (a) XRD patterns. (b) Absorbance spectra. (c) Tauc plot for estimating the size of the optically allowed direct bandgap. (d) Optical bandgap from Tauc plots as a function of halide composition. (e) PL spectra. (f) PLQY.

To isolate the effects of the inclusion of the molecular dopant 4PACz on the structural, optical and electronic properties of the mixed-halide perovskite materials with different compositions, all the films were also fabricated without dissolving the phosphonic acid in the precursor solutions. The XRD patterns (**Figure 4.4a**) confirmed that the crystallization takes place in the same perovskite structure, with negligible changes in the diffraction peak positions with respect to the doped samples, in accordance with the reported 4PACz preference to adhere only to the perovskite crystals' grain boundaries rather than being incorporated into the crystal lattice.[118] Therefore, in the non-doped samples too, a clear shift in the peaks' angle was noticeable as the halide composition is changed (**Table 4.2**). However, non-doped films displayed a less accentuated preferred crystal orientation and wider peaks, which could be due to increased strain or phase segregation. Their optical properties were also measured. The Tauc plots (**Figure 4.4b**) show that the optical bandgap values for non-doped and doped samples are virtually identical (with an average difference across compositions of 0.02 eV, **Table 4.3**),

confirming that the 4PACz has no effect on the perovskite bandgap either.[118] However, in sharp contrast with the doped films, the non-doped films exhibited much lower PLQYs (**Table 4.3**), giving evidence of the dopant's ability to passivate non-radiative deep-level traps. Moreover, the peaks in the PL spectra were broad (**Figure 4.4c**) and asymmetric (with a tail towards lower wavelength values corresponding to intermediate mixing ratios), which signifies phase segregation in the as-prepared films, as also suggested by the broader XRD peaks. This might be an additional effect of the dopant's ability to fill the halide vacancies at the grain boundaries,[118] since defect passivation has already been demonstrated to mitigate phase segregation in mixed-halide perovskite solar cells.[126]

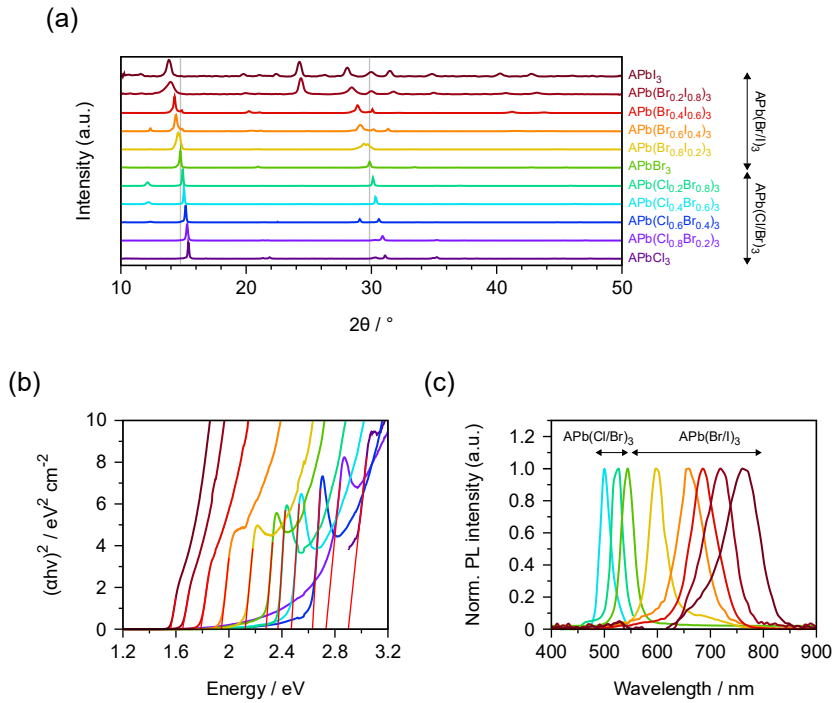

Figure 4.4. (a) XRD patterns of non-doped $APb(Cl_xBr_{1-x})_3$ and $APb(Br_{1-x}I_x)_3$ films. (b) Tauc plots for the same films. (c) PL spectra of the same films.

Table 4.2. Structural properties of pristine (non-doped) and 4PACz-doped mixed-halide perovskite films obtained from the analysis of the XRD patterns.

Composition ↓	Pristine		Doped			
	$2\theta_{(100)}$ / °	a / Å[a]	$2\theta_{(100)}$ / °	$2\theta_{(200)}$ / °	$2\theta_{(110)}$ / °	a / Å[a]
$APbCl_3$	15.38	5.75	15.42	31.10	21.85	5.74
$APb(Cl_{0.8}Br_{0.2})_3$	15.30	5.78	15.30	30.86	21.70	5.79
$APb(Cl_{0.6}Br_{0.4})_3$	15.19	5.83	15.19	30.63	21.58	5.83
$APb(Cl_{0.4}Br_{0.6})_3$	15.03	5.89	15.07	30.40	21.35	5.88
$APb(Cl_{0.2}Br_{0.8})_3$	14.95	5.92	14.95	30.16	21.23	5.92
$APbBr_3$	14.76	5.99	14.83	29.97	21.07	5.96
$APb(Br_{0.8}I_{0.2})_3$	14.56	6.05	14.68	29.62	20.84	6.03
$APb(Br_{0.6}I_{0.4})_3$	14.41	6.15	14.44	29.19	20.53	6.12
$APb(Br_{0.4}I_{0.6})_3$	14.29	6.18	14.33	28.87	20.29	6.18
$APb(Br_{0.2}I_{0.8})_3$	13.98	6.29	14.13	28.48	20.06	6.26
$APbI_3$	13.82	6.37	13.98	28.13	19.79	6.34

a. Average value from applying Bragg's law to the families of planes (100), (200) and (110) (at 14.835 °, 29.967 ° and 21.075 ° respectively for $APbBr_3$).

Table 4.3. Optical properties of pristine and 4PACz-doped mixed-halide perovskite films obtained from absorption and PL spectroscopy measurements.

Composition ↓	Pristine					Doped				
	λ_{PL} / nm	FWHM / nm	E_{peak} / eV	E_{opt} / eV	PLQY (%)	λ_{PL} / nm	FWHM / nm	E_{peak} / eV	E_{opt} / eV	PLQY (%)
$APbCl_3$	-	-	-	2.90	<0.01	-	-	-	2.93	< 0.01
$APb(Cl_{0.8}Br_{0.2})_3$	-	-	-	2.73	<0.01	-	-	-	2.76	< 0.01
$APb(Cl_{0.6}Br_{0.4})_3$	-	-	-	2.63	<0.01	-	-	-	2.63	< 0.01
$APb(Cl_{0.4}Br_{0.6})_3$	500.0	24.0	2.48	2.47	3.78	499.2	18.0	2.48	2.50	3.12
$APb(Cl_{0.2}Br_{0.8})_3$	527.0	25.1	2.35	2.37	7.74	523.4	18.2	2.37	2.36	10.8
$APbBr_3$	544.0	27.5	2.28	2.28	3.25	544.6	22.0	2.28	2.23	19.8
$APb(Br_{0.8}I_{0.2})_3$	596.8	36.5	2.08	2.12	<0.01	598.2	29.5	2.07	2.08	0.10
$APb(Br_{0.6}I_{0.4})_3$	659.8	56.8	1.88	1.94	<0.01	650.4	33.9	1.91	1.91	0.55
$APb(Br_{0.4}I_{0.6})_3$	685.9	57.8	1.81	1.79	0.72	691.2	40.0	1.79	1.78	4.06
$APb(Br_{0.2}I_{0.8})_3$	718.8	65.3	1.72	1.65	2.15	742.7	39.5	1.67	1.66	32.0
$APbI_3$	760.3	76.5	1.63	1.56	3.38	787.5	44.8	1.58	1.54	11.0

Finally, the impact of the dopant on the electronic structure of mixed-halide perovskite semiconductors was evaluated. The non-doped and doped samples were characterized using photoelectron spectroscopy in air (PESA) that, together with the optical spectroscopy measurements, allowed for the determination of the energy band edges and Fermi levels (**Table 4.4**).[127] First, in both the non-doped and doped samples, a decrease in bandgap corresponded (as expected from the VB states' contributions from Pb and X) to a shallower VBM (non-doped $APbCl_3$: -5.86 eV, non-doped $APbI_3$: -5.73 eV; doped $APbCl_3$: -5.67 eV, doped $APbI_3$: -5.50 eV) and a shallower Fermi level (E_F). Secondly, the downward movement of the Fermi level already reported for pure-bromide perovskites[118] also held true for mixed $APb(Cl_xBr_{1-x})_3$ and

$APb(Br_{1-x}I_x)_3$ compositions (average: -0.42 eV), as well as the upward movement of the VBM (average: +0.09 eV).

Table 4.4. Electronic properties of pristine and 4PACz-doped mixed-halide perovskite films obtained from PESA measurements.

Composition ↓	Pristine			Doped		
	E_{HOMO} / eV	E_{LUMO} / eV [a]	E_F / eV	E_{HOMO} / eV	E_{LUMO} / eV [a]	E_F / eV
$APbCl_3$	5.86	2.96	5.24	5.67	2.74	5.30
$APb(Cl_{0.8}Br_{0.2})_3$	5.80	3.07	4.44	5.64	2.88	5.11
$APb(Cl_{0.6}Br_{0.4})_3$	5.85	3.22	5.29	5.75	3.12	5.17
$APb(Cl_{0.4}Br_{0.6})_3$	5.79	3.42	4.52	5.79	3.29	5.05
$APb(Cl_{0.2}Br_{0.8})_3$	5.69	3.41	4.17	5.71	3.35	4.85
$APbBr_3$	5.88	3.76	4.09	5.79	3.56	5.07
$APb(Br_{0.8}I_{0.2})_3$	5.77	3.83	4.26	5.74	3.66	4.91
$APb(Br_{0.6}I_{0.4})_3$	5.82	3.88	4.72	5.84	3.93	5.10
$APb(Br_{0.4}I_{0.6})_3$	5.69	3.90	4.67	5.58	3.80	4.81
$APb(Br_{0.2}I_{0.8})_3$	5.81	4.16	4.70	5.67	4.01	4.84
$APbI_3$	5.73	4.17	4.28	5.50	3.96	4.80

a. $E_{LUMO} = E_{HOMO} + E_g$. E_g estimated from the Tauc plots.

4.3.2. Perovskite light-emitting diodes

The stark increase in PLQY motivated for the employment of the 4PACz-doped mixed-halide perovskites in light-emitting diodes, where the PLQY is one of the key parameters that determine the resulting devices' EQE (Paragraph 1.3.4).[128] The PESA measurements also showed that for 4PACz-doped $APb(Br_{1-x}I_x)_3$ films the energetic offset between the Fermi level of ITO and the VBM of the perovskite is reduced and possibly small enough to ensure direct hole injection from the anode, as can be seen from the energy level diagram of the envisioned devices (**Figure 4.5a**). Therefore, PeLEDs with an HTL-free architecture of ITO (150 nm)/4PACz-doped perovskite (150 nm)/PO-T2T (20 nm)/Ba (3 nm)/Ag (100 nm) (**Figure 4.5b**) were fabricated. Only the compositions that exhibited a measurable PLQY ($APb(Br_{1-x}I_x)_3$ for $0 \leq x \leq 1$, and $APb(Cl_xBr_{1-x})_3$ for $x \leq 0.4$) and $APb(Cl_{0.6}Br_{0.4})_3$ were incorporated into LEDs. PeLEDs with such simpler structures (cross-sectional SEM image of one of the devices in **Figure 4.5c**) are desirable as they lower fabrication costs.

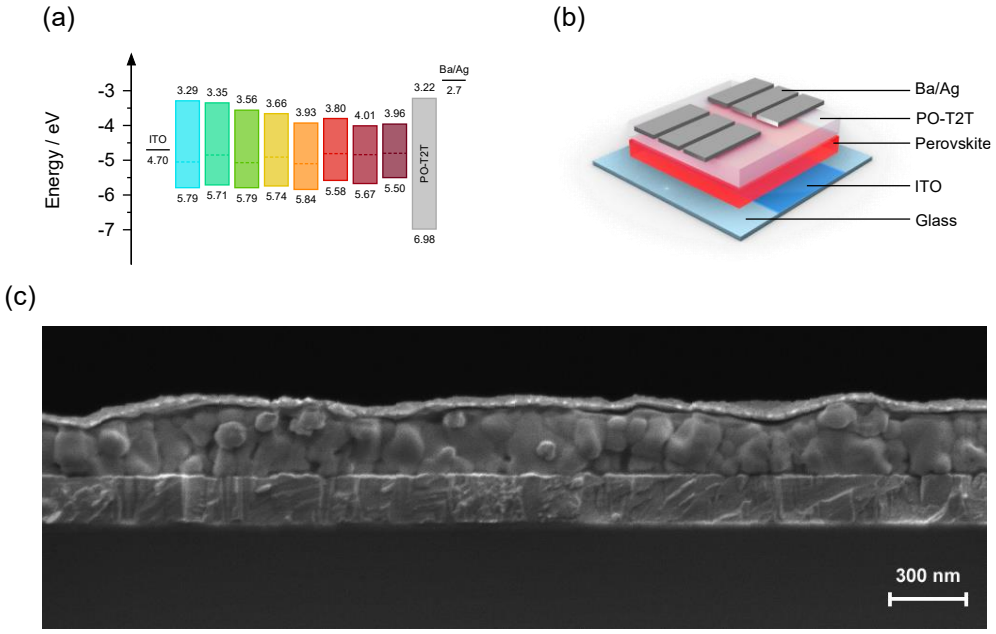

Figure 4.5. PeLEDs with doped $APb(Cl_xBr_{1-x})_3$ and $APb(Br_{1-x}I_x)_3$ films. (a) Energy level diagram including the energies of the conduction and valence band edges for the perovskite samples and their Fermi level (dashed line). (b) Scheme of devices' architecture. (c) Cross-sectional SEM image of a PeLED with an $APb(Br_{0.2}I_{0.8})_3$ emissive layer.

Devices turned on starting from a voltage of 1.6 V – 2.5 V (photos of working devices in **Figure 4.6a**). Their EL consisted in a single narrow peak (**Figure 4.6b**), which overlaps with each film's respective PL spectrum and confirmed the color tunability in the visible spectral range (above 491 nm) and in the NIR (until 793 nm). The narrow emission widths (18.5 – 43.5 nm, 85 – 100 meV) provide points covering the edge of the CIE chromaticity diagram (**Figure 4.6c**), while the luminous efficacy decreases for higher chloride or iodide ratios as the EL spectrum overlap with the photopic luminous efficiency function becomes smaller.

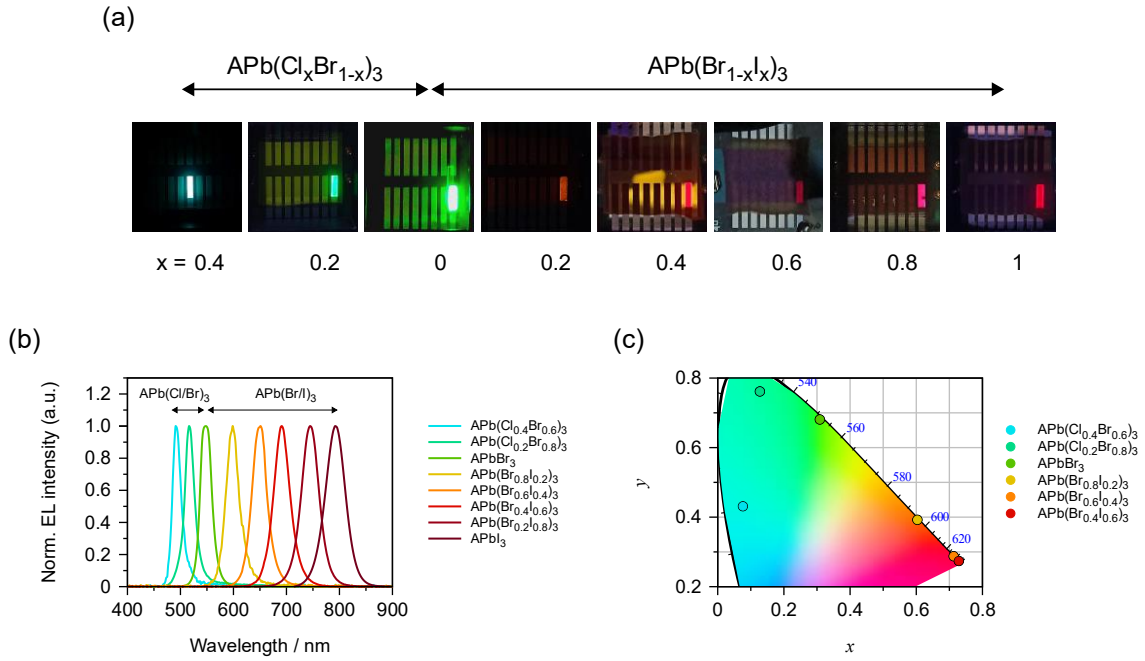

Figure 4.6. (a) Photos of working PeLEDs with different EML compositions. (b) Their EL spectra. (c) Corresponding color points in the chromaticity diagram.

The *J–V–L* curves for all the devices are shown in **Figure 4.7a-b**. Despite analogous spectral characteristics, the performances vary significantly across compositions (**Table 4.5**). Devices with $APbBr_3$, which can be taken as a reference, turned on at 1.80 V, reached a peak luminance of 231 095 cd m^{-2} and a maximum EQE of 17.0%. By stark contrast, devices with $APb(Br_{0.8}I_{0.2})_3$ and $APb(Br_{0.6}I_{0.4})_3$ had higher turn-on voltages (2.20 and 2.10 V, respectively) and their luminance was more than 4 orders of magnitude lower, with an efficiency that did not surpass 0.1%. A further increase in the iodine molar ratio actually caused the turn-on voltage to decrease (below 1.70 V) and the efficiency to increase.

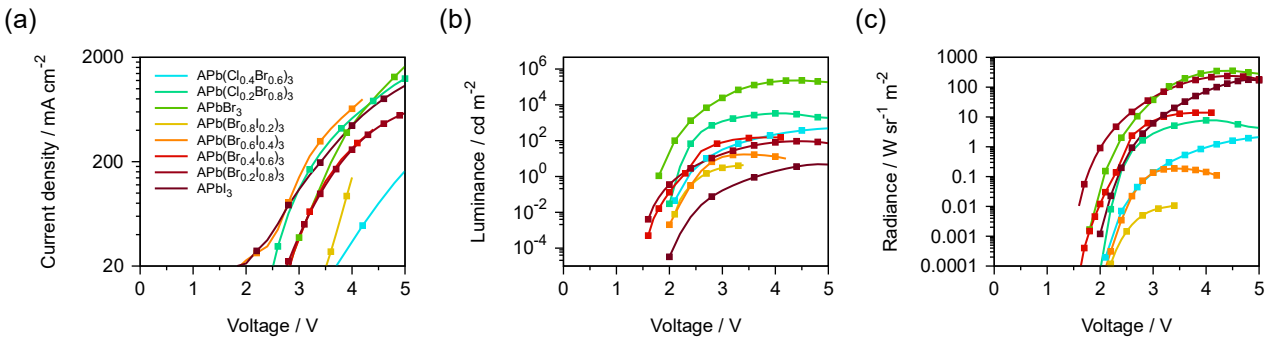

Figure 4.7. *J-V-L* characteristics of PeLEDs with $APb(Br_{1-x}I_x)_3$ ($0 < x < 1$) or $APb(Cl_xBr_{1-x})_3$ ($x \leq 0.4$). The plots show (a) the current density, (b) the luminance and (c) the radiance as a function of voltage.

Since different bandgaps imply a different spectral overlap with the photopic luminous efficiency function, radiance should be considered in place of luminance for comparison purposes (**Figure 4.7c**). Devices with $APb(Br_{0.2}I_{0.8})_3$ achieved the best performance among the mixed iodide-bromide compositions, with a turn-on voltage of 1.5 V and a peak radiance of 236 W sr^{-1} m^{-2} (**Figure 4.8a**). While still lower than that of $APbBr_3$ (354 W sr^{-1} m^{-2}), the value is two order of magnitude higher than that of typical organic NIR OLEDs.[129] Furthermore, their maximum efficiency of 25.9% (**Figure 4.8b**) is the highest among the tested devices and higher than most state-of-the-art NIR PeLEDs;[130–133] as far as is known in the literature, there is only one report of more efficient near-infrared PeLEDs, but their fabrication requires at least three extra steps.[134] The devices also had a suppressed efficiency roll-off, with the EQE being maintained over 20% for a wide range of current density values from 0.01 to 100 mA cm^{-2}. For these devices, the operational lifetime was also assessed, finding an LT_{50} value at an initial radiance of 24 mW sr^{-1} m^{-2} of 133 minutes (**Figure 4.8c**). Finally, devices with $APbI_3$ reached a lower maximum radiance of 177 W sr^{-1} m^{-2} and efficiency of 3.2%, but with the advantage that their EL peak centered around 792 nm made their emission completely invisible. In fact, in visible light communications or security applications, the unintended visible spectral component of NIR OLEDs, unavoidable consequence of their broader emission spectrum, may be detrimental.[135] In other words, perovskites are more desirable also as NIR luminophores by virtue of their narrowband emission.

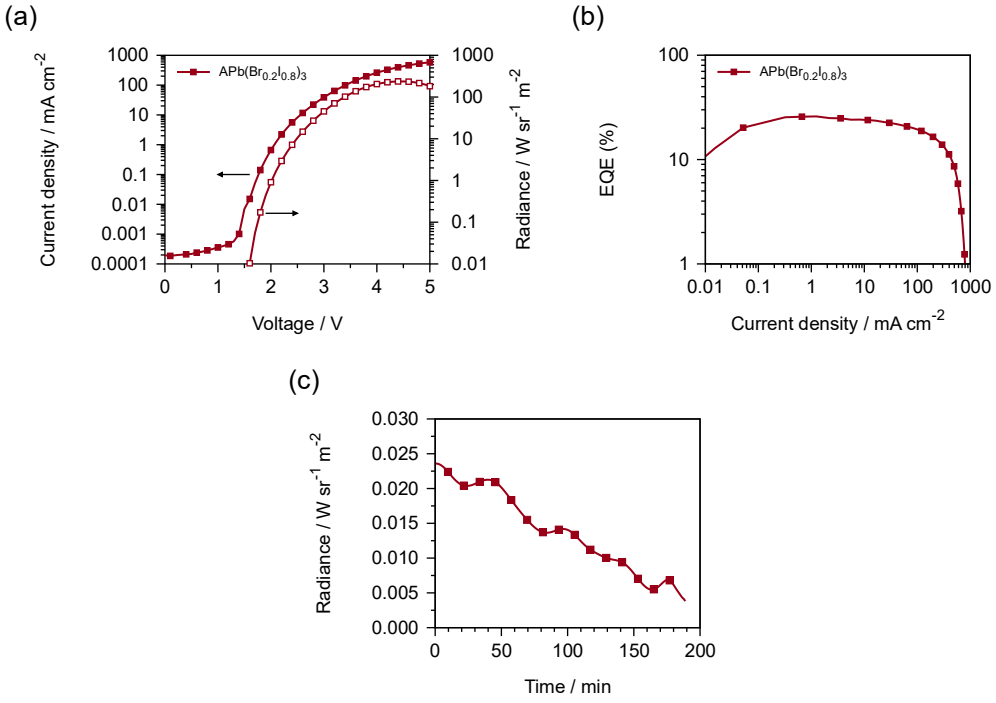

Figure 4.8. (a) Current density and radiance as a function of voltage for devices with a doped $APb(Br_{0.2}I_{0.8})_3$ EML. (b) EQE vs current density plot for the same devices. (c) Operational lifetime of the devices driven with a constant current density and at an initial radiance of 24 mW sr^{-1} m^{-2}.

On the other hand, devices with chloride-bromide mixing ($APb(Cl_{0.2}Br_{0.8})_3$ or $APb(Cl_{0.4}Br_{0.6})_3$) had higher turn-on voltages (2.19 and 2.47 V, respectively) in accordance with their higher bandgap, and reached relatively small maximum radiance values (< 10 W sr^{-1} m^{-2}, **Figure 4.7c**). Since both the VBM and the Fermi level become deeper as the bandgap increases, their low radiance could be the result of inefficient

carrier injection from the ITO. Therefore, devices with a GraHIL deposited before the perovskite films were fabricated. The additional layer did not influence the perovskite bandgap, but it enabled more than double peak luminance values (**Table 4.5**). This seemed to be due to a facilitated hole injection in the case of $APb(Cl_{0.4}Br_{0.6})_3$ (**Figure 4.9**c) and a higher stability at high voltage values in the case of $APb(Cl_{0.2}Br_{0.8})_3$ (**Figure 4.9**a), even though the precise effect of the extra layer still needs to be clarified. In both cases, the maximum efficiency slightly decreased (**Figure 4.9b,d**).

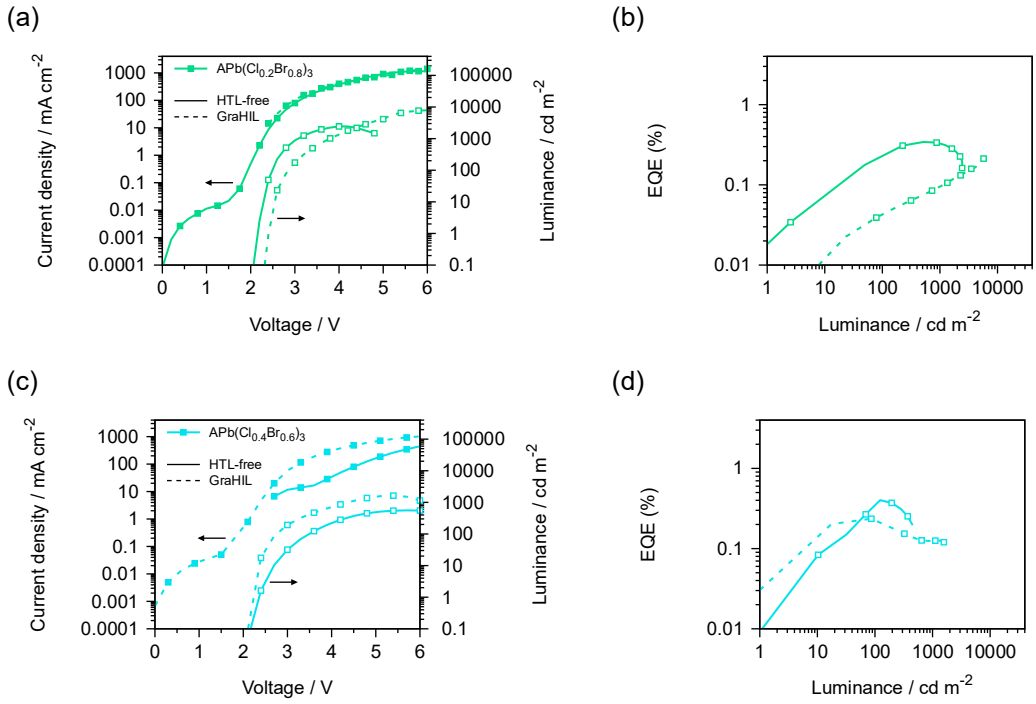

Figure 4.9. (a) *J-V-L* characteristics of PeLEDs with $APb(Cl_{0.2}Br_{0.8})_3$, either with an HTL-free architecture or with a GraHIL. (b) EQE *vs* luminance plot for the same devices. (c) *J-V-L* characteristics of PeLEDs with $APb(Cl_{0.4}Br_{0.6})_3$, either with an HTL-free architecture or with a GraHIL. (d) EQE *vs* luminance plot for the same devices.

Table 4.5. Electric characteristics of PeLEDs.

Composition ↓	V_{on} / V	L_{max} / cd m^{-2}	$L_{e,\Omega,max}$ / W sr^{-1} m^{-2}	EQE$_{max}$ (%)
$APb(Cl_{0.4}Br_{0.6})_3$	2.47	406	1.750, at 5.7 V	0.401
$APb(Cl_{0.2}Br_{0.8})_3$	2.19	3175	7.323, at 6.0 V	0.350
$APbBr_3$	1.80	231 095	354.4, at 4.5 V	16.9
$APb(Br_{0.8}I_{0.2})_3$	2.20	4.35	0.01068, at 3.4 V	0.0663
$APb(Br_{0.6}I_{0.4})_3$	2.10	17.1	0.1871, at 3.4 V	0.0164
$APb(Br_{0.4}I_{0.6})_3$	1.65	152	13.95, at 4.1 V	5.31
$APb(Br_{0.2}I_{0.8})_3$	1.51	93.0[a]	236.4, at 4.5 V	25.9
$APbI_3$	1.95	4.84[a]	177.3, at 4.8 V	3.89

a. Most of the emission is in the NIR spectral range.
b. With GraHIL.

Finally, devices with a doped $APb(Cl_{0.6}Br_{0.45})_3$ EML had a spectrally unstable emission, and their color quickly and visibly changed from yellowish-green to greenish-blue to green within a few seconds of operation under constant voltage (**Figure 4.10**), which indicates electric field-induced halide migration.

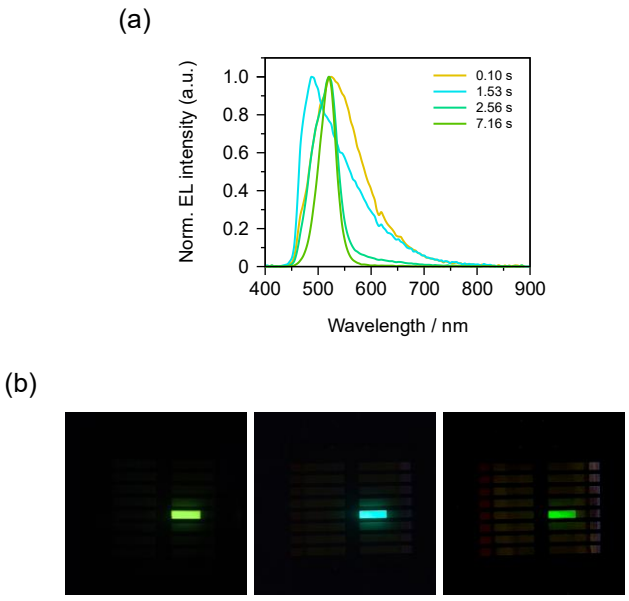

Figure 4.10. PeLEDs with $APb(Cl_{0.6}Br_{0.4})_3$. (a) EL spectrum of the device operated with a constant voltage of 3.5 V at different times. (b) Photo of a working device at different times; from left to right: 0.10 s (λ_{max} = 524.6 nm), 1.53 s (λ_{max} = 487.4 nm), 7.16 s (λ_{max} = 520.5 nm).

4.3.3. Origin of devices' performance differences

More than one factor likely contributes to the performance differences across compositions, both in terms of efficiency, maximum radiance and spectral stability. First of all, the maximum EQE for each composition correlates almost directly with their PLQY. For example, for the iodine-containing films,

both the PLQY and the maximum EQE of the corresponding devices followed the trend: $APb(Br_{0.2}I_{0.8})_3$ > $APb(Br_{0.4}I_{0.6})_3$ ≈ $APbI_3$ >> $APb(Br_{0.8}I_{0.2})_3$ ≈ $APb(Br_{0.6}I_{0.4})_3$. High PLQY values, like the ones found in $APb(Br_{0.2}I_{0.8})_3$, are likely the origin of the superior device performance for the devices, and hint at fewer defects present in the active perovskite layer.

However, in the case of the $APb(Cl_xBr_{1-x})_3$ compositions, the devices showed lower EQEs than the expected values based on the PLQY, which might be due to non-radiative losses by electrical injection. Suspecting that these losses are predominantly due to high leakage currents,[136] AFM images of the perovskite films were acquired and, together with the SEM ones used to assess the compositional homogeneity (**Figure 4.2**), they were used to study the morphology of the perovskite films (**Figure 4.11**). The films were deposited on ITO to ensure that the data were representative of the perovskite layers in the PeLED structures.

The first thing that was examined was the film coverage, as it is known that complete perovskite coverage enhances device radiance and quantum efficiency.[136] It was found that the surface coverage of the $APb(Cl_{0.6}Br_{0.4})_3$ perovskite is incomplete (~33% voids, **Figure 4.11a**), as evident from both the SEM and AFM images, causing possible contact between the ITO and PO-T2T layers. The coverage in $APb(Cl_{0.4}Br_{0.6})_3$ and $APb(Cl_{0.2}Br_{0.8})_3$ films is slightly higher (**Figure 4.11b-c**); nevertheless, even the visibly uniform films contain pinholes. These morphological pinholes reduce device performance and carrier recombination by introducing shunt pathways and decreasing the effective active area.[137] On the other hand, iodine-rich compositions exhibit excellent uniformity and compactness (**Figure 4.11e-i**), which reduce the leakage current[114] and further contributes to the exceptional device performances for the $APb(Br_{0.2}I_{0.8})_3$ devices (as also visible in the cross-sectional SEM image in **Figure 4.5c**).

The ability to continuously tune the bandgap by incorporating different halides is among the most appealing properties of perovskites; however, this alloying also induces ion migration and other dynamic effects that restrict the stability and practical use of mixed-halide systems.[138] This was the case for devices with an $APb(Cl_{0.6}Br_{0.4})_3$ emissive layer, which suffered from severe electric field-induced halide migration and subsequent phase segregation under working conditions. Once again, what makes this specific composition particularly susceptible to the problem can be traced back to the film's morphology, whose crystallites do not only incompletely cover the surface but also clump into big grains (~ 1 μm, **Figure 4.11a**), allowing the halide ions to more readily redistribute among adjacent crystallites within a single domain.[139] On the contrary, iodine-rich compositions exhibit a grain size, as measured from the SEM and AFM images, comparable to the crystallite size estimated from the corresponding XRD patterns, effectively protecting them against halide redistribution.

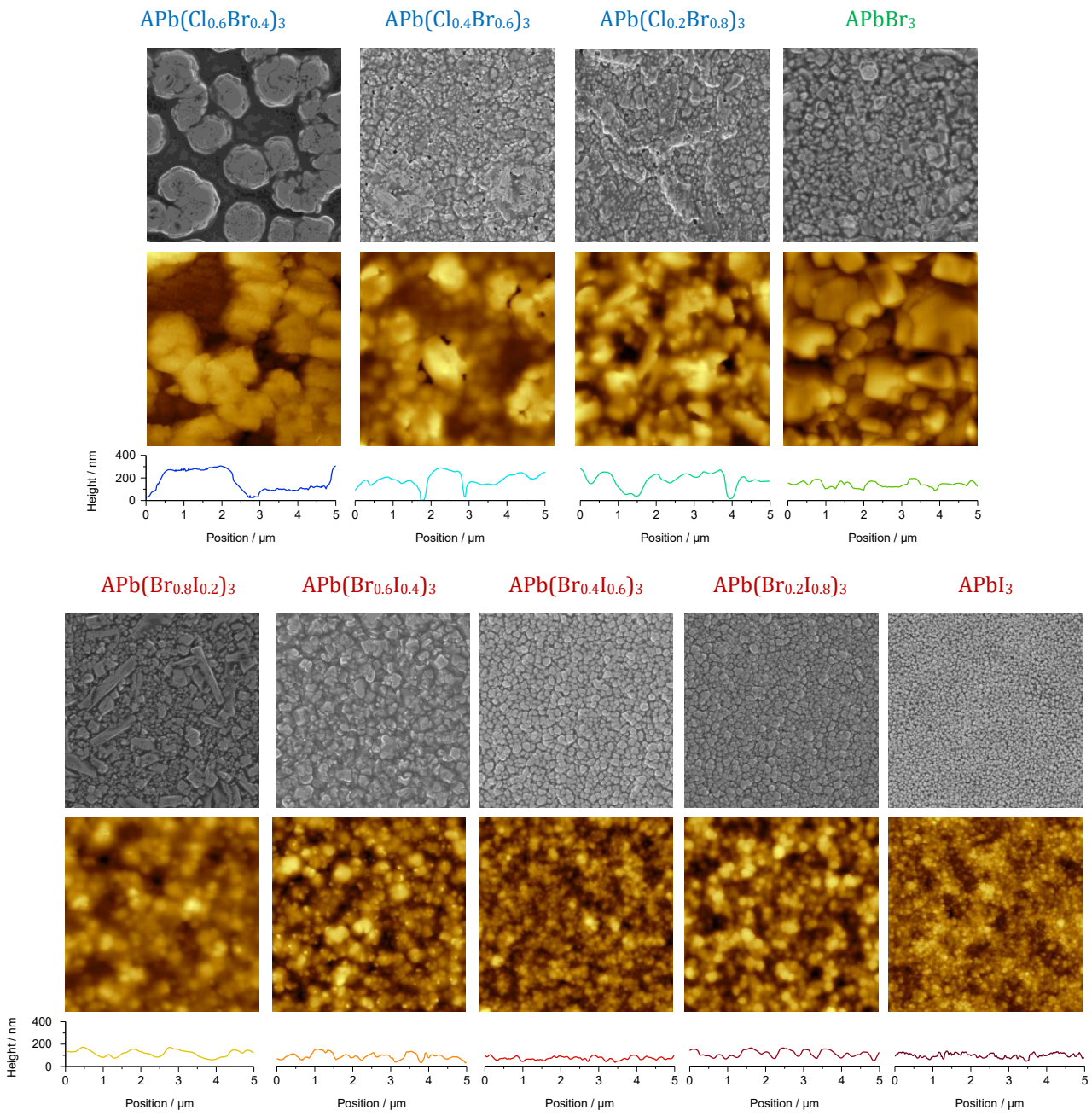

Figure 4.11. Morphological characterization of doped perovskite films. (a) $APb(Cl_{0.6}Br_{0.4})_3$, (b) $APb(Cl_{0.4}Br_{0.6})_3$, (c) $APb(Cl_{0.2}Br_{0.8})_3$, (d) $APbBr_3$, (e) $APb(Br_{0.8}I_{0.2})_3$, (f) $APb(Br_{0.6}I_{0.4})_3$, (g) $APb(Br_{0.4}I_{0.6})_3$, (h) $APb(Br_{0.2}I_{0.8})_3$, (i) $APbI_3$. Top row: SEM images (magnification: 6000×). The brighter areas represent perovskite because they have a higher electron density than the substrate underneath. Middle row: AFM topographic images. Each SEM and AFM image represents a square area with a side of 5 µm. Bottom row: AFM height profiles.

Overall, these findings further evidence the ability of the films' surface morphology to substantially influence the devices performance.[61,134,136,140,141]

4.4. Conclusions

In summary, films of mixed-halide perovskites incorporating the electron-withdrawing phosphonic acid 4PACz were fabricated and used as active layers in light-emitting diodes. The 4PACz molecules enhanced the optical properties of the films, increasing their PLQY up to 32.0% for the best ($APb(Br_{0.2}I_{0.8})_3$) composition. They also had a beneficial role on the prevention of halide segregation and thus on the color purity (the average PL peak width over 8 compositions decreased from 46 to 31 nm), beneficial for downconversion-type display applications. These improved properties translated into superior optoelectronic devices' performance: PeLEDs with a simple HTL-free structure showed tunable emission in the range of 499 – 788 nm and reached maximum EQE values up to 25.9%. Finally, AFM and SEM were used to study the morphological properties of the films, which helped to explain the differences in performances across compositions. A further optimization of film formation and morphology towards complete perovskite coverage could allow all the compositions to reach efficiencies comparable to commercial OLEDs but with superior color purity, wavelength tunability and a simpler architecture.

4.5. Author contribution and acknowledgements

In this chapter, Michele Forzatti and Sergio Martínez-Saiz developed the main experiments (deposition and characterization of films, fabrication and characterization of devices). Dr. Kassio Zanoni performed the AFM measurements. Dr. Cristina Roldán-Carmona acquired the SEM images.

Chapter 5.

Transparent perovskite light-emitting diodes based on a conductive oxide top electrode

5.1. Introduction

Transparent light-emitting diodes (TrLEDs) allow for simultaneous display of data and visibility of the surroundings, thus unlocking a new range of applications from their integration into building facades, windows and head-up panels in cars, as well as smart wearables.[92] Unlike traditional LEDs, in which just one electrode is transparent while the other one is a reflective metal for the efficient redirection of the light, TrLEDs use transparent electrodes at both ends and thus light can exit in both directions.

Although most reported transparent devices rely on organic materials for light generation in the EML, the applications they enable can definitely benefit from the remarkable emission properties of MHPs, as well as from the simpler and thinner design of the most recently reported PeLEDs. The first ever reported transparent perovskite light-emitting diodes (TrPeLEDs) employed a 3D film of $MAPbBr_3$ as EML and a $LiF/Al/Ag/MoO_3$ (dielectric–metal–dielectric, DMD) multilayer as the transparent top electrode.[142] The devices had an average transmittance of 47.2% and achieved a luminance of 6380 cd m^{-2}, with a maximum EQE of 1.21%. To date, six more publications have reported on TrPeLEDs, but in all cases except two, a DMD electrode was used (**Table 5.1**).[143–148] The efforts led to a maximum total luminance of 12 000 cd m^{-2} and a two-side combined EQE of 16.1% (still maintaining a high average transmittance of above 48.7% in the range of 400–650 nm) for green-emitting devices[146] and a combined brightness of 2294 cd m^{-2} and a total EQE of 11.7% (with a transmittance between 400 and 700 nm in the range 40-68.75%) for blue-emitting devices.[147]

Table 5.1. Summary of the reported electric and transparency characteristics of transparent perovskite light-emitting diodes with different EMLs and cathodes.

Year	EML	λ_{max} / nm	Cathode	L_{max} / cd m^{-2}	EQE_{max}	T_{avg} [a]	$T_{\lambda max}$	T (range)[b]	Ref.
2017	3D $MAPbBr_3$	530 nm	DMD ($LiF/Al/Ag/MoO_3$)	9760	1.21%	47.2%[c]	52%	< 59.6%	142
2017	3D $MAPbBr_3$	532 nm	Silver NW - polyurethane	> 1000	-	68%	-	-	143
2018	$CsPbBr_3$ NC	518 nm	DMD ($MoO_x/Au/MoO_x$)	4212	0.58%	73%	57.5%	42% - 61%	144
2020	3D $FAPbI_3$	799 nm	Al/ITO/Ag/ ITO	3.6[c]	5.7%	66.6%	62%	55% - 72%	145
2022	3D $CsPbBr_3$	512 nm	DMD ($LiF/Mg:Ag/MoO_3$)	12 000	16.1%	48.7%[d]	48%	35% - 52.5%[e]	146
2024	Quasi-2D (Br perovskite)	494 nm	DMD ($Cs_2CO_3/Ag/MoO_3$)	2294	11.73%	59.3%	65.4%	41% - 68.8%	147
2024	Quasi 2D (Br perovskite)	512 nm	DMD (Mg:Ag/TPBi/Mg:Ag)	-	12.5%	-	-	< 49.6%	148

a. The average transmittance refers to the range 400 nm – 700 nm, unless otherwise specified.
b. Minimum and maximum value in the wavelength range (400 nm – 700 nm).
c. Radiance in W sr^{-1} m^{-2}.
d. In the 380 nm – 780 nm range.
e. In the 400 nm – 650 nm range.

DMD multilayer structures have been the most popular option for TrPeLEDs because of their decent transparency (≥70%) and good flexibility, which also makes them suitable for flexible optoelectronics. However, their requirement of precise thickness control and the high cost issues of metal films (Ag, Au) have prompted the search for alternative transparent electrode materials.[149] TCOs appear to be a rather natural alternative,[92] as they feature high optical transparency and electrical conductivity. For example, ITO deposited via DC magnetron sputtering has a transmittance above 80% and a sheet resistance below 10 Ω sq^{-1}.[150] Regrettably, the energetic ions in this deposition technique can easily damage soft organic semiconductor layers, making it very challenging to deposit these TCOs on top of the fragile thin film structure of perovskite LEDs and leading to the need for an additional buffer layer to lessen the extent of sputter damage.[149] Furthermore, a high temperature annealing is often required to achieve high quality TCO. Because of this, TCOs have only been used in TrPeLEDs once,[145] and a 10 nm Al interlayer was needed to protect the organic and perovskite layers. The resulting infrared light-emitting diodes reached a maximum EQE of 5.7% and had an average transmittance in the visible range (400-700 nm) of 66.6%. While the metal layer could effectively protect the underlying layers, its strong reflectivity in the visible range compromises device transparency, as observed during the fabrication of semitransparent OLEDs with a perovskite HTL (**Chapter 3**). In essence, the use of TCOs for TrPeLEDs remains basically unexplored, in spite of the advancements in buffer layers and of the development of softer deposition techniques that could preserve both optical transmittance and structural integrity.

In this chapter, the potential of TCOs for use in transparent PeLEDs is explored. The study began with the investigation of the effects of ITO sputtering deposition on perovskite-based devices, followed by the introduction of a highly transparent metal oxide buffer layer deposited by atomic layer deposition (ALD) to mitigate possible damage during electrode fabrication. Subsequently, magnetron sputtering was replaced with the pulsed laser deposition (PLD) technique to achieve gentler processing conditions compatible with perovskite layers. The optical and aesthetic properties of the resulting devices were systematically examined, with particular attention to their tunability for various applications. Finally, the universality of this approach was evaluated by extending it to PeLEDs based on different perovskite compositions and device architectures.

5.2. Experimental section

5.2.1. Materials

Lead bromide ($PbBr_2$, >99.999%), formamidinium bromide (FABr, >99.5%), 4PACz (>99%), TPBi (>99.8%) and PO-T2T (>99%) were purchased from Lumtec. Cesium bromide (CsBr, >99.999%) and anhydrous toluene (99.8%) were purchased from Alfa Aesar. Methylammonium bromide (MABr, >99.99%) was purchased from Greatcellsolar. Guanidinium bromide (GABr, >98%), chloroform ($CHCl_3$, ≥99%), toluene (≥99.5%), 1-butanol (99.8%), oleic acid (OA, 90%), decylamine (DAm, ≥99.0%), chlorobenzene (99.8%), tetrahydrofuran (THF, ≥99.9%) and DMSO (≥99.5%) were purchased from Sigma Aldrich. Benzylphosphonic acid (BPA, 97%) was purchased from Thermo Scientific Chemicals. PEDOT:PSS (Clevios P VP AL 4083) was purchased from Heraeus. 2-[1-[difluoro[(trifluoroethenyl)oxy]methyl]-1,2,2,2-tetrafluoroethoxy]-1,1,2,2-tetrafluoroethanesulfonic acid (Nafion™ Dispersion Solution, 5%, DE520 CS type) was purchased from Fujifilm. ZADN (2-[4-(9,10-di-naphthalen-2-yl-anthracen-2-yl)-phenyl]-1-phenyl-1H-benzoimidazole, >99%) was purchased from Ossila.

5.2.2. Device fabrication

Perovskite precursor solution preparation

The precursor solution for the p-type in situ perovskite NCs films was prepared by dissolving FABr, MABr, GABr, CsBr, $PbBr_2$ and 4PACz at a molar ratio of 0.8:0.1:0.1:0.15:1:0.05 in DMSO with a concentration of 0.95 mol l^{-1}. For the thinner p-type in situ perovskite NCs films, the solution was further diluted to a final concentration of 0.425 mol l^{-1}. The precursor solution for the in situ core/shell perovskite NCs films was prepared by dissolving FABr, MABr, GABr, CsBr, $PbBr_2$ and BPA at a molar ratio of 0.7:0.1:0.2:0.15:1:0.1 in DMSO with a concentration of 1.20 mol l^{-1}. Both solutions were then stirred overnight in an N_2-filled glovebox at room temperature. After full powder solubilization, the solutions were filtered using 0.22 µm polytetrafluoroethylene filters.

Synthesis of colloidal PeNCs

Colloidal $FA_{0.9}GA_{0.1}PbBr_3$ PeNCs were prepared by LARP method. The precursor solution was prepared by dissolving FABr (0.18 mmol), GABr (0.02 mmol), and $PbBr_2$ (0.1 mmol) in 0.5 ml of N,N-dimethylformamide (DMF). The non-polar solvent mixture used for reprecipitation, containing ligands, consisted of toluene (5 ml), 1-butanol (2 ml), OA (300 µl), and DAm (24.2 µl). Under vigorous stirring, 0.15 ml of the precursor solution was added dropwise to this solvent mixture. After 10 minutes, the resulting colloidal PeNCs were washed via sequential centrifugation and redispersed in anhydrous toluene. Finally, the PeNCs-toluene solution was combined with a TPBi solution in toluene (5 mM) at a volume ratio of 10:1.

Perovskite film deposition

For the p-type in situ perovskite NCs films, the films were deposited according to the procedure described in Paragraph 4.2.2. For the in situ core/shell perovskite NCs films, the precursor solution was spin-cast at 6 000 rpm for 90 s. During the spinning step, a 2 mg ml^{-1} TPBi solution in chlorobenzene was dropped onto the spinning film after 60 s. Then, a 3 mg ml^{-1} BPA solution in THF was loaded on top of the perovskite, followed by a reaction time of 30 s and direct spin drying afterwards. Then, the samples were annealed at 70 °C for 10 min. For colloidal PeNCs, the PeNCs dispersion in toluene mixed with TPBi was spin-coated on the substrates at 500 rpm for 60 s to form PeNCs films.

Device fabrication

After cleaning the ITO-coated glass substrates, the perovskite films were deposited directly on top according to the procedure described above. For some devices, a GraHIL was deposited before the perovskite according to the procedure described in Paragraph 4.2.2. After the perovskite film deposition, the substrates were transferred to a thermal evaporation system where the ETL was evaporated at a rate of 0.06 nm s^{-1}.

For opaque reference devices, Ba (3 nm) and Ag (100 nm) were sequentially evaporated on top of the ETL at a rate of 0.1 nm s^{-1}.

For transparent devices, a 20 nm-thick layer of SnO_x and a 100 nm-thick ITO cathode were deposited by ALD and either a PLD or a DC sputtering deposition equipment, respectively, according to the procedure described in Section 2.1. The devices were completed by thermally evaporating 100 nm-thick Ag grids around the edges of the ITO cathode, leaving the active area uncovered. This enhanced the conductivity of the ITO top cathode to a level comparable with devices employing metal top contacts.[67,151]

5.2.3. Device characterization

Due to the particular nature of transparent light-emitting diodes, which emit light from both sides, the slightly adapted characterization procedure already described in Chapter 3 was used. Briefly, the devices were repeatedly flipped to measure EL spectra and photodiode currents from both the bottom and top

sides under three current densities. The average ratio of bottom-to-top photodiode currents was taken as the emission ratio between the two sides. Finally, the devices were returned to their original orientation, and the *J–V–L* characteristics were measured from the bottom side, using the emission ratio to estimate the combined luminance and efficiency.

5.2.4. Device simulations

The emission simulations for the devices were obtained by simulating the full device stack with the electro-optical simulation software Setfos 5.5 (FLUXiM). In this work, only the optical characteristics were modeled, while the electronic processes were neglected. For simplicity, the spatial distribution of the emitter molecules was assumed to be gaussian, with the peak located at the center of the emitter layer (relative position = 0.5) with a width of 50 nm. The refractive index (n, k) values used in the simulation were sourced from literature.[50] For the p-type in situ NCs film and for glass, constant n values of 2.15 and 1.5 were employed, respectively.

5.3. Results and discussion

5.3.1. Cathode engineering for semitransparent perovskite light-emitting diodes

The design of the transparent PeLEDs revolved around an active layer consisting of 4PACz-doped $(FA_{0.8}MA_{0.1}GA_{0.1})_{0.87}Cs_{0.13}PbBr_3$.[118] In the **previous Chapter**, it was confirmed that the A-NCP deposition technique limits the size of the grains, while the dopant has the effect of transforming the electrical conductivity of the perovskite from n-type to p-type. Therefore, such films of in-situ formed nano-crystalline domains will henceforth be referred to as *p-type in situ NCs*.

The perovskite layer (150 nm) was deposited directly on top of ITO, thanks to the doping of 4PACz in the perovskite which eliminates the need for HTLs, as also shown in **Chapter 4**.[118] It was subsequently covered with a thin (20 nm) layer of PO-T2T and, to alleviate potential damage during ITO deposition, the stack was finished by a thin layer (20 nm) of SnO_x. Its deposition took place in a damage-free way via ALD, which enabled excellent coverage on all surfaces with sub-nanometer thickness control and, importantly, is adaptable for mass production since it allows the deposition of multiple substrates in a single batch.[149] SnO_x was used because its conduction band lies in between that of ITO and the lowest unoccupied molecular orbital (LUMO) of PO-T2T (energy level diagram in **Figure 5.1b**). Additionally, its wide bandgap ensures a high optical transmission and broadband transparency (detailed transmittance spectrum in **Figure 5.13a**), its high carrier concentration and conductivity aid the charge injection and reduce injection voltages, and the matching refractive index with the adjacent ITO layer reduces reflection.[152] The top transparent electrode was then deposited. As an initial approach, DC magnetron sputtering was employed, as it is the most commonly used technique for depositing TCOs at both laboratory and industrial scales.[67] Finally, thin Ag gridlines were positioned outside of the pixel area to reduce the sheet resistance of the top electrode. For clarity, devices with this architecture will be referred to as "1a". A schematic of this device stack (ITO (160 nm)/active layer (150 nm)/PO-T2T (20 nm)/SnO_x (20 nm)/ITO (100 nm)) is depicted in **Figure 5.1a**. The thicknesses of all the layers were confirmed with scanning electron microscopy (**Figure 5.1c**). To confirm the protective role of the SnO_x layer, devices without it were also fabricated (devices "1b"). Devices with an identical architecture but featuring an opaque cathode were described in the **previous Chapter** and will be frequently referenced throughout this one, as they serve as a useful comparison (devices "1f").

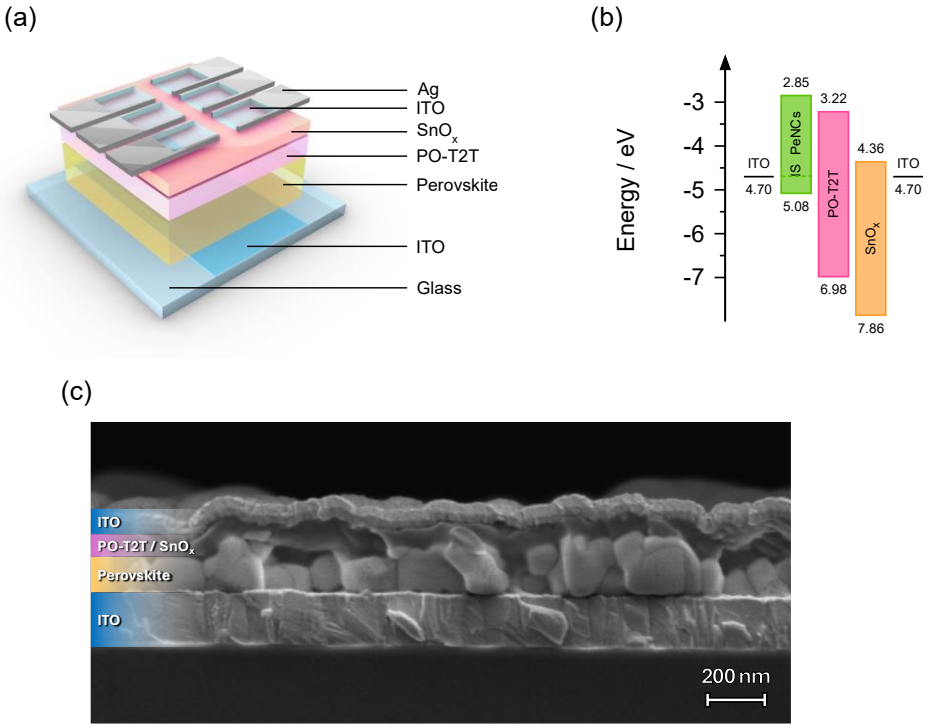

Figure 5.1. (a) Schematic representation of the structure of the transparent PeLEDs (devices "1a"). (b) Energy level diagram for the same devices. (c) Cross-sectional SEM image of a device.

All the devices were characterized by means of *J-V-L* scans (**Figure 5.2a-b**). Since emission occurs on both sides, from now on the emission from the substrate side will be defined as *bottom* emission, and that from the SnO_x/ITO side as *top* emission. If not specified, the reported luminance and efficiency values will refer to the total, combined values. Finally, a practical definition of the turn-on voltage as the voltage at which the luminance is equal to 20 cd m^{-2} will be used unless otherwise specified.

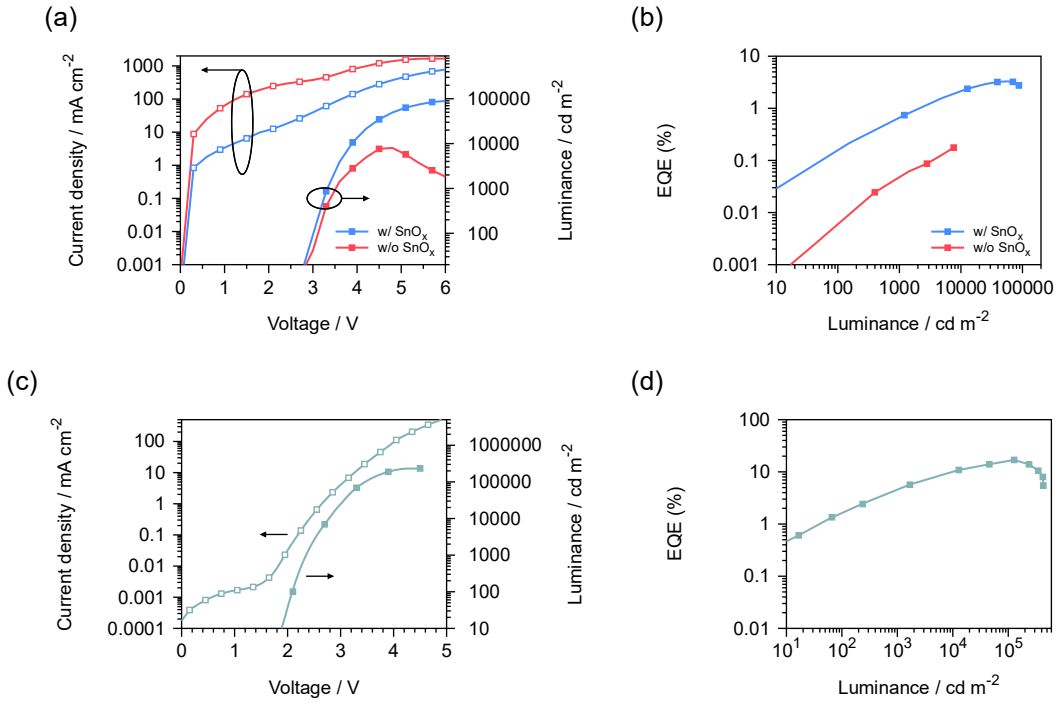

Figure 5.2. (a) *J–V–L* characteristics of the TrPeLEDs with a sputtered ITO cathode and either with or without the SnO_x buffer layer (devices "1a" and "1b"). (b) Efficiency *vs* luminance plot for the same devices. The reported data refer to the combined top and bottom emission. (c) *J–V–L* characteristics of opaque PeLEDs based on the same p-type in situ NCs. (d) Efficiency *vs* luminance plot for the opaque devices.

The relevant performance figures of merit are summarized in **Table 5.4**. In short, the devices incorporating the SnO_x buffer layer turned on at a low voltage of 2.8 V, which is indicative of an efficient carrier injection from the top electrode, and then reached a peak luminance of 90 000 cd m^{-2} at 6 V, while their efficiency was just short of 4%. On the contrary, the devices without the protective SnO_x buffer layer had a peak luminance more than 10 times lower and a maximum EQE of only 0.18%. The SnO_x-free devices conducted a significantly greater amount of current in the 0 – 2.5 V range (approximately 2 orders of magnitude higher than the corresponding devices that contained the SnO_x layer). In this low-voltage regime, the electronic current is dominated by leakage current rather than by carrier injection into the semiconductor bands, indicating that the ITO sputtering process has generated sub-gap defect states between the PO-T2T and the perovskite layer. This results in severe micro-shunting pathways and therefore in a large leakage current that does not contribute to radiative recombination, negatively impacting the efficiency.[145] These findings evidence the vulnerability of thin organic transport layers and perovskite active layers in PeLEDs to plasma damage from the ITO deposition process, as well as the effectiveness of SnO_x to addressing the limitations of sputtering TCOs fabrication.

However, even when SnO_x was employed, the transparent devices still possessed a higher leakage current compared to the opaque counterparts with a Ba/Ag top electrode (already described in **Chapter 4**, their *J-V-L* characteristics are reported again in **Figure 5.2c** for convenience), motivating for the development of alternative soft-landing deposition methods. In this regard, PLD allows for a wider choice of working pressures compared to sputtering, enabling more efficient thermalization of energetic particles which is advantageous for damage mitigation,[153] as demonstrated in perovskite solar cells.[154] For this reason, PLD was explored as an alternative method for the TCO deposition, keeping the device stack the same (devices "1c"). Details on the deposition conditions via PLD can be found in the

Experimental section. The softer character of PLD compared to magnetron sputtering questioned the need for a protective layer altogether, so to verify it, in some devices PLD ITO was also deposited directly on top of the ETL, as is common practice with opaque metal cathodes (devices "1d").

The current density versus voltage characteristics of these "1c" devices are shown in **Figure 5.3a**. After a steep rise, a plateau appeared up to 3 volts, after which the current density further increased. The devices turned on at 2.61 V (for 20 cd m^{-2}; 2.26 V for 1 cd m^{-2}). The bottom emission was more intense and reached a maximum luminance of over 80 000 cd m^{-2} at a driving voltage of 6.0 V, while the top emission had a luminance of 68 000 cd m^{-2} at the same voltage value (corresponding to a bottom/top emission ratio of 1.18). When summing up the two luminance (top and down) contributions, a total luminance of 148 000 cd m^{-2} and a maximum efficiency of 11% were obtained (**Figure 5.3b**). Hence, the PLD based ITO in combination with SnO_x allows for the forming of diodes with limited leakage currents and high efficiency electroluminescence.

The diode-like behavior with a plateau was less pronounced in devices without the SnO_x layer ("1d"), where a higher current density at the plateau was observed. They also turned on at a slightly higher voltage of 3.09 V (2.85 V for 1 cd m^{-2}), after which they only reached a lower combined emission of 10 000 cd m^{-2} and a maximum EQE of 0.416%. Both values are higher than for the sputtering ITO counterparts, confirming the damage mitigation in PLD, but are lower than for the devices with the buffer layer.

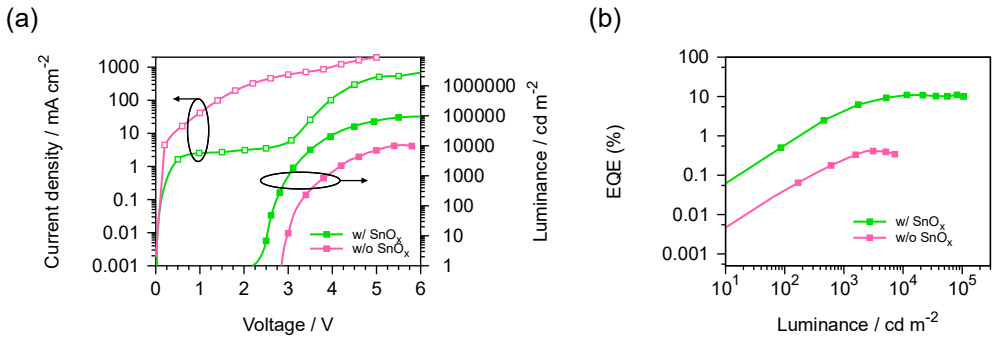

Figure 5.3. (a) Current density and combined luminance vs voltage curves for the TrPeLEDs with a PLD ITO cathode and either with or without the SnO_x buffer layer (devices "1c" and "1d"). (b) Efficiency *vs* luminance plot for the same devices.

While the efficiency of devices "1c" is in line with that of the best-performing TrPeLEDs based on DMD top cathodes with similar average transmittance (**Table 5.1**), their maximum luminance is more than one order of magnitude higher (**Figure 5.16**). This is thanks to the ultrahigh peak brightness of devices with an in situ NCs EML, whose excellent charge-transport characteristics are not impeded by organic ligands. Despite this, the TrPeLEDs were still slightly less efficient than the opaque counterparts (EQE of 16.9%, **Figure 5.2d**)[118] and had a higher turn-on voltage. The latter is most likely due to a more difficult charge injection from the higher work function transparent top contact electrode (ITO compared to Ba). As for the efficiency, optical simulations also showed that changing the thickness of any of the two electrodes would lead to a higher total radiance (**Figure 5.4a-b**), highlighting that some losses are also related to a high fraction of generated light being coupled into waveguided modes and trapped within the stack.[145]

Optical simulations were also used to confirm that the experimentally found bottom/top emission ratio of 1.18 does not originate from anisotropic emission. In fact, assuming completely isotropic emission and accounting for parasitic absorption and optical interference effects arising from refractive index mismatches between layers, the simulations accurately reproduced the experimentally observed ratio (**Figure 5.4c**).[155] In addition, the simulations hint at the possibility to tune the relative amount of light emitted in the two directions by means of variations in the electrodes' thickness, based on the implementation scenario. For example, in the case of a head-up display integrated in car windshields, the section of the display appointed to the speedometer, tachometer, and navigation system should mostly emit in the direction of the driver, while that designated to signal intent or messages to pedestrians, crucial in the autonomous vehicle era, should preferentially radiate in the opposite direction.

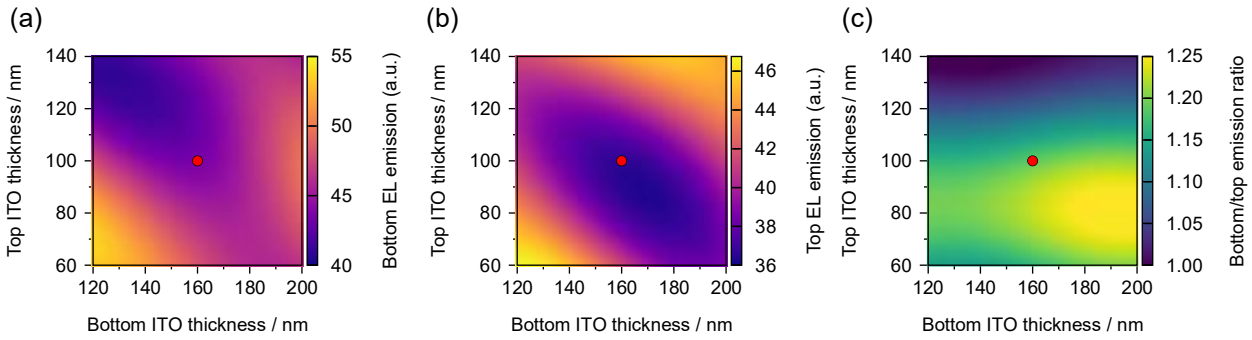

Figure 5.4. Simulated (a) bottom and (b) top perpendicular emission (radiance) for the TrPeLEDs with a SnO_x layer for different thickness values of the top and bottom ITO cathodes as a means of estimating photon losses via internal total reflection and absorption. (c) Theoretical ratio between radiance from the bottom side and from the top side. The red points indicate the experimental thickness values.

In addition to the electrical and optical characterization, the EL properties of the devices were also investigated to provide a comprehensive description of their performance. The EL spectrum of "1c" devices, measured from the substrate side and shown in **Figure 5.5a**, has the characteristic p-type in situ NCs emission at 538 nm (**Table 5.2**),[118] slightly blue-shifted when compared to the PL peak of the perovskite layer excited with a 375 nm source (**Figure 5.5d**), which may be due to a small shift of electron and hole states when an external electric field is applied.[156] Either way, the EL spectrum overlaps with that of the opaque device fabricated for reference purposes (**Figure 5.5e**), showing that the use of a transparent electrode does not affect the shape or the position of the emission. The emission was also acquired from the top side of the devices and at different voltage values, and no appreciable differences were found (**Figure 5.5f-g**). The narrow peak (full width at half maximum, FWHM, of 22 nm) translates to a bright, pure yellowish green emission (photo of a device in its on state in **Figure 5.5b**), as also confirmed by the near-edge position of the corresponding color point in the CIE chromaticity diagram (**Figure 5.5c**).

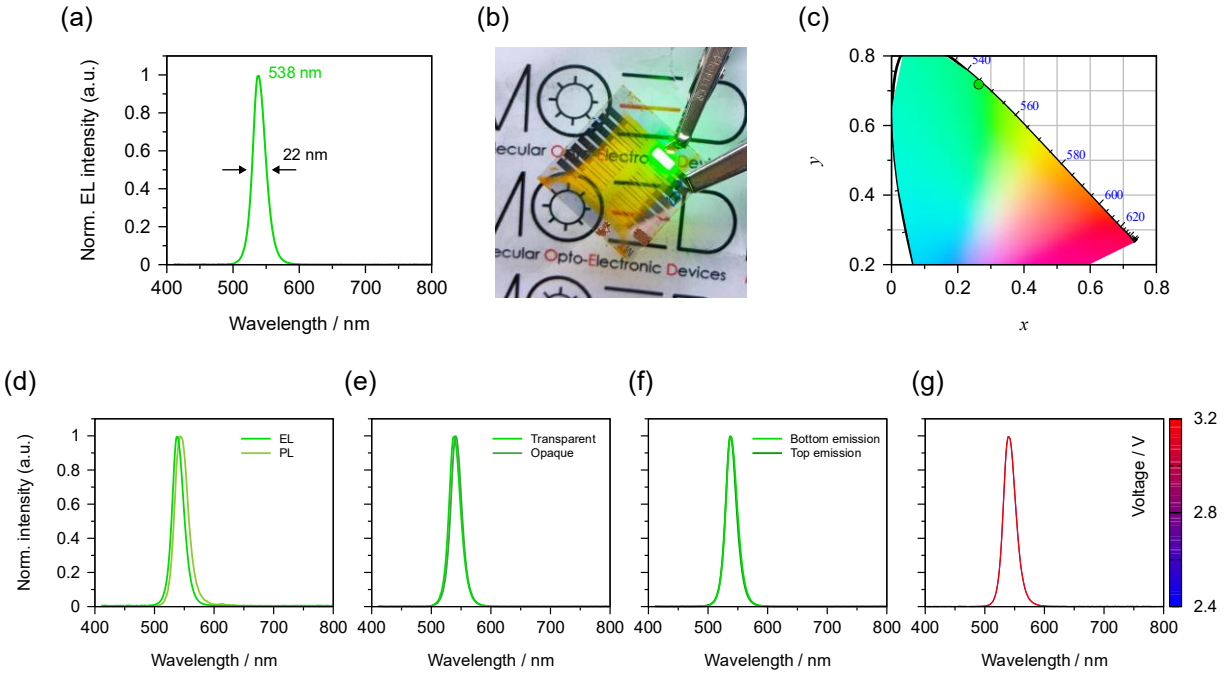

Figure 5.5. (a) EL spectrum of the TrPeLEDs with a PLD ITO cathode and a buffer SnO_x layer (devices "1c") measured from the bottom side. (b) Photo of the bottom side of a device turned on. (c) Corresponding point in the CIE 1931 xy chromaticity diagram. (d-f) EL spectrum from the bottom side compared with (d) the PL spectrum of a thin film of p-type in situ NCs, (e) the EL spectrum of a device with an opaque cathode ("1f") and (f) the EL spectrum recorded from the top side. (g) EL spectrum from the bottom side at different voltage values.

The lifetime of the devices with a buffer SnO_x layer was also assessed by driving them with a constant current density corresponding to an initial combined luminance value of 190 cd m^{-2}, conditions under which it took 4.0 minutes for the luminance to halve. The value, albeit comparable to other previously described TrPeLEDs,[145] is inferior to the lifespan of the corresponding opaque counterpart reported in literature.[118]

Collectively, the reduction in performance when not employing SnO_x (and the high leakage current in the low-voltage regime for these devices, **Figure 5.3a**), and the lower lifespan and efficiency of any of the transparent devices compared to the opaque references, all attest that even PLD can cause a slight damage to organic layers.[145] Nevertheless, the SnO_x/PLD ITO electrode still manages to meet the requirements of high conductivity, low light absorption, mild deposition and efficient charge injection, resulting in devices with high luminance (ca. 148 000 cd m^{-2}) and high efficiency (11% EQE), hence enabling the demonstration of transparent PeLEDs with solid optoelectronic characteristics.

To enable their integration into practical applications (e.g. lighting panels, see-through displays or architectural window glass), the appearance of the TrLEDs is just as important as their luminance and EQE. The first metric to consider is the transmittance, that is, the fraction of incident light that passes through them rather than being reflected or absorbed. The figures of merit that are usually reported are the average transmittance through the visible range (400 – 700 nm), the maximum and minimum value in the same range and/or the value at the maximum wavelength of emission. For the devices described in this study, the transmittance varied considerably from 6.5% at 400 nm to 75.9% at 700 nm, resulting in an average value of 46.7% (**Figure 5.6a**). At the maximum wavelength of the emission (538 nm), the transmittance was 35.3%. However, the average value does not always reflect how transparent the

devices appear, since our eyes perceive green light brighter than red or blue light of the same intensity (as explained in Paragraph 1.2.3). In addition, the light coming from the sun or artificial light sources is not equally intense at all wavelengths. The calculation of the so called average visible transmittance (AVT) keeps both the photopic response function and the spectral power distribution of the light source into account and thus yields a more meaningful figure of merit.[96] The most fitting usage scenario for "1c" TrPeLEDs in view of their remarkably high luminance, is for outdoor applications. For this, the reference terrestrial solar spectral irradiance spectrum or the D series of published CIE illuminants that represent natural daylight are recommended to be used in the colorimetric calculations by the CIE.[157] The AVT of the devices of this work calculated with the CIE standard illuminant D65 is 50.9%, which is higher than the average transmittance value which gets negatively affected by the high device absorption in the blue region of the spectrum, which is, however, neither intense in the natural daylight spectrum nor sensitive for the human eye.

On the other hand, the transparency alone is not enough to evaluate the aesthetic quality. In fact, since the transmittance spectrum is almost never flat through the visible spectrum, the color of objects behind the transparent devices will be rendered differently as compared to objects under natural daylight. The fidelity with which colors are reproduced is quantitatively evaluated by the color rendering index (CRI), the CIELAB color coordinates (a^*, b^*) and the CIE 1976 uniform chromaticity scale (UCS) color space coordinates (u', v'). Due to the above-mentioned unequal transmittance of the devices throughout the visible spectrum (**Figure 5.6a**), "1c" TrPeLEDs have a low CRI of 44.87, (u', v') coordinates of (0.24, 0.52), **Figure 5.6c** and (a^*, b^*) coordinates of (14.5, 43.8) that indicate a reddish-yellowish tint (**Figure 5.6b** and **Table 5.3**). Despite the tint, the very high brightness and the haze-free appearance still ensure a very high on/off contrast from both the bottom and the top side.

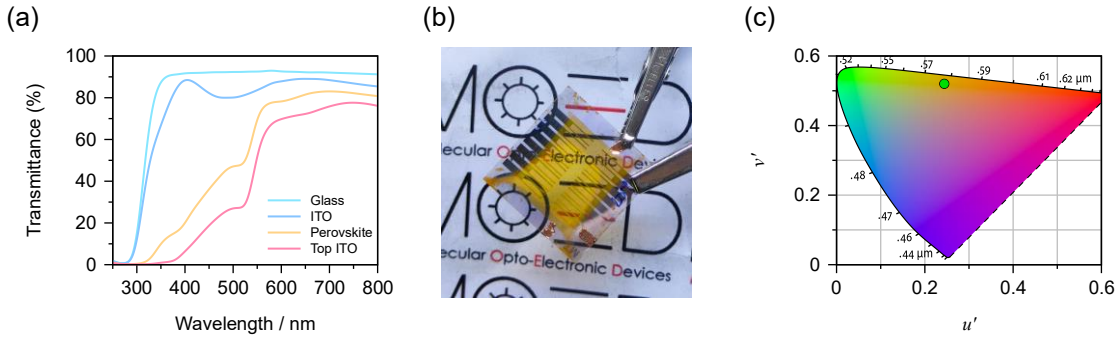

Figure 5.6. (a) Transmittance spectrum of TrPeLEDs with p-type in situ NCs and a PLD ITO cathode (devices "1c") after the deposition of each layer. The legend in the plot denotes the last layer deposited before the transmittance measurement. (b) Photo of the bottom side of a device on a white background with text. (c) Corresponding point in the CIE 1976 UCS diagram.

The thickness of the ITO top and bottom electrodes influences device transmittance by affecting interference and absorption within the stack. Optical simulations were performed to confirm this effect, but they showed that the influence is relatively small (**Figure 5.7**).

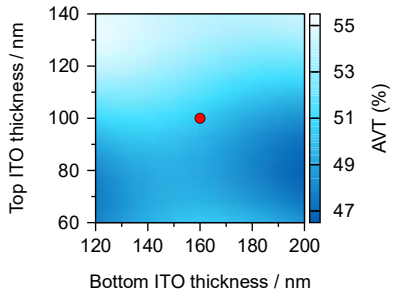

Figure 5.7. Simulated AVT of TrPeLEDs with p-type in situ NCs and a PLD ITO cathode (devices "1c") for different thickness values of the top and bottom ITO cathodes. The red point indicates the experimental thickness values.

5.3.2. Tuning of the emissive layer thickness

Despite their good emission properties, the unsatisfactory aesthetic quality of the type "1c" TrPeLEDs motivated the search for strategies to improve it. Simulations indicate that changes in the ITO electrode thickness minimally affect transmittance. Meanwhile, transmittance measurements (**Figure 5.6a**) show that the perovskite NCs film is responsible for most of the light absorption in the visible range, meaning that significant improvements of the overall device transmittance and aesthetic quality must follow from a reduction in the thickness of the emissive layer. Hence, transparent PeLEDs with the same architecture but halving perovskite layer thickness (devices "1e") were fabricated. The resulting devices appeared considerably more transparent (**Figure 5.8a**, left), as confirmed by the transmittance spectrum (**Figure 5.8b**) and by the average visible transmittance value (66.4%, compared to 50.9%, bringing it proximate to the usually accepted value of 70% for automotive industry requirements). As expected, the biggest increase in transmittance was recorded past the perovskite bandgap (< 550 nm), whereas the impact at higher wavelength, where light only gets either absorbed by the other layers or reflected, is small. The consequent favorable change in shape of the spectrum also ensures enhanced color aesthetic quality, with a particularly higher CRI value (89.2 vs 44.9) and smaller (a^*, b^*) coordinates, which result in a paler yellowish-white tint (**Figure 5.8c**) and in an even larger on/off contrast when the devices are operated (**Figure 5.8a**).

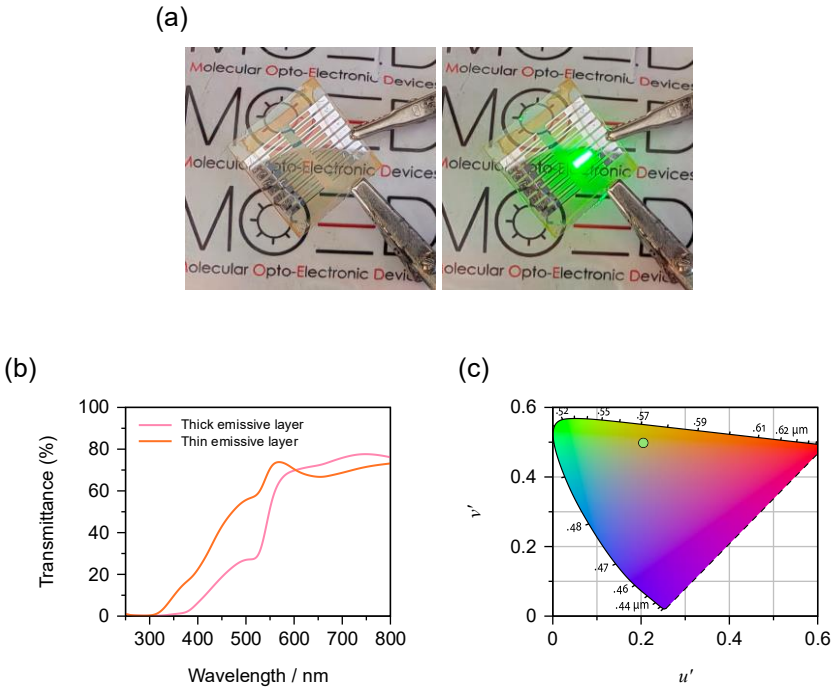

Figure 5.8. Top side in the off (left) and in the on (right) state of TrPeLEDs with a thinner layer of p-type in situ NCs (devices "1e"). (b) Transmittance spectrum of the devices compared to that of reference TrPeLEDs with a thicker emissive layer ("1c"). (c) Corresponding point in the CIE 1976 UCS diagram.

Halving the thickness enhanced the aesthetic properties of the devices but adversely affected their optoelectronic performance (**Figure 5.9a**). In fact, both the maximum luminance and the peak efficiency are lower (19 182 cd m^{-2} at 6.3 V and 1.48%, respectively, **Figure 5.9b**), which could be due to a more pronounced quenching of the emission in devices with a reduced emission area or due to worse light outcoupling. These results suggest that the device transmittance, luminance, and efficiency can be continuously tuned depending on the specific application scenario. To enable such optimization, optical simulations were performed to predict how the AVT and the total radiance varies with the thickness of the perovskite (**Figure 5.9c**). The simulations also helped to confirm that the lower efficiency in thinner devices is indeed partly due to less effective light outcoupling.

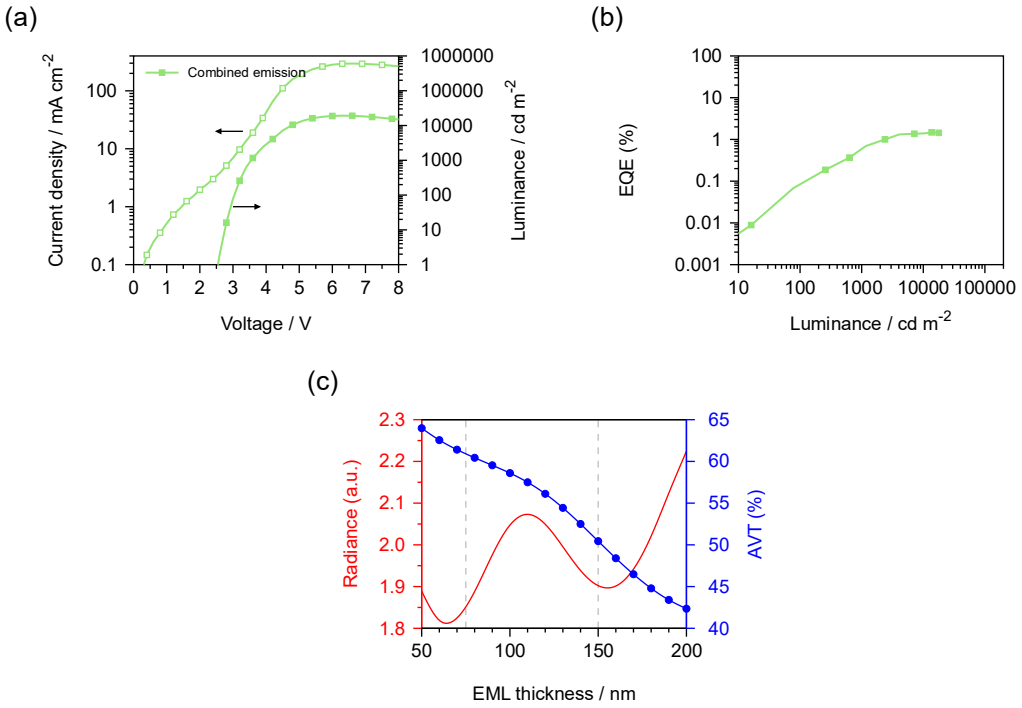

Figure 5.9. (a) *J–V–L* characteristics of TrPeLEDs with a thinner layer of p-type in situ NCs (devices "1e"). (b) External quantum efficiency *vs* luminance plot for the same devices. (c) Simulated combined perpendicular emission (red curve) and average visible transmittance (blue curve) for different EML thickness values. The vertical dashed lines indicate the experimental thickness values.

5.3.3. Application to other perovskite and device structures

As explained in **Chapter 1**, perovskites owe their successful application to many fields of optoelectronics and to that of light-emitting diodes to their rich parameter space for potential structure combinations. However, this variability also makes it impossible to develop a universal device architecture suitable for the whole range of possible perovskite structures, making it necessary to individually select appropriate transport layers and hence propagating to an even wider range of conceivable PeLEDs configurations. In spite of this, the particularly soft cathode deposition conditions detailed above lend universality to this approach to transparent LEDs, meaning it can straightforwardly be extended to a rich library of perovskite materials and to their most suitable device configurations. To demonstrate this, transparent PeLEDs with two more perovskite structures with different ETLs were fabricated.

First, LEDs based on core/shell perovskite NCs were obtained via the in situ reaction of benzylphosphonic acid (BPA) additive with polycrystalline perovskite films,[50] with the architecture ITO (160 nm)/GraHIL (75 nm)/active layer (280 nm)/2-[4-(9,10-di-naphthalen-2-yl-anthracen-2-yl)-phenyl]-1-phenyl-1H-benzoimidazole (ZADN; 45 nm)/SnO_x (20 nm)/ITO (100 nm) (devices "2a"). In summary, the perovskite thin films deposited on a hole-injection layer with a gradient work function (GraHIL) were exposed to a BPA solution, which can penetrate and intercalate into the large perovskite crystals, split them and bind to their surface (for more details, refer to the Experimental section of this Chapter). After the vacuum deposition of ZADN on top of the emissive layer, SnO_x and ITO were deposited using ALD and PLD method, respectively, as previously described. Despite the additional hole injection layer, the resulting devices have a similar average visible transmittance as the previously described ones (52.6%, **Figure 5.10a**) and no haze. This is due to the high transmittance of PEDOT:PSS in the visible

region. Any text or image positioned behind them therefore remains readable (**Figure 5.10b**), albeit with the same yellow tint ($CIEL_{u'v'}$ = 0.24, 0.54, **Figure 5.10c**).

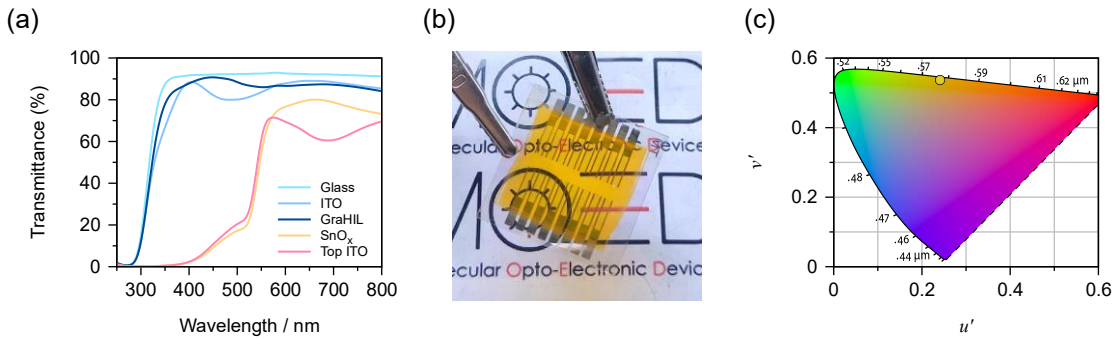

Figure 5.10. (a) Transmittance spectrum of TrPeLEDs based on in situ core/shell NCs and a PLD ITO cathode (devices "2a") after the deposition of each layer. The legend in the plot denotes the last layer deposited before the transmittance measurement. (b) Bottom side of the devices in the off state. (c) Corresponding point in the CIE 1976 UCS diagram for the full devices.

When operated, their EL spectrum (**Figure 5.11a**), measured from the bottom, shows a green narrowband emission (λ_{max} = 539 nm, FWHM = 21 nm, $CIE_{x,y}$ = 0.26, 0.72, **Figure 5.11b-c**), almost superimposable with the PL spectrum of in situ core/shell PeNCs films (**Figure 5.11d**), identical to that of opaque devices with a conventional thick metal cathode (**Figure 5.11e**) and independent of both the side of observation (**Figure 5.11f**) and the voltage applied (**Figure 5.11g**).

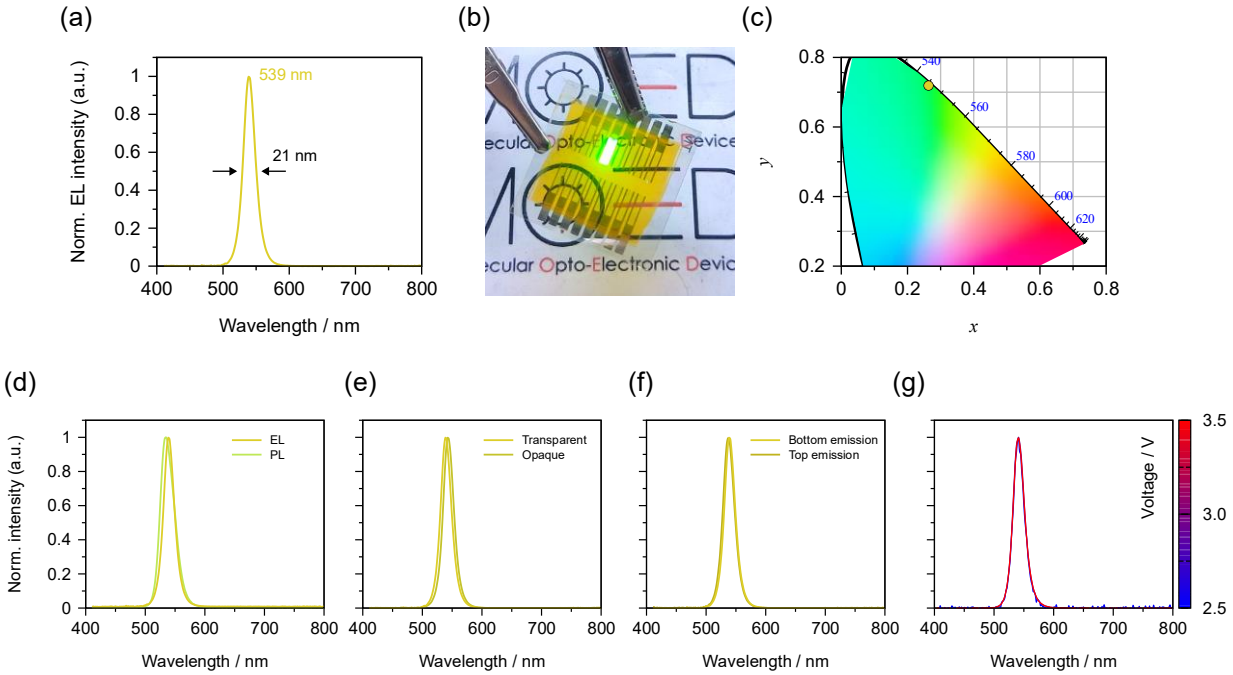

Figure 5.11. (a) EL spectrum of TrPeLEDs with in situ core/shell NCs and a PLD ITO cathode (devices "2a") measured from the bottom side. (b) Photo of the bottom side of a device turned on. (c) Corresponding point in the CIE 1931 xy chromaticity diagram. (d-g) EL spectrum from the bottom side compared with (d) the PL spectrum of a thin film of p-type in situ NCs, (e) the EL spectrum of a device with an opaque cathode ("2c"), (f) the EL spectrum recorded from the top side and (g) at different voltage values.

Their emission is visible starting from 6.23 V (for 1 cd m^{-2}, 8.54 for 20 cd m^{-2}, **Figure 5.12b**), a higher value than for the "type 1" devices. The difference could be a consequence of a difficult electron injection from SnO_x into the ETL, as ZADN has a substantially shallower LUMO energy (-2.90 eV) when compared to PO-T2T (-3.22 eV) and SnO_x itself (-4.36 eV, **Figure 5.12a**). This inevitably limits the maximum power efficiency of the devices (EQE_{max} = 1.28%, **Figure 5.12c**) and the maximum combined luminance (14 929 cd m^{-2}). To confirm the importance of the protective tin oxide layer and the damages induced by sputtering ITO deposition regardless of the device architecture, devices in which the cathode was directly deposited on top of the organic ETL via sputtering were also fabricated (devices "2b"). The variation lent the devices a lower turn-on voltage (**Table 5.4**), possibly related to the smaller overall device thickness and to the higher conductivity of ITO layers deposited via sputtering, but negatively affected the maximum luminance (1070 cd m^{-2}) and efficiency (0.07%), confirming that the harmfulness of direct sputtering ITO deposition for light-emitting diodes transcends the structure of the EML or ETL.

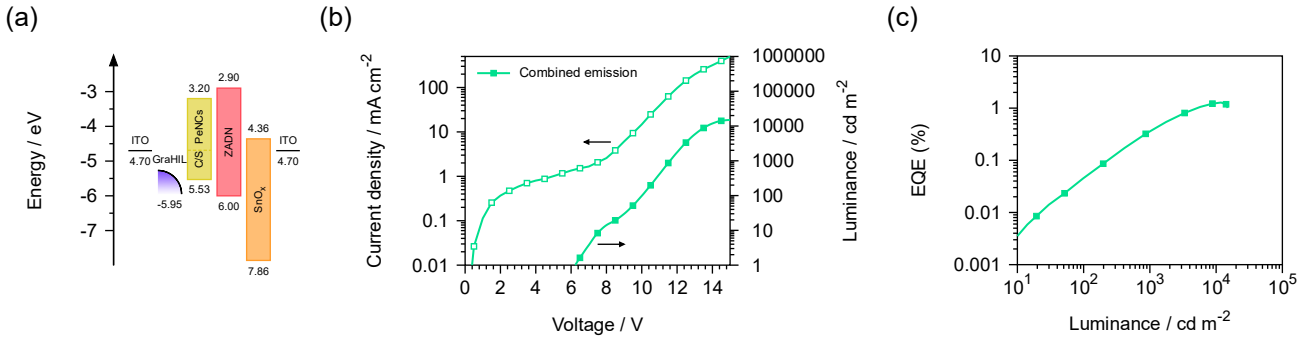

Figure 5.12. (a) Energy level diagram for TrPeLEDs based on in situ core/shell NCs (devices "2a"). (b) *J*–*V*–*L* characteristics of the same devices. (b) External quantum efficiency *vs* luminance plot.

Alternatively, the PeNCs that constitute the EML of PeLEDs can also be synthesized prior to the layer deposition rather than concurrently. The obtained suspensions, which can then be spin-coated to form a homogeneous film, usually have a low concentration, a limit imposed by the colloidal stability. As a consequence, the resulting films tend to be thin, which is beneficial for transparent devices as they allow most of the light through. For this reason, LEDs based on colloidally synthesized $FA_{0.9}GA_{0.1}PbBr_3$ nanocrystal structures with organic ligands and incorporating TPBi (devices "3a") were also fabricated. Cation alloying generates smaller particles,[158] which confines electrons and holes and boosts radiative recombination, while TPBi adsorbs onto the perovskite surface, reduces nonradiative recombination and improves the PLQY of PeNCs films.[159] The devices had the architecture ITO (160 nm)/GraHIL (75 nm)/colloidal PeNCs/TPBi (45 nm)/SnO_x (20 nm)/ITO (100 nm). As expected, the devices were extremely transparent. The text or images on top of which the devices were placed could be perfectly observed without any distortions, haze or blurring and with only minimal luminosity or color altering (**Figure 5.13b**). Indeed, the stack has an exceptional average visible transmittance around 80% (**Figure 5.13a**), which represents, as far as is known in the literature, the highest value for TrPeLEDs (**Figure 5.16**), and a very high CRI value above 90. At the same time, the near-the-origin values for a^* and b^* stand for an almost neutral color (**Figure 5.13c**).

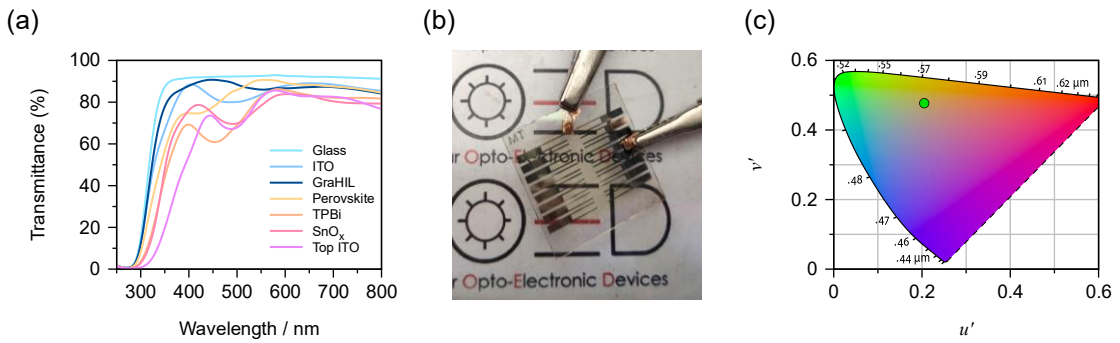

Figure 5.13. (a) Transmittance spectrum of TrPeLEDs based on colloidal NCs (devices "3a") after the deposition of each layer. The legend in the plot denotes the last layer deposited before the transmittance measurement. (b) Bottom side of the devices in the off state. (c) Corresponding point in the CIE 1976 UCS diagram for the full devices.

Similarly to "type 2" devices (with in situ core/shell PeNCs), devices with colloidal PeNCs have a relatively high turn-on voltage of 8.64 V (**Figure 5.15b**), possibly for the same misalignment between the LUMO levels of SnO_x and of the employed ETL (TPBi, **Figure 5.15a**). The bandgap of these NCs is also slightly higher, which could further contribute to the higher operating voltage; their emission is centered at a slightly smaller wavelength of 530 nm (**Figure 5.14a-b**). This, together with a small FWHM value of 21 nm indicating monodispersed particles, results in a CIE_y value of >0.79 (**Figure 5.14c**) necessary for achieving the green primary color specified in the ITU-R Recommendation BT.2020 (Rec. 2020) standard, recommended for ultra-high-definition vivid displays.[160] Analogously to the previously described devices, their emission overlaps with the PL spectrum of the film and is independent of the cathode, of the viewing direction and of the voltage applied (**Figure 5.14d-g**).

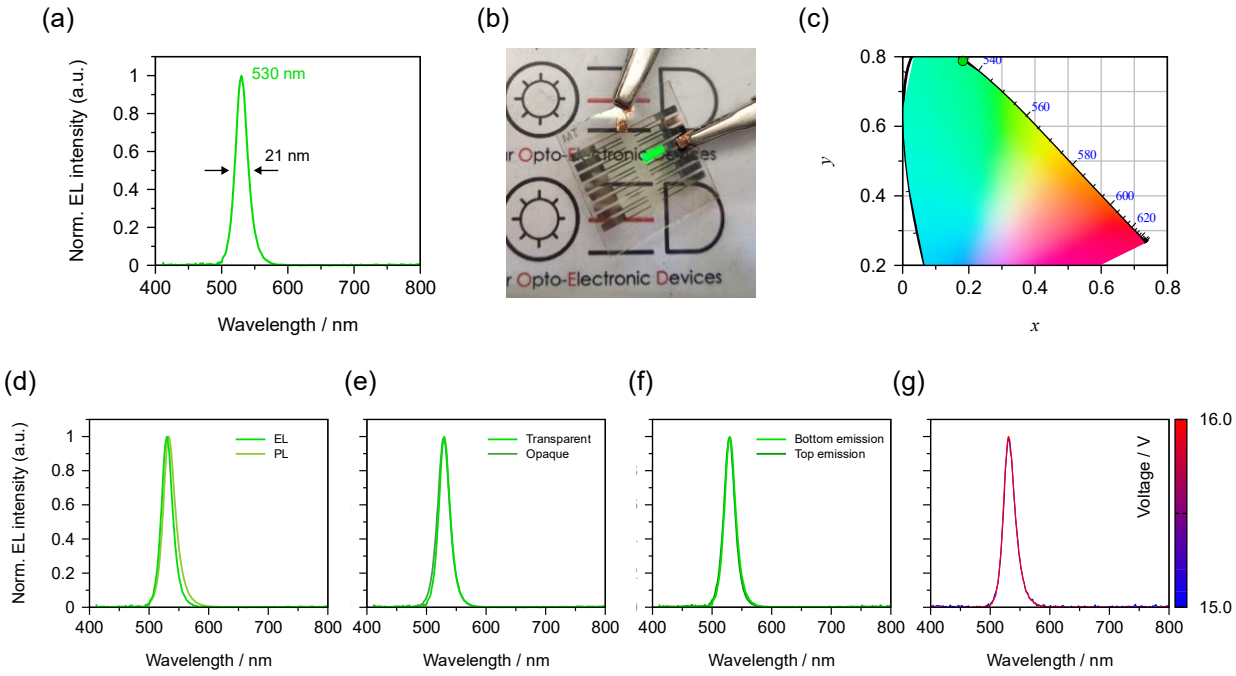

Figure 5.14. (a) EL spectrum of TrPeLEDs with colloidal NCs (devices "3a") measured from the bottom side. (b) Photo of the bottom side of a device turned on. (c) Corresponding point in the CIE 1931 xy chromaticity diagram. (d-g) EL spectrum from the bottom side compared with (d) the PL spectrum of a thin film of p-type in situ NCs, (e) the EL spectrum of a device with an opaque cathode ("3b"), (f) the EL spectrum recorded from the top side and (g) at different voltage values.

Finally, a voltage scan was performed until 20 V, at which the devices reached a luminance of 178.22 cd m^{-2} and an EQE slightly short of 0.1% (**Figure 5.15c**). This is mainly caused by the low current densities observed, likely due the insulating characteristics of the organic ligands that can impede charge injection and transport, and thereby limit the brightness and the operational lifetime.[161,162] The impeded charge injection could also contribute to the high turn-on voltage. The leakage current, however, is not very high, indicating that the damage of the TCO deposition is not the main problem, which is interesting in view of the thin emitting layer.

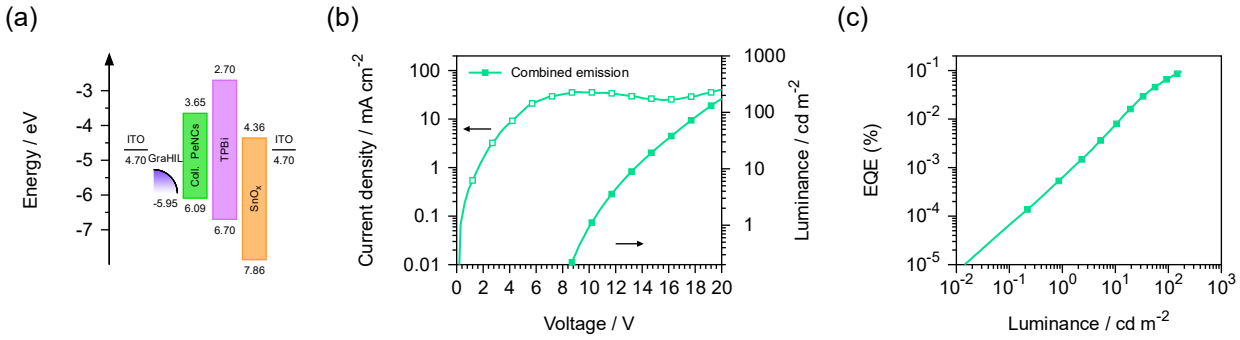

Figure 5.15. (a) Energy level diagram for TrPeLEDs based on colloidal NCs (devices "3a"). (b) *J*–*V*–*L* characteristics of the same devices. (b) External quantum efficiency *vs* luminance plot.

For ease of comparison and reference, the following tables compile the main data presented and discussed throughout this Chapter.

Table 5.2. Spectral properties of perovskite films and their light-emitting diodes with either an opaque Ba/Ag or a transparent SnO_x/PLD ITO top electrode.

Perovskite EML↴	#	Cathode	Notes	λ_{max} / nm	FWHM / nm	$CIE_{x,y}$
p-type in situ NCs	-	-	PL	544.03	25.28	-
	1f	Opaque	-	541.09	20.59	0.276, 0.710
	1c	Transparent	Bottom emission	538.14	20.00	0.263, 0.718
			Top emission	537.56	21.18	0.257, 0.723
In situ core/shell NCs	-	-	PL	534.61	27.07	-
	2c	Opaque	-	542.85	19.99	0.289, 0.699
	2a	Transparent	Bottom emission	539.32	20.59	0.264, 0.719
			Top emission	537.56	22.36	0.252, 0.728
Colloidal NCs	-	-	PL	532.61	22.41	-
	3b	Opaque	-	529.31	22.38	0.197, 0.752
	3a	Transparent	Bottom emission	530.49	22.38	0.205, 0.761
			Top emission	529.31	22.61	0.190, 0.792

Table 5.3. Key metrics to evaluate the visible transparency and aesthetic quality of transparent perovskite light-emitting diodes.

Perovskite EML ↴	T_{avg} [a]	$T_{\lambda max}$	T (range) [a]	AVT% [b,c]	CRI [c]	$CIEL_{u'v'}$ [c,d]	$CIELAB_{a^*,b^*}$ [c]
p-type in situ NCs	46.7%	35.3%	6.5% - 75.9%	50.93	44.87	0.244,0.520	14.47, 43.77
p-type in situ NCs (thin layer)	58.7%	63.8%	22.3% - 74.5%	66.38	89.25	0.205, 0.498	-3.72, 22.48
In situ core/shell NCs	42.2%	43.4%	2.2% - 72.3%	52.63	59.79	0.241, 0.537	8.08, 63.25
Colloidal NCs	77.0%	75.8%	53.8% - 86.3%	79.99	93.39	0.205, 0.477	2.80, 7.36

a. In the 400 nm – 650 nm range.
b. AVT%: average visible transmittance.
c. Calculated with the CIE standard illuminant D65.
d. Uniform Chromaticity Coordinates, 1976.

Table 5.4. Electrical characteristics of transparent perovskite light-emitting diodes.

Perovskite EML↴	#	ETL	ITO fabrication	V_{on} / V	L_{max} / cd m^{-2}	EQE_{max}
p-type in situ NCs (thick layer)	1a	PO-T2T/SnO_x	Sputtering	2.79[a]	89 749.0 (6.0 V)	3.99%
	1b	PO-T2T	Sputtering	2.86[a]	7998.82 (4.8 V)	0.176%
	1c	PO-T2T/SnO_x	PLD	2.61[a]	148 532 (13 V)	11.0%
	1d	PO-T2T	PLD	3.09[a]	10 575 (5.6 V)	0.416%
(thin layer)	1e	PO-T2T/SnO_x	PLD	2.83[a]	19 182 (6.3 V)	1.48%
In situ core/shell NCs	2a	ZADN/SnO_x	PLD	8.54[a]	14 929 (15.0 V)	1.28%
	2b	ZADN	Sputtering	2.27[a]	1070.6 (3.8 V)	0.0689%
Colloidal NCs	3a	TPBi/SnO_x	PLD	8.64	178.22 (20.1 V)	0.0965%

a. Defined as the voltage needed to reach a luminance of 20 cd m^{-2}.

Together, these findings support the claim that the described approach to fabricating transparent PeLEDs is applicable to a wide range of device architectures revolving around different perovskite compositions, synthesis procedures and structures.

5.4. Conclusions

In conclusion, in this work a combination of ALD and PLD, scalable techniques that are adaptable to mass production, was shown to be a powerful approach to fabricate transparent perovskite light-emitting diodes. The obtained devices were thoroughly characterized from both an electrical and optical point of view, as well as their transparency figures of merit, in order to elucidate the precise relationship between cathode deposition technique, use of a buffer layer, emissive layer thickness and nature, and the devices' transmittance, electrical characteristics and performance. The valuable qualities of transparent conductive oxides as well as the damage mitigation strategies devised enabled the demonstration of both the brightest (~150 000 cd m^{-2}) and the most transparent (AVT ≈ 80%) perovskite LEDs, covering a wide range of use cases (**Figure 5.16**).

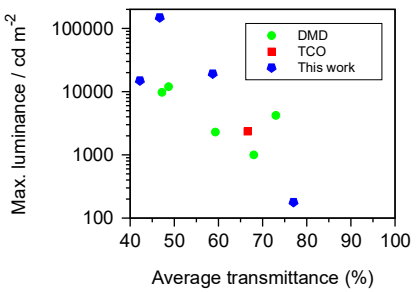

Figure 5.16. Summary of the reported TrPeLEDs characteristics on the basis of maximum luminance and average transmittance, categorized according to their cathode material. Ref: [142–148]. For NIR-emitting devices, a fictitious maximum luminance value that assumes emission at 538 nm was used for comparison.

The possibility of turning perovskite-based devices with potentially any structure into transparent ones with valid optoelectronic properties can unlock novel applications, from see-through displays and lighting panels to smart windows, walls and doors.

Moreover, the results obtained in developing top transparent electrodes can be applied also to the realization of modern high-resolution displays for the smartphone industry, where the OLED panels nowadays typically employ a top-emitting structure[163,164] consisting of a reflective anode, organic layers, and a semi-transparent cathode, and emitting light away from the substrate and the backplane electric circuit.

5.5. Author contribution and acknowledgements

In this chapter, Michele Forzatti developed the main experiments (fabrication and characterization of devices). Sergio Martínez-Saiz and Morena Cervino helped with the experiments. Edoardo Stanzani and Dr. Sandra Jenatsch performed the optical simulations. Kassio Zanoni established the SnO_x and ITO deposition procedures.

Chapter 6.

Efficient blue narrowband emission from an ultrathin hyperfluorescent MR-TADF emissive layer

6.1. Introduction

Third-generation OLEDs rely on TADF to harness triplet excitons and convert them into singlet excitons for light emission, achieving near-100% IQE using purely organic materials. Despite holding great potential, there are still challenges to overcome for them to remain at the forefront of display and lighting technology innovation. First, the long-lived triplet excitons make TADF-based OLEDs especially sensitive to the unproductive aggregation-caused quenching (ACQ), which can significantly reduce the efficiency of the devices.[165–167] Secondly, TADF emitters generally exhibit broad emission bands with FWHM over 40 nm, limiting their color purity and hindering their use for the smartphone and high-definition television displays sector. While color filters can be used to improve the color purity,[168] they lead to a considerable decrease in efficiency.

It is therefore no surprise that narrowband emitters have attracted considerable attention for improving display quality.[169,170] In particular, achieving pure-blue emission ($CIE_{x,y}$ coordinates with a y value under 0.2)[171] with purely organic electroluminescent materials presents a significant challenge. In 2015, Hatakeyama et al. reported organic molecules consisting of benzene rings connected by boron and nitrogen atoms that exhibit a multiresonance (MR) effect.[172] In this design, the HOMO is localized on the nitrogen atoms and at the meta-position relative to the boron atom, while the LUMO is confined to the boron atoms and the ortho- and para-positions. The planar and conjugate structure of the rigid polycyclic framework without separation between donor and acceptor moieties limits the rotation of the emitters and, in turn, the variety of charge-transfer (CT) states of the emitters. The molecules therefore exhibit ultrapure-blue TADF.

Since then, the molecular design attracted increasing attention for their high PLQY and narrow FWHM, and many more MR-TADF emitters have been developed and employed in OLEDs.[173] However, in nearly all cases, a host material had to be co-evaporated to prevent ACQ, leading to inefficient material usage, higher demand for specialized equipment and elevated manufacturing costs, as explained in detail in **Chapter 3**. The few examples of non-doped OLED devices have unsatisfactory FWHM values ≥57 nm[174–176] that fail to meet the aforementioned pure-blue emission criterion. On top of that, MR-TADF typically exhibit a small k_{rISC}, which causes efficiency roll-off at high luminance[177,178] and poor electrochemical stability[179] (especially in the case of pure-blue OLEDs, where the long-lived triplets generate highly reactive triplet excitons through exciton annihilation),[180] which further limits their application in commercial displays.

This led to the introduction of TADF molecules as assistant dopants ("sensitizers") to sensitize pure-blue emitters in an approach known as hyperfluorescence (HF),[180,181] which represents the so-called 4th generation of OLED technology. The emissive layer comprises a host molecule, the TADF molecule as sensitizer and the narrow-emission fluorescence molecule as "terminal emitter". In this approach, the TADF sensitizer achieves an overall shorter triplet lifetime, as the triplet excitons are quickly converted through fast spin-flip to the singlet excited state. This reduces the triplet exciton density inside the device and improves its electro-chemical stability. Most importantly, the TADF sensitizers do not compromise the color purity of the narrow-emission fluorescence emitter, because the electrically generated energy of the excited sensitizer can be transferred to the excited state of the terminal emitter as a Förster resonance energy transfer (FRET) between the S_1 states of the two molecules. Unfortunately, the implementation of the hyperfluorescence technology presents serious technical challenges: since the TADF sensitizer is co-deposited alongside the terminal emitter in the host matrix, the deposition of the emissive layer, already difficult, becomes even more demanding in terms of equipment and inefficient in terms of material utilization.

Ultrathin emissive layers may offer a strategy to employ MR-TADF emitters without requiring host co-evaporation to prevent ACQ. Moreover, this approach could provide a straightforward route to

implement hyperfluorescence by sequentially evaporating the two materials (sensitizer and terminal emitter) and exploiting their two-dimensional dispersion to keep them in close proximity. However, two key questions arise: would the narrowband emission characteristic of MR-TADF emitters be preserved in ultrathin layers, and could efficient energy transfer be achieved to realize hyperfluorescence?

In this work, these questions were addressed through a stepwise approach. First, OLEDs incorporating an ultrathin MR-TADF emissive layer were developed, successfully demonstrating narrowband pure-blue emission with an external quantum efficiency of up to 17%. Building upon this result, the same ultrathin-layer architecture was used to realize hyperfluorescent OLEDs, which exhibited reduced efficiency roll-off while maintaining the advantages of simplified device structures and lower fabrication costs.

6.2. Experimental section

6.2.1. Materials

Aqueous PEDOT:PSS dispersion was obtained from Clevios™ (P VP AI 4083). N7,N7,N13,N13,5,9,11,15-octaphenyl-5,9,11,15-tetrahydro-5,9,11,15-tetraaza-19b,20b-diboradinaphtho[3,2,1-de:1',2',3'-jk]pentacene-7,13-diamine (ν-DABNA) was purchased from Ossila. The rest of the organic materials (TAPC, mCP, DMAC-TRZ, PO-T2T) were purchased from Lumtec.

6.2.2. Device fabrication

After cleaning the ITO-coated glass substrates, a PEDOT:PSS film was deposited following the procedure described in Section 3.2.3. These substrates were transferred to a thermal evaporation system, where the organic layers (TAPC, mCP, the ultrathin emissive layer and PO-T2T) were thermally deposited. In the case of dual-component emissive layers, the two compounds were evaporated sequentially (with the sensitizer being evaporated first). The vacuum evaporation rates were 0.06 nm s^{-1}, 0.001 nm s^{-1} and 0.06 nm s^{-1} for the HTLs, ultrathin EML and ETL, respectively. Finally, the substrates were transferred to another thermal evaporation system where Ba and Ag were deposited at 0.1 nm s^{-1}.

6.2.3. Device characterization

After fabrication, the devices were measured to obtain current density and luminance versus voltage (*J*–*V*–*L*) characteristics (for more details, see Section 2.2). Besides standard characterization, the light emission of the devices over varied emission and polarization angles was measured with an angular luminescence spectrometer (Phelos, FLUXiM) with a constant current density of 10 mA cm^{-2} and a polarization angle of 0 ° (*p* polarization). The capacitance *vs* frequency curves and the transient electroluminescence signal were measured with Paios (FLUXiM). The temperature-dependent transient electroluminescence signal and *J*-*V*-*L* curves were measured with Paios (FLUXiM) equipped with a liquid nitrogen-based temperature module which was cooled by liquid nitrogen and heated via a heating resistor.

6.3. Results and discussion

6.3.1. Pure-blue OLEDs with a MR-TADF-based ultrathin emissive layer

The structure of ν-DABNA, the emitter used in this study, is shown in **Figure 6.1**. It is composed of five benzene rings linked by nitrogen and boron atoms and diphenylamino groups. The frontier molecular orbitals are localized on different atoms and are non-bonding in character, which causes the vibronic

coupling to be weak and the emission band to be sharp.[179] Its unrivaled narrow PL emission (**Figure 6.3b**), together with the high PLQY in TADF type hosts, made ν-DABNA the ideal choice as the emitter for this study.

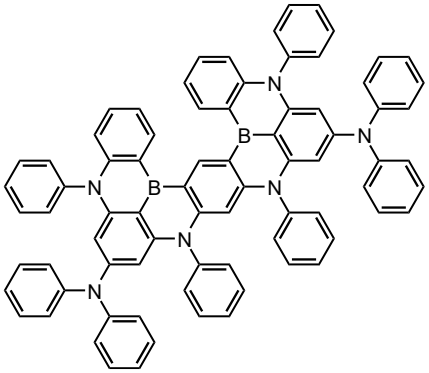

Figure 6.1. Chemical structure of ν-DABNA.

Devices were therefore fabricated using the device structure ITO/PEDOT:PSS (35 nm)/1,1-bis[(di-4-tolylamino)phenyl]cyclohexane (TAPC, 10 nm)/mCP (20 nm)/EML/PO-T2T (60 nm)/Ba (5 nm)/Ag (100 nm) (**Figure 6.2a**). In these devices, TAPC was employed as the hole-transport material. Like in devices in **Chapter 3**, mCP and PO-T2T were selected for their ability to form highly efficient exciplexes, which play a key role in harvesting excitons.[182,183] The EML consisted in a non-doped ultrathin layer of ν-DABNA with thicknesses of 0.03 nm, 0.05 nm, 0.1 nm, 0.3 nm and 1 nm, to determine the optimal thickness of the ultrathin EML based on the performances of the devices

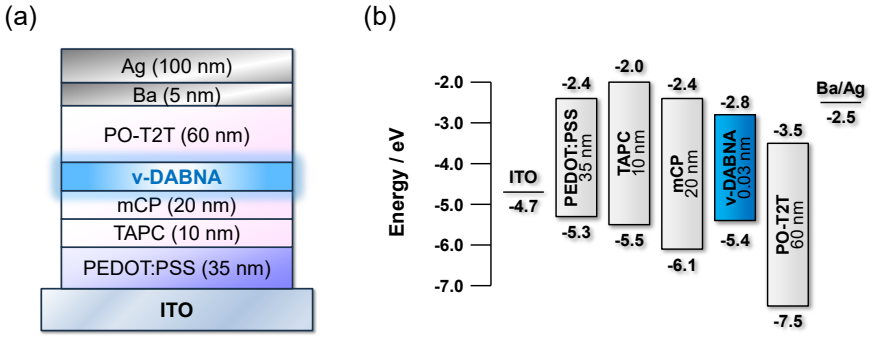

Figure 6.2. (a) Schematic representation of the architecture of the devices with a UEML of ν-DABNA. (b) Energy level diagram for the devices.

Their EL spectral characteristics are shown in **Figure 6.3a**. The devices with a 0.03 nm-thick EML have the spectrum that most closely resembles the PL of the emitter in a diluted solution (**Figure 6.3b**): the narrow emission peak is centered at 473 nm, has a FWHM of 18 nm, and it presents the same low energy

shoulder emission at around 503 nm (**Figure 6.3c**). Owing to these remarkable spectral features, the devices realize pure-blue emission (inset in **Figure 6.3c**) with $CIE_{x,y}$ color coordinates of (0.13, 0.19) (**Figure 6.3d**), which match the same standard as gallium nitride-based LEDs. Moreover, the spectrum remains unchanged when the devices are driven at higher voltages (**Figure 6.3e**), which is notable as it shows no contribution from interfacial exciplex EL emission and indicates that the recombination only occurs on the ν-DABNA molecules even for substantial current values.

When the thickness is progressively increased, from 0.03 nm to 0.1 nm (**Figure 6.3a**), the color purity deteriorates, as displayed by the relative points in the CIE chromaticity diagram moving away from the spectral locus (**Figure 6.3f**). However, the peak broadening is not immediately apparent from the FWHM values, which remain nearly unchanged, since it only manifests as a widening of the shoulder emission. As the thickness is increased past the 0.1 nm mark, the shoulder springs up until a second peak at higher wavelengths appears; at 1 nm, the situation has reversed and the deep blue ν-DABNA emission only remains as a high energy shoulder of the main broad peak at 553 nm, which has a FWHM of 70 nm. The trend is not exclusive to the EL of ultrathin layers as it also observed in the PL of ν-DABNA solutions in toluene: for concentrations lower than 10^{-4} M only one extremely sharp PL band with a FWHM of 14 nm is present, but as the concentration is increased, the peak shifts and the shoulder emission becomes more intense (**Figure 6.3b**). In the solid state, only the "shoulder emission" is visible, shifted to 500 nm and followed by an even broader band above 600 nm. These observations highlight the compound's tendency to aggregate at higher concentrations, altering its energy level distribution as seen in the PL spectra. Thus, when the thickness of the ultrathin EML is increased, aggregates form and their emission becomes more prevalent, at first existing alongside and eventually replacing the emission from individual molecules, with a detrimental impact on the color purity.

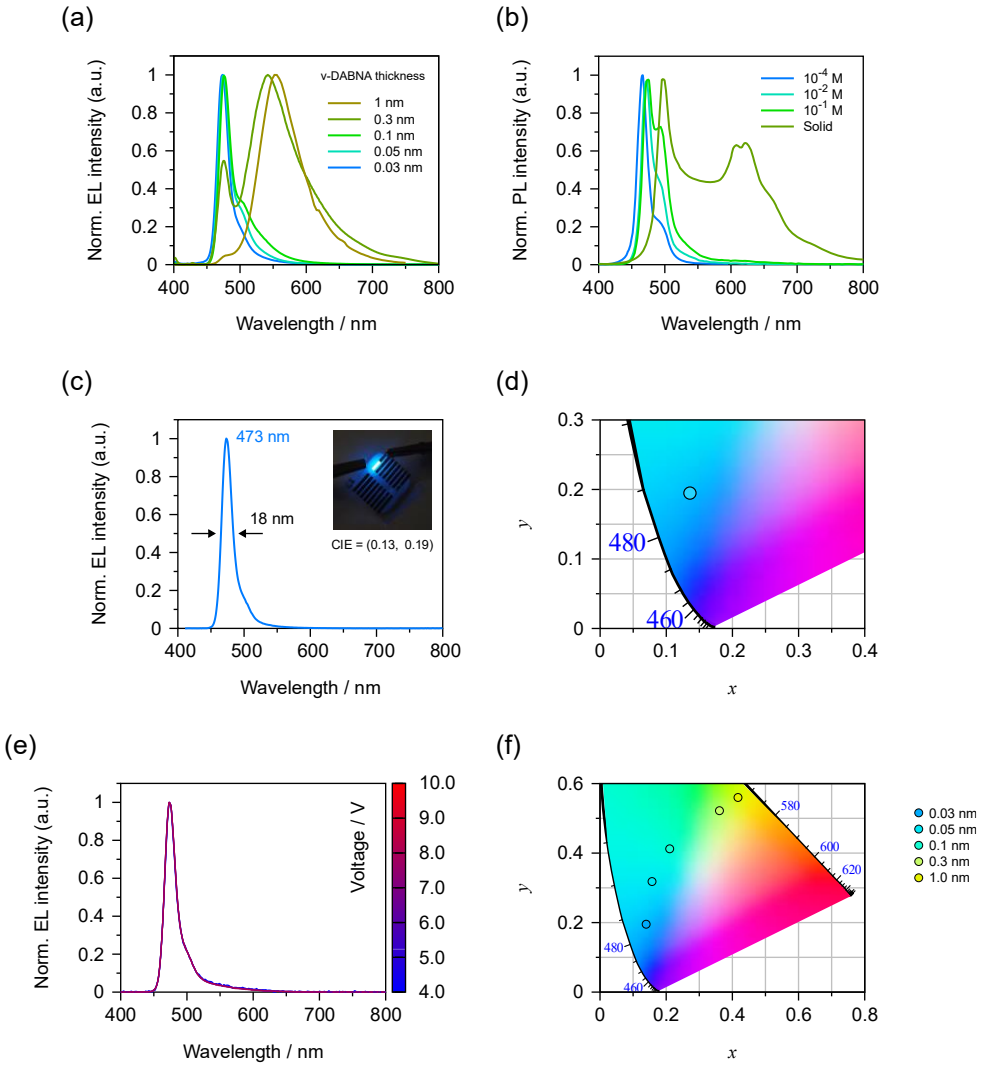

Figure 6.3. (a) EL spectra of OLEDs with different thickness of the non-doped, ultrathin ν-DABNA emissive layer. (b) PL spectra of ν-DABNA solutions in toluene with different concentrations and of the compound in the solid state. (c) EL spectrum of a device with a thickness of 0.03 nm, with the FWHM and peak wavelength highlighted. Inset: photo of the working device. (d) CIE chromaticity coordinates for the same device. (e) EL spectrum of the same device measured at different voltage values in the range of 4.0 V – 10.0 V. (f) Color coordinates in the CIE chromaticity diagram for OLEDs with different ν-DABNA UEML thicknesses.

The p-polarized angular emission patterns for devices with a thickness of the EML of either 0.03 nm or 1 nm were measured to study the orientation of the emissive dipoles in the two cases and are shown in **Figure 6.4**. The two types of devices show different p-polarized angular emission, meaning that not only the extent of aggregation but also the orientation of the emissive dipoles differ between them. By fitting the experimental profiles using optical dipole emission models that simulate how light propagates through the multilayer stack, it is possible to extract the horizontal dipole ratio and the order parameter. While such quantitative analysis of the emitter dipole orientation was beyond the scope of this work, the observed angular emission differences suggest that optimizing dipole alignment could guide future outcoupling strategies to recover trapped light and enhance device efficiency.

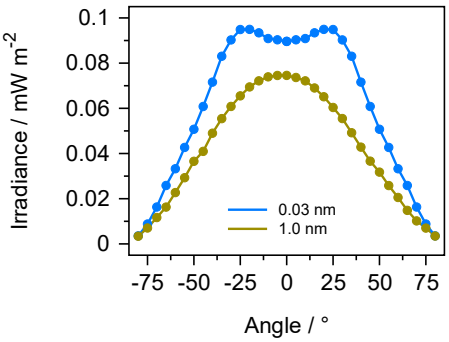

Figure 6.4. Angle dependence of the p-polarized light emission of devices with a thickness of the EML of either 0.03 nm or 1 nm.

Because of their superior spectral properties, only devices with a 0.03 nm-thick EML were considered for further characterization. The *J-V-L* characteristics of the devices are illustrated in **Figure 6.5a**. The devices turned on at 2.9 V (for 1 cd m^{-2}) and reached a peak luminance of 13 242 cd m^{-2} at 15.8 V. Their maximum current efficiency was 29.0 cd A^{-1} at a luminance of 15 cd m^{-2}, corresponding to a EQE of 17.0% (**Figure 6.5b**). The EQE then decreased to less than 10% at 1 000 cd m^{-2} and to less than 3% at 10 000 cd m^{-2}, indicating severe roll-off.

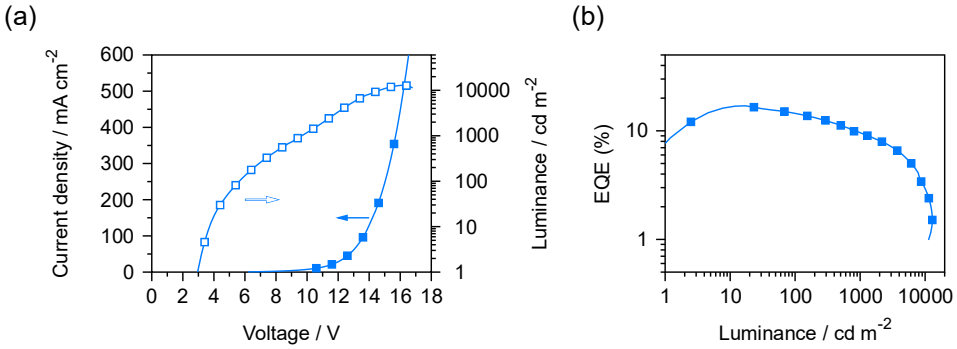

Figure 6.5. (a) *J-V-L* characteristics and (b) efficiency *vs* luminance plot for the devices with a 0.03 nm-thick ν-DABNA UEML.

The lifetime of the devices was also determined by driving them with a constant current (three different amplitudes, **Figure 6.6a**), finding an extrapolated lifetime at an initial luminance of 100 cd m^{-2} of 31 hours (**Figure 6.6b**). Interestingly, this value is identical to the one reported in literature for doped devices with the same emitter and for the same initial luminance value.[179] This correspondence highlights that the short operational lifetime found for the devices described in this study is not due to their peculiar architecture; as a matter of fact, it is a well-known hurdle, which currently limits the use of pure-blue OLEDs exhibiting 100% of IQE in industry.[184–187]

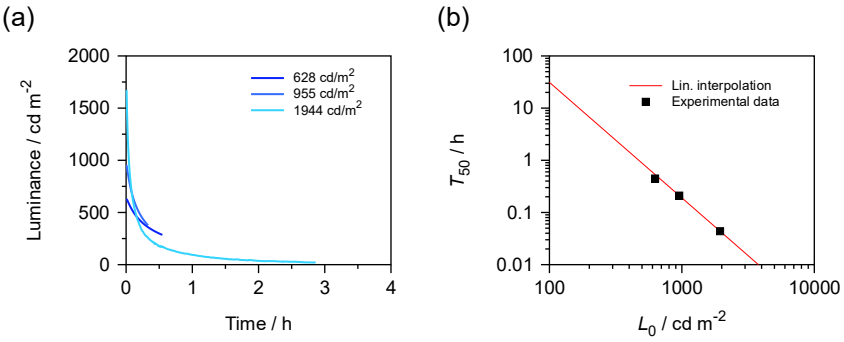

Figure 6.6. (a) Evolution of the luminance in time for devices driven with a constant current of different amplitudes (accelerated tests). In the legend, the initial luminance is listed. (b) Lifetime extrapolation from the accelerated tests. The black squares represent the experimental data and the red line represents the linear interpolation.

6.3.2. Hyperfluorescent devices

The described approach to reduce the thickness of the EML to the nanometer regime successfully affords a simplification of the fabrication process while still ensuring high color purity, reduced ACQ and a remarkable peak efficiency, but it does not fully cope with the efficiency roll-off at high luminance.

MR-TADF materials usually present relatively slow k_{RISC}, which is attributed to large ΔE_{ST} values and negligible spin–orbit coupling (SOC) matrix elements.[188] This exposes them to exciton losses via TTA and single-triplet annihilation (STA) under high excitation densities, causing significant roll-off. However, the improved molecular design of ν-DABNA with a π-extended structure lends the compound a fast k_{RISC} of $2.0 \cdot 10^5$ s^{-1},[189] suggesting that the roll-off is not inherent to the emitter but rather to its incorporation as an ultrathin emissive layer. Either way, the hyperfluorescent approach presents a promising solution thanks to improved singlet-excited-state energy transfer,[180] which is why its use to increase the performance of the devices described hitherto was investigated. Hyperfluorescent devices are usually fabricated by co-depositing the terminal emitter with a TADF sensitizer in the host matrix, which makes the deposition of the emissive layer, already difficult, even more demanding in terms of equipment. To apply the hyperfluorescence emission mechanism to devices with an ultrathin emissive layer, where no host matrix is present, an approach to sequentially deposit the terminal emitter and the TADF sensitizer was explored. A sequential deposition is made possible by the fact that molecules in ultrathin layers are not forming a continuous film but are rather dispersed, so the molecules of the next deposited material are intermixed with those already present, and by virtue of the host-like behavior of the adjacent layers (see **Figure 6.7a** and Paragraph 1.2.1). The fact that it is much simpler to carry out a sequential deposition than the co-evaporation of the three components with substantially different sublimation rates represents the main advantage of this approach, together with the reduction in material consumption.

First, a TADF sensitizer was selected. In order for the FRET to be effective, the absorption spectrum of the terminal emitter needs to overlap with the emission spectrum of the sensitizer.[190] Hence, DMAC-TRZ was employed (chemical structure in **Figure 3.1b**), the same well-known TADF emitter[191] that was already used in this thesis work (**Chapter 3**). It possesses high PLQY, small ΔE_{ST} leading to a high rISC rate constant[192] ($k_{rISC} = 2.9 \cdot 10^5$ s^{-1}) and, more importantly, a photoluminescence emission peak in neat films centered around 522 nm. While the edge of the DMAC-TRZ PL emission overlaps with the absorption spectrum of ν-DABNA only to a small extent (**Figure 6.7b**), the binary system has surprisingly already been reported to achieve very high FRET efficiency.[178] Therefore, a new set of

devices using DMAC-TRZ as a triplet harvesting/singlet sensitizer for ν-DABNA were fabricated, where both compounds were inserted into the stack in the form of ultrathin layers (**Figure 6.7c-d**) keeping the same device architecture of ITO/PEDOT:PSS/TAPC/mCP/EML/PO-T2T/Ba/Ag.

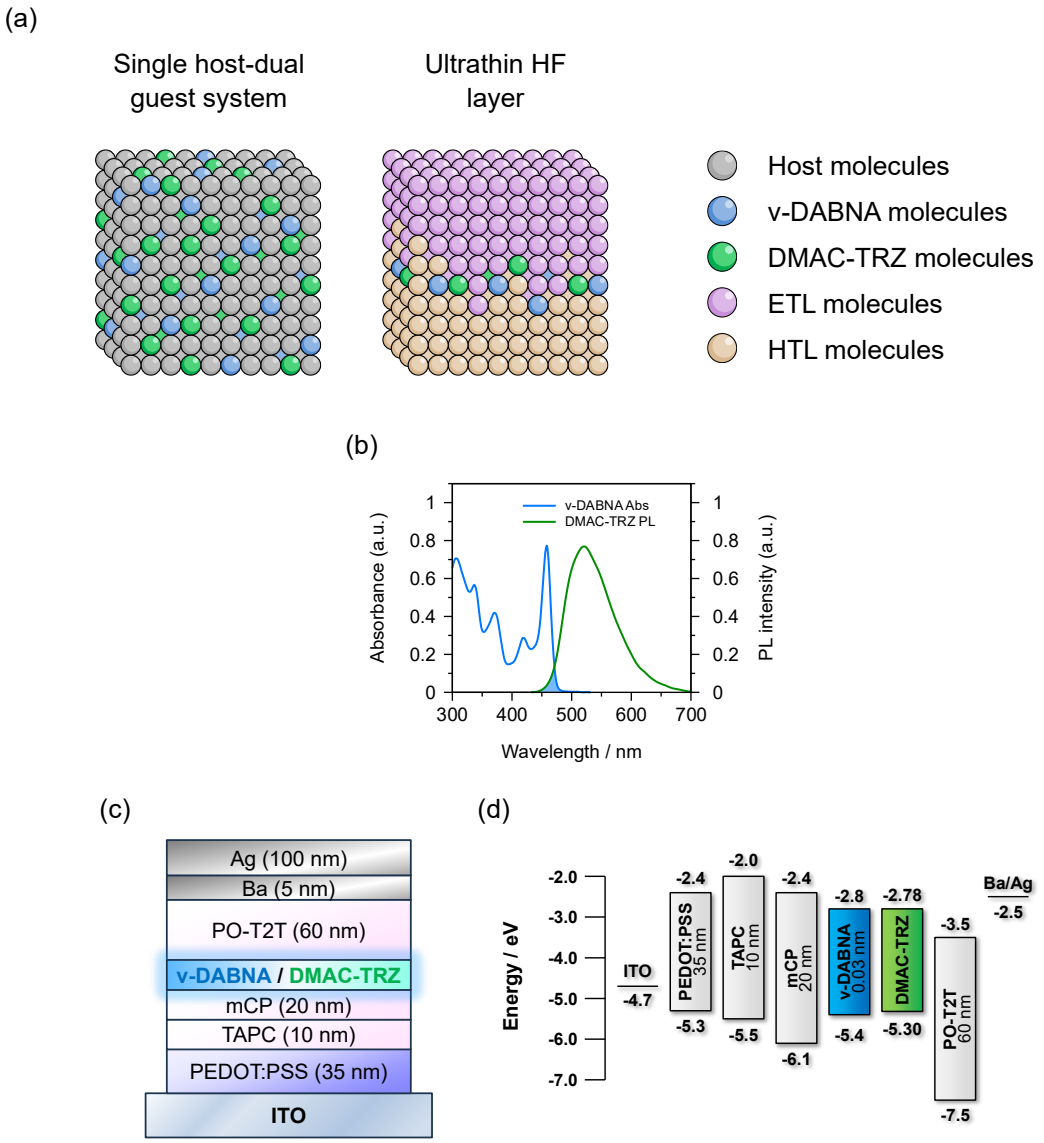

Figure 6.7. (a) Schematic structure of the ultrathin hyperfluorescent emissive layer of the devices in this work (right) compared to the "single host-dual guest" emissive layer of traditional hyperfluorescent devices (left). (b) Absorption spectrum of ν-DABNA in a toluene solution (10^{-4} M) overlapped to the PL spectrum of a thermally evaporated 275 nm-thick neat film of DMAC-TRZ. (c) Schematic representation of the architecture of the devices with a HF UEML of ν-DABNA and DMAC-TRZ. (d) Energy level diagram for the devices.

To be precise, a set of 5 devices with different nominal thicknesses of the ultrathin DMAC-TRZ layer (corresponding to different amounts of deposited molecules) were fabricated, namely 0.01 nm, 0.03 nm, 0.1 nm, 0.3 nm and 1.0 nm, while keeping the thickness of the ν-DABNA layer at 0.03 nm as in the previously described stack. The slightly higher thickness values (compared to the ν-DABNA layer) for

DMAC-TRZ were selected to ensure that the TADF sensitizer would get electrically excited preferentially. Then, the extent of the energy transfer for the 5 devices was evaluated by measuring their EL spectrum (**Figure 6.8a**). For comparison purposes, the spectrum of a device that does not contain DMAC-TRZ (and hence only has a 0.03 nm-thick ν-DABNA layer as EML) was added to the plot (dark-blue curve).

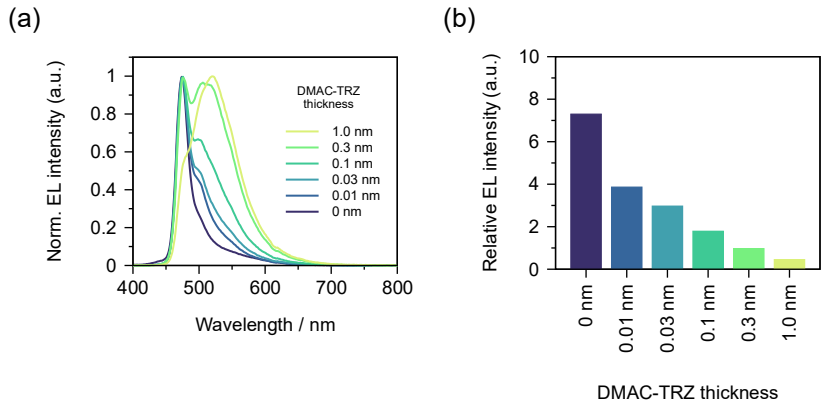

Figure 6.8. (a) EL spectra of OLEDs with an ultrathin emissive layer comprising both ν-DABNA (0.03 nm) and DMAC-TRZ (0 nm – 1.0 nm). (b) Relative intensity of the electroluminescence emission at 473 nm with respect to 520 nm for the same devices.

An EL spectrum showing features of both emitters (mixed emission) is the simplest and most direct indicator of incomplete energy transfer. One way to quantitatively assess mixed emission consists in comparing, for the different devices, the relative intensity of the ν-DABNA band (centered around 473 nm) and of the DMAC-TRZ one (around 520 nm, **Figure 6.8b**). The plot revealed that the amounts of DMAC-TRZ in 0.3 nm or 1.0 nm-thick layers were too high to ensure preferential emission from the terminal emitter. To be precise, in the 0.3 nm case, the two bands had the same intensity, while when the thickness of the DMAC-TRZ layer was 1.0 nm, only a small percentage of the electroluminescence emission came from ν-DABNA, just in the form of a shoulder to the main DMAC-TRZ emission peak centered at 520 nm, with detrimental effects on the color purity (**Table 6.1**). This is surprising when considering that in previous reports, where ν-DABNA was employed in devices with a hyperfluorescence architecture, its concentration was from 10 to 40 times smaller than that of the sensitizer.[180] This could be due to a higher tendency of the DMAC-TRZ molecules to aggregate when sublimed alone, which limits their dispersion on the surface of the underlying layer and favors an island growth mode (**Chapter 3**). When the dispersion of the sensitizer is limited and the average distance between the sensitizer and the emitter molecules is higher than the FRET radius, there cannot be efficient energy transfer, and the emission will be predominantly from the more abundant species.

Table 6.1. Spectral and chromatic characteristics of devices with a dual-component EML and different DMAC-TRZ layer thickness values.

ν-DABNA thickness = 0.03 nm	DMAC-TRZ thickness ↓	λ_{EL} / nm	CIE (x, y)	$I_{473\ nm}$ / $I_{520\ nm}$
	0 nm	473	0.13, 0.19	7.30
	0.01 nm	475	0.15, 0.31	3.87
	0.03 nm	475	0.22, 0.54	2.97
	0.1 nm	475	0.23, 0.56	1.79
	0.3 nm	477	0.26, 0.58	0.97
	1.0 nm	520	0.28, 0.60	0.46

Unfortunately, it is not possible to reduce the average distance between the sensitizer and the emitter molecules by increasing the number of the latter, as this would induce the formation of ν-DABNA aggregates and severely deteriorate the color purity, as in the case of devices with ν-DABNA only discussed in the previous Paragraph. As a confirmation, devices with an EML comprising a 1 nm-thick ultrathin layer of DMAC-TRZ and an ultrathin ν-DABNA layer with different thicknesses in the range 0 nm – 1.5 nm were also prepared, using the same device stack. Their respective EL spectra were measured (**Figure 6.9** and **Table 6.2**).

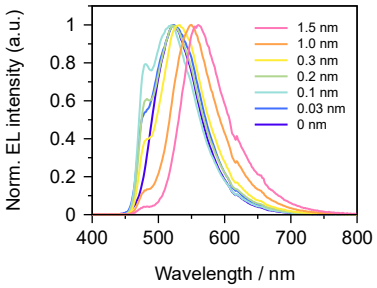

Figure 6.9. EL spectra of OLEDs with an EML comprising a 1 nm-thick DMAC-TRZ layer and an ultrathin layer of ν-DABNA with different thickness values in the range 0 nm – 1.5 nm.

At a wavelength of 473 nm, isolated ν-DABNA molecules have their emission maximum, while the emission of DMAC-TRZ is small and that of ν-DABNA aggregates is negligible. The relative intensity of the emission at this wavelength can therefore be used to qualitatively estimate the fraction of emission from each species. For ν-DABNA layer's thickness values up to 0.1 nm, a thickness increase corresponds to an increase in the relative intensity at 473 nm due to a progressively bigger contribution from isolated ν-DABNA molecules and a progressively smaller one from DMAC-TRZ. Past 0.1 nm, as the thickness further increases, the relative intensity of the peak at 473 nm begins to decrease, which is counterintuitive but in line with the behavior observed in devices without DMAC-TRZ, until the point that the ν-DABNA aggregates become the principal emitting species (550 nm peak), even supplanting

DMAC-TRZ for values equal or greater than 1.0 nm, proving that the presence of DMAC-TRZ does not prevent nor influence the formation of ν-DABNA aggregates.

Table 6.2. Spectral and chromatic characteristics of devices with a dual-component EML and different ν-DABNA layer thickness.

	ν-DABNA thickness ↓	λ_{EL} / nm	CIE (x, y)
DMAC-TRZ thickness = 1.0 nm	**0 nm**	523	0.28, 0.60
	0.03 nm	523	0.28, 0.56
	0.1 nm	520	0.25, 0.54
	0.2 nm	523	0.28, 0.56
	0.3nm	528	0.31, 0.58
	1.0 nm	550	0.39, 0.57
	1.5 nm	560	0.45, 0.53

Based on the results of the thickness sweeps performed for the two EML components, the selected thicknesses for ν-DABNA and DMAC-TRZ were both set to 0.03 nm. Larger amounts of ν-DABNA lead to aggregation, while increasing the DMAC-TRZ thickness or reducing the ν-DABNA thickness causes the sensitizer to dominate the emission, thereby degrading color purity in both cases. Conversely, smaller amounts of DMAC-TRZ may result in insufficient sensitization of the terminal emitter. From now on, the devices with an emissive layer consisting of an ultrathin layer of ν-DABNA with a thickness of 0.03 nm and an ultrathin layer of DMAC-TRZ with a thickness of 0.03 nm will be referred to as "hyperfluorescent devices" ("HF" for short). The ν-DABNA peak in their EL spectrum is centered around 474 nm and has a FWHM of 22 nm. Before anything else, the relative contribution to the emission of each component of the emissive layer was precisely quantified. To do so, a device only comprising DMAC-TRZ (with a thickness of 0.03 nm) in the emissive layer was first fabricated and its EL spectrum was measured (green curve in **Figure 6.10a**). Then, the EL spectrum of the hyperfluorescent devices was fit with the equation $I_{\text{EL,hyperfluorescent}}(\lambda) = a \cdot I_{\text{EL, ν-DABNA}}(\lambda) + b \cdot I_{\text{EL, DMAC-TRZ}}(\lambda)$, where $I_{\text{EL, ν-DABNA}}(\lambda)$ and $I_{\text{EL, DMAC-TRZ}}(\lambda)$ are the normalized EL spectra of devices only comprising ν-DABNA (discussed at the beginning of this Chapter) and of devices only comprising DMAC-TRZ, respectively. The constants were found to be 0.65 and 0.35 (**Figure 6.10a**), meaning that 65% of the electroluminescence emission of the hyperfluorescent devices comes from ν-DABNA. Inevitably, the contribution of DMAC-TRZ to the emission negatively affects the color purity of the resulting devices, even though their $CIE_{x,y}$ coordinates of (0.17, 0.34) still position the emission in the blue-green region of the chromaticity diagram (**Figure 6.10b**) and are distinctively lower than those relative to the device with DMAC-TRZ only (0.22, 0.54).

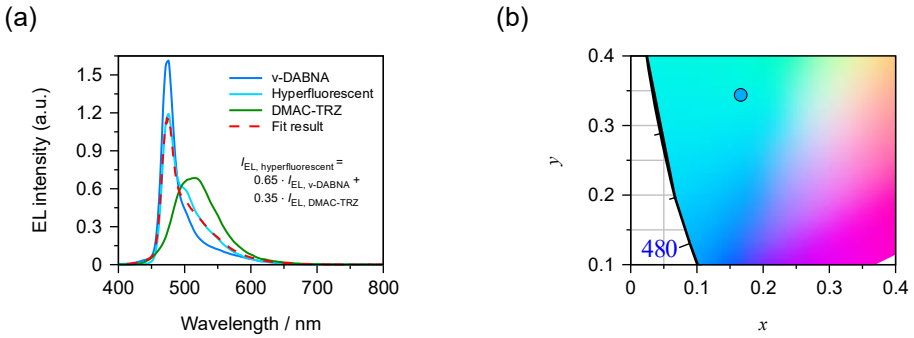

Figure 6.10. (a) Relative contributions to the emission of hyperfluorescent devices with an ultrathin emissive layer comprising 0.03 nm of ν-DABNA and 0.03 nm of DMAC-TRZ. (b) CIE coordinates for the same devices.

Next, the *J-V-L* characteristics of the hyperfluorescent devices were measured (**Figure 6.11a**). Similarly to the devices with ν-DABNA only, the hyperfluorescent devices turned on at 2.9 V, and reached a higher peak luminance of 17 887 cd m^{-2} at 17.2 V.

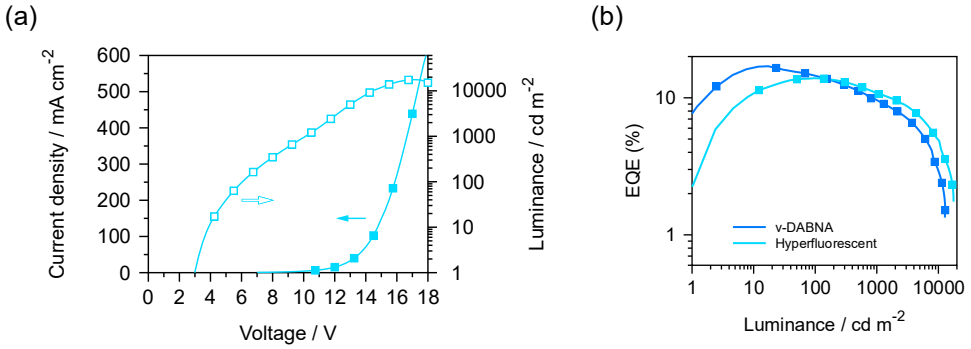

Figure 6.11. (a) *J-V-L* characteristics of HF devices. (c) EQE *vs* luminance plot for HF devices compared to devices with ν-DABNA only.

As for the efficiency, the hyperfluorescent devices reached a lower peak value of 13.9%. However, they suffered less from efficiency roll-off at high luminance values (**Figure 6.11b** and **Table 6.3**), at which their efficiency is higher than that of the devices with only ν-DABNA (10.77% vs 9.62% at 1 000 cd m^{-2}, 4.95% vs 2.94% at 10 000 cd m^{-2}). The reduced roll-off is consistent with DMAC-TRZ efficiently harvesting and up-converting triplets, which would keep the triplet population low and suppress TTA.[177,180] However, this result should be interpreted with caution, as the broader emission spectrum introduced by DMAC-TRZ influences the measured luminous efficacy and thus the apparent EQE at high luminance.

Table 6.3. EQE at different luminance values for hyperfluorescent devices and for devices with ν-DABNA only. Hyperfluorescent devices suffer from efficiency roll-off to a lesser extent.

Emissive layer ↓	EQE at different luminance values (in cd m^{-2})			
	10	100	1000	10 000
ν-DABNA	16.81%	14.49%	9.62%	2.94%
Hyperfluorescent	11.08%	13.90%	10.77%	4.95%

Finally, it was attested that the addition of DMAC-TRZ molecules in this form does not have any influence on the geometrical properties of the devices. In particular, it was found that the geometric capacitance, as extracted from impedance spectroscopy measurements in the dark (**Figure 6.12**), remains unchanged, meaning that the changes in the device's efficiency are due to electronic or excitonic effects, not due to a change in the device's geometry or charge storage properties.

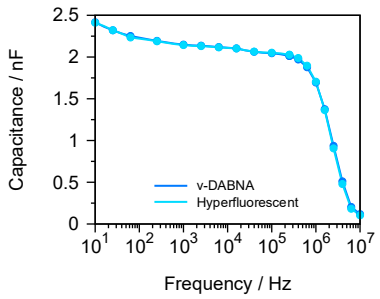

Figure 6.12. Capacitance *vs* frequency plot for hyperfluorescent devices and for devices with an EML comprising ν-DABNA only.

Transient electroluminescence (TEL) can be a powerful tool for confirming whether energy transfer between the TADF sensitizer and the terminal emitter (e.g., ν-DABNA) is actually taking place. TEL tracks the time evolution of light emission when an electrical pulse is applied (turn-on) or removed (turn-off) from the device, providing information about carrier recombination dynamics and energy transfer pathways between species in the emissive layer.

The TEL of the devices was measured by applying rectangular voltage pulses *V* with an amplitude of 4.8 V and with a length of 1000 μs, long enough to reach the steady-state conditions. The decay of the electroluminescence in time after the end of the voltage pulse was recorded for the hyperfluorescent devices and, for comparison purposes, also for devices only comprising either ν-DABNA or DMAC-TRZ in the emissive layer (with a thickness of 0.03 nm in both cases). The EL decay profiles for the three devices, shown in **Figure 6.13a**, reveal an initial "fast" decay in the time domain of micro-seconds, followed by a "slow" decay in the time domain of hundreds of micro-seconds.

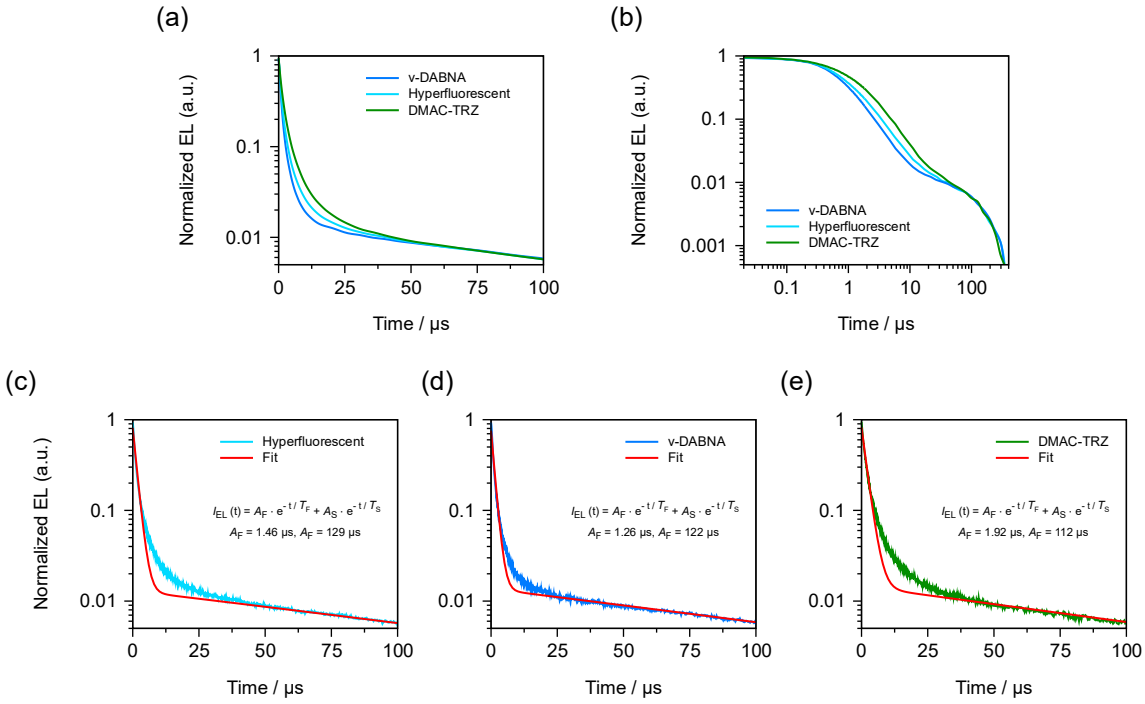

Figure 6.13. (a-b) TEL decay of hyperfluorescent devices compared to devices with ν-DABNA or DMAC-TRZ only in (a) semi-logarithmic and (b) logarithmic display. (c-e) Fitted TEL decay profiles for devices with different emissive layer compositions. (c) Hyperfluorescent devices. (d) ν-DABNA only. (e) DMAC-TRZ only.

Hence, a second order exponential decay function was successfully fit to the EL decay profiles (**Figure 6.13c-e** and **Table 6.4**). The value of the initial "fast" decay indicates that luminescence in these systems is governed by long-lived excitons, since the obtained values, in the time domain of microseconds, are significantly larger than the lifetime of excitons in fluorescence processes (sub-nano to nanoseconds). A confirmation of the reliability of the measurement is given by the lifetime value extracted from the "fast" decay for the devices with only DMAC-TRZ in the emissive layer (1.92 µs), which matches the delayed recombination lifetime of the TADF emitter doped in a host determined from transient PL experiments (1.9 µs).[191] For devices with only ν-DABNA, the lifetime was shorter (1.26 µs), while for hyperfluorescent devices, it lies in between the two extremes (1.46 µs). The differences in the decay constants are also evident in the log-log plot of the decay profiles (**Figure 6.13b**), in which the curves relative to devices with different emissive layer compositions differ significantly in the region 0.03 µs – 40 µs (with the curve relative to the hyperfluorescent devices being interposed between the curves of the devices with a single-component EML). The intermediate electroluminescence decay rate in devices containing both emitters is consistent with the predicted hyperfluorescence mechanism (that is, a first electrical excitation of the assistant dopant DMAC-TRZ, followed by a triplet to singlet exciton upconversion and a successive resonant singlet energy transfer to the states of ν-DABNA molecules),[181] but also with mixed emission. In other words, the hyperfluorescence interpretation cannot be unambiguously confirmed with the present data and would require further spectrally resolved measurements.

Table 6.4. TEL decay lifetimes and relative population fitting for devices with different emissive layer compositions.

Emissive layer ↓	$I_{EL}(t) = A_F \cdot e^{-t/T_F} + A_S \cdot e^{-t/T_S}$			
	A_F	T_F / μs	A_S	T_S / μs
v-DABNA	0.74	1.26	0.014	122.00
Hyperfluorescent	0.80	1.46	0.013	129.01
DMAC-TRZ	0.81	1.92	0.015	112.00

The different curves then overlap for longer time values (> 50 μs). In fact, the "slow" EL decay exhibits a lifetime of ~120 μs that hardly changes with the EML composition. This suggests that the "slow" decay is governed by a drift of the pre-existing mobile charges that form the space charge regions during discharge.[193] In other words, even after the OLED is driven to an open-circuit condition, the electric field does not decay immediately due to the existence of charged regions that have formed under the steady-state conditions. These charge densities discharge slowly, over the course of several tenths of microseconds, via a drift, exciton formation and radiative recombination. The electroluminescence that originates from this process thus has a time constant that is only marginally affected by the intrinsic decay lifetime of the emitters. It is important to note, however, that just a small fraction of the involved charge carriers undergo this path, as indicated from the population amplitude values (that is, the pre-exponential factors) obtained through the fit of the TEL decay profiles.

Finally, the deviation from linear traces in the semi-logarithmic representations of the decays, as made evident by the fitted curves, indicates the presence of additional processes of higher orders, e.g. annihilation processes, that were not kept into account.[194]

In conventional thick host:guest EMLs, an overshoot (electroluminescence spike) is usually observed in the first 2-3 μs after voltage OFF and can be attributed to traps. During steady state, charges build up at the blocking layers adjacent to the EML. When the voltage is reversed, electrons and holes flow back toward the cathode and ITO, meeting near the center of the EML,[180,195,196] producing the short-lived TEL overshoot. In the present devices, which employ ultrathin emissive layers, only a small overshoot is observed in the normalized transient electroluminescence traces (**Figure 6.14**). This reduction is consistent with the fact that the interfaces of the two blocking layers are in close proximity, leaving little room for charge accumulation within the emissive region. The TEL of the devices was also measured for rectangular voltage pulses *V* with different amplitudes in the range 4.0 V -6.0 V (and with the same length of 1000 μs), finding that both the normalized decay profile and the intensity of the overshoot are independent of the pulse voltage.

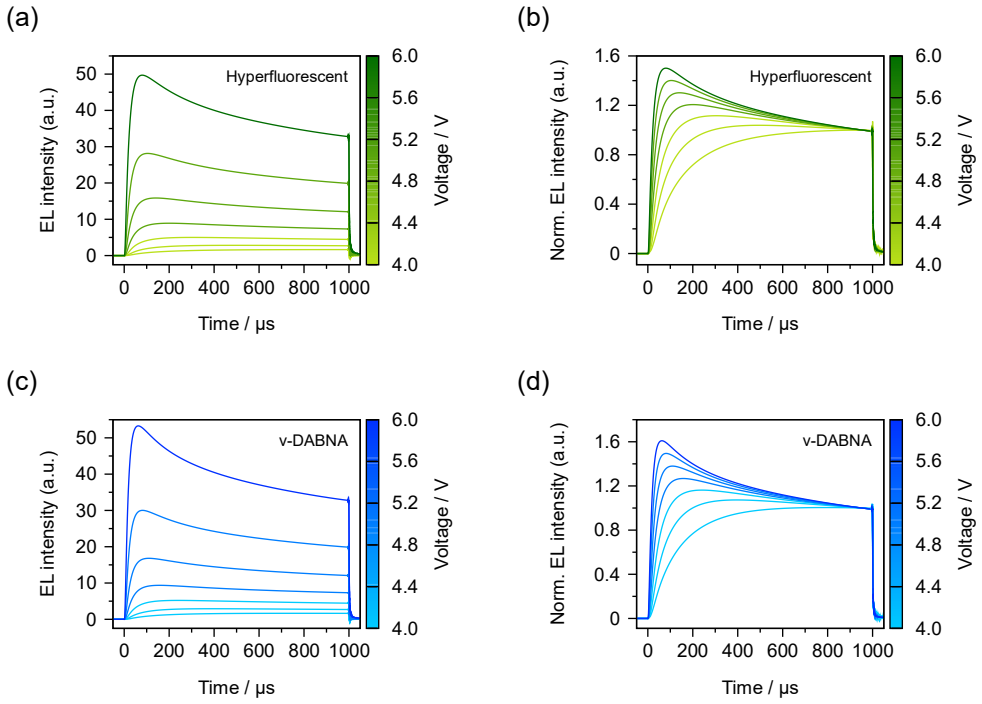

Figure 6.14. Full TEL curves for hyperfluorescent (a: non-normalized, b: normalized) and ν-DABNA only (c: non-normalized, d: normalized) devices measured with different pulse voltages.

TEL can provide insights not only about the luminescence lifetime in OLEDs but also about the charge carrier mobility from the onset time. In fact, the measured characteristic onset time in the TEL signal directly reflects the charge carrier mobility of electrons and holes μ, as it can be related to the transit time t_{tr} (that is, the time it takes for the charge carriers to be injected and transported before meeting and recombining radiatively) with the analytical relation $\mu = d^2 / [t_{tr} (V - V_{bi})]$, where d is the device thickness and V_{bi} the built-in potential (that is, the voltage corresponding to the internal electric field across the device created by the redistribution of charges according to the work function difference between anode and cathode).[197] When comparing the normalized TEL traces of the hyperfluorescent devices and those containing only ν-DABNA in the EML on a semilogarithmic scale, it becomes evident that the two sets of devices differ only in their decay dynamics, while the rise behavior remains identical (**Figure 6.15**). Therefore, the analysis of the charge carrier mobility was carried out using the traces of the hyperfluorescent devices, as identical rise characteristics are expected given the same device architecture apart from the emissive layer composition.

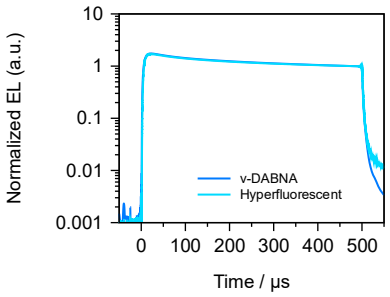

Figure 6.15. Normalized full TEL curves for hyperfluorescent and ν-DABNA-only devices plotted on a semilogarithmic scale, showing identical rise behavior and differing decay dynamics.

A room-temperature charge carrier mobility of $9.23 \cdot 10^{-6}$ cm^2 V^{-1} s^{-1} could therefore be extracted. This compares to an electron mobility of $10^{-7} \sim 10^{-5}$ cm^2 V^{-1} s^{-1} for OLEDs with doped emissive layers determined using TEL and time-of-flight photoconductivity measurements.[198,199] As predicted by the analytical expression above, when repeating the measurement for varied voltage pulse values, it was observed that the higher the *V*, the faster the luminescence rise time is (**Figure 6.14b,d**); for values higher than 4 V, this effect leads to an initial overshoot, suggesting that a longer waiting time or, even more likely, a negative bias are needed to return to the initial equilibrium state.

rISC, the mechanism underlying the efficiency-enhancing up-conversion of non-emissive triplet states to emissive singlet states in TADF, is driven by thermal energy. To assess the influence of the rISC process in these hyperfluorescent devices, temperature-dependent TEL measurements were performed. **Figure 6.16a** shows TEL measurements of hyperfluorescent devices for temperatures from 190 K to 330 K in 20 K steps. The pulse intensity was increased to 8 V to ensure good signal/noise ration even at low temperatures and the pulse length was increased to 10 ms to ensure the attainment of steady state conditions. Expectedly, the higher the temperature, the higher the steady state luminance, as an increased temperature enlarges the charge carrier mobility in organic thin films and the recombination rates.[200,201] The same effect is visible in steady state EL intensity *vs* voltage curves (**Figure 6.16b**). When normalizing the decay profiles and representing them semi-logarithmically, a temperature activated process was observed since they become faster with increasing temperature (**Figure 6.16c**).[194]

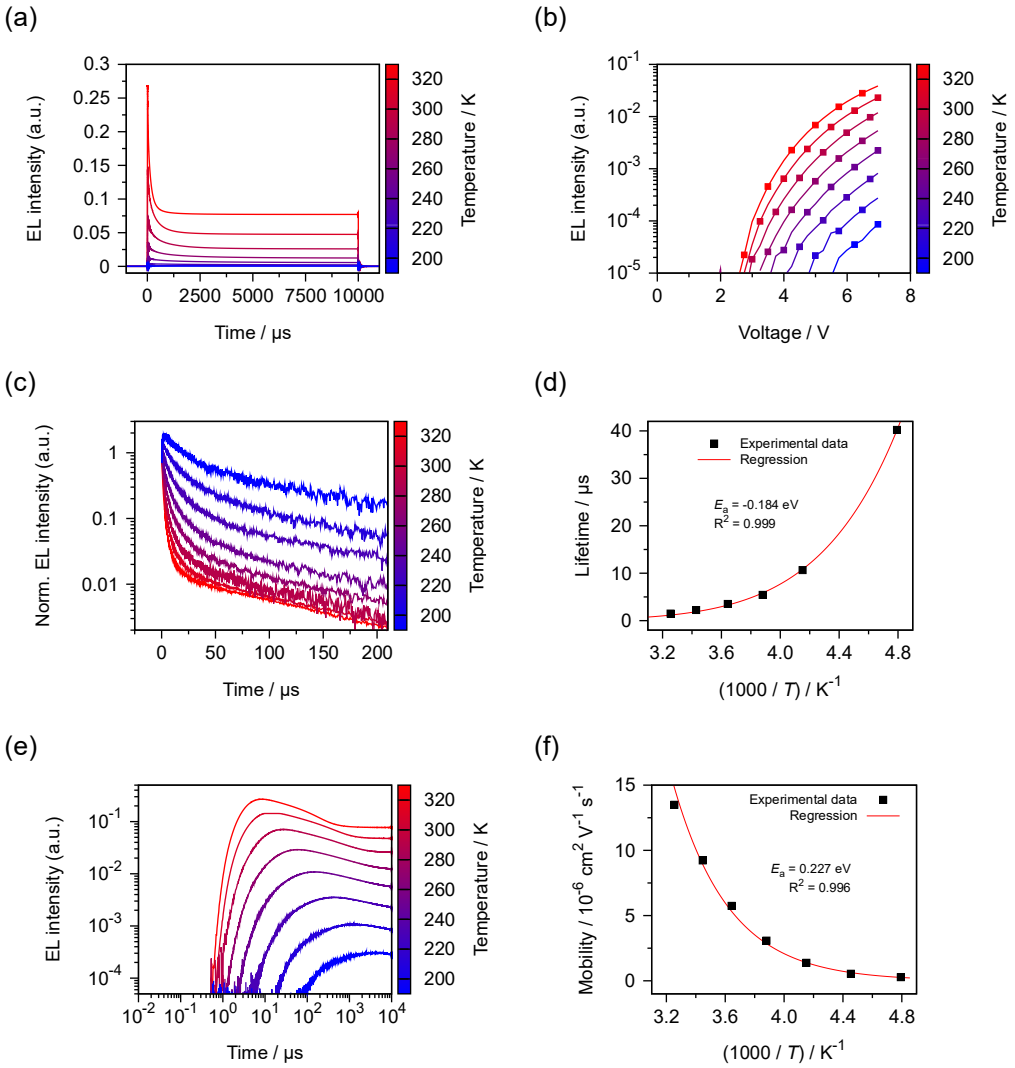

Figure 6.16. (a) Transient EL measurement of hyperfluorescent devices in linear representation for temperatures from 330 K to 190 K in 20 K steps. (b) Steady state EL intensity *vs* voltage curves for the same devices measured at different temperatures. (c) Transient EL decays of hyperfluorescent devices in semi-logarithmic representation for temperatures from 330 K to 190 K in 20 K steps. (d) Arrhenius plot for the evaluation of the thermal activation energy of the "fast" decay. (e) Transient EL signal in logarithmic representation for the extraction of the characteristic onset time at different temperatures. (f) Arrhenius plot for the evaluation of the thermal activation energy of the carriers' mobility.

The same second order exponential decay function was then fit to all the profiles, noting that only the value of the initial "fast" decay changes with temperature and is hence associated to a temperature activated process (**Table 6.5**). On the contrary, the "slow" decay rate remains nearly constant in the explored temperature range. An Arrhenius plot could be created with the evaluated "fast" decay rates (**Figure 6.16d**) and a thermal activation energy value of 0.184 eV (R^2 = 0.999) was extracted. The increase in carrier mobility affects not only the steady state luminance but also the rise of the luminance signal (**Figure 6.16e**), which becomes faster in accordance with the relationship between mobility and transit time. Analogously to the decay processes activation energy, when extracting the mobility value for the same voltage but for the different temperatures at which the TEL responses were recorded, it

was possible to extract the thermal activation energy of the mobility by means of the Arrhenius plot (**Figure 6.16f**), finding a value of 0.227 eV (R^2 = 0.996).

Table 6.5. TEL lifetime and charge carrier mobility for hyperfluorescent devices measured at different temperatures.

	Temperature / K ↓	TEL lifetime / µs	Mobility / $cm^2\ V^{-1}\ s^{-1}$
Hyper-fluorescent	**208.6**	40.21	$2.77 \cdot 10^{-7}$
	240.9	10.66	$1.38 \cdot 10^{-6}$
	257.7	5.43	$3.08 \cdot 10^{-6}$
	274.5	3.52	$5.75 \cdot 10^{-6}$
	290.1	2.23	$9.23 \cdot 10^{-6}$
	307.3	1.49	$1.35 \cdot 10^{-5}$

6.4. Conclusions

In summary, the novel introduction of a MR-TADF compound, ν-DABNA, in the form of an ultrathin layer was explored. This approach yielded pure-blue devices with a maximum efficiency of 17% and a peak luminance of 13 242 cd m^{-2}. Then, the feasibility of realizing hyperfluorescent devices with ultrathin emissive layers was investigated by sequentially depositing ν-DABNA and DMAC-TRZ. Fine tuning of the individual layer thicknesses enabled devices that reached a peak EQE of 13.9%, together with higher efficiencies at elevated luminance (10.8% at 1000 cd m^{-2} and 5.0% at 10 000 cd m^{-2}, compared with 9.6% and 2.9% for the devices without the TADF sensitizer).

The electroluminescence spectra and transient EL responses of these devices are compatible with a hyperfluorescence mechanism in which DMAC-TRZ acts as a triplet-harvesting sensitizer transferring energy to ν-DABNA. However, the data cannot exclude the presence of mixed emission from both species. To unequivocally confirm the occurrence of energy transfer, additional experiments such as time-resolved and spectrally resolved transient measurements or selective band-pass filtering of the transient emission would be required. Nevertheless, this original approach demonstrates that sequential deposition of ultrathin TADF and deep-blue MR-TADF layers can achieve high efficiency, tunable emission, and ease of fabrication simultaneously; it therefore holds strong potential for adoption in next-generation OLEDs with wide-color-gamut displays.

6.5. Author contribution and acknowledgements

In this chapter, Michele Forzatti developed the main experiments (fabrication and routine characterization of devices). Edoardo Stanzani and Sandra Jenatsch helped with the advanced device characterization (angle-dependent emission, capacitance, transient measurements, temperature-dependent measurements).

Chapter 7.

Conclusions and outlook

7.1. General conclusions

Despite the excellent efficiency and display quality of LEDs and OLEDs, their potential impact remains limited if the technology is not adopted on a large scale. High performance alone is not sufficient to drive widespread use; factors such as fabrication cost and scalability also play a critical role in determining whether these devices reach the broader market.

Device design for wider technology adoption

Building on this perspective, the primary goal of this doctoral work was to address the barriers that limit the widespread adoption of OLEDs and PeLEDs, namely high fabrication costs, while preserving their key advantages, like high efficiency and color quality. To this end, novel device architectures were developed, involving perovskites (inherently low-cost materials that possess exceptional optoelectronic properties), ultrathin emissive layers and TADF molecules.

In **Chapter 3**, a combination of a thick perovskite HTL, TADF emitters and UEMLs was demonstrated. Thick perovskite HTLs increase device production yield, TADF compounds do not contain expensive elements and UEMLs minimize material consumption. At the same time, perovskites enhance charge injection and transport even in thick layers, TADF compounds can achieve 100% IQE and UEMLs can realize complete exciton utilization. Devices with a 0.03 nm-thick $Ir(ppy)_2(acac)$ UEML and a micrometer-thick perovskite HTL reached a peak luminance above 10 000 cd m^{-2} and an efficiency of 54.1 cd A^{-1}. The Ir-containing emitter was then replaced with the TADF DMAC-TRZ (to avoid costly heavy metals) in an ultrathin layer (1 nm), achieving a luminance of 11 152 cd m^{-2} and a current efficiency of 67.6 cd A^{-1}, and subsequently, the compatibility of the perovskite film with solution processing enabled OLEDs with a spin-coated TADF dendrimer EML (tBuCz2m2pTRZ) reaching 4660 cd m^{-2} and 15 cd A^{-1} at 1000 cd m^{-2}. In **Chapter 4**, color-tunable PeLEDs with a simple HTL-free architecture, which has benefits of reduced fabrication costs and improved reproducibility, were fabricated. The devices had a tunable emission in the range 491 – 793 nm and reached EQE values up to 25.9%. In **Chapter 6**, the library of compounds that have been implemented as ultrathin layers was increased, highlighting the broader applicability of the approach, through the successful demonstration of ν-DABNA-based devices. The characteristic pure-blue emission remained unaffected and an EQE of 17% and a luminance of 13 242 cd m^{-2} were obtained. Sequential evaporation of DMAC-TRZ in the UEML lowered the efficiency roll-off while retaining the simpler fabrication process. These results showed that the design of devices that are sustainable, affordable and industrially manufacturable can be achieved while maintaining their functional properties.

Another objective of this thesis was to improve the user experience, which is also important for encouraging broader adoption of the technology. To achieve this, in **Chapter 5** transparent PeLEDs were realized, which preserve the intrinsic benefits of perovskites (narrow-band emission of 20 nm, high EQE up to 11% and high combined luminance of up to ≈ 150 000 cd m^{-2}) in devices with AVT values of 51%, which could enable their integration into innovative applications including augmented and virtual reality, smart windows, head-up displays, transparent televisions, and wearable electronics.

Fundamental insights into materials and devices

In addition to these practical advancements, this work also investigated the fundamental properties of the materials and devices.

In **Chapter 3**, a simple strategy to passivate interfacial defects in co-evaporated perovskite films was presented and its compatibility with the processing from solution of subsequent layers was confirmed. The nature of UEMLs was also studied and their island growth mode was backed up, as well as its noninterference with the exciplex formation in heterojunction interfaces. In **Chapter 4**, the effect of a phosphonic acid molecular dopant with strong electron-withdrawing abilities on mixed-halide perovskites was assessed. 4PACz molecules enhance the optical properties of the films, have a beneficial

role on the prevention of halide segregation and shift the Fermi level across the bandgap. **Chapter 5** highlighted how the protective barrier provided by SnO_x, in combination with the gentle processing of PLD, enables a universal route to transparent PeLEDs. Finally, **Chapter 6** provided indications that hyperfluorescence may be achievable in an ultrathin emissive layer.

Understanding these optical, electronic, and morphological behaviors provides valuable insights that can guide future optimization and the design of next-generation devices, supporting further progress in the field.

7.2. Outlook

Looking ahead, the broader diffusion of OLEDs and PeLEDs would not only support the global effort to reduce electricity demand and mitigate climate change but also make high-quality displays and lighting accessible to a wider public.

The results presented in this thesis represent a step forward in that direction, showcasing progress in the development of efficient and accessible light-emitting devices. However, despite the advancements achieved, the methods and results presented still face several challenges, like the lower efficiency of devices with UEMLs compared to their conventional thick EML counterparts, the unsatisfactory film morphology observed in certain mixed-halide perovskite compositions, and the limited operational stability of TrPeLEDs. The widespread adoption of OLEDs and PeLEDs will also rely on the ability to address them.

UEMLs suffer from exciton annihilation and higher TTA probability due to the high exciton concentration at the interface,[70] so higher efficiencies might be obtained by using spacers[101,202] or new TADF emitters with faster rISC.[203] With respect to film morphology, additive engineering[204] and the development of deposition techniques that promote uniform nucleation and growth (including blade-coating, slot-die coating, or vapor-based hybrid methods)[205] hold significant promise. For TrPeLEDs, evidence in this work suggested that the poor lifetime was caused by damage introduced during the deposition of the transparent cathode, so future strategies may include refining pulsed laser deposition parameters[67] or protective transparent interlayers to promote gentler cathode deposition.

Outside the results of this thesis, recent advances in alternative perovskite deposition techniques offer the potential to further simplify device fabrication, eliminating the need for co-evaporation.[206,207] Another important challenge is the presence of lead in the perovskites used in this work, whose toxicity raises environmental and health concerns that must be addressed before large-scale commercialization.[208] Promising strategies include the development of lead-free perovskite alternatives,[209] robust encapsulation methods to prevent leakage,[210] and recycling approaches to recover lead from discarded devices.[211]

In summary, continued progress in materials design and fabrication methods will be essential to overcome the remaining limitations and unlock the full potential of organic and perovskite emitters, enabling their key role in the next generation of optoelectronic devices.

Bibliography

(1) Edgar, R. S.; Green, E. W.; Zhao, Y.; van Ooijen, G.; Olmedo, M.; Qin, X.; Xu, Y.; Pan, M.; Valekunja, U. K.; Feeney, K. A.; Maywood, E. S.; Hastings, M. H.; Baliga, N. S.; Merrow, M.; Millar, A. J.; Johnson, C. H.; Kyriacou, C. P.; O'Neill, J. S.; Reddy, A. B. Peroxiredoxins Are Conserved Markers of Circadian Rhythms. *Nature* **2012**, *485* (7399), 459–464. https://doi.org/10.1038/nature11088.

(2) Bedrosian, T. A.; Nelson, R. J. Timing of Light Exposure Affects Mood and Brain Circuits. *Transl. Psychiatry* **2017**, *7* (1), e1017–e1017. https://doi.org/10.1038/tp.2016.262.

(3) Olajiga, O. K.; Ani, E. C.; Sikhakane, Z. Q.; Olatunde, T. M. A COMPREHENSIVE REVIEW OF ENERGY-EFFICIENT LIGHTING TECHNOLOGIES AND TRENDS. *Eng. Sci. Technol. J.* **2024**, *5* (3), 1097–1111. https://doi.org/10.51594/estj.v5i3.973.

(4) *Lighting*. IEA. https://www.iea.org/energy-system/buildings/lighting (accessed 2025-08-06).

(5) Balaram, V. Rare Earth Elements: A Review of Applications, Occurrence, Exploration, Analysis, Recycling, and Environmental Impact. *Geosci. Front.* **2019**, *10* (4), 1285–1303. https://doi.org/10.1016/j.gsf.2018.12.005.

(6) Bernanose, A.; Comte, M.; Vouaux, P. Sur un nouveau mode d'émission lumineuse chez certains composés organiques. *J. Chim. Phys.* **1953**, *50*, 64–68. https://doi.org/10.1051/jcp/1953500064.

(7) Tang, C. W.; VanSlyke, S. A. Organic Electroluminescent Diodes. *Appl. Phys. Lett.* **1987**, *51* (12), 913–915. https://doi.org/10.1063/1.98799.

(8) Xing, K. Z.; Fahlman, M.; Chen, X. W.; Inganäs, O.; Salaneck, W. R. The Electronic Structure of Poly(3,4-Ethylene-Dioxythiophene): Studied by XPS and UPS. *Synth. Met.* **1997**, *89* (3), 161–165. https://doi.org/10.1016/S0379-6779(97)81212-X.

(9) Cho, H.; Jeong, S.-H.; Park, M.-H.; Kim, Y.-H.; Wolf, C.; Lee, C.-L.; Heo, J. H.; Sadhanala, A.; Myoung, N.; Yoo, S.; Im, S. H.; Friend, R. H.; Lee, T.-W. Overcoming the Electroluminescence Efficiency Limitations of Perovskite Light-Emitting Diodes. *Science* **2015**, *350* (6265), 1222–1225. https://doi.org/10.1126/science.aad1818.

(10) Zhang, D.; Huang, T.; Duan, L. Emerging Self-Emissive Technologies for Flexible Displays. *Adv. Mater.* **2020**, *32* (15), 1902391. https://doi.org/10.1002/adma.201902391.

(11) Köhler, A.; Bässler, H. *Electronic Processes in Organic Semiconductors: An Introduction*; John Wiley & Sons, 2015.

(12) Ma, R. Organic Light-Emitting Diodes (OLEDS). In *Handbook of Visual Display Technology*; Springer, Berlin, Heidelberg, 2016; pp 1–22. https://doi.org/10.1007/978-3-642-35947-7_79-2.

(13) Thoms, T.; Okada, S.; Chen, J.-P.; Furugori, M. Improved Host Material Design for Phosphorescent Guest–Host Systems. *Thin Solid Films* **2003**, *436* (2), 264–268. https://doi.org/10.1016/S0040-6090(03)00569-8.

(14) Liu, J.; Shi, X.; Wu, X.; Wang, J.; Min, Z.; Wang, Y.; Yang, M.; Chen, C. H.; He, G. Achieving above 30% External Quantum Efficiency for Inverted Phosphorescence Organic Light-Emitting Diodes Based on Ultrathin Emitting Layer. *Org. Electron.* **2014**, *15* (10), 2492–2498. https://doi.org/10.1016/j.orgel.2014.07.027.

(15) Liu, B.; Xu, T.; Xu, X.; Wang, Y.; Sun, Y.; Li, Y. Energy Absorption Mechanism of Polyvinyl Butyral Laminated Windshield Subjected to Head Impact: Experiment and Numerical Simulations. *Int. J. Impact Eng.* **2016**, *90*, 26–36. https://doi.org/10.1016/j.ijimpeng.2015.11.010.

(16) Zhao, C.; Zhang, T.; Chen, J.; Yan, D.; Ma, D. High-Performance Hybrid White Organic Light-Emitting Diodes with Simple Emitting Structures and Low Efficiency Roll-off Based on Blue Thermally Activated Delayed Fluorescence Emitters with Bipolar Transport Characteristics. *J. Mater. Chem. C* **2018**, *6* (35), 9510–9516. https://doi.org/10.1039/C8TC02628A.

(17) Meng, L.; Wang, H.; Wei, X.; Liu, J.; Chen, Y.; Kong, X.; Lv, X.; Wang, P.; Wang, Y. Highly Efficient Nondoped Organic Light Emitting Diodes Based on Thermally Activated Delayed Fluorescence Emitter with Quantum-Well Structure. *ACS Appl. Mater. Interfaces* **2016**, *8* (32), 20955–20961. https://doi.org/10.1021/acsami.6b07563.

(18) Zhou, Y.; Gao, H.; Wang, J.; Yeung, F. S. Y.; Lin, S.; Li, X.; Liao, S.; Luo, D.; Kwok, H. S.; Liu, B. Organic Light-Emitting Diodes with Ultrathin Emitting Nanolayers. *Electronics* **2023**, *12* (14), 3164. https://doi.org/10.3390/electronics12143164.
(19) Qi, Y.; Hou, S.; Li, J.; Guo, H.; Yu, J. Highly Efficient Organic Light-Emitting Devices Employing an Ultrathin Non-Doped Phosphorescence Emitter within a Thermally Activated Delayed Fluorescence Interface Exciplex. *J. Lumin.* **2017**, *192*, 1242–1249. https://doi.org/10.1016/j.jlumin.2017.08.063.
(20) Kim, K.-H.; Moon, C.-K.; Lee, J.-H.; Kim, S.-Y.; Kim, J.-J. Highly Efficient Organic Light-Emitting Diodes with Phosphorescent Emitters Having High Quantum Yield and Horizontal Orientation of Transition Dipole Moments. *Adv. Mater.* **2014**, *26* (23), 3844–3847. https://doi.org/10.1002/adma.201305733.
(21) Hong, G.; Gan, X.; Leonhardt, C.; Zhang, Z.; Seibert, J.; Busch, J. M.; Bräse, S. A Brief History of OLEDs—Emitter Development and Industry Milestones. *Adv. Mater.* **2021**, *33* (9), 2005630. https://doi.org/10.1002/adma.202005630.
(22) Wang, D.; Zhang, Q. 2 - Fundamental Theories of TADF. In *Thermally Activated Delayed Fluorescence Organic Light-Emitting Diodes (TADF-OLEDs)*; Duan, L., Ed.; Woodhead Publishing, 2022; pp 71–89. https://doi.org/10.1016/B978-0-12-819810-0.00006-5.
(23) Sharpe, L. T.; Stockman, A.; Jagla, W.; Jägle, H. A Luminous Efficiency Function, V*(λ), for Daylight Adaptation. *J. Vis.* **2005**, *5* (11), 3. https://doi.org/10.1167/5.11.3.
(24) Zou, W.; Li, R.; Zhang, S.; Liu, Y.; Wang, N.; Cao, Y.; Miao, Y.; Xu, M.; Guo, Q.; Di, D.; Zhang, L.; Yi, C.; Gao, F.; Friend, R. H.; Wang, J.; Huang, W. Minimising Efficiency Roll-off in High-Brightness Perovskite Light-Emitting Diodes. *Nat. Commun.* **2018**, *9* (1), 608. https://doi.org/10.1038/s41467-018-03049-7.
(25) Wright, W. D. A Re-Determination of the Trichromatic Coefficients of the Spectral Colours. *Trans. Opt. Soc.* **1929**, *30* (4), 141. https://doi.org/10.1088/1475-4878/30/4/301.
(26) Guild, J.; Petavel, J. E. The Colorimetric Properties of the Spectrum. *Philos. Trans. R. Soc. Lond. Ser. Contain. Pap. Math. Phys. Character* **1997**, *230* (681–693), 149–187. https://doi.org/10.1098/rsta.1932.0005.
(27) Wang, Z.; Lyu, M.; Zhang, B. W.; Xiao, M.; Zhang, C.; Han, E.; Wang, L. Thermally Evaporated Metal Halide Perovskites and Their Analogues: Film Fabrication, Applications and Beyond. *Small Methods* **2025**, *9* (2), 2301633. https://doi.org/10.1002/smtd.202301633.
(28) Quan, L. N.; Rand, B. P.; Friend, R. H.; Mhaisalkar, S. G.; Lee, T.-W.; Sargent, E. H. Perovskites for Next-Generation Optical Sources. *Chem. Rev.* **2019**, *119* (12), 7444–7477. https://doi.org/10.1021/acs.chemrev.9b00107.
(29) Fu, Y.; Zhu, H.; Chen, J.; Hautzinger, M. P.; Zhu, X.-Y.; Jin, S. Metal Halide Perovskite Nanostructures for Optoelectronic Applications and the Study of Physical Properties. *Nat. Rev. Mater.* **2019**, *4* (3), 169–188. https://doi.org/10.1038/s41578-019-0080-9.
(30) Brenner, T. M.; Egger, D. A.; Kronik, L.; Hodes, G.; Cahen, D. Hybrid Organic—Inorganic Perovskites: Low-Cost Semiconductors with Intriguing Charge-Transport Properties. *Nat. Rev. Mater.* **2016**, *1* (1), 15007. https://doi.org/10.1038/natrevmats.2015.7.
(31) Valadares, F.; Guilhon, I.; Teles, L. K.; Marques, M. Electronic Structure Panorama of Halide Perovskites: Approximated DFT-1/2 Quasiparticle and Relativistic Corrections. *J. Phys. Chem. C* **2020**, *124* (34), 18390–18400. https://doi.org/10.1021/acs.jpcc.0c03672.
(32) Hwang, S.; Kim, W.; Kim, K.; Ko, M. J. Theoretical Studies on the Electronic Structures of Halide Perovskites: A Critical Review. *Korean J. Chem. Eng.* **2024**, *41* (14), 3737–3749. https://doi.org/10.1007/s11814-024-00336-6.
(33) Lee, J.-H.; Bristowe, N. C.; Lee, J. H.; Lee, S.-H.; Bristowe, P. D.; Cheetham, A. K.; Jang, H. M. Resolving the Physical Origin of Octahedral Tilting in Halide Perovskites. *Chem. Mater.* **2016**, *28* (12), 4259–4266. https://doi.org/10.1021/acs.chemmater.6b00968.
(34) Umebayashi, T.; Asai, K.; Kondo, T.; Nakao, A. Electronic Structures of Lead Iodide Based Low-Dimensional Crystals. *Phys. Rev. B* **2003**, *67* (15), 155405. https://doi.org/10.1103/PhysRevB.67.155405.
(35) Boyer-Richard, S.; Katan, C.; Traoré, B.; Scholz, R.; Jancu, J.-M.; Even, J. Symmetry-Based Tight Binding Modeling of Halide Perovskite Semiconductors. *J. Phys. Chem. Lett.* **2016**, *7* (19), 3833–3840. https://doi.org/10.1021/acs.jpclett.6b01749.

(36) du Fossé, I.; Mulder, J. T.; Almeida, G.; Spruit, A. G. M.; Infante, I.; Grozema, F. C.; Houtepen, A. J. Limits of Defect Tolerance in Perovskite Nanocrystals: Effect of Local Electrostatic Potential on Trap States. *J. Am. Chem. Soc.* **2022**, *144* (25), 11059–11063. https://doi.org/10.1021/jacs.2c02027.
(37) Zakutayev, A.; Caskey, C. M.; Fioretti, A. N.; Ginley, D. S.; Vidal, J.; Stevanovic, V.; Tea, E.; Lany, S. Defect Tolerant Semiconductors for Solar Energy Conversion. *J. Phys. Chem. Lett.* **2014**, *5* (7), 1117–1125. https://doi.org/10.1021/jz5001787.
(38) Kovalenko, M. V.; Protesescu, L.; Bodnarchuk, M. I. Properties and Potential Optoelectronic Applications of Lead Halide Perovskite Nanocrystals. *Science* **2017**, *358* (6364), 745–750. https://doi.org/10.1126/science.aam7093.
(39) Maculan, G.; Sheikh, A. D.; Abdelhady, A. L.; Saidaminov, M. I.; Haque, M. A.; Murali, B.; Alarousu, E.; Mohammed, O. F.; Wu, T.; Bakr, O. M. CH3NH3PbCl3 Single Crystals: Inverse Temperature Crystallization and Visible-Blind UV-Photodetector. *J. Phys. Chem. Lett.* **2015**, *6* (19), 3781–3786. https://doi.org/10.1021/acs.jpclett.5b01666.
(40) Matsushima, T.; Bencheikh, F.; Komino, T.; Leyden, M. R.; Sandanayaka, A. S. D.; Qin, C.; Adachi, C. High Performance from Extraordinarily Thick Organic Light-Emitting Diodes. *Nature* **2019**, *572* (7770), 502–506. https://doi.org/10.1038/s41586-019-1435-5.
(41) Stranks, S. D.; Eperon, G. E.; Grancini, G.; Menelaou, C.; Alcocer, M. J. P.; Leijtens, T.; Herz, L. M.; Petrozza, A.; Snaith, H. J. Electron-Hole Diffusion Lengths Exceeding 1 Micrometer in an Organometal Trihalide Perovskite Absorber. *Science* **2013**, *342* (6156), 341–344. https://doi.org/10.1126/science.1243982.
(42) Stoumpos, C. C.; Malliakas, C. D.; Kanatzidis, M. G. Semiconducting Tin and Lead Iodide Perovskites with Organic Cations: Phase Transitions, High Mobilities, and Near-Infrared Photoluminescent Properties. *Inorg. Chem.* **2013**, *52* (15), 9019–9038. https://doi.org/10.1021/ic401215x.
(43) Protesescu, L.; Yakunin, S.; Bodnarchuk, M. I.; Krieg, F.; Caputo, R.; Hendon, C. H.; Yang, R. X.; Walsh, A.; Kovalenko, M. V. Nanocrystals of Cesium Lead Halide Perovskites (CsPbX3, X = Cl, Br, and I): Novel Optoelectronic Materials Showing Bright Emission with Wide Color Gamut. *Nano Lett.* **2015**, *15* (6), 3692–3696. https://doi.org/10.1021/nl5048779.
(44) Dey, A.; Ye, J.; De, A.; Debroye, E.; Ha, S. K.; Bladt, E.; Kshirsagar, A. S.; Wang, Z.; Yin, J.; Wang, Y.; Quan, L. N.; Yan, F.; Gao, M.; Li, X.; Shamsi, J.; Debnath, T.; Cao, M.; Scheel, M. A.; Kumar, S.; Steele, J. A.; Gerhard, M.; Chouhan, L.; Xu, K.; Wu, X.; Li, Y.; Zhang, Y.; Dutta, A.; Han, C.; Vincon, I.; Rogach, A. L.; Nag, A.; Samanta, A.; Korgel, B. A.; Shih, C.-J.; Gamelin, D. R.; Son, D. H.; Zeng, H.; Zhong, H.; Sun, H.; Demir, H. V.; Scheblykin, I. G.; Mora-Seró, I.; Stolarczyk, J. K.; Zhang, J. Z.; Feldmann, J.; Hofkens, J.; Luther, J. M.; Pérez-Prieto, J.; Li, L.; Manna, L.; Bodnarchuk, M. I.; Kovalenko, M. V.; Roeffaers, M. B. J.; Pradhan, N.; Mohammed, O. F.; Bakr, O. M.; Yang, P.; Müller-Buschbaum, P.; Kamat, P. V.; Bao, Q.; Zhang, Q.; Krahne, R.; Galian, R. E.; Stranks, S. D.; Bals, S.; Biju, V.; Tisdale, W. A.; Yan, Y.; Hoye, R. L. Z.; Polavarapu, L. State of the Art and Prospects for Halide Perovskite Nanocrystals. *ACS Nano* **2021**, *15* (7), 10775–10981. https://doi.org/10.1021/acsnano.0c08903.
(45) Li, M.; Begum, R.; Fu, J.; Xu, Q.; Koh, T. M.; Veldhuis, S. A.; Grätzel, M.; Mathews, N.; Mhaisalkar, S.; Sum, T. C. Low Threshold and Efficient Multiple Exciton Generation in Halide Perovskite Nanocrystals. *Nat. Commun.* **2018**, *9* (1), 4197. https://doi.org/10.1038/s41467-018-06596-1.
(46) Kim, Y.-H.; Cho, H.; Lee, T.-W. Metal Halide Perovskite Light Emitters. *Proc. Natl. Acad. Sci.* **2016**, *113* (42), 11694–11702. https://doi.org/10.1073/pnas.1607471113.
(47) Ma, C.; Ni, M.; Liu, X.; Zhan, K.; Chen, M.; Li, S.; Li, F.; Wang, H.; Dang, Y. Recent Progress in Perovskite Light-Emitting Diodes with High External Quantum Efficiency and Stability. *CrystEngComm* **2025**, *27* (23), 3853–3876. https://doi.org/10.1039/D5CE00222B.
(48) Sun, S.-Q.; Tai, J.-W.; He, W.; Yu, Y.-J.; Feng, Z.-Q.; Sun, Q.; Tong, K.-N.; Shi, K.; Liu, B.-C.; Zhu, M.; Wei, G.; Fan, J.; Xie, Y.-M.; Liao, L.-S.; Fung, M.-K. Enhancing Light Outcoupling Efficiency via Anisotropic Low Refractive Index Electron Transporting Materials for Efficient Perovskite Light-Emitting Diodes. *Adv. Mater.* **2024**, *36* (24), 2400421. https://doi.org/10.1002/adma.202400421.
(49) Jiang, P.; Miao, J.; Cao, X.; Xia, H.; Pan, K.; Hua, T.; Lv, X.; Huang, Z.; Zou, Y.; Yang, C. Quenching-Resistant Multiresonance TADF Emitter Realizes 40% External Quantum Efficiency in Narrowband Electroluminescence at High Doping Level. *Adv. Mater.* **2022**, *34* (3), 2106954. https://doi.org/10.1002/adma.202106954.

(50) Kim, J. S.; Heo, J.-M.; Park, G.-S.; Woo, S.-J.; Cho, C.; Yun, H. J.; Kim, D.-H.; Park, J.; Lee, S.-C.; Park, S.-H.; Yoon, E.; Greenham, N. C.; Lee, T.-W. Ultra-Bright, Efficient and Stable Perovskite Light-Emitting Diodes. *Nature* **2022**, *611* (7937), 688–694. https://doi.org/10.1038/s41586-022-05304-w.

(51) Gerhardt, J.; Miller, M. E.; Yoo, H.; Akhavan, T.; Miller, M. E.; Yoo, H.; Akhavan, T. Estimating OLED Display Device Lifetime from Pixel and Screen Brightness and Its Application. *Color Imaging Conf.* **2019**, *27*, 331–338. https://doi.org/10.2352/issn.2169-2629.2019.27.60.

(52) Tian, Y.; Ling, Y.; Shu, Y.; Zhou, C.; Besara, T.; Siegrist, T.; Gao, H.; Ma, B. A Solution-Processed Organometal Halide Perovskite Hole Transport Layer for Highly Efficient Organic Light-Emitting Diodes. *Adv. Electron. Mater.* **2016**, *2* (7), 1600165. https://doi.org/10.1002/aelm.201600165.

(53) Zhang, Y.; Yu, F.-X.; Ma, X.-J.; Xiong, Z.-Y.; Wang, Z.-Q.; Chen, P.; Xiong, Z.-H.; Gao, C.-H. Efficient Red Phosphorescent Organic Light Emitting Diodes Based on Solution Processed All-Inorganic Cesium Lead Halide Perovskite as Hole Transporting Layer. *Org. Electron.* **2017**, *50*, 411–417. https://doi.org/10.1016/j.orgel.2017.08.015.

(54) Xu, Q.-Y.; Yuan, D.-X.; Mu, H.-R.; Igbari, F.; Bao, Q.; Liao, L.-S. Efficiency Enhancement of Perovskite Solar Cells by Pumping Away the Solvent of Precursor Film Before Annealing. *Nanoscale Res. Lett.* **2016**, *11* (1), 248. https://doi.org/10.1186/s11671-016-1467-9.

(55) Feng, Y.; Xu, J.; Shan, H.; Dong, L.; Sun, X.; Hu, Q.; Wang, Y.; Roy, V. A. L.; Xu, Z.-X. Organometal Halide Perovskite as Hole Injection Enhancer in Organic Light-Emitting Diode. *Org. Electron.* **2017**, *51*, 257–263. https://doi.org/10.1016/j.orgel.2017.09.027.

(56) Ahn, N.; Son, D.-Y.; Jang, I.-H.; Kang, S. M.; Choi, M.; Park, N.-G. Highly Reproducible Perovskite Solar Cells with Average Efficiency of 18.3% and Best Efficiency of 19.7% Fabricated via Lewis Base Adduct of Lead(II) Iodide. *J. Am. Chem. Soc.* **2015**, *137* (27), 8696–8699. https://doi.org/10.1021/jacs.5b04930.

(57) Zhou, T.; Liu, C.; Gong, S.; Xiang, Y.; Xie, G.; Yang, C. Boosting the Electroluminescence Efficiency of Solution-Processed Thermally Activated Delayed Fluorescence OLEDs with a Versatile Hole-Transporting Layer of Organic–Inorganic Hybrid Perovskite. *J. Mater. Chem. C* **2018**, *6* (23), 6305–6311. https://doi.org/10.1039/C8TC01567H.

(58) Jeon, N. J.; Noh, J. H.; Kim, Y. C.; Yang, W. S.; Ryu, S.; Seok, S. I. Solvent Engineering for High-Performance Inorganic–Organic Hybrid Perovskite Solar Cells. *Nat. Mater.* **2014**, *13* (9), 897–903. https://doi.org/10.1038/nmat4014.

(59) Park, M.-H.; Jeong, S.-H.; Seo, H.-K.; Wolf, C.; Kim, Y.-H.; Kim, H.; Byun, J.; Kim, J. S.; Cho, H.; Lee, T.-W. Unravelling Additive-Based Nanocrystal Pinning for High Efficiency Organic-Inorganic Halide Perovskite Light-Emitting Diodes. *Nano Energy* **2017**, *42*, 157–165. https://doi.org/10.1016/j.nanoen.2017.10.012.

(60) Xiao, Z.; Kerner, R. A.; Zhao, L.; Tran, N. L.; Lee, K. M.; Koh, T.-W.; Scholes, G. D.; Rand, B. P. Efficient Perovskite Light-Emitting Diodes Featuring Nanometre-Sized Crystallites. *Nat. Photonics* **2017**, *11* (2), 108–115. https://doi.org/10.1038/nphoton.2016.269.

(61) Xiao, Z.; Zhao, L.; Tran, N. L.; Lin, Y. L.; Silver, S. H.; Kerner, R. A.; Yao, N.; Kahn, A.; Scholes, G. D.; Rand, B. P. Mixed-Halide Perovskites with Stabilized Bandgaps. *Nano Lett.* **2017**, *17* (11), 6863–6869. https://doi.org/10.1021/acs.nanolett.7b03179.

(62) Park, S. M.; Abtahi, A.; Boehm, A. M.; Graham, K. R. Surface Ligands for Methylammonium Lead Iodide Films: Surface Coverage, Energetics, and Photovoltaic Performance. *ACS Energy Lett.* **2020**, *5* (3), 799–806. https://doi.org/10.1021/acsenergylett.0c00054.

(63) Schmidt, L. C.; Pertegás, A.; González-Carrero, S.; Malinkiewicz, O.; Agouram, S.; Mínguez Espallargas, G.; Bolink, H. J.; Galian, R. E.; Pérez-Prieto, J. Nontemplate Synthesis of CH3NH3PbBr3 Perovskite Nanoparticles. *J. Am. Chem. Soc.* **2014**, *136* (3), 850–853. https://doi.org/10.1021/ja4109209.

(64) Zhao, L.; Yeh, Y.-W.; Tran, N. L.; Wu, F.; Xiao, Z.; Kerner, R. A.; Lin, Y. L.; Scholes, G. D.; Yao, N.; Rand, B. P. In Situ Preparation of Metal Halide Perovskite Nanocrystal Thin Films for Improved Light-Emitting Devices. *ACS Nano* **2017**, *11* (4), 3957–3964. https://doi.org/10.1021/acsnano.7b00404.

(65) Chin, S.-H.; Cortecchia, D.; Forzatti, M.; Wu, C.-S.; Alvarado-Leaños, A. L.; Folpini, G.; Treglia, A.; Kalluvila Justin, I. A.; Paliwal, A.; Cho, C.; Roldán-Carmona, C.; Sessolo, M.; Petrozza, A.; Bolink, H. J. Stabilizing Single-Source Evaporated Perovskites with Organic Interlayers for Amplified Spontaneous Emission. *Adv. Opt. Mater.* **2024**, *12* (13), 2302701. https://doi.org/10.1002/adom.202302701.

(66) Zanoni, K. P. S.; Pérez-del-Rey, D.; Dreessen, C.; Rodkey, N.; Sessolo, M.; Soltanpoor, W.; Morales-Masis, M.; Bolink, H. J. Tin(IV) Oxide Electron Transport Layer via Industrial-Scale Pulsed Laser Deposition for Planar Perovskite Solar Cells. *ACS Appl. Mater. Interfaces* **2023**, *15* (27), 32621–32628. https://doi.org/10.1021/acsami.3c04387.
(67) Zanoni, K. P. S.; Paliwal, A.; Hernández-Fenollosa, M. A.; Repecaud, P.-A.; Morales-Masis, M.; Bolink, H. J. ITO Top-Electrodes via Industrial-Scale PLD for Efficient Buffer-Layer-Free Semitransparent Perovskite Solar Cells. *Adv. Mater. Technol.* **2022**, *7* (10), 2101747. https://doi.org/10.1002/admt.202101747.
(68) *OLED Display Fundamentals and Applications*, 1st ed.; John Wiley & Sons, Ltd, 2017. https://doi.org/10.1002/9781119187493.
(69) Nanda, G. P.; Sk, B.; Yadav, N.; Rajamanickam, S.; Deori, U.; Mahashaya, R.; Zysman-Colman, E.; Rajamalli, P. Ultrathin Non-Doped Thermally Activated Delayed Fluorescence Emitting Layer for Highly Efficient OLEDs. *Chem. Commun.* **2021**, *57* (100), 13728–13731. https://doi.org/10.1039/D1CC04972K.
(70) Wu, S.; Li, S.; Sun, Q.; Huang, C.; Fung, M.-K. Highly Efficient White Organic Light-Emitting Diodes with Ultrathin Emissive Layers and a Spacer-Free Structure. *Sci. Rep.* **2016**, *6* (1), 25821. https://doi.org/10.1038/srep25821.
(71) Yamamori, A.; Adachi, C.; Koyama, T.; Taniguchi, Y. Doped Organic Light Emitting Diodes Having a 650-Nm-Thick Hole Transport Layer. *Appl. Phys. Lett.* **1998**, *72* (17), 2147–2149. https://doi.org/10.1063/1.121304.
(72) Woo, J. Y.; Park, M.-H.; Jeong, S.-H.; Kim, Y.-H.; Kim, B.; Lee, T.-W.; Han, T.-H. Advances in Solution-Processed OLEDs and Their Prospects for Use in Displays. *Adv. Mater.* **2023**, *35* (43), 2207454. https://doi.org/10.1002/adma.202207454.
(73) Kang, J.; Wang, K. Inkjet Printing of Amorphous Indium Aluminum Oxide Active Layers for High-Performance Thin-Film Transistors. *Sci. Rep.* **2025**, *15* (1), 19471. https://doi.org/10.1038/s41598-025-04896-3.
(74) Aizawa, N.; Pu, Y.-J.; Watanabe, M.; Chiba, T.; Ideta, K.; Toyota, N.; Igarashi, M.; Suzuri, Y.; Sasabe, H.; Kido, J. Solution-Processed Multilayer Small-Molecule Light-Emitting Devices with High-Efficiency White-Light Emission. *Nat. Commun.* **2014**, *5* (1), 5756. https://doi.org/10.1038/ncomms6756.
(75) Sun, D.; Duda, E.; Fan, X.; Saxena, R.; Zhang, M.; Bagnich, S.; Zhang, X.; Köhler, A.; Zysman-Colman, E. Thermally Activated Delayed Fluorescent Dendrimers That Underpin High-Efficiency Host-Free Solution-Processed Organic Light-Emitting Diodes. *Adv. Mater.* **2022**, *34* (23), 2110344. https://doi.org/10.1002/adma.202110344.
(76) Zhang, S.; Tang, M.-C.; Nguyen, N. V.; Anthopoulos, T. D.; Hacker, C. A. Wide-Band-Gap Mixed-Halide 3D Perovskites: Electronic Structure and Halide Segregation Investigation. *ACS Appl. Electron. Mater.* **2021**, *3* (5), 2277–2285. https://doi.org/10.1021/acsaelm.1c00191.
(77) Ahn, N.; Kwak, K.; Jang, M. S.; Yoon, H.; Lee, B. Y.; Lee, J.-K.; Pikhitsa, P. V.; Byun, J.; Choi, M. Trapped Charge-Driven Degradation of Perovskite Solar Cells. *Nat. Commun.* **2016**, *7* (1), 13422. https://doi.org/10.1038/ncomms13422.
(78) Ganose, A. M.; Scanlon, D. O.; Walsh, A.; Hoye, R. L. Z. The Defect Challenge of Wide-Bandgap Semiconductors for Photovoltaics and Beyond. *Nat. Commun.* **2022**, *13* (1), 4715. https://doi.org/10.1038/s41467-022-32131-4.
(79) Liao, Y.; Tian, N.; Wang, J.; Yao, D.; Zheng, G.; Zhou, B.; Yang, Y.; Long, F. Performance Enhancement of Evaporated CsPbI2Br Perovskite Solar Cells with a CuSCN Hole Transport Layer via a Cesium Bromide Buffer Layer. *ACS Appl. Energy Mater.* **2022**, *5* (8), 9542–9548. https://doi.org/10.1021/acsaem.2c01155.
(80) Adachi, C.; Baldo, M. A.; Thompson, M. E.; Forrest, S. R. Nearly 100% Internal Phosphorescence Efficiency in an Organic Light-Emitting Device. *J. Appl. Phys.* **2001**, *90* (10), 5048–5051. https://doi.org/10.1063/1.1409582.
(81) Hung, W.-Y.; Fang, G.-C.; Chang, Y.-C.; Kuo, T.-Y.; Chou, P.-T.; Lin, S.-W.; Wong, K.-T. Highly Efficient Bilayer Interface Exciplex For Yellow Organic Light-Emitting Diode. *ACS Appl. Mater. Interfaces* **2013**, *5* (15), 6826–6831. https://doi.org/10.1021/am402032z.
(82) Lee, J.-H.; Cheng, S.-H.; Yoo, S.-J.; Shin, H.; Chang, J.-H.; Wu, C.-I.; Wong, K.-T.; Kim, J.-J. An Exciplex Forming Host for Highly Efficient Blue Organic Light Emitting Diodes with Low Driving Voltage. *Adv. Funct. Mater.* **2015**, *25* (3), 361–366. https://doi.org/10.1002/adfm.201402707.

(83) Zhou, D.-Y.; Zamani Siboni, H.; Wang, Q.; Liao, L.-S.; Aziz, H. Host to Guest Energy Transfer Mechanism in Phosphorescent and Fluorescent Organic Light-Emitting Devices Utilizing Exciplex-Forming Hosts. *J. Phys. Chem. C* **2014**, *118* (41), 24006–24012. https://doi.org/10.1021/jp508228z.
(84) Liehm, P.; Murawski, C.; Furno, M.; Lüssem, B.; Leo, K.; Gather, M. C. Comparing the Emissive Dipole Orientation of Two Similar Phosphorescent Green Emitter Molecules in Highly Efficient Organic Light-Emitting Diodes. *Appl. Phys. Lett.* **2012**, *101* (25), 253304. https://doi.org/10.1063/1.4773188.
(85) Ahmad, M.; Rehman, G.; Ali, L.; Shafiq, M.; Iqbal, R.; Ahmad, R.; Khan, T.; Jalali-Asadabadi, S.; Maqbool, M.; Ahmad, I. Structural, Electronic and Optical Properties of CsPbX3 (X=Cl, Br, I) for Energy Storage and Hybrid Solar Cell Applications. *J. Alloys Compd.* **2017**, *705*, 828–839. https://doi.org/10.1016/j.jallcom.2017.02.147.
(86) Meng, G.; Feng, Y.; Song, X.; Shi, Y.; Ji, M.; Xue, Y.; Hao, C. Theoretical Insight into the Carrier Mobility Anisotropy of Organic-Inorganic Perovskite CH3NH3PbI3. *J. Electroanal. Chem.* **2018**, *810*, 11–17. https://doi.org/10.1016/j.jelechem.2017.12.069.
(87) Tailor, N. K.; Satapathi, S. Anisotropy in Perovskite Single Crystals: From Fundamentals to Applications. *J. Phys. Chem. C* **2022**, *126* (42), 17789–17803. https://doi.org/10.1021/acs.jpcc.2c05534.
(88) Miao, Y.; Yin, M. Recent Progress on Organic Light-Emitting Diodes with Phosphorescent Ultrathin (<1nm) Light-Emitting Layers. *iScience* **2022**, *25* (2), 103804. https://doi.org/10.1016/j.isci.2022.103804.
(89) Zhong, P.-L.; Zheng, C.-J.; Zhang, M.; Zhao, J.-W.; Yang, H.-Y.; He, Z.-Y.; Lin, H.; Tao, S.-L.; Zhang, X.-H. Highly Efficient Ternary Polymer-Based Solution-Processable Exciplex with over 20% External Quantum Efficiency in Organic Light-Emitting Diode. *Org. Electron.* **2020**, *76*, 105449. https://doi.org/10.1016/j.orgel.2019.105449.
(90) Sarma, M.; Wong, K.-T. Exciplex: An Intermolecular Charge-Transfer Approach for TADF. *ACS Appl. Mater. Interfaces* **2018**, *10* (23), 19279–19304. https://doi.org/10.1021/acsami.7b18318.
(91) Buckley, A. *Organic Light-Emitting Diodes (OLEDs): Materials, Devices and Applications*; Elsevier, 2013.
(92) Huseynova, G.; Lee, J.-H.; Kim, Y. H.; Lee, J. Transparent Organic Light-Emitting Diodes: Advances, Prospects, and Challenges. *Adv. Opt. Mater.* **2021**, *9* (14), 2002040. https://doi.org/10.1002/adom.202002040.
(93) Tak, Y.-H.; Kim, K.-B.; Park, H.-G.; Lee, K.-H.; Lee, J.-R. Criteria for ITO (Indium–Tin-Oxide) Thin Film as the Bottom Electrode of an Organic Light Emitting Diode. *Thin Solid Films* **2002**, *411* (1), 12–16. https://doi.org/10.1016/S0040-6090(02)00165-7.
(94) Gu, G.; Bulović, V.; Burrows, P. E.; Forrest, S. R.; Thompson, M. E. Transparent Organic Light Emitting Devices. *Appl. Phys. Lett.* **1996**, *68* (19), 2606–2608. https://doi.org/10.1063/1.116196.
(95) Hsieh, T.-C.; Shih, C.-Y.; Chao, Y.-C.; Cheng, I.-C.; Chen, J.-Z. Improved Efficiency and Air Stability of Two-Dimensional p-i-n Inverted Perovskite Solar Cells by Cs Doping. *RSC Adv.* **2021**, *11* (33), 20200–20206. https://doi.org/10.1039/D1RA02574K.
(96) Yang, C.; Liu, D.; Bates, M.; Barr, M. C.; Lunt, R. R. How to Accurately Report Transparent Solar Cells. *Joule* **2019**, *3* (8), 1803–1809. https://doi.org/10.1016/j.joule.2019.06.005.
(97) Traverse, C. J.; Pandey, R.; Barr, M. C.; Lunt, R. R. Emergence of Highly Transparent Photovoltaics for Distributed Applications. *Nat. Energy* **2017**, *2* (11), 849–860. https://doi.org/10.1038/s41560-017-0016-9.
(98) Yamasaki, T.; Sumioka, K.; Tsutsui, T. Organic Light-Emitting Device with an Ordered Monolayer of Silica Microspheres as a Scattering Medium. *Appl. Phys. Lett.* **2000**, *76* (10), 1243–1245. https://doi.org/10.1063/1.125997.
(99) Mardegan, L.; Paliwal, A.; Zanoni, K. P. S.; Tordera, D.; Bolink, H. J. Transparent Light-Emitting Electrochemical Cells. *Adv. Opt. Mater.* **2022**, *10* (24), 2201953. https://doi.org/10.1002/adom.202201953.
(100) Wu, T.-L.; Lei, J.; Hsieh, C.-M.; Chen, Y.-K.; Huang, P.-Y.; Lai, P.-T.; Chou, T.-Y.; Lin, W.-C.; Chen, W.; Yu, C.-H.; Hsu, L.-Y.; Lin, H.-W.; Cheng, C.-H. Substituent Engineering of the Diboron Molecular Architecture for a Nondoped and Ultrathin Emitting Layer. *Chem. Sci.* **2022**, *13* (44), 12996–13005. https://doi.org/10.1039/D2SC04725J.

(101) Zhao, Y.; Chen, J.; Ma, D. Ultrathin Nondoped Emissive Layers for Efficient and Simple Monochrome and White Organic Light-Emitting Diodes. *ACS Appl. Mater. Interfaces* **2013**, *5* (3), 965–971. https://doi.org/10.1021/am3026097.
(102) Dai, X.; Yao, F.; Li, J.; Yu, H.; Cao, J. Color-Stable Non-Doped White Phosphorescent Organic Light-Emitting Diodes Based on Ultrathin Emissive Layers. *J. Phys. Appl. Phys.* **2019**, *53* (5), 055106. https://doi.org/10.1088/1361-6463/ab5698.
(103) Tsai, W.-L.; Huang, M.-H.; Lee, W.-K.; Hsu, Y.-J.; Pan, K.-C.; Huang, Y.-H.; Ting, H.-C.; Sarma, M.; Ho, Y.-Y.; Hu, H.-C.; Chen, C.-C.; Lee, M.-T.; Wong, K.-T.; Wu, C.-C. A Versatile Thermally Activated Delayed Fluorescence Emitter for Both Highly Efficient Doped and Non-Doped Organic Light Emitting Devices. *Chem. Commun.* **2015**, *51* (71), 13662–13665. https://doi.org/10.1039/C5CC05022G.
(104) Kahle, F.-J.; Rudnick, A.; Bässler, H.; Köhler, A. How to Interpret Absorption and Fluorescence Spectra of Charge Transfer States in an Organic Solar Cell. *Mater. Horiz.* **2018**, *5* (5), 837–848. https://doi.org/10.1039/C8MH00564H.
(105) Bartels, W. J. Characterization of Thin Layers on Perfect Crystals with a Multipurpose High Resolution X-ray Diffractometer. *J. Vac. Sci. Technol. B Microelectron. Process. Phenom.* **1983**, *1* (2), 338–345. https://doi.org/10.1116/1.582553.
(106) El Ajjouri, Y.; Palazon, F.; Sessolo, M.; Bolink, H. J. Single-Source Vacuum Deposition of Mechanosynthesized Inorganic Halide Perovskites. *Chem. Mater.* **2018**, *30* (21), 7423–7427. https://doi.org/10.1021/acs.chemmater.8b03352.
(107) Ullah, S.; Yang, P.; Li, Y.; Wang, J.; Liu, L.; Mahmood, R.; Yang, S.-E.; Xia, T.; Guo, H.; Chen, Y. Two Step Vapor-Processing and Experimental Investigations of All-Inorganic CsPbCl3 Perovskite Films for Optoelectronic Applications. *Mater. Lett.* **2021**, *294*, 129819. https://doi.org/10.1016/j.matlet.2021.129819.
(108) Rodkey, N.; Kaal, S.; Sebastia-Luna, P.; Birkhölzer, Y. A.; Ledinsky, M.; Palazon, F.; Bolink, H. J.; Morales-Masis, M. Pulsed Laser Deposition of Cs2AgBiBr6: From Mechanochemically Synthesized Powders to Dry, Single-Step Deposition. *Chem. Mater.* **2021**, *33* (18), 7417–7422. https://doi.org/10.1021/acs.chemmater.1c02054.
(109) Sculley, J.; Kowkabany, J.; LaFollette, D. K.; Perini, C.; Xin, Y.; Correa-Baena, J.-P.; Gao, H. Super-Bandgap Electroluminescence from Cesium Lead Bromide. arXiv October 13, 2024. https://doi.org/10.48550/arXiv.2410.09702.
(110) Zhang, T.; Yang, M.; Benson, E. E.; Li, Z.; Lagemaat, J. van de; Luther, J. M.; Yan, Y.; Zhu, K.; Zhao, Y. A Facile Solvothermal Growth of Single Crystal Mixed Halide Perovskite CH3NH3Pb(Br1−xClx)3. *Chem. Commun.* **2015**, *51* (37), 7820–7823. https://doi.org/10.1039/C5CC01835H.
(111) Levchuk, I.; Osvet, A.; Tang, X.; Brandl, M.; Perea, J. D.; Hoegl, F.; Matt, G. J.; Hock, R.; Batentschuk, M.; Brabec, C. J. Brightly Luminescent and Color-Tunable Formamidinium Lead Halide Perovskite FAPbX3 (X = Cl, Br, I) Colloidal Nanocrystals. *Nano Lett.* **2017**, *17* (5), 2765–2770. https://doi.org/10.1021/acs.nanolett.6b04781.
(112) Karlsson, M.; Yi, Z.; Reichert, S.; Luo, X.; Lin, W.; Zhang, Z.; Bao, C.; Zhang, R.; Bai, S.; Zheng, G.; Teng, P.; Duan, L.; Lu, Y.; Zheng, K.; Pullerits, T.; Deibel, C.; Xu, W.; Friend, R.; Gao, F. Mixed Halide Perovskites for Spectrally Stable and High-Efficiency Blue Light-Emitting Diodes. *Nat. Commun.* **2021**, *12* (1), 361. https://doi.org/10.1038/s41467-020-20582-6.
(113) Zou, Y.; Yuan, Z.; Bai, S.; Gao, F.; Sun, B. Recent Progress toward Perovskite Light-Emitting Diodes with Enhanced Spectral and Operational Stability. *Mater. Today Nano* **2019**, *5*, 100028. https://doi.org/10.1016/j.mtnano.2019.100028.
(114) Bai, W.; Xuan, T.; Zhao, H.; Dong, H.; Cheng, X.; Wang, L.; Xie, R.-J. Perovskite Light-Emitting Diodes with an External Quantum Efficiency Exceeding 30%. *Adv. Mater.* **2023**, *35* (39), 2302283. https://doi.org/10.1002/adma.202302283.
(115) Yao, J.; Huang, Y.; Sun, H.; Wang, Z.; Xue, J.; Huang, Z.; Dong, S.-C.; Chen, X.; Lu, H. Efficient Spin-Light-Emitting Diodes With Tunable Red to Near-Infrared Emission at Room Temperature. *Adv. Mater. n/a* (n/a), 2413669. https://doi.org/10.1002/adma.202413669.
(116) Vashishtha, P.; Halpert, J. E. Field-Driven Ion Migration and Color Instability in Red-Emitting Mixed Halide Perovskite Nanocrystal Light-Emitting Diodes. *Chem. Mater.* **2017**, *29* (14), 5965–5973. https://doi.org/10.1021/acs.chemmater.7b01609.
(117) Ruth, A.; Brennan, M. C.; Draguta, S.; Morozov, Y. V.; Zhukovskyi, M.; Janko, B.; Zapol, P.; Kuno, M. Vacancy-Mediated Anion Photosegregation Kinetics in Mixed Halide Hybrid Perovskites: Coupled

Kinetic Monte Carlo and Optical Measurements. *ACS Energy Lett.* **2018**, *3* (10), 2321–2328. https://doi.org/10.1021/acsenergylett.8b01369.
(118) Xiong, W.; Tang, W.; Zhang, G.; Yang, Y.; Fan, Y.; Zhou, K.; Zou, C.; Zhao, B.; Di, D. Controllable P- and n-Type Behaviours in Emissive Perovskite Semiconductors. *Nature* **2024**, *633* (8029), 344–350. https://doi.org/10.1038/s41586-024-07792-4.
(119) Roy, M.; Vikram; Banerjee, S.; Mitra, A.; Alam, A.; Aslam, M. Composition-Controlled Synthesis of Hybrid Perovskite Nanoparticles by Ionic Metathesis: Bandgap Engineering Studies from Experiments and Theoretical Calculations. *Chem. – Eur. J.* **2019**, *25* (42), 9892–9901. https://doi.org/10.1002/chem.201805859.
(120) Jong, U.-G.; Yu, C.-J.; Ri, J.-S.; Kim, N.-H.; Ri, G.-C. Influence of Halide Composition on the Structural, Electronic, and Optical Properties of Mixed CH3NH3Pb(I1-xBrx)3 Perovskites Calculated Using the Virtual Crystal Approximation Method. *Phys. Rev. B* **2016**, *94* (12), 125139. https://doi.org/10.1103/PhysRevB.94.125139.
(121) Marongiu, D.; Saba, M.; Quochi, F.; Mura, A.; Bongiovanni, G. The Role of Excitons in 3D and 2D Lead Halide Perovskites. *J. Mater. Chem. C* **2019**, *7* (39), 12006–12018. https://doi.org/10.1039/C9TC04292J.
(122) Comin, R.; Walters, G.; Thibau, E. S.; Voznyy, O.; Lu, Z.-H.; Sargent, E. H. Structural, Optical, and Electronic Studies of Wide-Bandgap Lead Halide Perovskites. *J. Mater. Chem. C* **2015**, *3* (34), 8839–8843. https://doi.org/10.1039/C5TC01718A.
(123) Akkerman, Q. A.; D'Innocenzo, V.; Accornero, S.; Scarpellini, A.; Petrozza, A.; Prato, M.; Manna, L. Tuning the Optical Properties of Cesium Lead Halide Perovskite Nanocrystals by Anion Exchange Reactions. *J. Am. Chem. Soc.* **2015**, *137* (32), 10276–10281. https://doi.org/10.1021/jacs.5b05602.
(124) Pellet, N.; Teuscher, J.; Maier, J.; Grätzel, M. Transforming Hybrid Organic Inorganic Perovskites by Rapid Halide Exchange. *Chem. Mater.* **2015**, *27* (6), 2181–2188. https://doi.org/10.1021/acs.chemmater.5b00281.
(125) Kim, J. I.; Zeng, Q.; Park, S.; Lee, H.; Park, J.; Kim, T.; Lee, T.-W. Strategies to Extend the Lifetime of Perovskite Downconversion Films for Display Applications. *Adv. Mater.* **2023**, *35* (43), 2209784. https://doi.org/10.1002/adma.202209784.
(126) Abdi-Jalebi, M.; Andaji-Garmaroudi, Z.; Cacovich, S.; Stavrakas, C.; Philippe, B.; Richter, J. M.; Alsari, M.; Booker, E. P.; Hutter, E. M.; Pearson, A. J.; Lilliu, S.; Savenije, T. J.; Rensmo, H.; Divitini, G.; Ducati, C.; Friend, R. H.; Stranks, S. D. Maximizing and Stabilizing Luminescence from Halide Perovskites with Potassium Passivation. *Nature* **2018**, *555* (7697), 497–501. https://doi.org/10.1038/nature25989.
(127) Harwell, J. R.; Baikie, T. K.; Baikie, I. D.; Payne, J. L.; Ni, C.; Irvine, J. T. S.; Turnbull, G. A.; Samuel, I. D. W. Probing the Energy Levels of Perovskite Solar Cells via Kelvin Probe and UV Ambient Pressure Photoemission Spectroscopy. *Phys. Chem. Chem. Phys.* **2016**, *18* (29), 19738–19745. https://doi.org/10.1039/C6CP02446G.
(128) Pan, J.; Su, L.; Du, L.; Guan, X.; Zhang, G.; SaeidNahaei, S. Applying a Time-Saving and Cost-Effective Postprocessing Method to Achieve a High-Quality Perovskite Light Emitting Diode. *Opt. Mater.* **2023**, *140*, 113889. https://doi.org/10.1016/j.optmat.2023.113889.
(129) Sassi, M.; Buccheri, N.; Rooney, M.; Botta, C.; Bruni, F.; Giovanella, U.; Brovelli, S.; Beverina, L. Near-Infrared Roll-off-Free Electroluminescence from Highly Stable Diketopyrrolopyrrole Light Emitting Diodes. *Sci. Rep.* **2016**, *6* (1), 34096. https://doi.org/10.1038/srep34096.
(130) Guo, B.; Lai, R.; Jiang, S.; Zhou, L.; Ren, Z.; Lian, Y.; Li, P.; Cao, X.; Xing, S.; Wang, Y.; Li, W.; Zou, C.; Chen, M.; Hong, Z.; Li, C.; Zhao, B.; Di, D. Ultrastable Near-Infrared Perovskite Light-Emitting Diodes. *Nat. Photonics* **2022**, *16* (9), 637–643. https://doi.org/10.1038/s41566-022-01046-3.
(131) Cao, Y.; Wang, N.; Tian, H.; Guo, J.; Wei, Y.; Chen, H.; Miao, Y.; Zou, W.; Pan, K.; He, Y.; Cao, H.; Ke, Y.; Xu, M.; Wang, Y.; Yang, M.; Du, K.; Fu, Z.; Kong, D.; Dai, D.; Jin, Y.; Li, G.; Li, H.; Peng, Q.; Wang, J.; Huang, W. Perovskite Light-Emitting Diodes Based on Spontaneously Formed Submicrometre-Scale Structures. *Nature* **2018**, *562* (7726), 249–253. https://doi.org/10.1038/s41586-018-0576-2.
(132) Guo, Y.; Apergi, S.; Li, N.; Chen, M.; Yin, C.; Yuan, Z.; Gao, F.; Xie, F.; Brocks, G.; Tao, S.; Zhao, N. Phenylalkylammonium Passivation Enables Perovskite Light Emitting Diodes with Record High-Radiance Operational Lifetime: The Chain Length Matters. *Nat. Commun.* **2021**, *12* (1), 644. https://doi.org/10.1038/s41467-021-20970-6.

(133) Kuang, C.; Hu, Z.; Yuan, Z.; Wen, K.; Qing, J.; Kobera, L.; Abbrent, S.; Brus, J.; Yin, C.; Wang, H.; Xu, W.; Wang, J.; Bai, S.; Gao, F. Critical Role of Additive-Induced Molecular Interaction on the Operational Stability of Perovskite Light-Emitting Diodes. *Joule* **2021**, *5* (3), 618–630. https://doi.org/10.1016/j.joule.2021.01.003.
(134) Baek, S.-D.; Shao, W.; Feng, W.; Tang, Y.; Lee, Y. H.; Loy, J.; Gunnarsson, W. B.; Yang, H.; Zhang, Y.; Faheem, M. B.; Kaswekar, P. I.; Atapattu, H. R.; Qin, J.; Coffey, A. H.; Park, J. Y.; Yang, S. J.; Yang, Y.-T.; Zhu, C.; Wang, K.; Graham, K. R.; Gao, F.; Qiao, Q.; Guo, L. J.; Rand, B. P.; Dou, L. Grain Engineering for Efficient Near-Infrared Perovskite Light-Emitting Diodes. *Nat. Commun.* **2024**, *15* (1), 10760. https://doi.org/10.1038/s41467-024-55075-3.
(135) Santos, P. L. dos; Stachelek, P.; Takeda, Y.; Pander, P. Recent Advances in Highly-Efficient near Infrared OLED Emitters. *Mater. Chem. Front.* **2024**, *8* (7), 1731–1766. https://doi.org/10.1039/D3QM01067H.
(136) Tan, Z.-K.; Moghaddam, R. S.; Lai, M. L.; Docampo, P.; Higler, R.; Deschler, F.; Price, M.; Sadhanala, A.; Pazos, L. M.; Credgington, D.; Hanusch, F.; Bein, T.; Snaith, H. J.; Friend, R. H. Bright Light-Emitting Diodes Based on Organometal Halide Perovskite. *Nat. Nanotechnol.* **2014**, *9* (9), 687–692. https://doi.org/10.1038/nnano.2014.149.
(137) Gardner, K. L.; Tait, J. G.; Merckx, T.; Qiu, W.; Paetzold, U. W.; Kootstra, L.; Jaysankar, M.; Gehlhaar, R.; Cheyns, D.; Heremans, P.; Poortmans, J. Nonhazardous Solvent Systems for Processing Perovskite Photovoltaics. *Adv. Energy Mater.* **2016**, *6* (14), 1600386. https://doi.org/10.1002/aenm.201600386.
(138) Hoke, E. T.; Slotcavage, D. J.; Dohner, E. R.; Bowring, A. R.; Karunadasa, H. I.; McGehee, M. D. Reversible Photo-Induced Trap Formation in Mixed-Halide Hybrid Perovskites for Photovoltaics. *Chem. Sci.* **2014**, *6* (1), 613–617. https://doi.org/10.1039/C4SC03141E.
(139) Bischak, C. G.; Hetherington, C. L.; Wu, H.; Aloni, S.; Ogletree, D. F.; Limmer, D. T.; Ginsberg, N. S. Origin of Reversible Photoinduced Phase Separation in Hybrid Perovskites. *Nano Lett.* **2017**, *17* (2), 1028–1033. https://doi.org/10.1021/acs.nanolett.6b04453.
(140) Li, G.; Tan, Z.-K.; Di, D.; Lai, M. L.; Jiang, L.; Lim, J. H.-W.; Friend, R. H.; Greenham, N. C. Efficient Light-Emitting Diodes Based on Nanocrystalline Perovskite in a Dielectric Polymer Matrix. *Nano Lett.* **2015**, *15* (4), 2640–2644. https://doi.org/10.1021/acs.nanolett.5b00235.
(141) Huang, L.; Liu, C.; Ren, C.; Nie, Z.; Xiong, X.; Zeng, L.; Zhu, W.; Yang, W.; Wang, L. The Phase-Controllable Crystallization Induced by Low Pressure Flashing in Chloride Anion Doped Quasi-2D Hybrid Perovskite Thin Films for Blue Light-Emitting Diodes. *Surf. Interfaces* **2022**, *28*, 101653. https://doi.org/10.1016/j.surfin.2021.101653.
(142) Liang, J.; Guo, X.; Song, L.; Lin, J.; Hu, Y.; Zhang, N.; Liu, X. Transparent Perovskite Light-Emitting Diodes by Employing Organic-Inorganic Multilayer Transparent Top Electrodes. *Appl. Phys. Lett.* **2017**, *111* (21), 213301. https://doi.org/10.1063/1.4992039.
(143) Chou, S.-Y.; Ma, R.; Li, Y.; Zhao, F.; Tong, K.; Yu, Z.; Pei, Q. Transparent Perovskite Light-Emitting Touch-Responsive Device. *ACS Nano* **2017**, *11* (11), 11368–11375. https://doi.org/10.1021/acsnano.7b05935.
(144) Wu, H.; Zhang, Y.; Zhang, X.; Lu, M.; Sun, C.; Bai, X.; Zhang, T.; Sun, G.; Yu, W. W. Fine-Tuned Multilayered Transparent Electrode for Highly Transparent Perovskite Light-Emitting Devices. *Adv. Electron. Mater.* **2018**, *4* (1), 1700285. https://doi.org/10.1002/aelm.201700285.
(145) Xie, C.; Zhao, X.; Ong, E. W. Y.; Tan, Z.-K. Transparent Near-Infrared Perovskite Light-Emitting Diodes. *Nat. Commun.* **2020**, *11* (1), 4213. https://doi.org/10.1038/s41467-020-18110-7.
(146) Cai, L.; Zhou, J.; Bai, G.; Zang, J.; El-Shaer, A.; Song, T.; Fung, M.-K.; Sun, B. High-Efficiency Top-Emitting Green Perovskite Light Emitting Diode with Quasi Lambertian Emission. *Adv. Opt. Mater.* **2022**, *10* (2), 2101137. https://doi.org/10.1002/adom.202101137.
(147) He, Z.; Bao, Z.; Guo, X.; Lv, Y.; Wang, T.; Ma, Y.; Liu, X. Efficient Transparent Blue-Emitted Perovskite Light-Emitting Diodes Based on Multilayer Transparent Top Electrodes. *J. Mater. Chem. C* **2024**, *12* (20), 7162–7168. https://doi.org/10.1039/D4TC00934G.
(148) Qi, Y.; Liu, R.; Li, Z.; Song, Y.; Wang, C.; Cai, L. Microcavity Forming Electrode for Efficient Color-Tunable Semitransparent Perovskite Light-Emitting Diodes. *Opt. Laser Technol.* **2024**, *169*, 110002. https://doi.org/10.1016/j.optlastec.2023.110002.
(149) Aydin, E.; Altinkaya, C.; Smirnov, Y.; Yaqin, M. A.; Zanoni, K. P. S.; Paliwal, A.; Firdaus, Y.; Allen, T. G.; Anthopoulos, T. D.; Bolink, H. J.; Morales-Masis, M.; De Wolf, S. Sputtered Transparent Electrodes

for Optoelectronic Devices: Induced Damage and Mitigation Strategies. *Matter* **2021**, *4* (11), 3549–3584. https://doi.org/10.1016/j.matt.2021.09.021.
(150) Liu, L.; Cao, K.; Chen, S.; Huang, W. Toward See-Through Optoelectronics: Transparent Light-Emitting Diodes and Solar Cells. *Adv. Opt. Mater.* **2020**, *8* (22), 2001122. https://doi.org/10.1002/adom.202001122.
(151) Moeini, A.; Martínez-Sarti, L.; S. Zanoni, K. P.; Sessolo, M.; Tordera, D.; J. Bolink, H. Semitransparent Near-Infrared Sn–Pb Hybrid Perovskite Photodetectors. *J. Mater. Chem. C* **2022**, *10* (37), 13878–13885. https://doi.org/10.1039/D2TC01052F.
(152) Altinkaya, C.; Aydin, E.; Ugur, E.; Isikgor, F. H.; Subbiah, A. S.; De Bastiani, M.; Liu, J.; Babayigit, A.; Allen, T. G.; Laquai, F.; Yildiz, A.; De Wolf, S. Tin Oxide Electron-Selective Layers for Efficient, Stable, and Scalable Perovskite Solar Cells. *Adv. Mater.* **2021**, *33* (15), 2005504. https://doi.org/10.1002/adma.202005504.
(153) Smirnov, Y.; Repecaud, P.-A.; Tutsch, L.; Florea, I.; P.S. Zanoni, K.; Paliwal, A.; J. Bolink, H.; Cabarrocas, P. R. i; Bivour, M.; Morales-Masis, M. Wafer-Scale Pulsed Laser Deposition of ITO for Solar Cells: Reduced Damage vs. Interfacial Resistance. *Mater. Adv.* **2022**, *3* (8), 3469–3478. https://doi.org/10.1039/D1MA01225H.
(154) Smirnov, Y.; Schmengler, L.; Kuik, R.; Repecaud, P.-A.; Najafi, M.; Zhang, D.; Theelen, M.; Aydin, E.; Veenstra, S.; De Wolf, S.; Morales-Masis, M. Scalable Pulsed Laser Deposition of Transparent Rear Electrode for Perovskite Solar Cells. *Adv. Mater. Technol.* **2021**, *6* (2), 2000856. https://doi.org/10.1002/admt.202000856.
(155) Park, C. H.; Kim, J. G.; Jung, S.-G.; Lee, D. J.; Park, Y. W.; Ju, B.-K. Optical Characteristics of Refractive-Index-Matching Diffusion Layer in Organic Light-Emitting Diodes. *Sci. Rep.* **2019**, *9* (1), 8690. https://doi.org/10.1038/s41598-019-45000-w.
(156) Shi, Z.; Li, Y.; Zhang, Y.; Chen, Y.; Li, X.; Wu, D.; Xu, T.; Shan, C.; Du, G. High-Efficiency and Air-Stable Perovskite Quantum Dots Light-Emitting Diodes with an All-Inorganic Heterostructure. *Nano Lett.* **2017**, *17* (1), 313–321. https://doi.org/10.1021/acs.nanolett.6b04116.
(157) ISO 10526:1999/CIE S005/E-1998, CIE Standard Illuminants for Colorimetry.
(158) Kim, Y.-H.; Kim, S.; Kakekhani, A.; Park, J.; Park, J.; Lee, Y.-H.; Xu, H.; Nagane, S.; Wexler, R. B.; Kim, D.-H.; Jo, S. H.; Martínez-Sarti, L.; Tan, P.; Sadhanala, A.; Park, G.-S.; Kim, Y.-W.; Hu, B.; Bolink, H. J.; Yoo, S.; Friend, R. H.; Rappe, A. M.; Lee, T.-W. Comprehensive Defect Suppression in Perovskite Nanocrystals for High-Efficiency Light-Emitting Diodes. *Nat. Photonics* **2021**, *15* (2), 148–155. https://doi.org/10.1038/s41566-020-00732-4.
(159) Kim, D.-H.; Woo, S.-J.; Huelmo, C. P.; Park, M.-H.; Schankler, A. M.; Dai, Z.; Heo, J.-M.; Kim, S.; Reuveni, G.; Kang, S.; Kim, J. S.; Yun, H. J.; Park, J.; Park, J.; Yaffe, O.; Rappe, A. M.; Lee, T.-W. Surface-Binding Molecular Multipods Strengthen the Halide Perovskite Lattice and Boost Luminescence. *Nat. Commun.* **2024**, *15* (1), 6245. https://doi.org/10.1038/s41467-024-49751-7.
(160) Han, T.-H.; Jang, K. Y.; Dong, Y.; Friend, R. H.; Sargent, E. H.; Lee, T.-W. A Roadmap for the Commercialization of Perovskite Light Emitters. *Nat. Rev. Mater.* **2022**, *7* (10), 757–777. https://doi.org/10.1038/s41578-022-00459-4.
(161) Hassan, Y.; Park, J. H.; Crawford, M. L.; Sadhanala, A.; Lee, J.; Sadighian, J. C.; Mosconi, E.; Shivanna, R.; Radicchi, E.; Jeong, M.; Yang, C.; Choi, H.; Park, S. H.; Song, M. H.; De Angelis, F.; Wong, C. Y.; Friend, R. H.; Lee, B. R.; Snaith, H. J. Ligand-Engineered Bandgap Stability in Mixed-Halide Perovskite LEDs. *Nature* **2021**, *591* (7848), 72–77. https://doi.org/10.1038/s41586-021-03217-8.
(162) Dong, Y.; Wang, Y.-K.; Yuan, F.; Johnston, A.; Liu, Y.; Ma, D.; Choi, M.-J.; Chen, B.; Chekini, M.; Baek, S.-W.; Sagar, L. K.; Fan, J.; Hou, Y.; Wu, M.; Lee, S.; Sun, B.; Hoogland, S.; Quintero-Bermudez, R.; Ebe, H.; Todorovic, P.; Dinic, F.; Li, P.; Kung, H. T.; Saidaminov, M. I.; Kumacheva, E.; Spiecker, E.; Liao, L.-S.; Voznyy, O.; Lu, Z.-H.; Sargent, E. H. Bipolar-Shell Resurfacing for Blue LEDs Based on Strongly Confined Perovskite Quantum Dots. *Nat. Nanotechnol.* **2020**, *15* (8), 668–674. https://doi.org/10.1038/s41565-020-0714-5.
(163) Hong, S.-K.; Sim, J.-H.; Seo, I.-G.; Kim, K.-C.; Bae, S.-I.; Lee, H.-Y.; Lee, N.-Y.; Jang, J. New Pixel Design on Emitting Area for High Resolution Active-Matrix Organic Light-Emitting Diode Displays. *J. Disp. Technol.* **2010**, *6* (12), 601–606.
(164) Yoo, J.-S.; Jung, S.-H.; Kim, Y.-C.; Byun, S.-C.; Kim, J.-M.; Choi, N.-B.; Yoon, S.-Y.; Kim, C.-D.; Hwang, Y.-K.; Chung, I.-J. Highly Flexible AM-OLED Display With Integrated Gate Driver Using Amorphous Silicon TFT on Ultrathin Metal Foil. *J. Disp. Technol.* **2010**, *6* (11), 565–570. https://doi.org/10.1109/JDT.2010.2048998.

(165) Ban, X.; Liu, Y.; Pan, J.; Chen, F.; Zhu, A.; Jiang, W.; Sun, Y.; Dong, Y. Blocking Exciton-Quenching Pathways in Host and Guest Interfaces for High Performance Solution-Processed TADF OLEDs with External Quantum Efficiency Approaching 25%. *Org. Electron.* **2020**, *80*, 105601. https://doi.org/10.1016/j.orgel.2019.105601.
(166) Hasan, M.; Saggar, S.; Shukla, A.; Bencheikh, F.; Sobus, J.; McGregor, S. K. M.; Adachi, C.; Lo, S.-C.; Namdas, E. B. Probing Polaron-Induced Exciton Quenching in TADF Based Organic Light-Emitting Diodes. *Nat. Commun.* **2022**, *13* (1), 254. https://doi.org/10.1038/s41467-021-27739-x.
(167) Young, R. H.; Tang, C. W.; Marchetti, A. P. Current-Induced Fluorescence Quenching in Organic Light-Emitting Diodes. *Appl. Phys. Lett.* **2002**, *80* (5), 874–876. https://doi.org/10.1063/1.1445271.
(168) Takada, N.; Tsutsui, T.; Saito, S. Control of Emission Characteristics in Organic Thin-film Electroluminescent Diodes Using an Optical-microcavity Structure. *Appl. Phys. Lett.* **1993**, *63* (15), 2032–2034. https://doi.org/10.1063/1.110582.
(169) Wang, T.; Zou, Y.; Huang, Z.; Li, N.; Miao, J.; Yang, C. Narrowband Emissive TADF Conjugated Polymers towards Highly Efficient Solution-Processible OLEDs. *Angew. Chem. Int. Ed.* **2022**, *61* (46), e202211172. https://doi.org/10.1002/anie.202211172.
(170) Ha, J. M.; Hur, S. H.; Pathak, A.; Jeong, J.-E.; Woo, H. Y. Recent Advances in Organic Luminescent Materials with Narrowband Emission. *NPG Asia Mater.* **2021**, *13* (1), 1–36. https://doi.org/10.1038/s41427-021-00318-8.
(171) Xue, J.; Chen, S.; Liang, J.; Bi, H.; Liu, Y.; Wang, Y. Finely-Tuned Heteroleptic Phosphorescent Ir(III) Complexes for CIEy < 0.2-Based Pure Blue Organic Light-Emitting Diodes with External Quantum Efficiencies > 30%. *Chem. Eng. J.* **2023**, *463*, 142493. https://doi.org/10.1016/j.cej.2023.142493.
(172) Hatakeyama, T.; Ikuta, T.; Shiren, K.; Nakajima, K.; Nomura, S.; Ni, J. Efficient HOMO-LUMO Separation by Multiple Resonance Effect toward Ultrapure Blue Thermally Activated Delayed Fluorescence. In *Organic Light Emitting Materials and Devices XX*; SPIE, 2016; Vol. 9941, pp 2–9. https://doi.org/10.1117/12.2239211.
(173) Teng, J.-M.; Wang, Y.-F.; Chen, C.-F. Recent Progress of Narrowband TADF Emitters and Their Applications in OLEDs. *J. Mater. Chem. C* **2020**, *8* (33), 11340–11353. https://doi.org/10.1039/D0TC02682D.
(174) Zou, S.-J.; Xie, F.-M.; Xie, M.; Li, Y.-Q.; Cheng, T.; Zhang, X.-H.; Lee, C.-S.; Tang, J.-X. High-Performance Nondoped Blue Delayed Fluorescence Organic Light-Emitting Diodes Featuring Low Driving Voltage and High Brightness. *Adv. Sci.* **2020**, *7* (3), 1902508. https://doi.org/10.1002/advs.201902508.
(175) Matsuo, K.; Yasuda, T. Blue Thermally Activated Delayed Fluorescence Emitters Incorporating Acridan Analogues with Heavy Group 14 Elements for High-Efficiency Doped and Non-Doped OLEDs. *Chem. Sci.* **2019**, *10* (46), 10687–10697. https://doi.org/10.1039/C9SC04492B.
(176) Park, I. S.; Matsuo, K.; Aizawa, N.; Yasuda, T. High-Performance Dibenzoheteraborin-Based Thermally Activated Delayed Fluorescence Emitters: Molecular Architectonics for Concurrently Achieving Narrowband Emission and Efficient Triplet–Singlet Spin Conversion. *Adv. Funct. Mater.* **2018**, *28* (34), 1802031. https://doi.org/10.1002/adfm.201802031.
(177) Stavrou, K.; Danos, A.; Hama, T.; Hatakeyama, T.; Monkman, A. Hot Vibrational States in a High-Performance Multiple Resonance Emitter and the Effect of Excimer Quenching on Organic Light-Emitting Diodes. *ACS Appl. Mater. Interfaces* **2021**. https://doi.org/10.1021/acsami.0c20619.
(178) Stavrou, K.; Franca, L. G.; Böhmer, T.; Duben, L. M.; Marian, C. M.; Monkman, A. P. Unexpected Quasi-Axial Conformer in Thermally Activated Delayed Fluorescence DMAC-TRZ, Pushing Green OLEDs to Blue. *Adv. Funct. Mater.* **2023**, *33* (25), 2300910. https://doi.org/10.1002/adfm.202300910.
(179) Kondo, Y.; Yoshiura, K.; Kitera, S.; Nishi, H.; Oda, S.; Gotoh, H.; Sasada, Y.; Yanai, M.; Hatakeyama, T. Narrowband Deep-Blue Organic Light-Emitting Diode Featuring an Organoboron-Based Emitter. *Nat. Photonics* **2019**, *13* (10), 678–682. https://doi.org/10.1038/s41566-019-0476-5.
(180) Chan, C.-Y.; Tanaka, M.; Lee, Y.-T.; Wong, Y.-W.; Nakanotani, H.; Hatakeyama, T.; Adachi, C. Stable Pure-Blue Hyperfluorescence Organic Light-Emitting Diodes with High-Efficiency and Narrow Emission. *Nat. Photonics* **2021**, *15* (3), 203–207. https://doi.org/10.1038/s41566-020-00745-z.
(181) Nakanotani, H.; Higuchi, T.; Furukawa, T.; Masui, K.; Morimoto, K.; Numata, M.; Tanaka, H.; Sagara, Y.; Yasuda, T.; Adachi, C. High-Efficiency Organic Light-Emitting Diodes with Fluorescent Emitters. *Nat. Commun.* **2014**, *5* (1), 4016. https://doi.org/10.1038/ncomms5016.

(182) Lee, J.-H.; Cheng, S.-H.; Yoo, S.-J.; Shin, H.; Chang, J.-H.; Wu, C.-I.; Wong, K.-T.; Kim, J.-J. An Exciplex Forming Host for Highly Efficient Blue Organic Light Emitting Diodes with Low Driving Voltage. *Adv. Funct. Mater.* **2015**, *25* (3), 361–366. https://doi.org/10.1002/adfm.201402707.
(183) Dai, X.; Yao, F.; Li, J.; Yu, H.; Cao, J. Color-Stable Non-Doped White Phosphorescent Organic Light-Emitting Diodes Based on Ultrathin Emissive Layers. *J. Phys. Appl. Phys.* **2019**, *53* (5), 055106. https://doi.org/10.1088/1361-6463/ab5698.
(184) Zhang, D.; Song, X.; Gillett, A. J.; Drummond, B. H.; Jones, S. T. E.; Li, G.; He, H.; Cai, M.; Credgington, D.; Duan, L. Efficient and Stable Deep-Blue Fluorescent Organic Light-Emitting Diodes Employing a Sensitizer with Fast Triplet Upconversion. *Adv. Mater.* **2020**, *32* (19), 1908355. https://doi.org/10.1002/adma.201908355.
(185) Cui, L.-S.; Gillett, A. J.; Zhang, S.-F.; Ye, H.; Liu, Y.; Chen, X.-K.; Lin, Z.-S.; Evans, E. W.; Myers, W. K.; Ronson, T. K.; Nakanotani, H.; Reineke, S.; Bredas, J.-L.; Adachi, C.; Friend, R. H. Fast Spin-Flip Enables Efficient and Stable Organic Electroluminescence from Charge-Transfer States. *Nat. Photonics* **2020**, *14* (10), 636–642. https://doi.org/10.1038/s41566-020-0668-z.
(186) Kim, E.; Park, J.; Jun, M.; Shin, H.; Baek, J.; Kim, T.; Kim, S.; Lee, J.; Ahn, H.; Sun, J.; Ko, S.-B.; Hwang, S.-H.; Lee, J. Y.; Chu, C.; Kim, S. Highly Efficient and Stable Deep-Blue Organic Light-Emitting Diode Using Phosphor-Sensitized Thermally Activated Delayed Fluorescence. *Sci. Adv.* **2022**, *8* (41), eabq1641. https://doi.org/10.1126/sciadv.abq1641.
(187) Meng, Q.-Y.; Wang, R.; Wang, Y.-L.; Guo, X.-W.; Liu, Y.-Q.; Wen, X.-L.; Yao, C.-Y.; Qiao, J. Longevity Gene Responsible for Robust Blue Organic Materials Employing Thermally Activated Delayed Fluorescence. *Nat. Commun.* **2023**, *14* (1), 3927. https://doi.org/10.1038/s41467-023-39697-7.
(188) Samanta, P. K.; Kim, D.; Coropceanu, V.; Brédas, J.-L. Up-Conversion Intersystem Crossing Rates in Organic Emitters for Thermally Activated Delayed Fluorescence: Impact of the Nature of Singlet vs Triplet Excited States. *J. Am. Chem. Soc.* **2017**, *139* (11), 4042–4051. https://doi.org/10.1021/jacs.6b12124.
(189) Mamada, M.; Aoyama, A.; Uchida, R.; Ochi, J.; Oda, S.; Kondo, Y.; Kondo, M.; Hatakeyama, T. Efficient Deep-Blue Multiple-Resonance Emitters Based on Azepine-Decorated ν-DABNA for CIEy below 0.06. *Adv. Mater.* **2024**, *36* (30), 2402905. https://doi.org/10.1002/adma.202402905.
(190) Forster, Th. Energiewanderung und Fluoreszenz. *Naturwissenschaften* **1946**, *33* (6), 166–175. https://doi.org/10.1007/BF00585226.
(191) Tsai, W.-L.; Huang, M.-H.; Lee, W.-K.; Hsu, Y.-J.; Pan, K.-C.; Huang, Y.-H.; Ting, H.-C.; Sarma, M.; Ho, Y.-Y.; Hu, H.-C.; Chen, C.-C.; Lee, M.-T.; Wong, K.-T.; Wu, C.-C. A Versatile Thermally Activated Delayed Fluorescence Emitter for Both Highly Efficient Doped and Non-Doped Organic Light Emitting Devices. *Chem. Commun.* **2015**, *51* (71), 13662–13665. https://doi.org/10.1039/C5CC05022G.
(192) Crovini, E.; Dhali, R.; Sun, D.; Matulaitis, T.; Comerford, T.; Z. Slawin, A. M.; Sissa, C.; Azzolin, F.; Maiolo, F. D.; Painelli, A.; Zysman-Colman, E. Molecular Geometry and the Photophysics of Thermally Activated Delayed Fluorescence: The Strange Case of DMAC-Py-TRZ. *J. Mater. Chem. C* **2023**, *11* (24), 8284–8292. https://doi.org/10.1039/D2TC05213J.
(193) Nabha-Barnea, S.; Gotleyb, D.; Yonish, A.; Shikler, R. Relating Transient Electroluminescence Lifetime and Bulk Transit Time in OLED during Switch-Off. *J. Mater. Chem. C* **2021**, *9* (2), 719–726. https://doi.org/10.1039/D0TC04143B.
(194) Grüne, J.; Bunzmann, N.; Meinecke, M.; Dyakonov, V.; Sperlich, A. Kinetic Modeling of Transient Electroluminescence Reveals TTA as Efficiency-Limiting Process in Exciplex-Based TADF OLEDs. *J. Phys. Chem. C* **2020**, *124* (47), 25667–25674. https://doi.org/10.1021/acs.jpcc.0c06528.
(195) Hassine, L.; Bouchriha, H.; Roussel, J.; Fave, J.-L. Transient Response of a Bilayer Organic Electroluminescent Diode: Experimental and Theoretical Study of Electroluminescence Onset. *Appl. Phys. Lett.* **2001**, *78* (8), 1053–1055. https://doi.org/10.1063/1.1350419.
(196) Tanaka, M.; Noda, H.; Nakanotani, H.; Adachi, C. Effect of Carrier Balance on Device Degradation of Organic Light-Emitting Diodes Based on Thermally Activated Delayed Fluorescence Emitters. *Adv. Electron. Mater.* **2019**, *5* (5), 1800708. https://doi.org/10.1002/aelm.201800708.
(197) Pinner, D. J.; Friend, R. H.; Tessler, N. Transient Electroluminescence of Polymer Light Emitting Diodes Using Electrical Pulses. *J. Appl. Phys.* **1999**, *86* (9), 5116–5130. https://doi.org/10.1063/1.371488.
(198) Lee, C.; Baek, H.-I.; Kwak, J.; Kim, J. Y.; Chin, B. D. Optimization of White OLEDs Based on Charge Carrier Conduction Properties of Phosphorescent Emitting Layers. In *Organic Light Emitting*

Materials and Devices XII; SPIE, 2008; Vol. 7051, pp 106–113. https://doi.org/10.1117/12.800786.
(199) Lin, M.-T.; Li, M.; Chen, W.-H.; Omary, M. A.; Shepherd, N. D. Transient Electroluminescence Determination of Carrier Mobility and Charge Trapping Effects in Heavily Doped Phosphorescent Organic Light-Emitting Diodes. *Solid-State Electron.* **2011**, *56* (1), 196–200. https://doi.org/10.1016/j.sse.2010.10.018.
(200) Baessler, H. Charge Transport in Disordered Organic Photoconductors. A Monte Carlo Simulation Study. *Phys. Status Solidi B Basic Res. Ger.* **1993**, *175:1*. https://doi.org/10.1002/pssb.2221750102.
(201) Krikun, G.; Zojer, K. Impact of Thermal Transport Parameters on the Operating Temperature of Organic Light Emitting Diodes. *J. Appl. Phys.* **2019**, *125* (8), 085501. https://doi.org/10.1063/1.5079531.
(202) Zhang, T.; Shi, C.; Zhao, C.; Wu, Z.; Sun, N.; Chen, J.; Xie, Z.; Ma, D. High Efficiency Phosphorescent White Organic Light-Emitting Diodes with Low Efficiency Roll-off Achieved by Strategic Exciton Management Based on Simple Ultrathin Emitting Layer Structures. *J. Mater. Chem. C* **2017**, *5* (48), 12833–12838. https://doi.org/10.1039/C7TC04705C.
(203) dos Santos, P. L.; de Sa Pereira, D.; Oh, C. S.; Kukhta, N.; Lee, H. L.; Lee, J. Y.; Monkman, A. P. Influence of Multiple rISC Channels on the Maximum Efficiency and Roll-Off of TADF OLEDs. *J. Phys. Chem. C* **2024**, *128* (39), 16308–16319. https://doi.org/10.1021/acs.jpcc.4c02993.
(204) Bae, S.; Jo, J. W.; Lee, P.; Ko, M. J. Controlling the Morphology of Organic–Inorganic Hybrid Perovskites through Dual Additive-Mediated Crystallization for Solar Cell Applications. *ACS Appl. Mater. Interfaces* **2019**, *11* (19), 17452–17458. https://doi.org/10.1021/acsami.9b03929.
(205) Kosasih, F. U.; Erdenebileg, E.; Mathews, N.; Mhaisalkar, S. G.; Bruno, A. Thermal Evaporation and Hybrid Deposition of Perovskite Solar Cells and Mini-Modules. *Joule* **2022**, *6* (12), 2692–2734. https://doi.org/10.1016/j.joule.2022.11.004.
(206) Uličná, S.; Dou, B.; Kim, D. H.; Zhu, K.; Walls, J. M.; Bowers, J. W.; van Hest, M. F. A. M. Scalable Deposition of High-Efficiency Perovskite Solar Cells by Spray-Coating. *ACS Appl. Energy Mater.* **2018**, *1* (5), 1853–1857. https://doi.org/10.1021/acsaem.8b00328.
(207) Khorasani, A.; Mohamadkhani, F.; Marandi, M.; Luo, H.; Abdi-Jalebi, M. Opportunities, Challenges, and Strategies for Scalable Deposition of Metal Halide Perovskite Solar Cells and Modules. *Adv. Energy Sustain. Res.* **2024**, *5* (7), 2300275. https://doi.org/10.1002/aesr.202300275.
(208) Li, J.; Cao, H.-L.; Jiao, W.-B.; Wang, Q.; Wei, M.; Cantone, I.; Lü, J.; Abate, A. Biological Impact of Lead from Halide Perovskites Reveals the Risk of Introducing a Safe Threshold. *Nat. Commun.* **2020**, *11* (1), 310. https://doi.org/10.1038/s41467-019-13910-y.
(209) Ahmed, S.; Gondal, M. A.; Alzahrani, A. S.; Parvaz, M.; Ahmed, A.; Hussain, S. Recent Trends and Challenges in Lead-Free Perovskite Solar Cells: A Critical Review. *ACS Appl. Energy Mater.* **2024**, *7* (4), 1382–1397. https://doi.org/10.1021/acsaem.3c02327.
(210) Li, Z.; Wu, X.; Wu, S.; Gao, D.; Dong, H.; Huang, F.; Hu, X.; Jen, A. K.-Y.; Zhu, Z. An Effective and Economical Encapsulation Method for Trapping Lead Leakage in Rigid and Flexible Perovskite Photovoltaics. *Nano Energy* **2022**, *93*, 106853. https://doi.org/10.1016/j.nanoen.2021.106853.
(211) Chen, B.; Fei, C.; Chen, S.; Gu, H.; Xiao, X.; Huang, J. Recycling Lead and Transparent Conductors from Perovskite Solar Modules. *Nat. Commun.* **2021**, *12* (1), 5859. https://doi.org/10.1038/s41467-021-26121-1.

Resum en valencià

Introducció i objectius de la tesi

La llum es fonamental en la vida humana, no sols permetent la visió, sinó també regulant els ritmes circadiaris, l'estat d'ànim, la productivitat i la salut. Històricament, els éssers humans depenien dels cicles de llum natural; hui dia la il·luminació artificial prolonga l'activitat més enllà de la llum diürna.

Les fonts de llum primerenques, com el foc, els llums d'oli i els ciris, eren ineficients i perilloses. La il·luminació de gas va millorar la il·luminació urbana, fins que va arribar un gran avenç tecnològic amb la invenció de la bombeta incandescent per part de Thomas Edison (1879), la qual proporcionava una llum càlida i constant, però malgastava la major part de l'energia en forma de calor. Els llums fluorescents de mitjan segle XX oferien major eficiència, però presentaven problemes com el parpelleig i el contingut de mercuri. Hui dia, els díodes emissors de llum (LEDs) dominen gràcies a la seua alta eficiència energètica, llarga vida útil, menor toxicitat, i lluentor i color ajustables.

Al mateix temps, en dispositius moderns com a telèfons, tauletes i televisors, la pantalla determina la qualitat visual. Entre les diverses tecnologies, els OLEDs oferixen major contrast, angles de visió, puresa de color i eficiència energètica, crucial en dispositius portàtils.

Per estes raons, la investigació en il·luminació sòlida continua sent clau per a millorar el rendiment de pantalles, l'eficiència energètica i reduir l'impacte ambiental.

Funcionament dels díodes emissors de llum

Els díodes orgànics emissors de llum (OLEDs) són dispositius d'estat sòlid que convertixen energia elèctrica en llum visible mitjançant la recombinació radiativa de càrregues en capes de semiconductors orgànics. Els semiconductors orgànics són molècules que poden formar pel·lícules amorfes fines capaces de conduir electricitat i emetre llum. Els electrons en estes molècules ocupen orbitals específics: el més alt ocupat es diu HOMO i el més sota desocupat es diu LUMO, anàlegs a les bandes de València i conducció en semiconductors inorgànics convencionals. Quan un electró passa a un orbital buit, la molècula entra en un estat excitat (excitó) i pot alliberar energia com a llum, fenomen anomenat luminescència. L'emissió de llum induïda per corrent elèctric es denomina electroluminescència.

L'OLED més simple consta d'un ànode, una capa emissora i un càtode. Sota voltatge, s'injecten electrons i buits que es recombinen formant excitons, alliberant energia com a llum. Les arquitectures multicapa milloren l'eficiència en incloure capes d'injecció i transport d'electrons i buits i capes blocadores, ajustades segons els nivells HOMO/LUMO i les funcions de treball dels elèctrodes. Este disseny reduïx la barrera d'injecció, disminuïx el voltatge d'encesa i garantix que la recombinació ocórrega preferentment sota polarització directa, atorgant a l'OLED característiques de díode.

Els excitons generats per la recombinació de càrregues poden adoptar quatre possibles estats de espín: un singlet (estat quàntic amb espín 0) i tres triplets (estats d'espín total 1). Els triplets són degenerats i tenen menor energia que els singlets. Pel fet que la recombinació és independent de l'espín, només el 25% dels excitons generats són singlets, mentres que el 75% són triplets. Els singlet poden decaure ràpidament emetent llum mitjançant fluorescència, per tant, en OLEDs basats només en fluorescència, com a màxim un quart dels portadors injectats produïx llum. Alguns compostos orgànics amb metalls pesants (iridi o platí) permeten la relaxació radiativa de triplets mitjançant fosforescència, convertint

teòricament tots els portadors en fotons. No obstant això, la fosforescència és més lenta, i els triplets, amb major semivida, són més susceptibles a pèrdues d'energia.

Estos processos ocorren amb major probabilitat quan les molècules emissores estan massa pròximes. Per a evitar-ho, els emissors solen dispersar-se en una matriu, on el material "amfitrió" transporta les càrregues i transferix l'energia a les molècules emissores. Com a alternativa, s'empren capes emissores ultra fines (ultrathin EMLs, UEMLs), que consistixen en mono-capes de menys d'1 nm depositades en forma d'illes. Estes simplifiquen el procés de fabricació en evitar la co-evaporació, complexa i costosa, i reduïxen el consum de material.

La tecnologia de OLEDs fosforescents permet convertir pràcticament tots els portadors injectats en fotons, però presenta limitacions per l'alt cost i la toxicitat dels compostos amb metalls pesants. Una estratègia alternativa prometedora és la conversió ascendent tèrmica dels excitons triplet a singlets (encreuament intersistema invers) que després emet llum a l'estat fonamental singlet en un procés retardat anomenat fluorescència retardada activada tèrmicament (TADF).

Figures de mèrit

Per a avaluar el rendiment d'un dispositiu OLED se solen mesurar la densitat de corrent i la luminància en funció del voltatge aplicat, representant els resultats en gràfiques semilogarítmiques amb doble eix y. Estes gràfiques es coneixen com a característiques *J–V–L* (densitat de corrent–voltatge –luminància).

La densitat de corrent (J) correspon a la quantitat de càrrega que fluïx per unitat d'àrea en el dispositiu, expressada en amperes per metre quadrat (A m^{-2}). La luminància (L) es defineix com la intensitat lluminosa en una direcció donada per unitat d'àrea. La unitat de mesura de la luminància en el Sistema Internacional d'Unitats és la candela per metre quadrat (cd m^{-2}). A diferència de la potència radiant, la luminància considera la sensibilitat espectral de l'ull humà, sent per tant un paràmetre directament lligat a la lluentor percebuda.

L'eficiència d'un OLED pot avaluar-se mitjançant diferents paràmetres. L'eficiència quàntica externa (EQE) mesura la fracció d'electrons injectats que es convertixen en fotons emesos fora del dispositiu, mentres l'eficàcia de corrent exprés la quantitat de llum generada per unitat de corrent elèctric (cd A^{-1}). L'eficiència depén de diversos factors clau, que se solen expressar en l'equació:

$$\mathrm{EQE} = \gamma\, \zeta_s\, q\, \eta_o$$

On γ mesura el balanç de càrregues, η_o és l'eficiència d'extracció de llum, ζ_s és l'eficiència de formació de excitones radiatius i q és el rendiment quàntic de fotoluminescència.

Altres paràmetres són la cromaticitat (especificació objectiva de la qualitat d'un color amb independència de la seua lluminositat) i la vida operativa (el temps durant el qual la luminància inicial del dispositiu es reduïx sota condicions d'operació constants) que determina la durabilitat del dispositiu en aplicacions pràctiques.

Perovskites

Les perovskites d'halur de plom són materials que segueixen la fórmula general $APbX_3$, on A representa un catió monovalent (com Cs^+ o $CH_3NH_3^+$) i X és un anió halur com Cl^- , Br^-, o I^-. Tenen una estructura cristal·lina cúbica o tetragonal que pot descriure's com una xarxa 3D d'octaedres PbX_6 amb el catió A ocupant el centre de la cel·la unitària i balancejant la càrrega.

A diferència dels semiconductors inorgànics convencionals, en els quals defectes puntuals solen introduir estats dins de la banda prohibida, en les perovskites estos defectes tendixen a generar nivells poc profunds, que no afecten de manera significativa la recombinació radiativa. Gràcies a esta resistència a defectes, les perovskites són materials prometedors per a moltes aplicacions optoelectròniques, com LEDs i cèl·lules solars.

Les perovskites poden emprar-se en dos modes principals dins de l'arquitectura del dispositiu: com a capes de transport de càrrega, gràcies a la seua alta mobilitat de càrrega i bona alineació de nivells energètics, o com a capes emissores de llum (LEDs de perovskita o PeLEDs), gràcies a la seua elevada eficiència d'emissió i elevada puresa de color.

L'emissió de llum en els PeLEDs es produïx mitjançant la recombinació radiativa d'electrons i buits injectats en la capa activa com en els OLEDs. No obstant això, a diferència dels OLEDs, on les transicions electròniques ocorren entre orbitals moleculars, en les perovskites la injecció de càrrega té lloc directament en la part inferior de la banda de conducció i la part superior de la banda de València, propis d'un semiconductor inorgànic. Els electrons s'injecten en la banda de conducció i els buits en la banda de València, i la seua recombinació genera un excitó feblement lligat, la relaxació radiativa del qual dona lloc a l'emissió lluminosa.

Mètodes

Síntesis i deposició de pel·lícules fines

Les capes orgàniques en els OLEDs poden depositar-se principalment mitjançant dos mètodes: evaporació tèrmica i dissolució.

En l'evaporació tèrmica, les molècules orgàniques se sublimen en una cambra de buit i es condensen sobre el substrat. Este mètode permet un control molt precís de la grossària a escala nanomètrica i la fabricació d'arquitectures multicapa amb interfícies ben definides. No obstant això, és un procés lent.

Una alternativa és el processament en dissolució, que inclou tècniques com el “spin coating". En este cas, els semiconductors orgànics es dissolen en un dissolvent i es depositen sobre el substrat. Gràcies a la força centrífuga, la solució s'estén, i durant el procés, l'evaporació del dissolvent induïx la formació de capa contínua. El gruix de la pel·lícula depèn de la velocitat de rotació, la viscositat i la concentració del material aplicat. El mètode s'utilitza de manera generalitzada en investigació; la seua principal limitació és la dificultat per a apilar múltiples capes, ja que els dissolvents poden dissoldre les capes ja depositades.

La deposició del càtode es realitza principalment mitjançant evaporació tèrmica en buit, la qual cosa assegura pel·lícules uniformes i netes. Encara que també pot emprar-se la polvorització catòdica, esta tècnica pot danyar les capes orgàniques a causa del bombardeig de partícules d'alta energia, per la qual cosa s'usa amb menys freqüència (i només per a elèctrodes transparents).

Les dos tècniques s'utilitzen també per a depositar les capes emissores en els PeLEDs. Durant el procés de spin coating per a perovskites, en molts casos, l'addició d'un antidissolvent o un tractament tèrmic posterior ajuden la cristal·lització en una capa contínua. En l'evaporació tèrmica de capes de perovskites, els diferents precursors se sublimen simultàniament (co-evaporació) des de diferents cresols i es condensen sobre el substrat. Este mètode permet un control molt precís de l'estequiometria i del gruix de la pel·lícula, així com una major reproductibilitat i uniformitat en grans àrees. No obstant això, requerix equips costosos i un control acurat de les taxes d'evaporació de cada component, la qual cosa ho fa més complex que el spin coating.

Caracterització dels dispositius

Després de la fabricació completa dels dispositius, les mostres es introdueixen en un sistema de caracterització fet a mida. Primer, es determina el voltatge d'encesa (V_{on}), augmentant manualment el voltatge amb una unitat font-mesura (Keithley 2400), fins que l'OLED emet llum. Després, s’adquireix l'espectre d'electroluminescència (EL) amb un espectrofotòmetre Avantes AvaSpec-2048L, necessari per a calcular l'eficàcia lluminosa, la responsivitat del fotodíode, l'energia mitjana dels fotons i les coordenades de color, a més d'avaluar l'estabilitat espectral sota diferents voltatges. Posteriorment, es registra el corrent del dispositiu i la generada en el fotodíode (Hamamatsu Photonics S1337-21) mentres

s'agrana el voltatge, la qual cosa permet calcular la densitat de corrent, la luminància i l'eficiència. Estos resultats es representen en corbes *J–V–L* i en gràfics d'eficiència enfront de luminància o densitat de corrent; en dispositius emissors en l'infraroig proper (NIR) s'utilitza la radiància en lloc de la luminància. Finalment, s'avalua la vida operativa mantenint el dispositiu sota corrent constant i mesurant l'evolució temporal de la luminància.

Resultats experimentals

OLEDs amb una capa de transport de buits de perovskita i capes emissores de llum no dopades

La reducció de costos de materials i de fabricació és clau per a la comercialització massiva dels OLEDs. Els materials orgànics són molt cars, i en els dispositius evaporats tèrmicament a penes s'aprofita un 2%–3% del material preparat, la qual cosa incrementa els costos. A més, la típica estructura amfitrió–dopant requerix equips especialitzats i dificulta la reproductibilitat en producció a gran escala.

Com a alternativa, les capes emissores ultrafines no dopades (<1 nm) reduïxen dràsticament el consum de material (fins a un 97% d'estalvi estimat). No obstant això, la seua implementació efectiva exigix que les molècules no tendisquen a agregar-se i que l'aprimament de la capa emissora es compense amb capes més gruixudes en el dispositiu per a evitar inestabilitat. Això resulta difícil a causa de la baixa mobilitat de portadors en els materials orgànics comuns.

Una altra estratègia és el processament en solució, en particular la impressió per injecció de tinta, que aconseguix quasi un 100% d'aprofitament del material. Els dendrímers són candidats ideals, perquè la seua estructura ramificada reduïx l'agregació i permet capes emissores sense amfitrió a baix cost. No obstant això, els processos en solució presenten el problema de dissoldre capes prèviament depositades, la qual cosa dificulta arquitectures multicapa.

En este context, les perovskites d'halur oferixen una solució doble: els seus precursors són barats i presenten excel·lents propietats de transport de càrrega, la qual cosa permet augmentar el gruix de les capes sense sacrificar eficiència. A més, la seua baixa solubilitat en dissolvents orgànics de baixa polaritat possibilita la deposició de capes superiors, afavorint estructures multicapa. També ajuden a augmentar el rendiment de producció en cobrir partícules o defectes del substrat i reduir curtcircuits locals.

En este treball es reporten OLEDs amb una capa de transport de perovskita gruixuda, explorant dos estratègies: la seua combinació amb una capa emissora de llum ultrafina no dopada i de baix cost, i la seua integració amb una capa emissora de llum de dendrímer processada en solució.

L'estudi investiga la fabricació i el rendiment de capes de transport de càrrega basades en perovskita de clorur de cesi i plom ($CsPbCl_3$), depositades mitjançant evaporació tèrmica simultània de CsCl i $PbCl_2$. $CsPbCl_3$ es va triar enfront d'altres perovskites d'halurs a causa de la seua transparència en el rang visible, la qual cosa evita absorcions no desitjades. No obstant això, les perovskites de clorur presenten estats profunds a causa de vacants d'halur. Per a mitigar-los, es van afegir fines capes de CsCl (2 nm) abans i després de $CsPbCl_3$, formant una estructura $CsCl/CsPbCl_3/CsCl$, denominada m-$CsPbCl_3$. Esta estratègia va reduir defectes superficials, va millorar la fotoluminescència i va induir un creixement cristal·lí preferent, com van confirmar els patrons de difracció de rajos X.

Es van fabricar dispositius OLED amb m-$CsPbCl_3$ com a capa de transport de buits en l'arquitectura òxid d'indi estany (ITO)/PEDOT:PSS/m-$CsPbCl_3$/mCP/$Ir(ppy)_2(acac)$/PO-T2T/Ba/Ag. La capa emissora ultrafina (0,03 nm) va permetre alta eficiència minimitzant el consum de material. Imatges de microscopi electrònic de rastreig van revelar grans verticals compactes i superfícies planes, la qual cosa va reduir curtcircuits. Els dispositius van aconseguir baix voltatge d'encesa (3,3 V), alta luminància (15 145 cd m^{-2}) i eficiència màxima de 52,9 cd A^{-1} (EQE 14,3%) amb escassa pèrdua a altes intensitats. L'emissió verda-groga (557 nm) es va mantindre estable, amb coordenades CIE invariants. Augmentar

el gruix de la capa de transport fins a 1000 nm no va reduir l'eficiència, demostrant la idoneïtat de $CsPbCl_3$ fins i tot en capes gruixudes. La passivació amb CsCl va ser essencial: dispositius amb $CsPbCl_3$ sense les modificacions van aconseguir només 30,7 cd A^{-1}. Estudis de AFM i angle de contacte van mostrar que les capes ultrafines de $Ir(ppy)_2(acac)$ creixen per illes, evitant agregació i *quenching*.

També es van fabricar OLEDs transparents amb m-$CsPbCl_3$ i un càtode Ba/Ag/ITO. Estos van mostrar transmitància del 40–70% en el visible, amb una transmitància mitjana del 50,6% i un índex de reproducció cromàtica de 88,5. Encara que la luminància va ser menor que en dispositius opacs, l'eficiència (41,3 cd A^{-1}, EQE de 11,2%) i la transparència els fan atractius per a finestres intel·ligents i pantalles.

Es va explorar substituir emissors d'iridi per molècules TADF com DMAC-TRZ. Capes ultrafines (0,1–1 nm) van mostrar creixement per illes i espectres dependents del voltatge. La grossària òptima va ser 1 nm, amb eficiències de 67,6 cd A^{-1} i EQE de 20,8%, comparable a dispositius més gruixuts però amb molt menor consum de material. Capes més fines van patir pèrdues per recombinació en la perovskita i menor puresa de color.

La resistència de $CsPbCl_3$ a dissolvents comuns (tolué, clorobenzé i cloroform) es va confirmar: les pel·lícules van conservar gruix, morfologia i propietats òptiques després del tractament. Això va permetre fabricar OLEDs amb emissors TADF processats en dissolució, com el dendrímer tBuCz2m2pTRZ. Els dispositius resultants van emetre en verd (565 nm), amb luminància de 4660 cd m^{-2} i eficiència >15 cd A^{-1}. Encara que el rendiment va ser inferior, es va demostrar la resistència de les capes de perovskita als solvents.

En conjunt, les capes de transport de perovskita $CsPbCl_3$ amb passivació de CsCl permeten OLEDs eficients, estables i versàtils. Suporten capes gruixudes, possibiliten capes emissores ultrafines, dispositius transparents i processaments en dissolució, mostrant gran potencial per al futur de la tecnologia OLED.

Mescla d'halurs en perovskites dopades per a díodes emissors de llum d'alta eficiència, amb color ajustable i sense capa de transport de buits.

Els semiconductors són essencials en tecnologies clau com a cèl·lules solars, fotodetectors, LEDs i làsers, i el seu rendiment depén de l'optimització de la banda prohibida. Les perovskites d'halur destaquen per oferir una "tunabilitat" de la banda prohibida molt major que els semiconductors tradicionals (III-V o II-VI), gràcies a la gran varietat de combinacions possibles d'ions A, B i X en la seua estructura. L'aliatge de diferents halurs permet ajustar la banda prohibida de manera senzilla, sense alterar les propietats fonamentals del material, la qual cosa ha permés obtindre cristalls únics, nanocristalls col·loidals i pel·lícules fines de perovskita amb emissió blava, verda, en el roig i infraroig proper (NIR).

No obstant això, la implementació pràctica d'estes mescles d'halurs en PeLEDs ha sigut desafiador a causa de problemes d'estabilitat de color, baixa vida útil sota voltatge i apagada de la fotoluminescència. Estos dispositius solen requerir estructures complexes amb múltiples capes o tractaments addicionals en les pel·lícules, la qual cosa augmenta la complexitat i el cost. La principal causa d'inestabilitat cromàtica és la segregació d'halurs, originada per la migració d'ions sota estímul elèctric o fotònic. Esta migració provoca regions riques en diferents halurs dins de la capa emissora, iniciant sovint en defectes vacants. Per això, estratègies que reduïsquen els defectes vacants i passiven superfícies i interfícies ajuden a mitigar este efecte.

Recentment, Xiong et al. van introduir un dopant molecular d'àcid fosfònic, (4PACz), capaç de passivar defectes superficials (principalment defectes vacants de Br) i modificar la conducció de càrrega. La seua forta capacitat de atreure electrons induïx la transició de conductivitat tipus n a p, desplaçant el nivell de Fermi i la part superior de la banda de valència sense perdre alta eficiència fotoluminescent. Això va permetre PeLEDs amb major eficiència i lluentor extrema usant una arquitectura sense capa de

transport de buits. Encara que inicialment aplicat a perovskites de bromur pur, el potencial de 4PACz per a estabilitzar el color va motivar el seu estudi en perovskites d'halurs mixtos.

Es van fabricar pel·lícules dopades de $(FA_{0,8}MA_{0,1}GA_{0,1})_{0,87}Cs_{0,13}Pb(Cl_xBr_{1-x})_3$ i $(FA_{0,8}MA_{0,1}GA_{0,1})_{0,87}Cs_{0,13}Pb(Br_{1-x}I_x)_3$ mitjançant el mètode A-NCP, variant x de 0 a 1. La quantitat dels diferents halurs en les pel·lícules va coincidir amb les solucions precursores, i la difracció de rajos X va confirmar la formació d'una fase de perovskita cúbica pura, amb pics desplaçant-se segons el radi iònic de l'halur. L'absorció òptica va mostrar un desplaçament lineal cap al blau en augmentar el Cl i cap al roig en augmentar el I, seguint la llei de Vegard. Les pel·lícules van exhibir un pic excitònic i una banda d'absorció estés, amb espectres de PL de línia única, estreta i simètrica, permetent una àmplia tunabilitat d'emissió entre 499 i 788 nm.

La PLQY va disminuir en afegir xicotetes quantitats de iode a $APbBr_3$, però va augmentar notablement amb major proporció de iode, aconseguint un 32% en $APb(Br_{0,2}I_{0,8})_3$. Les pel·lícules amb Cl van mostrar eficiència baixa, reflectint característiques intrínseques de les perovskites. Comparant amb pel·lícules no dopades, les dopades amb 4PACz van mantindre la mateixa banda prohibida, però amb PLQY superior a 10%, confirmant la capacitat del dopant de passivar estats profunds i reduir la segregació de fases.

Es va avaluar l'estructura electrònica mitjançant espectroscòpia de fotoelectrons a pressió atmosfèrica (PESA). En els dos casos, la disminució de la banda prohibida es correlaciona amb una part superior de la banda de València més superficial i un nivell de Fermi menys profund, i el dopant 4PACz desplaça el nivell de Fermi cap avall i la part superior de la banda de València cap amunt, facilitant la injecció de buits.

Finalment, es van fabricar PeLEDs sense capa de transport de buits usant perovskites dopades. Els dispositius van encendre entre 1,6 i 2,5 V, amb emissió de línia única estreta, cobrint visible i NIR (491–793 nm). L'eficiència màxima va aconseguir 25,9% en $APb(Br_{0,2}I_{0,8})_3$, superior a la majoria de NIR PeLEDs actuals, amb estabilitat del EQE sobre 20% en un ampli rang de densitat de corrent i radiància màxima de 236 W sr^{-1} m^{-2}. La vida operativa LT_{50} a radiància inicial de 24 mW sr^{-1} m^{-2} va ser de 133 minuts, demostrant el potencial de les perovskites dopades amb 4PACz en LEDs d'alta eficiència i estabilitat cromàtica.

Díodes emissors de llum de perovskita transparents basats en un elèctrode superior d'òxid conductor.

Els díodes emissors de llum transparents (TrLEDs) permeten mostrar informació sense obstruir la visibilitat de l'entorn, la qual cosa obri noves possibilitats d'aplicació, des de panells en finestres i parets fins a pantalles de realitat augmentada en vehicles i roba intel·ligent. A diferència dels LED tradicionals que posseïxen un elèctrode reflector i un altre transparent, els TrLEDs utilitzen elèctrodes transparents en els dos extrems, permetent l'emissió de llum en les dos direccions. Encara que la majoria dels dispositius transparents utilitzen materials orgànics per a l'emissió, les perovskites d'halur han demostrat propietats d'emissió superiors, particularment en els PeLEDs, a causa de la seua estructura prima i disseny eficient.

Els primers PeLEDs transparents (TrPeLEDs) van usar una pel·lícula de perovskita 3D ($MAPbBr_3$) i un elèctrode superior basat en una estructura dielèctric-metall-dielèctric (DMD). Estos dispositius van aconseguir una luminància de 6380 cd m^{-2} i una EQE del 1,21%. Posteriors desenrotllaments van aconseguir luminàncies de fins a 12 000 cd m^{-2} i una EQE del 16,1% per a emissió verda. No obstant això, les estructures DMD presenten desafiaments com a alt cost i la necessitat de controlar amb precisió el seu gruix. Per això, s'ha buscat l'ús d'òxids conductors transparents (TCOs) com a alternativa, sent l'òxid d'indi estany (ITO) el més prometedor per la seua alta transmissió òptica i baixa resistència.

Això no obstant, la deposició de l'ITO per polvorització catòdica pot danyar les delicades capes orgàniques i de perovskita, generant curtcircuits. Per a mitigar este problema, es va utilitzar una capa intermèdia d'òxid d'estany SnO_x, que protegix eficaçment durant el procés de deposició i millora el

transport de càrrega. La inclusió d'esta capa va permetre aconseguir luminàncies de fins a 90 000 cd m^{-2} i una EQE pròxima al 4%. En contrast, dispositius sense esta capa van mostrar un rendiment 10 vegades menor, amb EQE de 0,18%.

Una altra tècnica explorada va ser la deposició per làser polsat (PLD), que permet una deposició més suau comparada amb la polvorització, resultant en menor danys a les capes subjacents. Usant esta tècnica, es van fabricar en este treball dispositius que van aconseguir luminàncies combinades de 148 000 cd m^{-2} i una EQE de l'11%, superant àmpliament els TrPeLEDs prèvies basades en DMD. L'emissió va ser homogènia des dels dos costats del dispositiu, encara que la cara inferior va mostrar major intensitat, atribuïda a fenòmens òptics com la interferència i absorció parasitària.

A més, es van avaluar les propietats estètiques i de transparència. La transmitància mitjana en el rang visible va ser de 46,7%, amb una transmitància visible mitjana (AVT) ajustada a l'ull humà del 50,9%. Encara que estes xifres són acceptables, la fidelitat del color (CRI) va ser baixa (44,87), donant una tonalitat groguenca-vermellosa. Per a millorar este aspecte, es va reduir a la mitat el gruix de la capa emissora, aconseguint una AVT de 66,4% i un CRI de 89,2, la qual cosa millora considerablement la qualitat visual, encara que a costa d'una menor luminància i eficiència.

Es va provar també l'aplicabilitat d'esta tecnologia amb diferents estructures i composicions de perovskita, incloent-hi estructures nuclis/revestiments (*core*/*shell*) i nanocristalls col·loidals. Encara que estos dispositius van mostrar menor rendiment elèctric, van aconseguir nivells de transparència excepcionals, amb AVT de fins a 80% i CRI superiors a 90, acostant-se als requisits de la indústria automotriu.

En conclusió, la combinació de tècniques com ALD i PLD va permetre fabricar TrPeLEDs altament eficients i transparents. Esta estratègia és escalable i adaptable a diferents arquitectures, obrint camí a aplicacions innovadores com a finestres intel·ligents, pantalles integrades i dispositius portàtils amb visibilitat bidireccional. L'enfocament provat podria fins i tot ser rellevant per a la indústria de pantalles mòbils, on es requerixen estructures emissores des de la part superior.

Emissió blava eficient i estreta a partir d'una capa emissora ultrafina hiperfluorescent

Els OLEDs de tercera generació utilitzen emissors amb fluorescència retardada activada tèrmicament (TADF) per a convertir eficientment els triplets en excitons singlets emissors, aconseguint així eficiències quàntiques internes (IQE) pròximes al 100% usant materials orgànics. No obstant això, esta tecnologia enfronta obstacles, com l'agregació de les molècules emissores (ACQ), que disminuïx l'eficiència, i la baixa puresa del color degut a bandes d'emissió amples (FWHM > 40 nm). Per a millorar la puresa del color, s'han desenrotllat emissors de banda estreta, destacant els compostos TADF de ressonància múltiple (MR-TADF), com ν-DABNA, que presenten emissió blava ultrapura.

ν-DABNA, amb una estructura rígida i orbitals electrònics localitzats, permet una emissió estreta i altament eficient. Es van fabricar dispositius OLED amb capes emissores ultrafines no dopades de ν-DABNA, amb grossàries entre 0.03 i 1 nm, observant-se que la puresa del color disminuïx amb l'augment de la grossària deguda a l'agregació molecular. Els dispositius amb capa de 0.03 nm van mostrar una emissió blava pura amb coordenades de color $CIE_{x,y}$ = (0,13, 0,19), una FWHM de 18 nm i una eficiència màxima de 17% EQE, encara que amb una vida operativa limitada (~31 h a 100 cd m^{-2}).

Per a resoldre el problema de caiguda d'eficiència a alts nivells de luminància, es va implementar la tecnologia de hiperfluorescència, que combina un emissor fluorescent (ν-DABNA) amb un sensibilitzador TADF (DMAC-TRZ). L'energia generada elèctricament per DMAC-TRZ es transferix eficientment a ν-DABNA mitjançant transferència d'energia per ressonància de Förster (FRET), permetent una vida útil del triplet més curta i millorant l'estabilitat electroquímica sense sacrificar la puresa del color. Per a evitar les complexitats de la tradicional co-deposició, es va explorar un enfocament de deposició seqüencial de capes ultrafines, amb ν-DABNA i DMAC-TRZ depositats per separat. Es va determinar que una capa de 0.03 nm de DMAC-TRZ juntament amb una altra de 0.03 nm

de ν-DABNA era la combinació òptima, aconseguint una eficiència màxima de 13,9% i reduint significativament la caiguda d'eficiència en altes lumināncies (68% augment de l'EQE a 10 000 cd m^{-2} en comparació amb dispositius sol amb ν-DABNA).

Es va utilitzar l'espectroscòpia d'electroluminescència transitòria (TEL) per a estudiar la dinàmica excitònica. Es va observar que els dispositius amb hiperfluorescència presentaven temps de decaïment intermedis, compatibles amb la transferència d'energia de DMAC-TRZ a ν-DABNA. A més, els temps d'encesa i decaïment van ser consistents amb processos excitònics governats per triplets de llarga vida.

Els experiments dependents de la temperatura van confirmar que el procés de rISC (encreuament intersistema invers), essencial per a l'eficiència TADF, és tèrmicament activat, amb una energia d'activació de 0.184 eV. També es va mesurar la mobilitat dels portadors de càrrega ($\sim 9.23 \cdot 10^{-6}$ $cm^2\ V^{-1}\ s^{-1}$), i es va extraure la seua energia d'activació tèrmica (0.227 eV).

En resum, este treball introduïx una arquitectura nova de OLEDs amb capes emissores ultrafines basades en TADF multiressonància, que aconseguix simultàniament alta eficiència, puresa de color, baix cost de fabricació i baixa caiguda d'eficiència, obrint camí a futures aplicacions en pantalles d'alta gamma i ampli espectre de color.

Perspectives generals i conclusions

Conclusions generals

Malgrat l'excel·lent rendiment i qualitat d'imatge que oferixen les tecnologies LED i OLED, el seu impacte potencial es veu limitat si no s'aconseguix una adopció a gran escala. Per a això, no n'hi ha prou amb tindre dispositius eficients; factors com els costos de fabricació i l'escalabilitat són determinants perquè estes tecnologies arriben al mercat massiu.

Amb esta perspectiva, l'objectiu principal d'este treball doctoral va ser superar les barreres que dificulten l'adopció generalitzada dels OLEDs i PeLEDs, principalment els alts costos de fabricació, sense sacrificar la seua alta eficiència ni la seua qualitat del color. Per a aconseguir-ho, es van desenvolupar noves arquitectures de dispositius que integren perovskites (materials de baix cost i excel·lents propietats optoelectròniques), capes emissores ultrafines (UEMLs) i molècules TADF.

En primer lloc, es va demostrar que una combinació d'una capa de transport de buits de perovskita gruixuda, UEMLs i emissors TADF permet mantindre alts nivells d'eficiència al mateix temps que es reduïx l'ús de materials costosos. Els dispositius van aconseguir una lumināncia màxima superior a 10 000 cd m^{-2} i eficiències de fins a 67,6 cd A^{-1}. L'ús de perovskites va permetre augmentar el gruix sense pèrdua d'eficiència, mentres que els emissors TADF i els UEMLs van optimitzar la utilització de excitons.

En segon lloc, es van fabricar PeLEDs amb emissió de color ajustable i una arquitectura sense HTL, la qual cosa reduïx els costos de producció i millora la reproductibilitat. Estos dispositius van mostrar una emissió que cobrix des de 491 fins a 793 nm i van aconseguir EQE de fins a 25,9%.

Finalment, es va ampliar el catàleg de compostos utilitzats en capes ultrafines, incloent-hi dispositius basats en ν-DABNA, els quals van conservar l'emissió blava pura i van aconseguir una EQE del 17% i una lumināncia de més de 13 000 cd m^{-2}. A més, l'evaporació seqüencial de DMAC-TRZ va ajudar a reduir la caiguda d'eficiència sense complicar el procés de fabricació.

Un altre objectiu del treball va ser millorar l'experiència de l'usuari, aspecte clau per a impulsar una adopció més àmplia. Es van desenvolupar PeLEDs transparents que combinen els avantatges òptics de les perovskites (emissió estreta de 20 nm, eficiència de fins a 11% i lumināncia combinada d'aproximadament 150 000 cd m^{-2}) amb la possibilitat d'integració en aplicacions innovadores com a realitat augmentada, finestres intel·ligents, pantalles transparents i dispositius electrònics portàtils.

A més dels desenvolupaments pràctics, este treball també va aprofundir en les propietats fonamentals dels materials i dispositius. Es va presentar una estratègia per a passivar defectes interfacials en pel·lícules de perovskites co-evaporades, i es va estudiar el comportament de creixement en illes dels UEMLs, que no interferixen amb la formació de excíplexos en heterojuncions.

Es va analitzar l'efecte de àcids fosfònics sobre perovskites mixtes, millorant les seues propietats òptiques i reduint la segregació d'halurs. Es va mostrar com la barrera de SnO_x i l'ús de deposició per làser polsat permeten fabricar PeLEDs transparents de manera universal. Finalment, l'últim capítol va demostrar que es pot aconseguir hiperfluorescència en capes emissores ultrafines.

Perspectives futures

L'adopció massiva de OLEDs i PeLEDs podria contribuir significativament a la reducció del consum energètic global i facilitar l'accés a il·luminació i pantalles d'alta qualitat. No obstant això, encara persistixen obstacles, com la menor eficiència dels UEMLs enfront de les capes emissores convencionals, problemes de morfologia en unes certes perovskites mixtes i la limitada estabilitat operativa dels PeLEDs transparents.

Possibles solucions inclouen l'ús d'espaiadors o emissors TADF amb velocitats de encreuament intersistema invers més ràpids, additius per a millorar la morfologia, noves tècniques de deposició més uniformes i mètodes menys agressius per a l'aplicació de càtodes transparents. Un altre repte crític és la toxicitat del plom present en les perovskites, per la qual cosa s'estan explorant alternatives sense plom i mètodes d'encapsulació i reciclatge.

Appendix

List of abbreviations and acronyms

3D	Three dimensional
4PACz	4-(9H-carbazol-9-yl)butyl)phosphonic acid
ACQ	Aggregation-caused quenching
AFM	Atomic force microscopy
ALD	Atomic layer deposition
Alq_3	Tris-(8-hydroxyquinoline) aluminum
A-NCP	Additive based nanocrystal pinning
AVT	Average visible transmittance
BA	n-butylammonium
BPA	Benzylphosphonic acid
CB	Conduction band
CBM	Conduction band minimum
CBP	4,4′-bis(N-carbazolyl)-1,1′-biphenyl
CIE	International Commission on Illumination
CRI	Color rendering index
CT	Charge-transfer
CVD	Chemical vapor deposition
CzEABr	2-(9H-carbazol-9-yl)ethanaminium bromide
DAm	Decylamine
DC	Direct current
DMD	Dielectric–metal–dielectric
DMF	Dimethylformamide
DMSO	Dimethyl sulfoxide
EBL	Electron blocking layer
EDS	Energy-dispersive X-ray spectroscopy
EIL	Electron injection layer
EL	Electroluminescence
EQE	External quantum efficiency
ETL	Electron transport layer
FA	Formamidinium
FWHM	Full width half maximum
GBL	γ-butyrolactone
GIWAXS	Grazing-incidence wide-angle X-ray scattering
GraHIL	Hole-injection layer with a gradient work function
HBL	Hole blocking layer
HF	Hyperfluorescence
HI	Hot-injection method
HIL	Hole injection layer
HOMO	Highest occupied molecular orbital
HTL	Hole transport layer
ICT	Intramolecular charge-transfer

IEA	International Energy Agency
IQE	Internal quantum efficiency
$Ir(ppy)_2acac$	Bis[2-(2-pyridinyl-N)phenyl-C](acetylacetonato)iridium(III)
ISC	Intersystem crossing
ITO	Indium tin oxide
IZO	Indium zinc oxide
J–V–L	Current density–voltage–luminance characteristics
LARP	Ligand-assisted re-precipitation method
LCD	Liquid crystal display
LED	Light-emitting diode
LOE	Light outcoupling efficiency
LUMO	Lowest unoccupied molecular orbital
MA	Methylammonium
mCP	1,3-bis(N-carbazolyl)benzene
MHPs	Metal halide perovskites
MR	Multiresonance (also called multiple resonance)
MR-TADF	Multiple resonance thermally activated delayed fluorescence
NCP	Nanocrystal pinning
NCs	Nanocrystals
NPs	Nanoparticles
OA	Oleic acid
OAm	Oleylamine
ODE	1-octadecene
OLED	Organic light-emitting diode
PCB	Printed circuit board
PEDOT:PSS	Poly(3,4-ethylenedioxythiophene) polystyrene sulfonate
PeLED	Perovskite light-emitting diode
PeNCs	Perovskite nanocrystals
PESA	Photoelectron spectroscopy in air
PFI	Tetrafluoroethylene – perfluoro-3,6-dioxa-4-methyl-7-octene-sulfonic acid copolymer
PhOLED	Phosphorescent organic light-emitting diode
PL	Photoluminescence
PLD	Pulsed laser deposition
PLQY	Photoluminescence quantum yield
PO-T2T	2,4,6-tris[3-(diphenylphosphinyl)phenyl]-1,3,5-triazine
PVD	Physical vapor deposition
QCM	Quartz crystal microbalance
rISC	Reverse intersystem crossing
RoHS	Restriction of Hazardous Substances
SEM	Scanning electron microscope
SI	International System of Units
SMU	Source measure unit
SOC	Spin-orbit coupling
SRH	Shockley–Read–Hall
STA	Singlet–triplet annihilation
TADF	Thermally activated delayed fluorescence
TAPC	1,1-bis[(di-4-tolylamino)phenyl]cyclohexane
tBuCz2m2pTRZ	9',9'''',9''''''',9'''''''''-((6-phenyl-1,3,5-triazine-2,4-diyl)bis(benzene-4,1,2-triyl))tetrakis(3,3'',6,6''-tetra-tert-butyl-9'H-9,3':6',9''-tercarbazole)
TCO	Transparent conducting oxide

TDAT	Tetrakis(dimethylamino)tin
TEL	Transient electroluminescence
THF	Tetrahydrofuran
TPBi	1,3,5-tris(N-phenylbenzimidizol–2-yl)benzene
TrLEDs	Transparent light-emitting diodes
TrPeLEDs	Transparent perovskite light-emitting diodes
TTA	Triplet–triplet annihilation
TV	Television
UCS	Uniform chromaticity scale
UEML	Ultrathin emissive layer
VB	Valence band
VBM	Valence band maximum
XRD	X-ray diffraction

List of symbols of physical quantities and their units

Symbol	Quantity	Unit
k_{rISC}	Reverse intersystem crossing rate	s^{-1}
k_{ISC}	Intersystem crossing rate	s^{-1}
ΔE_{ST}	Singlet-triplet energy gap	eV
k_{B}	Boltzmann constant	$eV\ K^{-1}$
T	Temperature	K
E_{g}	Bandgap	eV
E_{F}	Fermi level	eV
Φ_{e}	Radiant power	W
$\Phi_{\mathrm{e},\lambda}$	Spectral radiant power	$W\ nm^{-1}$
$I_{\mathrm{e},\lambda}$	Spectral radiant intensity	$W\ sr^{-1}\ nm^{-1}$
Φ_{v}	Luminous power	lm
I_{v}	Luminous intensity	$lm\ sr^{-1} = cd$
K	Luminous efficacy	$lm\ W^{-1}$
R_{λ}	Photodiode's spectral responsivity	$A\ W^{-1}\ nm^{-1}$
R	Photodiode's responsivity	$A\ W^{-1}$
I_{pd}	Photodiode's current	A
E_{ph}	Photon energy	eV
h	Planck constant	$eV\ Hz^{-1}$
c	Speed of light	$m\ s^{-1}$
η_{int}	Internal quantum efficiency	
γ	Electron/hole balance	
ζ_{s}	Exciton generation efficiency	
q	Photoluminescence quantum efficiency	
η_{o}	Light outcoupling efficiency	
I	Current	A
J	Current density	$A\ m^{-2} = 0.1\ mA\ cm^{-2}$
V	Voltage	V
V_{on}	Turn on voltage	V
L	Luminance	$cd\ m^{-2} = nt$
$L_{\mathrm{e},\Omega}$	Radiance	$W\ sr^{-1}\ m^{-2}$
A	Area	m^2
	Luminous current efficiency	$cd\ A^{-1}$
S_{q}	Root mean square roughness	nm
χ	Molar fraction	

List of Publications

Included in this PhD thesis

1. **Michele Forzatti**, Sang-Hyun Chin, M. Angeles Hernández-Fenollosa, Michele Sessolo, Daniel Tordera, and Henk J. Bolink. Organic Light-Emitting Diodes Combining Thick Inorganic Perovskite Hole Transport Layers and Ultrathin Emitting Layers. *Advanced Optical Materials 12* (27), 2401061 (**2024**).

2. **Michele Forzatti**, Vladimir Held, Edoardo Stanzani, David Hall, Dianming Sun, M. Angeles Hernández-Fenollosa, Isaac Brotons-Alcazar, Peter Siffalovic, Sandra Jenatsch, Eli Zysman-Colman, Henk J. Bolink, and Daniel Tordera. Organic light-emitting diodes comprising an undoped thermally activated delayed fluorescence emissive layer and a thick inorganic perovskite hole transport layer. *ACS Photonics 11* (10), 4151-4160 (**2024**).

3. **Michele Forzatti**, Sergio Martínez Saiz, Kassio Zanoni, Cristina Roldán Carmona, Daniel Tordera, and Henk J. Bolink. Halide mixing in doped perovskites for color-tunable, HTL-free and high-efficiency light-emitting diodes (manuscript in preparation).

4. **Michele Forzatti**, Sergio Martínez Saiz, Morena Cervino, Edoardo Stanzani, Sandra Jenatsch, Tae-Woo Lee, Daniel Tordera, and Henk J. Bolink. Transparent perovskite light-emitting diodes based on a conductive oxide top electrode (manuscript in preparation).

5. **Michele Forzatti**, Edoardo Stanzani, Sandra Jenatsch, Daniel Tordera, and Henk J. Bolink. Efficient blue narrowband emission from an ultrathin hyperfluorescent MR-TADF emissive layer (manuscript in preparation).

Other publications

1. Isabella A. Kalluvila Justin, David O. Tiede, Manuel Piot, **Michele Forzatti**, Cristina Roldán-Carmona, Juan F. Galisteo-López, Hernán Míguez, and Henk J. Bolink. Strong Grain Boundary Passivation Effect of Coevaporated Dopants Enhances the Photoemission of Lead Halide Perovskites. *ACS Applied Materials & Interfaces 16* (44), 61305-61313 (**2024**).

2. Jorge Roy, **Michele Forzatti**, Lorenzo Arnal, Antonio Martín, Sara Fuertes, Daniel Tordera, and Violeta Sicilia. Pyrazolate-Bridged NHC Cyclometalated [Pt_2] Complexes and [$Pt_2Ag(PPh_3)$]$^+$ Clusters in Electroluminescent Devices. *Inorganic Chemistry 63* (16), 7275-7285 (**2024**).

3. Jorge Roy, **Michele Forzatti**, Antonio Martín, Irene Ara, Edoardo Stanzani, Sandra Jenatsch, Henk J. Bolink, Sara Fuertes, Daniel Tordera, and Violeta Sicilia. Surfing the Color Map with Carbazole-Appended Cyclometalated N-Heterocyclic Carbene Pt Complexes and Their Application in Green Organic Light-Emitting Devices. *Advanced Optical Materials*, 2500051 (**2024**).

4. Purificación Cañadas, **Michele Forzatti**, Sara Fuertes, Antonio Martín, Daniel Tordera, and Violeta Sicilia. Platinum (II) Complexes Bearing Functionalized NHC-based Pincer Ligands: Synthesis and Application in Phosphorescent OLEDs. *Materials Chemistry Frontiers 9*, 2559-2570 (**2025**).

5. Qingsen Zeng, Yue Zhao, Sunghee Park, Huanyu Zhou, Hyun-Joon Shim, Min-Jun Sung, Jinseok Ryu, Xian Wei Chua, Eojin Yoon, Barney A.I. Lewis, Seung-Je Woo, **Michele Forzatti**, Min Ju Kim, Eun A Kim, Linjie Dai, Jinhyeong Jang, Yipeng Tang, Jin Jung Kweon, Hao Chen, Kyung Yeon Jang, Dong-Hyeok Kim, Woo Jin Jeong, Joo Sung Kim, Hyejin Lee, Kyueun Lim, Seong-Yong Cho, Chan Beum Park, Sung Keun Lee, Miyoung Kim, Henk J. Bolink, Bin Hu, Samuel D. Stranks, and Tae-Woo Lee. A hierarchical shell locks and stabilizes perovskite nanocrystals with near-unity quantum yield. *Science* (accepted for publication, **2025**).

6. Alessandro Ciccone, Ignacio Rosa-Pardo, Jagadeesh Metikoti, **Michele Forzatti**, Henk J. Bolink, Raquel E. Galian, and Julia Pérez-Prieto. Photohealing treatment of colloidal metal halide perovskites nanocrystals: reshaping and boosting their performance (manuscript in preparation).

7. Rita B. Cevallos-Toledo, Matteo Andrea Lucherelli, **Michele Forzatti**, Michele Sessolo, Henk J. Bolink, Raquel Gallian, Gonzalo Abellán, Julia Pérez-Prieto. Graphene-driven template effect and stability enhancement of in-situ synthesized perovskite-graphene supramolecular heterostructure (manuscript in preparation).

8. Surendra B. Anantharaman, Federico Fabrizi, Sana Khan, Liudmila Starodubtceva, Saeed Goudarzi, Manuel Runkel, Cedric Kreusel, Thomas Riedl, Felix Thiel, Peter Haring Bolivar, **Michele Forzatti**, Isabella Antony Kalluvila Justin, Andrea Zacheo, Giorgio Adamo, Daniele Cortecchia, Thorsten Wahlbrink, Antonio Fieramosca, Daniele Sanvitto, Cesare Soci, Henk J. Bolink, Annamaria Petrozza, Maryam Mohammadi, and Max C. Lemme. Progress, Challenges, and Emerging Opportunities toward Electrically driven Halide Perovskite Lasers (manuscript in preparation).

Acknowledgements

This thesis would not have been possible without the guidance, encouragement, and support of many people, to whom I am grateful.

I would like to start with my directors. Henk, I am sincerely thankful for the trust and confidence you placed in me when selecting me over the other candidates for this position. I hope that I have lived up to your expectations and that you do not regret your choice. I know for a fact that being the leader of such a large group takes up much of one's time, and while this may have prevented us from meeting frequently to discuss results and science, I have always interpreted that as a sign of confidence rather than a lack of interest. When we did find the time to meet, you demonstrated enviable experience and pragmatism. I will also always be grateful for the opportunity you gave me to carry out three research stays during my PhD, which I feel privileged to have experienced. I hope I have contributed in a meaningful way to the advancement of your group, at the very least as a sign of respect and gratitude.

Dani, I feel very lucky to have had you as my co-director. Our periodic meetings helped me stay on track with my work, and I felt that the interpretation of results and the writing of manuscripts and reports were always a joint effort. This has really brought me one step closer to being a scientist. More importantly, I want to thank you for being there whenever I needed someone to confide in. Your *older-brother-like* advice was just as important in helping me stay motivated and complete my PhD. Thank you also for the paellas in Xilxes and for the great company during the network meetings! The boat trip, the time in the spas, and the visit to the *Cité du Vin* were a lot of fun. I hope I was able to reciprocate a little by showing you around Sondrio!

Michelone, we haven't really interacted much, but every time we did, it was very educational. You emanate an aura of erudition, and I would have loved to have you as a supervisor, too.

Jorge, thank you for dedicating so much time to me (certainly more than I could proportionally ask for, given the size of the group). A big part of this thesis has also consisted in developing more convenient setups for OLED characterization, and if they now exist, it's also thanks to your creativity and skill. Thank you for making me part of their creation and for the electronics and programming knowledge you shared with me in the process!

Sang, all the colorful devices on this thesis cover are indirectly thanks to you, as you were the one to accompany me and hold my hand while I was taking my first steps into the realm of semiconductors and thin-film device fabrication! Some might not agree, but I always found you very methodical, something I later came to treasure and that has helped me throughout my PhD (감사합니다!). It was nice spending Christmas with you in Seoul, where you also showed me how to properly cook Korean barbecue, and I'm happy to share authorship with you on the perovskite-as-HTL manuscript.

I can only hope I did an equally good job with Sergio, to whom I am also deeply thankful. You are *el millor* student I could ever have the chance to supervise! I deem you very smart and diligent; you have all the prerequisites to achieve something scientifically remarkable over the course of your own doctorate. Thanks for all the help in the lab, and congratulations on making the most efficient light-emitting diode that the group has ever seen (I don't think your record will ever be beaten). Thanks for sharing (and sorry for making you put up with) my frustration when dropping the TPBi solution filled the substrates with stains and cracks.

Lorenzo, I also can't forget your help during my very first days here; your LEC knowledge is still passed down from one generation of students to another, and thanks for introducing me to the group dynamics. It's unfortunate you were finishing your PhD when I arrived and we didn't overlap much.

Qingsen, many, many thanks (*xièxiè*!) for your supervision during my stay at SNU. You are extremely knowledgeable and patient, and I learned so much during my time there. Above all, I understood that what I was doing there is what I am most passionate about and what I want to keep researching in the future. Prof. Tae-Woo Lee, I wanted to thank you too for hosting me in your group.

Similarly, a big thank-you goes to Sandra for supervising me during my stay at FLUXiM and for the super useful feedback you've always provided us with; to Beat for making me feel welcome there and for all the advice you gave me during the network meetings; to Miguel at ZHAW; and to Andy for greeting me in Durham.

María, you also played a big role in my and everyone else's PhD! You do your fundamental job very well, and I hope you can find a lot of satisfaction in that. *Ho sente molt* for mistaking you for Rosa at the beginning xD

There are many people who maybe didn't contribute much to the scientific part of my PhD but whom I need to thank nonetheless for their friendship and for creating a pleasant environment, both in and out of the lab! I'll remember all the moments together fondly, and I hope to recall some cherished episodes if you read this less serious and more playful part of the acknowledgements.

Cristina, I might not have always worn a lab coat in the lab, but it's good that we have an *ángel de la guarda andaluz* who watches over us and our safety, so thanks for that and for the SEM images. Kassio, thanks for composing the dubstep-like melodies that I was forced to listen to during device characterization, for the bread from the cafetería, for being an amazing Río Fraile guide, and for the AFM images. No amount of chocolate will ever pay that back! Lídon, your meticulousness should be a model for everyone! *Gràcies per les converses en valencià també*!

Fede, I can't comment on your scientific competence, but you certainly play ping-pong well. Thanks also for the climbing and life advice! Vlado, I'm not sure you're an example to follow (tell me the truth, how many times were you still in the office at 10 p.m.?), but your dedication is remarkable. Maybe one day we'll see you going around the world sticking in situ stuff into thermal evaporators. Sorry if the bike I gave you wasn't rated for very tall Slovakian people. Maxi, all those hours spent on the rooftop testing device stability gave you a really nice tan, perfect for going to the beach to surf. Yun, thanks for the dinner in Korea and for being a worthy tennis opponent!

I don't precisely remember when the sect agreed to my entrance, but I'm proud to be an honorable member of the *Office Bois*! Manu, sorry for dragging you into too many questionable ideas and trips, but I hope you had fun learning how to prepare agua de Valencia, cycling to Olocau and the Albufera, hiking in the Pyrenees or at Forat de Bèrnia, becoming thick with Jeroni, and coming to ESN or VLE events. So thank you for your company in all of that! If you fail as a "materials engineer and scientist," you can always be a nightingale in a choir. Serhii, or should I write Cepriй, without you my PhD would probably have been over half a year ago already, because that's the total time I spent reading Wikipedia with you or playing GeoGuesser. In your defense though, most things were interesting, so thanks for that and for giving us a taste of Ukrainian culture (literally). Also, if I find a job, there's a big chance it'll have been recommended by you. Hold on for the sake of your PhD, and try not to be too harsh with Spain's HDI or Lourdes. Joost, *mah boi*, you sound like a seagull when you shout that, a mother seagull that also fed us with Amaretto liqueur and "*tarta laminada*" from Consum, and provided us with shelter (= your house to watch movies). We have some photos to testify to those moments together, like the one above our desk, but not in the EsMolNa, because we didn't attend any talks and we missed the photo moment.

Abhi!! The night security personnel at ICMol miss you now that you don't keep them company at night, and we miss you too! It was crazy when you randomly took a cleanroom hairnet out of your shirt pocket. It was nice meeting you again in Berlin, and thanks for the invitation to your wedding (sorry I didn't attend!).

Carsen, our encounters have been as random as the English words I send you, but casually meeting you in Seattle was special! I should thank you for that with a walk in Burjassot followed by a romantic dinner at Mercadona. Hopefully that's enough, and I don't have to do the *salto del novio* in stormy water. Lennart, beneath the frank Dutch exterior lies a generous heart! Thanks for all the hiking, climbing, and ping-pong, and for organizing the workshop. Sofía and Javi, we started around the same time, thanks for your house parties and for being competitive ping-pong mates! Inma, you are unparalleled when it comes to breaking the silence and the CSS. You failed to kill me with an electric scooter, but overall it was a good evening and night. Jons, I could hear you coming from the office to the cleanroom, getting ready to play Four in a Row!

There is then a series of "old" PhD students that I could look up to when I was a puny newcomer! Argha, just so you know, I managed to finish my thesis without assembling the drawer, and my kakis are still in the fridge. Lucía, thanks for your energy, my aunt still asks about you! Isabella, in another life we'll make one of our joint devices work. Nathan, you sometimes had to put up with my outpourings of exasperation, but we had to put up with you and your trumpet noise at all times, so we're even. Thanks for introducing me to climbing, too! It was so random to meet you in Picos de Europa and in Switzerland, but hopefully we'll meet in the latter again. Isidora, I still haven't understood if you were a talisman or a jinx to me and my dates. Chris, thanks for your LabVIEW software and for making me appreciate that I can visualize things in my head.

Many more PhD and master's students and visiting researchers were part of the group over the years and also contributed to the good atmosphere: Bas, Paz, Roos, Rianne, Morena (sono orgoglioso di te e dei tuoi traguardi!), Giulio, Tamara, Ana, Alejandra, Manuel, Jasmine, Masha, Jae-In, Marly, Matthieu (thanks for our tennis rivalry!), Alex, Di, Carla, Miguel, Caroline, Nacho, Johan, Adrian, Jorge, and Giada.

Thank you also to all the members of the *TADFsolutions* doctoral network! To Claire for the organization, to Anna for the promotion, to Eli, Malte, and Reinder for bringing their scientific expertise to the consortium! And of course to Dodo and Vasilis, for the work together in Winterthur, to Kamile for the OLEDs in England, and to Anatolii, Papi, Christian, Mahni, and all the others for the frenzy of our meetings.

Our group was certainly cohesive and separate in some aspects, but I still managed to mingle a bit with the rest of ICMol! It was nice to have lunch, play ping-pong, or simply meet in the corridor for a quick chat with Anna, Pietro, Jana, Alessandro, Rita, Matteo, Pilar, Jagadeesh, Caterina, Delia, Alejandro, Paco, Marta, Mariluz, Christina, Alba, and Juanjo!

Finally, I can't forget about the people who might not have been directly involved in my thesis work but still indirectly contributed with their support, from Valencia (Hania and Sandra, Yolanda, Sofía, Barbora, Adrian, Dana, John, Laura), other countries (Florian! Should we bitte call? I had so much fun when you came here and had a video call with your professor from Buñol. And Thomas! If I'm here, it's because I ignored your advice, but it's nice that we managed to keep in touch and share PhD stories), and, of course, Italy (Giulia, Francesco, Simone, Denis, Palla, Andrea, and my siblings and father, *a i quài völi bée*. Grazie a tutti voi!).